

# **X-RAY EMISSION FROM CLUSTERS OF GALAXIES**

Thesis submitted by

**ALASTAIR CLOUSTON EDGE**

to the University of Leicester for the degree of  
Doctor of Philosophy

March 1989

X-ray Astronomy Group,  
Department of Physics,  
University of Leicester

UMI Number: U017635

All rights reserved

INFORMATION TO ALL USERS

The quality of this reproduction is dependent upon the quality of the copy submitted.

In the unlikely event that the author did not send a complete manuscript and there are missing pages, these will be noted. Also, if material had to be removed, a note will indicate the deletion.



UMI U017635

Published by ProQuest LLC 2015. Copyright in the Dissertation held by the Author.  
Microform Edition © ProQuest LLC.

All rights reserved. This work is protected against  
unauthorized copying under Title 17, United States Code.



ProQuest LLC  
789 East Eisenhower Parkway  
P.O. Box 1346  
Ann Arbor, MI 48106-1346



Declaration

I hereby declare that no part of this thesis has been previously submitted to this or any other University as part of the requirements for a higher degree. The work described here was conducted as indicated except for the contributions from colleagues as indicated in the text.

Alastair C. Edge  
March 1989

Astronomy is something like the ministry. No one should go into it without a 'call'. I got that unmistakable call, and I know that even if I were second rate or third rate, it was astronomy that mattered.

*Edwin Hubble*

I would to thank the staff of the AAO for my 'call' and my parents for allowing me to answer it.

## Publications

Edge, A.C., Stewart, G.C. & Smith, A. 1986. in *NRAO Greenbank Workshop No.16, Radio Continuum Processes in Clusters of Galaxies*, ed. C.P. O'Dea and J.M. Uson, p. 105.

Edge, A.C. & Stewart, G.C. 1988. in proceedings of NATO ASI "*Hot Thin Plasmas in Astrophysics*" ed Pallavicini, Reidel, p.335.

Edge, A.C., Johnstone, R.M., Fabian, A.C. & Takalo, L. 1989. In preparation.

Lahav, O., Edge, A.C., Fabian, A.C. & Putney, A. 1989. *Mon. Not. R. astr. Soc.*, **238**, 881.

M<sup>c</sup>Hardy, I.M., Stewart, G.C., Edge, A.C., Cooke, B.A., Yamashita, K. & Hatsukade, I. 1989. *Mon. Not. R. astr. Soc.* in press.

# Contents

<b>1 Clusters of Galaxies</b>	<b>1</b>
1.1 An Overview of Theoretical Models for Clusters . . . . .	1
1.1.1 The Distribution of Mass . . . . .	2
1.1.2 Cluster Dynamics and the Determination of Mass . . . . .	3
1.1.3 Cluster Morphology and Evolution . . . . .	6
1.1.4 The Origin of the ICM . . . . .	7
1.1.5 Clusters and Cosmology . . . . .	7
1.1.6 Cooling Flows . . . . .	8
1.2 Review of Previous Observations . . . . .	10
1.2.1 Optical . . . . .	10
1.2.2 Radio . . . . .	11
1.2.3 X-ray . . . . .	13
1.2.4 Recap . . . . .	15
1.3 Observations of Clusters with EXOSAT . . . . .	16
1.4 Summary . . . . .	17
<b>2 Analysis of EXOSAT Images</b>	<b>18</b>
2.1 Satellite Description . . . . .	18
2.1.1 Background . . . . .	19
2.1.2 Observing Strategy . . . . .	20
2.2 Data Analysis . . . . .	22
2.2.1 Surface Brightness Profile Fitting . . . . .	22

2.2.2	Deprojection . . . . .	23
2.3	Results . . . . .	24
2.3.1	Results from Surface Brightness Fitting . . . . .	27
2.3.2	Problems with Surface Brightness Fitting . . . . .	27
2.3.3	Results from Deprojection Analysis . . . . .	27
2.3.4	Effect of Input Parameters on Deprojection Results . . . . .	35
2.3.5	Problems with Deprojection Analysis . . . . .	38
2.3.6	Fitting Profiles to Derived Densities . . . . .	39
2.4	Comparison with <i>EINSTEIN</i> Results . . . . .	40
2.5	Summary . . . . .	42
<b>3</b>	<b>Analysis of the EXOSAT Spectra</b>	<b>45</b>
3.1	Instrument Description . . . . .	45
3.1.1	Performance during mission . . . . .	46
3.1.2	Observing Strategy . . . . .	46
3.2	Data Analysis . . . . .	46
3.2.1	Background Subtraction . . . . .	47
3.2.2	Collimator Corrections . . . . .	49
3.2.3	Spectral Fitting . . . . .	50
3.3	Results . . . . .	50
3.3.1	Comparing Bremsstrahlung and Raymond & Smith Models . . . . .	50
3.3.2	Iron Lines . . . . .	55
3.3.3	Column Densities . . . . .	59
3.4	Individual Clusters . . . . .	60
3.5	Comparison with Published <i>EXOSAT</i> Results . . . . .	62
3.6	Comparison with Previous X-ray Observations . . . . .	62
3.6.1	HEAO-1 . . . . .	62
3.6.2	MPC . . . . .	64
3.7	Conclusions . . . . .	64

<b>4</b>	<b>EXOSAT observations of the Virgo, Coma and Perseus Clusters</b>	<b>65</b>
4.1	Analysis of Highly Extended Sources with the ME . . . . .	65
4.2	Virgo . . . . .	67
4.2.1	Previous X-Ray Results . . . . .	67
4.2.2	<i>EXOSAT</i> Observations . . . . .	68
4.2.3	Implications of the <i>EXOSAT</i> results . . . . .	74
4.2.4	Summary . . . . .	75
4.3	Coma . . . . .	79
4.3.1	Previous X-Ray Results . . . . .	79
4.3.2	<i>EXOSAT</i> Observations . . . . .	80
4.3.3	Implications of <i>EXOSAT</i> Results . . . . .	87
4.3.4	Summary . . . . .	89
4.4	Perseus . . . . .	90
4.4.1	Previous X-Ray Results . . . . .	90
4.4.2	<i>EXOSAT</i> Observations . . . . .	91
4.4.3	Implications of <i>EXOSAT</i> Results . . . . .	100
4.4.4	Summary . . . . .	101
4.5	Conclusions . . . . .	101
<b>5</b>	<b>Correlation Analysis of the EXOSAT Sample</b>	<b>102</b>
5.1	X-ray Results . . . . .	102
5.2	Optical Results . . . . .	105
5.3	Radio Results . . . . .	109
5.4	Correlation Analysis . . . . .	109
5.4.1	Least Squares Fits . . . . .	111
5.4.2	Rank and Partial Rank Correlation Coefficients . . . . .	111
5.5	X-ray to X-ray Correlations . . . . .	112
5.6	X-ray to Optical Correlations . . . . .	117
5.7	X-ray to Radio Correlations . . . . .	127

5.8	Conclusions . . . . .	127
<b>6</b>	<b>Astrophysical Implications of the EXOSAT Sample</b>	<b>129</b>
6.1	Luminosity and Temperature . . . . .	129
6.2	Iron Abundances . . . . .	131
6.3	Cluster Mass . . . . .	133
6.3.1	The Distribution of Mass . . . . .	133
6.3.2	Deriving $\beta$ . . . . .	134
6.4	Mass-To-Light versus Luminous-to-Total Mass Ratios . . . . .	136
6.4.1	Gas Mass to Stellar Mass Ratio . . . . .	141
6.5	Stripping of Spiral Galaxies . . . . .	141
6.6	Cooling Flows . . . . .	142
6.7	Constraints on the Hubble Constant and Cosmology . . . . .	144
6.8	Conclusions . . . . .	144
	<b>Conclusions</b>	<b>146</b>
	Future Prospects . . . . .	147
	<b>References</b>	<b>i-ix</b>

# List of Figures

1.1	Total cooling function . . . . .	9
1.2	Examples of wide-angle tails . . . . .	12
1.3	Schematic diagram of the configuration of <i>EXOSAT</i> . . . . .	16
2.1	Schematic diagram of LE telescope design . . . . .	19
2.2	Example of LE image . . . . .	20
2.3	Surface brightness profile of blank LE image . . . . .	21
2.4	Effective areas of principal LE filters . . . . .	21
2.5	Examples of King model fitting . . . . .	28
2.6	Central surface brightness against core radius in arcmin . . . . .	31
2.7	Central surface brightness against core radius in kpc . . . . .	31
2.8	Examples of deprojection analysis . . . . .	34
2.9	Examples of varying the outer pressure on results for A2052 . . . . .	36
2.10	Examples of varying the core radius on results for A2052 . . . . .	36
2.11	Examples of varying the velocity dispersion on results for A2052 . . . . .	37
2.12	Examples of varying the potential on results for A2052 . . . . .	37
2.13	Comparing core radii obtained from fitting surface brightness and density profiles . . . . .	39
2.14	Results for core radius from <i>EXOSAT</i> and <i>EINSTEIN</i> . . . . .	42
2.15	Results for mass flow rate from <i>EXOSAT</i> and <i>EINSTEIN</i> . . . . .	43
2.16	Results for central density from <i>EXOSAT</i> and <i>EINSTEIN</i> . . . . .	43
2.17	Example of LE & HRI and LE & IPC deprojection for A2199 and A1060 . . . . .	44
3.1	Blow-up of ME detectors . . . . .	47

3.2	Examples the photon spectra of fitted Raymond & Smith models . . . . .	53
3.3	Plot of temperatures for bremsstrahlung model fits against RS model fits . . . . .	54
3.4	Plot of reduced $\chi^2$ for bremsstrahlung and RS models . . . . .	54
3.5	Equivalent width for 6.67 keV line plotted against temperature . . . . .	58
3.6	Iron abundance plotted against temperature from Raymond & Smith model . . . . .	58
3.7	Plot of galactic column density and measured column density . . . . .	60
3.8	Plot comparing temperatures determined by <i>EXOSAT</i> and HEAO-1 . . . . .	63
3.9	Plot comparing temperatures determined by <i>EXOSAT</i> and <i>EINSTEIN</i> MPC . . . . .	63
4.1	Predicted flux for the ME against offset angle . . . . .	66
4.2	Schematic map of the <i>EXOSAT</i> pointings on Virgo . . . . .	69
4.3	Low resolution LE image of M87 . . . . .	70
4.4	High resolution LE image of M87 . . . . .	70
4.5	Plots of parameters derived from the deprojection analysis of LE images of Virgo . . . . .	71
4.6	Best fit to the 1984 M87 observation . . . . .	73
4.7	Best fit to the offset quadrants for the 1984 M87 observation . . . . .	76
4.8	Best fit photon spectrum to 1983 Observation C . . . . .	76
4.9	2-10 keV flux against offset angle from M87 for the Virgo pointings . . . . .	77
4.10	Measured temperature against offset angle from M87 for Virgo . . . . .	77
4.11	Iron abundance against offset angle from M87 for Virgo . . . . .	78
4.12	Total gravitational mass for the Virgo cluster plotted against radius . . . . .	78
4.13	Schematic map of the <i>EXOSAT</i> pointings on Coma . . . . .	81
4.14	LE image of Coma . . . . .	81
4.15	Plots of results from deprojection of LE images of Coma . . . . .	82
4.16	Best fit to the 1983 Coma central observation . . . . .	84
4.17	Best fit to the offset quadrant 4 of the 1984 Coma eastern observation . . . . .	84
4.18	2-10 keV flux against offset angle from the centre of Coma . . . . .	85
4.19	Measured temperature against offset radius for Coma . . . . .	85
4.20	Iron abundance and Equivalent width against radius for Coma . . . . .	86

4.21	Calculated gravitational mass plotted against radius for Coma . . . . .	88
4.22	Schematic map of <i>EXOSAT</i> pointings on Perseus . . . . .	92
4.23	LE Image of Perseus . . . . .	92
4.24	Plots of parameters derived from deprojection analysis of LE images of Perseus . . . . .	94
4.25	Best fit to the central Perseus 1985 pointing for single Raymond & Smith model . . . . .	95
4.26	Best fit to the central Perseus 1985 pointing with two component model . . . . .	96
4.27	Best fit photon spectrum of central Perseus 1985 pointing for the two component model split into the two components . . . . .	96
4.28	Best fit to the eastern Perseus pointing . . . . .	97
4.29	Best fit to the northern Perseus pointing . . . . .	98
4.30	2–10 keV flux from the cluster against offset angle from NGC 1275 . . . . .	99
4.31	Measured temperature against offset radius for Perseus . . . . .	99
4.32	Iron abundance against offset radius for Perseus . . . . .	100
5.1	Bolometric correction for 2–10 keV flux plotted against temperature . . . . .	103
5.2	Histograms of X-ray data . . . . .	106
5.3	Histograms of optical data . . . . .	108
5.4	Histograms of radio data . . . . .	109
5.5	Bolometric luminosity plotted against temperature . . . . .	114
5.6	Bolometric luminosity plotted against gas mass . . . . .	114
5.7	Temperature plotted against gas mass . . . . .	115
5.8	2–10 keV flux plotted against redshift . . . . .	115
5.9	Bolometric luminosity plotted against redshift . . . . .	116
5.10	Temperature plotted against redshift . . . . .	116
5.11	Bolometric luminosity plotted against Bautz-Morgan type . . . . .	118
5.12	Bolometric luminosity plotted against Rood-Sastry type . . . . .	118
5.13	Temperature plotted against Bautz-Morgan type . . . . .	119
5.14	Temperature plotted against Rood-Sastry type . . . . .	119
5.15	Mass flow rate plotted against Bautz-Morgan type . . . . .	120
5.16	Mass flow rate plotted against Rood-Sastry type . . . . .	120

5.17	Bolometric luminosity plotted against velocity dispersion . . . . .	123
5.18	Bolometric luminosity plotted against Bahcall number density . . . . .	123
5.19	Bolometric luminosity plotted against optical luminosity of the brightest galaxy . .	124
5.20	Bolometric luminosity plotted against percentage of spiral galaxies . . . . .	124
5.21	Temperature plotted against velocity dispersion . . . . .	125
5.22	Temperature plotted against Bahcall number density . . . . .	125
5.23	Temperature plotted against optical luminosity of the brightest galaxy . . . . .	126
5.24	Temperature plotted against the percentage of spirals . . . . .	126
5.25	1.4 GHz radio power plotted against bolometric luminosity . . . . .	128
5.26	Radio spectral index plotted against bolometric luminosity . . . . .	128
6.1	Bolometric luminosity plotted against temperature split by measured central density	130
6.2	Temperature plotted against Bahcall number density and velocity dispersion split on mass flow rate . . . . .	131
6.3	Ratio of gas mass to total mass plotted against temperature . . . . .	132
6.4	Iron abundance plotted against bolometric luminosity . . . . .	132
6.5	Histograms of $\beta_i$ and $\beta_s$ . . . . .	135
6.6	Comparison of $\beta_s$ derived from <i>EXOSAT</i> temperature and to $\beta_i$ from <i>EINSTEIN</i> IPC data . . . . .	136
6.7	Derived value for $\beta_s$ plotted against temperature and velocity dispersion . . . . .	137
6.8	Total mass-to-blue light ratio plotted against temperature . . . . .	139
6.9	Luminous mass-to-total mass ratio plotted against temperature . . . . .	139
6.10	Ratio of the gas and stellar masses plotted against temperature . . . . .	140
6.11	Gas-to-total and stellar-to-total mass ratios for data from David <i>et al.</i> . . . . .	140
6.12	Fraction of galactic types plotted against derived bolometric luminosity . . . . .	142
6.13	Cooling luminosity plotted against derived bolometric luminosity . . . . .	143

# List of Tables

1.1	Summary of major X-ray satellites flown before <i>EXOSAT</i> . . . . .	14
2.1	Performance of LE telescopes . . . . .	19
2.2	Log of LE observations . . . . .	25
2.3	Results from King fits to surface brightness profiles . . . . .	29
2.4	Results from King fits to surface brightness profiles with $\beta$ free . . . . .	30
2.5	Parameters used in deprojection analysis . . . . .	32
2.6	Results from deprojection of surface brightness profiles . . . . .	33
2.7	Comparison of published and presented mass flow rates . . . . .	35
2.8	Results from King model fits to density profiles . . . . .	41
3.1	Performance of ME proportional counters . . . . .	46
3.2	Log of ME observations . . . . .	48
3.3	Results from bremsstrahlung model fits . . . . .	51
3.4	Results from Raymond & Smith model fits . . . . .	52
3.5	Values for F-statistic . . . . .	56
3.6	Results for line fits to spectra with fluxes greater than $5 \times 10^{-11}$ erg cm <sup>-2</sup> s <sup>-1</sup> . . . . .	57
3.7	Summary of previously published <i>EXOSAT</i> results . . . . .	62
4.1	Log of <i>EXOSAT</i> observations of Virgo . . . . .	68
4.2	Results of the spectral fits to ME data from Virgo. The quoted errors are 90% confidence. . . . .	72
4.3	Log of <i>EXOSAT</i> observations of Coma . . . . .	80
4.4	Results of spectral fits to ME data from Coma . . . . .	83

4.5	Comparison of the results for Coma with those from Hughes, Gorenstein & Fabricant (1988) . . . . .	87
4.6	Log of <i>EXOSAT</i> observations of Perseus . . . . .	91
4.7	Results for spectral fits to ME data from the central Perseus 1985 pointing . . . . .	94
4.8	Results for spectral fits to ME data from Perseus . . . . .	98
5.1	Table of derived X-ray luminosities . . . . .	104
5.2	Table of optical parameters from the literature . . . . .	107
5.3	Table of radio parameters from the literature . . . . .	110
5.4	Table with results for least squares fits to X-ray data . . . . .	113
5.5	Table of averages of X-ray properties for particular optical types . . . . .	121
5.6	Table with results from least squares fits for bolometric luminosity and optical parameters . . . . .	122
5.7	Table with results from least squares fits for temperature and optical parameters . . . . .	122

# Chapter 1

## Clusters of Galaxies

### Introduction

Clusters of galaxies are the largest gravitationally bound systems in the Universe. They contain 100–1000 galaxies in a volume of a few  $\text{Mpc}^3$ . The large relative velocities of these galaxies ( $\sim 1000 \text{ km s}^{-1}$ ) indicate that, if clusters are bound, large gravitational masses ( $10^{13-15} M_{\odot}$ ) are present. Clusters also contain large amounts of hot, X-ray emitting gas held in the potential well of the cluster. This gas is at temperatures of  $10^7-8 \text{ K}$  and densities of  $10^{-4}-10^{-2} \text{ cm}^{-3}$ . The gas is also enriched with heavy elements at around half solar abundance indicating it has been processed in stars. The mass of gas in clusters is as large as that in galaxies.

It is well established that only 5–20% of the mass in the Universe is in the form of stars or gas (*e.g.* Blumenthal *et al.* 1984). The rest of the mass is in some form that does not radiate at observable wavelengths (*i.e.* it is ‘Dark’) and possibly non-baryonic.

This thesis is based on observations of clusters by the European X-ray Observatory SATellite, *EXOSAT*. This Chapter reviews the basic properties of clusters. The theoretical and observational background are discussed with particular emphasis on the X-ray domain. The Chapter ends with an outline of the opportunities *EXOSAT* offered for the study of clusters and how *EXOSAT* was used to take advantage of these.

### 1.1 An Overview of Theoretical Models for Clusters

In this section a brief summary of the theoretical background in the area of clusters of galaxies is presented. Methods for the determination of the distribution of mass from optical and X-ray observations are given. The dynamics of the galaxies and gas are reviewed and the possibilities of

determining the total mass from either are discussed. The possible evolutionary scenarios are presented with particular reference to the role of the intra-cluster medium (ICM). The implications of the study of clusters on cosmological questions are mentioned. Finally the importance of radiative cooling of the gas in clusters is discussed and the phenomenon of "cooling flows" is mentioned.

### 1.1.1 The Distribution of Mass

The simplest assumption that can be made about the mass distribution is that the 'Dark' mass is distributed in the same way as the 'Light' mass, *i.e.* 'light follows mass'. From optical studies the galaxy distribution has been determined for a large number of clusters (*e.g.* Beers & Tonry 1986; Colless 1987). The exact form of the distribution is not well understood and a number of models fit the observed data. The most popular is the formalism of King (1966) where the projected number density of galaxies,  $N(r)$ , is

$$N(r) = N_0 \left(1 + \left(\frac{r}{a}\right)^2\right)^{-1} \quad (1.1)$$

and the galaxy space density,  $n_{\text{gal}}$ , is

$$n_{\text{gal}} = n_0 \left(1 + \left(\frac{r}{a}\right)^2\right)^{-\frac{3}{2}} \quad (1.2)$$

These models parameterise the distribution in terms of a central number density,  $N_0$  or a central space density,  $n_0$ , and a core radius,  $a$ . The King model implies the mass increases logarithmically with radius for radii  $\gg a$ . The other commonly used model is the de Vaucouleurs model (de Vaucouleurs 1948) which gives the number density of galaxies as

$$\log\left(\frac{N}{N_e}\right) = -3.33 \left(\left(\frac{r}{r_e}\right)^{\frac{1}{4}} - 1\right) \quad (1.3)$$

where  $r_e$  is the "effective radius" which contains half the total luminosity and  $N_e$  is the number density at that radius.

The gas distribution can also be parameterised using the King profile. In the formalism of Cavaliere & Fusco-Femiano (1976), the X-ray surface brightness,  $S(r)$ , can be expressed as

$$S(r) = S_0 \left(1 + \left(\frac{r}{a}\right)^2\right)^{\frac{1}{2} - 3\beta} \quad (1.4)$$

The King and de Vaucouleurs models have been compared with the X-ray surface brightness profiles by Pallister (1985). Pallister found that the overall agreement was good apart from the core regions, which are often complicated with cooling emission.

The gas density profile can be expressed as

$$\rho_{\text{gas}} = \rho_0 \left(1 + \left(\frac{r}{a}\right)^2\right)^{-\frac{3\beta}{2}} \quad (1.5)$$

$$i.e. \quad \rho_{\text{gas}} = \rho_{\text{gal}}^\beta \quad (1.6)$$

As both the gas and galaxies are responding to the same gravitational potential the difference in scale heights ( $\beta$  in Equation 1.6) can also be expressed as the ratio of the mean energy in the galaxies to that in the gas. For isotropic orbits this ratio is

$$\beta = \frac{\mu m_{\text{H}} \sigma_{los}^2}{kT} \quad (1.7)$$

where  $\sigma_{los}$  is the line of sight galaxy velocity dispersion,  $T$  is the X-ray gas temperature,  $\mu$  is the mean particle mass and  $m_{\text{H}}$  is the mass of a proton.

Therefore the parameter  $\beta$  can be derived by two independent methods; from the X-ray surface brightness profile and from the measured velocity dispersion and X-ray temperature. The imaging results from Jones and Forman (1984) give  $\langle\beta_{\text{imaging}}\rangle \approx 0.7$ , whereas the spectral data from Mushotzky (1984) give  $\langle\beta_{\text{spectral}}\rangle \approx 1.2$ . This inconsistency is commonly referred to as the ‘Beta problem’.

The implication of a  $\beta < 1$  is that the gas is ‘hotter’ than the galaxies. This could occur if the gas had been injected into the ICM with more energy than the galaxies. This possibility is considered in Section 1.1.4.

### 1.1.2 Cluster Dynamics and the Determination of Mass

The size and shape of a potential can be determined from the relative motions of test particles within it. In the case of clusters two sets of ‘test particles’ exist: galaxies and gas atoms. The sampling of the potential with the gas is much better than that of the galaxies as there are only a limited number of galaxies that can be studied. Also the interpretation of the galaxy dynamics requires an assumption about the distribution of galactic orbits (*i.e.* radial or tangential) as only

the line of sight component of the velocity can be determined. This does not apply to the gas where the measurement of the gas temperature is not dependent on the viewing angle.

The total cluster mass can be determined in two ways: from the optical data using the velocity dispersion, or from the X-ray data using the the density and temperature profiles. These two methods are outlined below.

### Optical Mass Determination

The cluster mass can be determined from the Virial Theorem. Assuming the cluster is bound

$$E = T + W < 0 \quad (1.8)$$

where  $E$  is the total energy of the cluster,  $T$  is the kinetic energy of the galaxies and  $W$  is the gravitational potential energy.

$$T = \frac{1}{2} \sum_i m_i v_i^2 \quad \text{and} \quad W = -\frac{1}{2} \sum_{i \neq j} \frac{G m_i m_j}{r_{ij}} \quad (1.9)$$

where the sum is over all the galaxies,  $m_i$  and  $v_i$  are mass and velocity of the  $i^{\text{th}}$  galaxy and  $r_{ij}$  is the separation of the  $i^{\text{th}}$  and  $j^{\text{th}}$  galaxies. Integrating the equations of motion of the galaxies gives

$$\frac{1}{2} \frac{d^2 I}{dt^2} = 2T + W \quad (1.10)$$

where  $I$  is the total moment of inertia,  $I = \sum m_i r_i^2$ . For a stationary, non-evolving configuration  $d^2 I / dt^2 = 0$ , so

$$W = -2T \quad \text{and} \quad E = -T \quad (1.11)$$

If  $\sum m_i = M_{\text{tot}}$  then

$$\sigma^2 = \frac{\sum m_i v_i^2}{M_{\text{tot}}} \quad (1.12)$$

Also the gravitational radius,  $R_G$ , is given as

$$R_G = 2M_{\text{tot}}^2 \left( \sum_{i \neq j} \frac{m_i m_j}{r_{ij}} \right)^{-1} \quad (1.13)$$

Therefore Equation 1.11 becomes

$$-\frac{1}{2}G \frac{2M_{\text{tot}}^2}{R_G} = -2\frac{1}{2}M_{\text{tot}} \sigma^2 \quad (1.14)$$

$$\Rightarrow M_{\text{tot}} = \frac{R_G \sigma^2}{G} \quad (1.15)$$

And if the galaxy orbits are isotropic then

$$M_{\text{tot}} = \frac{3R_G \sigma_{\text{los}}^2}{G} \quad (1.16)$$

where  $\sigma_{\text{los}}$  is the measured line-of-sight velocity dispersion.

Testing the validity of this method against numerical N-body calculations shows reasonable agreement between the 'true' and virial masses (White 1976; Fernley & Bhavsar 1984; Frenk 1988). However the dependence on assumptions about the galaxy orbits limits the accuracy of the Virial method.

### X-ray Mass Determination

As the sound crossing time in the gas held within the cluster is short ( $\sim 10^9$  yr) compared with probable age of a cluster (*i.e.* the Hubble time of  $2 \times 10^{10}$  yr), then the gas should be close to hydrostatic equilibrium. This implies that

$$\frac{dP_{\text{gas}}}{dr} = -\rho_{\text{gas}} \frac{d\phi}{dr} = -\rho_{\text{gas}} g \quad (1.17)$$

where  $P$  is the gas pressure,  $\phi$  is the gravitational potential and  $g = GM(< r)/r^2$ . As  $\mu m P_{\text{gas}} = \rho_{\text{gas}} kT$  then

$$kT \frac{d\rho_{\text{gas}}}{dr} + k\rho_{\text{gas}} \frac{dT}{dr} = -\rho_{\text{gas}} \mu m \frac{GM(< r)}{r^2} \quad (1.18)$$

Which simplifies to

$$M(< r) = -\frac{kTr}{\mu mG} \left( \frac{rd\rho_{\text{gas}}}{\rho_{\text{gas}}dr} + \frac{rdT}{Tdr} \right) \quad (1.19)$$

And as  $\frac{y}{x} \frac{dx}{dy} = \frac{d \log x}{d \log y}$  then

$$M(< r) = -\frac{kTr}{\mu mG} \left( \frac{d \log \rho_{\text{gas}}}{d \log r} + \frac{d \log T}{d \log r} \right) \quad (1.20)$$

So if the radial variation of density and temperature are known then the total enclosed mass can be determined model independently (unlike the optical determination which requires assumptions about the galactic orbits). The measurement of spatially resolved spectra has been not possible with any previous mission, but will be possible using the next generation of high throughput, nested foil telescopes with CCD detectors.

### 1.1.3 Cluster Morphology and Evolution

The optical and X-ray morphology are good indicators of the evolutionary state of a cluster. From models of violent relaxation (Lynden-Bell 1967) it follows that any substructure that exists soon after collapse will be ‘ironed-out’ by 2-body interactions. So clusters will tend to become more symmetrical with time. This implies that young clusters will be ‘clumpy’ and irregular, whereas the more evolved clusters will be symmetrical and regular. This is the basis of the morphological scheme of Jones and Forman (1984), where clusters are split into 4 groups; clusters with or without a central dominant galaxy (XD or nXD), which are either regular or irregular. The timescales for merging and virialising are comparable with the cluster age ( $\sim 10^9-10^{10}$  yr) so a wide range of morphologies would be expected. Comparing the observed morphologies to those expected from numerical N-body simulations (White 1976; Carnevali, Cavaliere & Santangelo 1981; West, Oemler & Dekel 1988; Frenk 1988) gives qualitative agreement.

The detailed study of cluster evolution requires a statistical analysis of a large sample of clusters at a wide range of redshifts. Most models for the formation and development of clusters predict that the X-ray luminosity increases with time as more gas enters the ICM (Perrenod 1980; Cavaliere & Colafrancesco 1988). Models of evolution must also include the influence of cluster mergers (*i.e.* hierarchical clustering). McGlynn & Fabian (1984) consider cluster mergers and conclude that two merging clusters exist as a “double” for a relatively long time compared to the merging timescale. This implies that there should be an enhanced probability of observing double clusters. The X-ray observations show some evidence that there is a high frequency of double clusters (Forman *et al.* 1981; Lahav *et al.* 1989). However, the small numbers of clusters involved and the ‘incompleteness’ of the sampling limit the conclusions that can be drawn about cluster evolution, from these double clusters.

#### 1.1.4 The Origin of the ICM

The existence of a large amount of gas (comparable to the mass in galaxies) which is enriched with heavy elements (and hence has been processed in stars) has strong ramifications on theories of galaxy and cluster formation.

There are two principal theories for the origin of the ICM. De Young (1978) proposed that the gas is a remnant of the short lived, high mass stars formed at the initial stage of galaxy formation. The large numbers of supernovæ push gas out of galaxies in a 'hot wind'. This model implies approximately solar abundance gas for clusters of all masses, does not require substantial amounts of primordial gas and, if the gas is expelled at velocities much larger than the galactic escape velocity, gives a higher specific energy in the gas to that in galaxies (*i.e.*  $\beta < 1$ ). This 'hot wind' model was also invoked by Bookbinder *et al.* (1980) to explain the 40 keV bremsstrahlung component in the diffuse X-ray background.

Alternatively Lea & de Young (1976) proposed stripping as a mechanism for removing enriched gas from galaxies into the ICM. This model requires a substantial amount of primordial gas to initiate the stripping process. However their models can only account for a few percent of the total gas mass seen. So, although stripping can have a large influence on the interstellar medium of a galaxy, it cannot account for all the gas in the ICM.

#### 1.1.5 Clusters and Cosmology

Clusters offer an important test-bed for cosmological models. The form of the 'Dark Matter' in the Universe is the most important element in modern cosmological models. These models break down into two main groups: 'Hot Dark Matter' (HDM) where the mass is in the form of non-interacting dissipationless particles mostly in the form of massive neutrinos; or 'Cold Dark Matter' (CDM) where the mass is in the form of very weak interacting particles such as axions (which are scalars proposed to conserve parity in 'strong' interactions) or photinos (which are the supersymmetric partners to photons). These models have implications for all areas of astrophysics. For clusters the main difference between the two models is that CDM models predict that the 'Dark' mass will be distributed on the same scale as the 'visible' mass. However HDM models predict the 'Dark' mass should be distributed on a much larger scale (Bond & Szalay 1983).

The spatial distribution of clusters is affected by the initial form and scale of the density fluctuations after the 'Big Bang'. Work on the distribution of X-ray clusters by Lahav *et al.* (1989) gives results consistent with the those from optical clusters and favour CDM models (Bahcall & Soniera 1983; Lahav, Rowan-Robinson & Lynden-Bell 1988).

Observations of clusters can also be used to determine the rate of expansion of the Universe, *i.e.* value of the Hubble Constant,  $H_0$ , and the deceleration parameter,  $q_0$ . Sunyaev & Zel'dovich (1972) predicted that the cosmic micro-wave background radiation would be Compton scattered by the thermal electrons in the ICM. The magnitude of the effect is dependent on the temperature and density profile of the gas, and produces a distance estimate independent of redshift. As yet this method has not been able to definitely determine  $H_0$  (McHardy *et al.* 1989) as the radio measurements have been limited to distant clusters (for instrumental reasons) which are difficult to obtain reliable X-ray temperatures for. However in the near future radio and X-ray instrumentation will allow  $H_0$  and  $q_0$  to be determined accurately and without relying on the assumptions used in the Distance Ladder.

The methods for determining the mass in a cluster mentioned above assume that the long range gravitational force scales as  $\frac{1}{r^2}$ . If this does not hold then the calculated masses are radically altered. The work of Milgrom (1983a,b & c) on Modified Newtonian Dynamics (MOND) can be applied to clusters. The & White (1988b) applied MOND to Coma and found solutions consistent with the optical and X-ray data. The expected temperature profile for MOND models is quite different from that of the standard models, so spatially resolved spectra will be able to put strong constraints on MOND models.

### 1.1.6 Cooling Flows

The cooling flow phenomenon has provoked intense theoretical and observational interest for the past 10 years. Since the proposals of Cowie & Binney (1977) and Fabian & Nulsen (1977) that radiative cooling at the centres of clusters would cause bulk flow of gas inward a large body of observational evidence has built up to support the idea. There are a number of points that are disputed. In this section the basic principles of cooling flows are reviewed, the evidence for cooling flows are summarised and some of the controversial points raised by cooling flows are discussed.

#### Radiative Cooling

As stated above the gas held within clusters is at temperatures of  $\sim 10^7$ - $10^8$ K. If the gas is in hydrostatic equilibrium and is not heated then the gas will lose energy gradually by radiating X-rays. The rate of this radiative cooling depends on the temperature and is shown in Figure 1.1.

As the emission rate is related to the square of the density, the cooling rate at the centre of a cluster will be higher than that further out. The increase in cooling toward the centre results in a pressure gradient above that from the gravitational potential. This pressure gradient leads to inward bulk motion of gas.

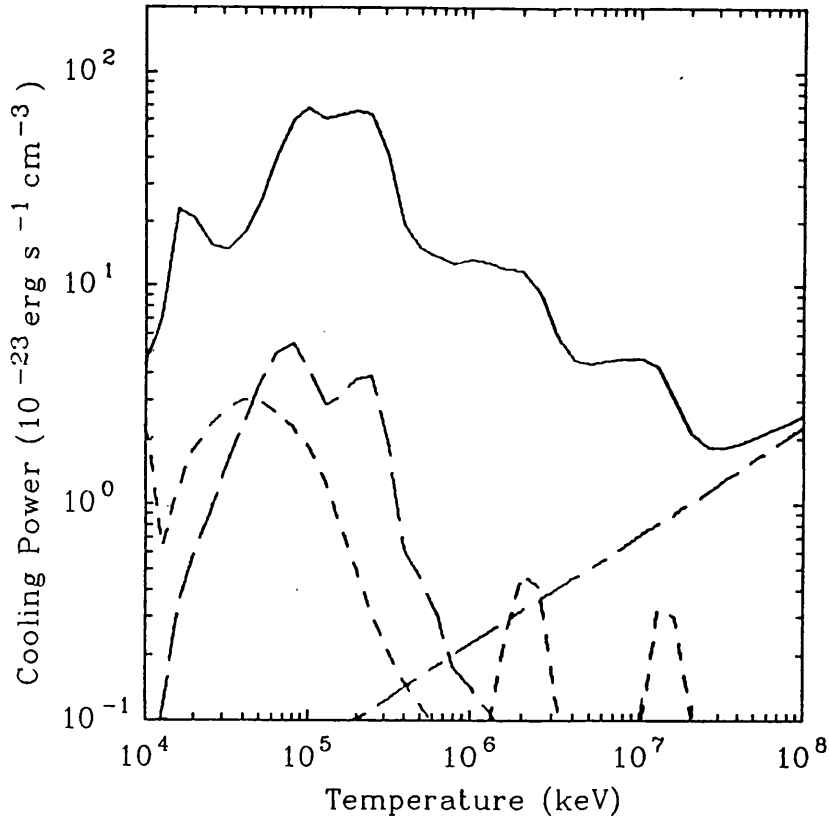


Figure 1.1: Total cooling function from Raymond, Cox & Smith (1976). The solid curve is the total cooling power, the short dashed curve is the forbidden line cooling, the long dashed line is the semiforbidden line cooling and the mixed dashed line is the bremsstrahlung emission.

The radiative cooling time for gas to cool from a temperature,  $T$ , to below  $10^4$ K is given by

$$t_{\text{cool}} = \frac{5}{2} kT \frac{2.3 \log T}{\rho \Lambda(T)} \approx 7 \times 10^{10} T_8^{1/2} \rho_{-3}^{-1} \text{ yr} \quad (1.21)$$

where  $\Lambda$  is the cooling function,  $T_8$  is the temperature in units of  $10^8$ K and  $\rho_{-3}$  is the gas density in units of  $10^{-3} \text{ cm}^{-3}$ . For densities and temperatures that give values of  $t_{\text{cool}}$  less than the age of the universe, gas will have cooled below  $10^4$ K (*i.e.* condensed). Given a moderate mass flow rate of  $100 M_{\odot} \text{ yr}^{-1}$  then over a Hubble time a mass of  $2 \times 10^{12} M_{\odot}$  will have been deposited.

### X-ray Evidence

There is a substantial body of X-ray evidence to support the cooling flow model. The evidence includes:

- X-ray images show excess central emission indicating cooler, denser gas (*e.g.* Stewart *et al.* 1984b; Arnaud 1988a; see Chapter 2).
- The temperatures measured in the centres of clusters with the *EINSTEIN* SSS are lower than the overall cluster temperature (Mushotzky *et al.* 1981; Lea, Mushotzky & Holt 1982).
- Several X-ray emission lines detected by the *EINSTEIN* FPCS are characteristic of gas at  $\sim 10^6$  K (Canizares, Markert & Donahue 1988).

## Controversial Points

The main criticism of the cooling flow model is that  $10^{10}$ – $10^{13} M_{\odot}$  of gas must condense into some form that is to date unobservable, *e.g.* low mass stars, brown dwarves, *etc.* (Fabian, Nulsen & Canizares 1982). There is optical evidence that the stellar population of the central galaxy in cooling flow clusters is different from that of galaxies in non-cooling clusters (Johnstone, Fabian & Nulsen 1987). The presence of optical filaments (Kent & Sargent 1979; Hu, Cowie & Wang 1983) also suggests substantial amounts of cooling gas. However the star formation rate in cooling flows is a factor of  $\sim 100$  lower than the X-ray determined cooling rate (*i.e.* a few  $M_{\odot} \text{ yr}^{-1}$  to a few hundred  $M_{\odot} \text{ yr}^{-1}$ ). Mechanisms to suppress the cooling rate have been suggested; conduction (Bertschinger & Meiksin 1986; Rosner & Tucker 1989), local heating from galaxies (Miller 1986), supernovæ (Silk *et al.* 1986) or cosmic rays (Tucker & Rosner 1982; Raphaeli 1987). However these suppression models cannot account for the X-ray line emission from low temperature gas in cooling clusters (Canizares *et al.* 1979 & 1982) and do not apply generally to the wide variety of cooling flow cluster masses and morphologies.

## 1.2 Review of Previous Observations

A short review of the previous observations is presented in this section. For an extensive review of work on clusters of galaxies the reader is referred to the recent book by Sarazin (1988).

### 1.2.1 Optical

The tendency for galaxies to cluster was noted by many observers in the last century but was first investigated by Wolf (1906). The most important work on clusters is undoubtedly the study performed by Abell (1958) which provided the first catalogue of rich clusters in the Northern sky. More recently, a similar study of the Southern sky was completed (Abell, Corwin & Olowin 1989).

These catalogues were compiled from visual searches of Palomar and UK Schmidt Sky Survey plates for enhancements in the number of galaxies above the background level. Clusters were assigned a 'richness' dependent on the number of galaxies present and a classification dependant on the structure of the cluster (*e.g.* Compact, Binary, Linear, *etc.*)

The northern Catalogue has provided the basis for nearly all the cluster observations at all wavelengths since it was published 30 years ago.

The principal observed optical properties of clusters are :-

**Redshift** Many Abell and most X-ray detected clusters have measured redshifts (Struble & Rood 1987). If a redshift is not available then the redshift can be estimated from the magnitude of the tenth brightest galaxy,  $m_{10}$ , (Postman *et al.* 1985).

**Velocity Dispersion** Velocity dispersions for a number of clusters have been measured (Struble & Rood 1987). The number of well determined velocity dispersions (i.e. more than 50 galaxies) has increased rapidly in the last few years with the advent of multi-object spectroscopy techniques (Ellis *et al.* 1984). These new results have shown that velocity substructure is common (Fitchett & Merritt 1988; Fitchett 1988) and in these cases the measured velocity dispersions are overestimated, *e.g.* Centaurus (Lucey, Dickens & Currie 1986a).

**Galactic Density** The number of galaxies in a cluster can be directly related to the visible mass in the cluster assuming all clusters have a similar galaxy luminosity function (Colless 1988). Bahcall (1981) has shown that the number of galaxies (or richness) correlates with the velocity dispersion of the cluster. The measurement of the galaxy density is relatively straight forward. However few published results exist and they differ in their magnitude and aperture limits.

**Galactic Content** The relative populations of elliptical, lenticular and spiral galaxies have been determined for a number of clusters (Bahcall 1977b; Dressler 1980b). For poor, irregular clusters the fraction of spirals is high ( $\sim 50\%$ ), but for rich, regular clusters the spiral fraction can be small ( $\sim 5\%$ ).

**Luminosity of cD** The luminosity of the brightest member galaxy (BCM) is often used as a standard candle in studies of  $H_0$  and  $q_0$  (*e.g.* Hoessel, Gunn & Thau 1980). In work by Valentijn & Bijleveld (1983) and Schombert (1987 & 1988) the optical luminosity of the central galaxy and any cD envelope is related to radio and X-ray properties.

**Line Emission** Gas emits distinctive optical and UV lines as it cools from  $10^5\text{K}$  to  $10^4\text{K}$  (Cowie, Fabian & Nulsen 1980). Lines have been studied by a number of groups (*e.g.* Cowie *et al.* 1983; Hu, Cowie & Wang 1985; Johnstone, Nulsen & Fabian 1987) and their detection provides an important piece of evidence supporting the existence of cooling flows. However the luminosities of these lines are several orders of magnitude larger than expected for the amount of cooling gas seen. This implies the gas is re-excited, possibly by shocks.

## 1.2.2 Radio

Many extragalactic radio sources lie in clusters, *e.g.* Virgo-A, Perseus-A, Hydra-A, Cygnus-A. Ten of the clusters in the sample presented in this thesis have 3C sources (Edge 1958) associated with them.

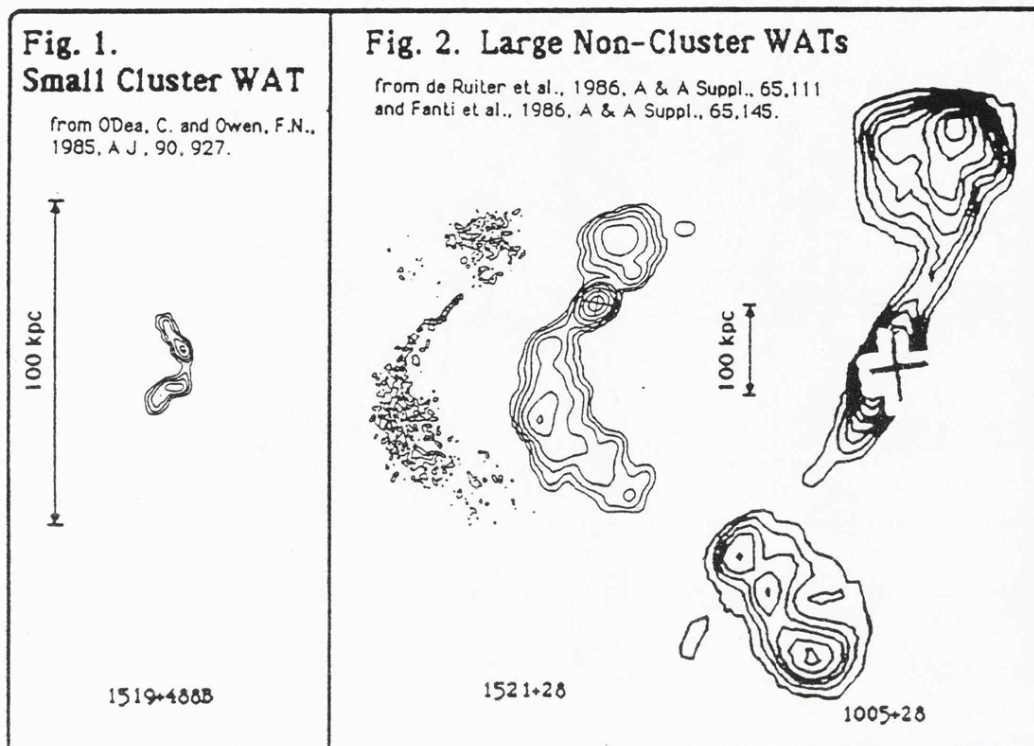


Figure 1.2: Examples of wide-angle tails from Rudnick & Birkinshaw 1986.

The radio spectra of these sources are steep ( $0.7 < \alpha < 2.0$ ) and are usually associated with a single galaxy. M<sup>c</sup>Hardy (1979) noted that sources are found preferentially toward the centre of clusters.

The radio morphologies of the sources are complex and show a wide variety of sizes and shapes. The 'Wide-Angle Tail' sources seen in Figure 1.2 show the interaction of galaxies with the ICM. The sources have been studied intensively by O'Dea & Owen (1985a & b) and Hanisch & Ulmer (1985).

There are also a number of large, diffuse sources, referred to as 'halo' sources, which are extended on scales of  $\sim 100$  kpc (Hanisch 1986). Due to the difficulty in detecting diffuse sources in the presence of strong point sources, there are few well-studied examples.

The steep spectra of both central and tail sources indicate that radio emission arises from some form of synchrotron mechanism involving the deceleration of energetic electrons ejected from a galaxy (van de Laan & Perola 1969). These ejected electrons interact with the gas in the ICM producing emission that depends on the ejection rate of electrons and the gas pressure. As a galaxy passes through a cluster the pressure will change, thus causing the radio output to vary on timescales of less than the galactic crossing time ( $\sim 10^9$  yr) irrespective of any variation in the ejection rate.

There have also been observations of nearby clusters in the 21 cm band searching for neutral Hydrogen (HI) emission (Giovanelli & Haynes 1985; Magri *et al.* 1988). These observations provide redshifts for member galaxies, from which velocity dispersions have been determined. These workers also note that spiral galaxies tend to be deficient in HI compared with field galaxies suggesting gas stripping.

Several clusters have also been observed at radio wavelengths for upscattering of the Cosmic microwave background by thermal electrons referred to as the Sunyaev-Zel'dovich effect (Birkinshaw 1986; Uson 1986). As mentioned above, combining the radio and X-ray data can give a distance to a cluster independent of the Distance ladder (McHardy *et al.* 1989).

### 1.2.3 X-ray

The discovery that clusters were X-ray emitters was made in 1966 when emission from M87 in Virgo was detected (Byram, Chubb & Friedman 1966; Bradt *et al.* 1967) using instruments on sounding rockets.

The launch of the *UHURU* satellite in 1970, which performed the first all-sky survey, provided many more detections of cluster emission (Gursky *et al.* 1971a & b) and established the emission was extended (Kellogg *et al.* 1972). The thermal nature of the emission from clusters was determined with the detection of an iron emission line in Perseus by *ARIEL-V* (Mitchell *et al.* 1976) and *OSO-8* (Serlemitsos *et al.* 1977). The most reliable survey was performed by *HEAO-1*, which provided an all-sky catalogue with a sensitivity of  $\sim 1-2$  mcrab (McKee *et al.* 1980; Piccinotti *et al.* 1982). The series of X-ray satellites launched after *UHURU* and before *EXOSAT* is summarised in Table 1.1.

The spectral results before the launch of *EXOSAT* are extensively reviewed by Mushotzky (1984). The temperatures and luminosities of around 30 clusters were determined by *OSO-8* (Mushotzky *et al.* 1978), *ARIEL-V* (Mitchell *et al.* 1979) and *HEAO-1* (Mushotzky 1984). These results are consistent, although a number of clusters were mis-identified or confused. A strong correlation between the temperature and luminosity was seen (Mitchell *et al.* 1979; Mushotzky 1984). Iron abundances of 22 clusters were determined by Rothenflug & Arnaud (1985) using *HEAO-1* spectra and the results are consistent with a constant value of 0.4 solar. The X-ray parameters were also shown to be well correlated with optical ones, *e.g.* the X-ray luminosity and velocity dispersion (Quintana & Melnick 1982) and the temperature and galaxy number density (Mushotzky 1984).

The only previous X-ray satellite with an imaging capability before *EXOSAT* was the *EINSTEIN* Observatory (Giacconi *et al.* 1979). The ability to image the X-rays gave an improvement in sensitivity of a factor of 100. There were two principal focal plane instruments: the Imaging Proportional Counter (IPC) which had a low internal background, angular resolution of  $\sim 1$  arcmin

Satellite	Nation	Launch	Instruments	Reference for Cluster Work
<i>UHURU</i>	USA	1970	Gas Prop. Counter	Giacconi <i>et al.</i> 1972
OSO-7	USA	1971	Gas Prop. Counter, Scintillation Counter	Markert <i>et al.</i> 1979
<i>COPERNICUS</i>	USA/UK	1972	Gas Prop. Counter, Focussing Mirrors	Fabian <i>et al.</i> 1974
<i>ANS</i>	USA/Neth.	1974	Gas Prop. Counter, Focussing Mirrors, Bragg Spectrometer	Brinkman <i>et al.</i> 1977
<i>ARIEL-V</i>	UK	1974	Gas Prop. Counter, Scintillation Counter, Bragg Spectrometer, Modulation Collimator, Pin Hole Camera	M <sup>c</sup> Hardy 1978 Mitchell <i>et al.</i> 1979
SAS-3	USA	1975	Gas Prop. Counter, Focussing Mirrors, Modulation Collimator	-
OSO-8	USA	1977	Gas Prop. Counter, Scintillation Counter, Polarimeter	Mushotzky <i>et al.</i> 1978 Smith <i>et al.</i> 1979
HEAO-1	USA	1977	Gas Prop. Counter, Scintillation Counter, Modulation Collimator	Mushotzky 1984 M <sup>c</sup> Kee <i>et al.</i> 1980
<i>EINSTEIN</i> (HEAO-2)	USA	1978	Imaging Telescope, Gas Prop. Counter	Jones & Forman 1984 See text
<i>ARIEL-VI</i>	UK	1979	Gas Prop. Counters, Focussing Mirror	-
<i>HAKUCHO</i> (ASTRO-A)	Japan	1979	Gas Prop. Counter, Scintillation Counter, Modulation Collimator	-
<i>TENMA</i> (ASTRO-B)	Japan	1983	Gas Prop. Counter, Focussing 1-D mirror, 1-D Hadamard Telescope	Okumura <i>et al.</i> 1988

Table 1.1: Summary of major X-ray satellites flown before *EXOSAT*

and modest energy resolution ( $\frac{E}{\Delta E} \approx 1$ ); and the High Resolution Imager (HRI) which had a high internal background, angular resolution of  $\sim 5$  arcsec and no energy resolution. The sensitivity and resolution of the IPC and HRI provided a vast amount of information on clusters. Around 200 clusters were observed by *EINSTEIN* (the majority using the IPC) and many of these observations are discussed in Abramopoulos & Ku (1983), Jones & Forman (1984), Stewart *et al.* (1984b) and Arnaud (1987 & 1988a). The images provided evidence for clumping in the ICM (Jones & Forman 1984), double clusters (Forman *et al.* 1981) and cooling flows (Stewart *et al.* 1984b). An attempt to determine the luminosity evolution of clusters was made by Henry *et al.* (1982) with luminosities for 25 clusters. They conclude that the slope of the luminosity function does not change out to redshifts of 0.5. However the normalisation of the luminosity function could not be determined because of the selection effects in the choice of clusters and the small sample used.

*EINSTEIN* also carried 3 spectroscopic instruments, two in the focal plane of the imaging telescope and one as a co-aligned experiment. The Solid State Spectrometer (SSS) provided good energy resolution ( $\frac{E}{\Delta E} \approx 3-25$ ) over the energy range of 0.5–4.5 keV with a circular field of view of 3 arcmin diameter. The SSS results showed evidence for near solar abundance of silicon and sulphur in clusters (Mushotzky *et al.* 1981) and evidence of cooling gas (Mushotzky & Szymkowiak 1988). The Focal Plane Crystal Spectrometer (FPCS) provided excellent energy resolution ( $\frac{E}{\Delta E} \approx 100-1000$ ) for a few particular energy bands with a field of view  $30 \times 3$  arcmin. The FPCS detected a number of lines which are characteristic of gas at  $10^6$  K at the centre of several clusters with cooling flows (Canizares *et al.* 1979 & 1982; Canizares, Markert & Donahue 1988). The detection of these lines is one of the strongest pieces of evidence for ‘cooling flows’. The Monitor Proportional Counter (MPC) was a collimated proportional counter with an energy range of 2–20 keV and a field of view of  $45 \times 45$  arcmin FWHM. The MPC had a moderate energy resolution ( $\frac{E}{\Delta E} \approx 5$ ) but only 8 energy bins for the 18 keV energy range. The MPC data allowed the determination of reliable temperatures for clusters with fluxes greater than  $1 \times 10^{-11}$  erg cm $^{-2}$  s $^{-1}$  (Arnaud 1988b).

#### 1.2.4 Recap

From the above review of the theoretical ideas and observational results, a number of questions arise.

- *Distribution of Mass* : What are the temperature and density profiles for each cluster?
- *Cluster Dynamics* : How do the X-ray and optical properties correlate?
- *Origin of ICM* : Is there a universal iron abundance?
- *Cooling Flows* : How does the presence of a cooling flow affect the properties of a cluster?
- *Cosmology* : What are the overall properties of a ‘complete’ sample?

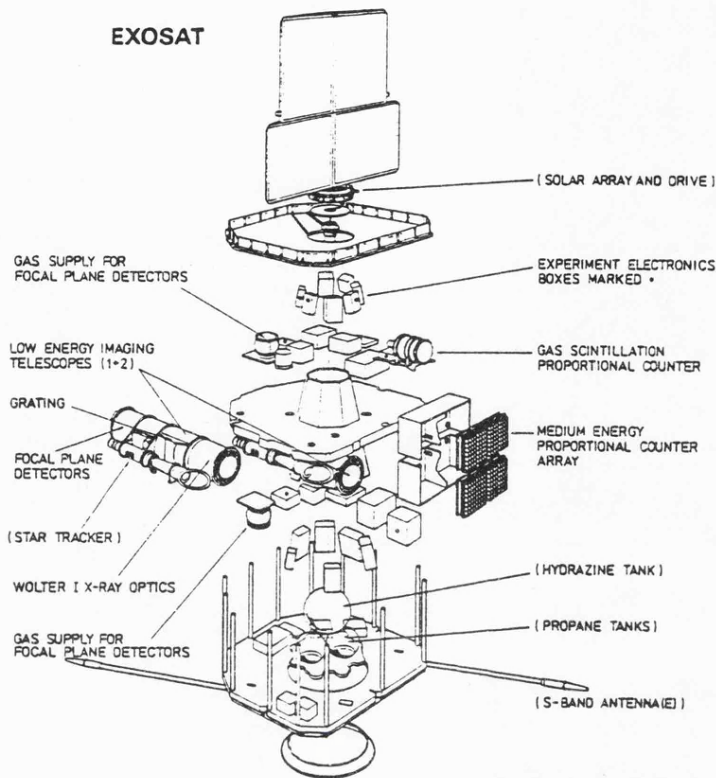


Figure 1.3: Schematic diagram of the configuration of *EXOSAT* from the *EXOSAT* Handbook

To answer these questions high quality X-ray spectra and images are required. The European X-ray Observatory SATellite, *EXOSAT*, was able to provide both of these.

### 1.3 Observations of Clusters with *EXOSAT*

*EXOSAT* was launched from Vandenberg Airforce Base on 26<sup>th</sup> May 1983 into a highly elliptical orbit ( $e \sim 0.93$ ) with a 90.6 hour period. This orbit provided continuous observations for 76 hours which allowed excellent time coverage for AGN and galactic sources. *EXOSAT* re-entered on 6<sup>th</sup> April 1986 after the natural decay of the orbit. The *EXOSAT* payload consisted of two Low Energy imaging telescopes (LE) giving 0.04–2 keV with angular resolution of  $\sim 15''$ , a Medium Energy proportional counter (ME) giving good energy resolution ( $\frac{E}{\Delta E} \approx 3-8$ ) in the 1–20 keV band and a Gas Scintillation Proportional Counter (GSPC) giving better energy resolution ( $\frac{E}{\Delta E} \approx 5-12$ ) for 2–30 keV spectra but poorer sensitivity compared to the ME. A full review of the *EXOSAT* mission is given in White & Peacock (1988). A schematic diagram of the satellite is shown in Figure 1.3. The performance of the LE is reviewed in Chapter 2 and of the ME and GSPC in Chapter 3.

The primary goals of the observational program proposed by Stewart & McHardy for *EXOSAT* were to

1. Obtain spectra and images of the 31 clusters in the HEAO-1 high galactic latitude catalogue (Piccinotti *et al.* 1982) to obtain a statistically 'complete' sample without the problems of confusion caused by the large field of view of HEAO-1.
2. Use the small field of view of the ME to determine the spatial variation of the temperature and iron abundance for nearby extended clusters.
3. Observe several distant clusters to determine temperatures to compare with those determined for nearby clusters.

In the three year of *EXOSAT* operations a large number of cluster observations were made and the results for all these observations are presented in this thesis. *EXOSAT* provided an excellent opportunity to investigate the problems mentioned above. Cooling flow rates could be estimated from the LE images (see Chapter 2) and reliable iron abundances, temperatures and luminosities could be obtained from the ME (see Chapter 3). Also the relatively small,  $45' \times 45'$  field of view of the ME allowed the variation in temperature in the Virgo, Coma and Perseus clusters to be determined using several pointings across each cluster (see Chapter 4). The majority of the data presented in this thesis came from the *EXOSAT* database.

## 1.4 Summary

Clusters of galaxies are of great astrophysical interest. The *EXOSAT* satellite offered an excellent opportunity to study clusters in detail. The following three chapters present imaging and spectral data for 38 clusters detected by *EXOSAT*. The results from correlation analysis of the X-ray, optical and radio parameters are given in Chapter 5. The implications of these results are discussed in Chapter 6.

## Chapter 2

# Analysis of EXOSAT Images

### Introduction

The Low Energy Imaging Telescopes carried on board *EXOSAT* provided high quality images of clusters. Analysis of these images using surface brightness fitting and deprojection techniques is described in this Chapter. The results are presented with particular emphasis on the deprojection analysis. The results are compared with previous *EINSTEIN* results.

### 2.1 Satellite Description

As mentioned in Chapter 1 *EXOSAT* carried two Low Energy telescopes. These consisted of nested electro-plated mirrors with both Channel Multiplier Array (CMA) and Position Sensitive Detector (PSD) instruments in the focal plane of each telescope. A schematic diagram of the telescope is shown in Figure 2.1 and a summary of the LE characteristics is given in Table 2.1. The LE telescopes are described in detail in de Korte *et al.* (1981).

Both LE telescopes were beset with operational difficulties throughout the mission. Firstly the PSD detectors both suffered from charge breakdown and had to be switched off after two months. In the brief time the PSDs were operational they were not used to observe any clusters so shall not be mentioned any further. Also the CMA detector in the second LE telescope (LE2) failed after four months thus leaving only one working detector out the original four. The failure of both detectors in LE2 resulted in only three observations of clusters being made with both telescopes.

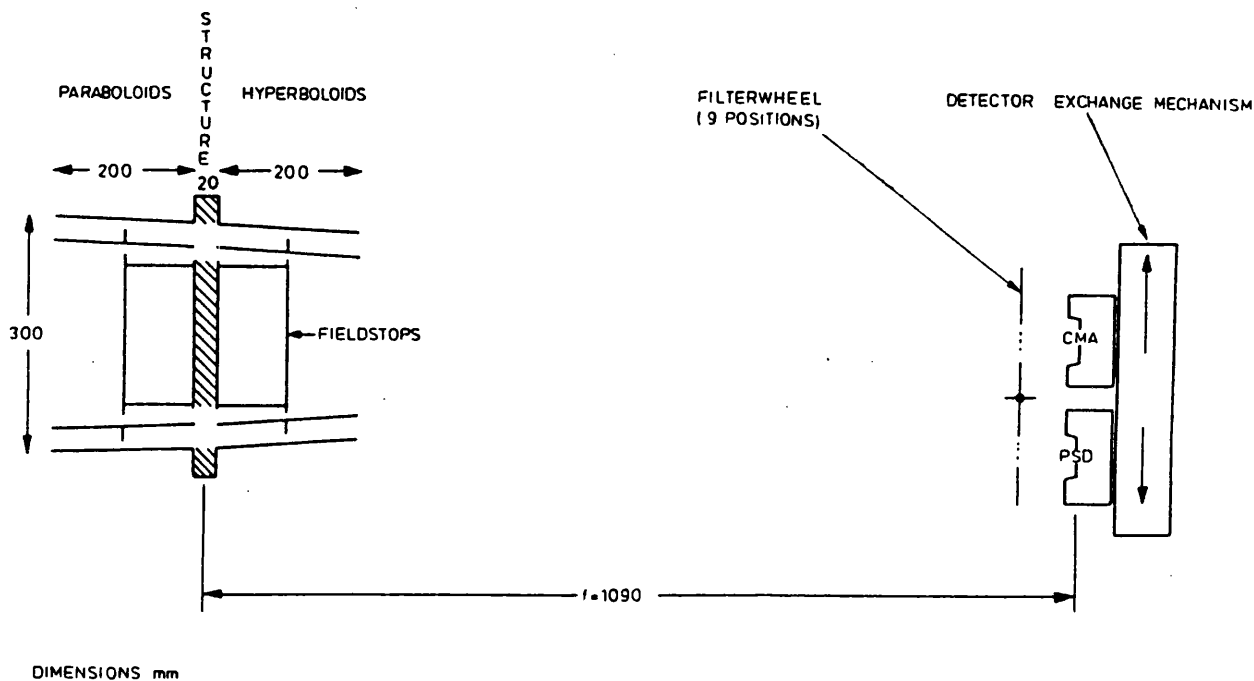


Figure 2.1: Schematic diagram of LE telescope design from the *EXOSAT* handbook.

### 2.1.1 Background

Figure 2.2 shows a greyscale image of a very long ( $\approx 80,000$  second) exposure on a empty field. The strong non-linearity can be seen clearly in the four corners. A diagonal “cross” structure and a “cold spot” in the bottom right hand corner can also be seen. However the background across the majority of the field of view was uniform. Figure 2.3 shows a surface brightness profile for the blank image showing background variations at the 1% level and an overall trend of 5% due to the vignetting of the diffuse X-ray background. In the analysis presented here no attempt was made

Energy Range	0.04–2 keV for CMA
Energy Resolution	Five filters for broad band spectroscopy
Spatial Resolution	18 arcsec – On axis 40 arcsec – 20 arcmin off-axis
Field of View	2.2° diameter
Average Steady Background	1.8 cnts s <sup>-1</sup> cm <sup>-2</sup> (full FOV)

Table 2.1: Performance of LE telescopes

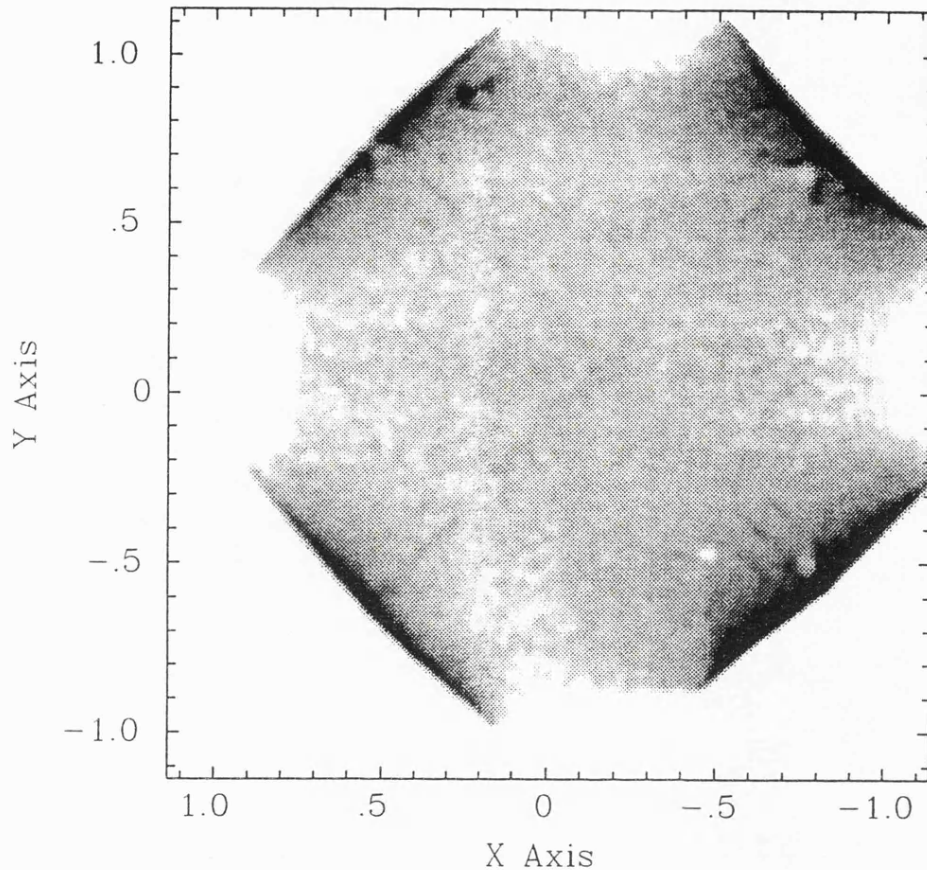


Figure 2.2: Example of LE image. The axes are marked in degrees.

to subtract a standard background as the normalisation of the background image was difficult to determine and the increased errors introduced were prohibitive.

The high background of the CMA was caused mainly by particle induced radioactive decays in the detector. However it also included a contribution of about 30% from radioactive decay of the potassium in the glass photomultiplier plates (Fraser, Pearson & Lees 1987) and a 10% contribution from the diffuse X-ray background and UV leakage of interplanetary He I and Lyman alpha emission. This high background made the LE insensitive to low surface brightnesses, thus introducing two selection effects.

- A bias against the detection of low density/low surface brightness clusters.
- Emission was only detected from the highest density region at the centre of a cluster so the LE surface brightness tended to underestimate the extent of the emission.

The impact of these selection effects on the LE results is discussed below.

### 2.1.2 Observing Strategy

The observing strategy adopted for the LE was to use filters in a photometric fashion to obtain some crude spectral information, principally on the galactic absorbing column in the line of sight.

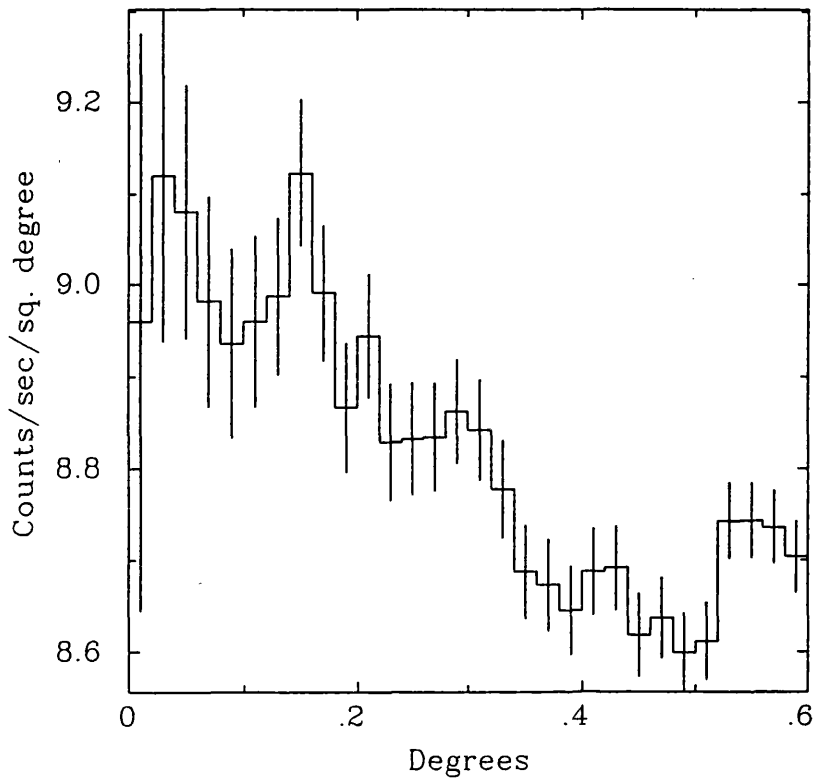


Figure 2.3: Surface brightness profile of blank LE image from the centre of the image. The errors are statistical.

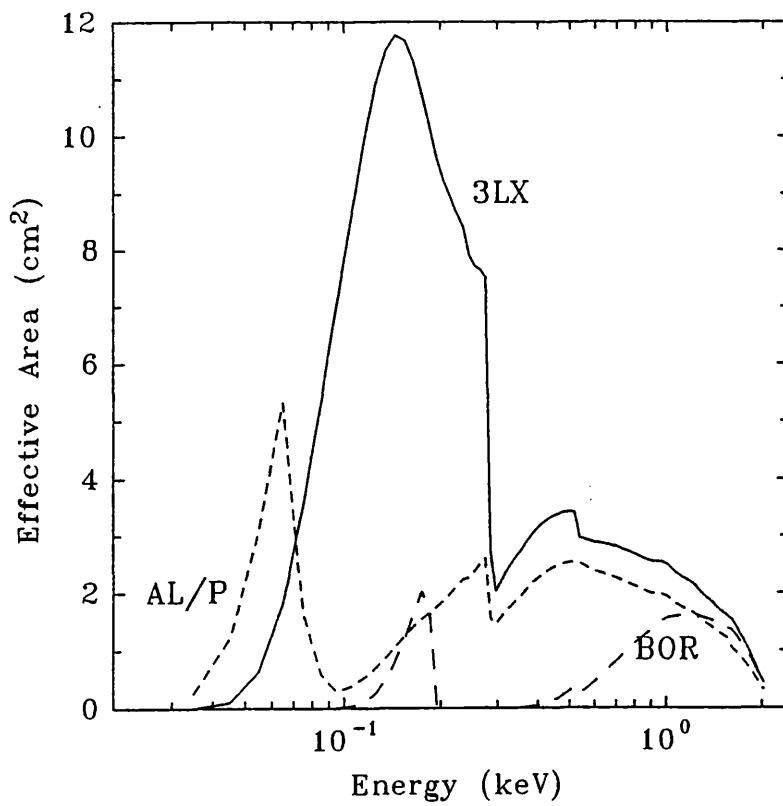


Figure 2.4: Effective areas of principal LE filters

The effective areas of the 3 principle filters used are shown in Figure 2.4.

The thin Lexan (3LX) filter had the highest throughput and was the standard filter used in observations. Its only disadvantage was that it suffered UV leakage (Chiappetti & Giommi 1985). This only affected sources where the ratio of UV to X-ray flux was high, so was not a concern for cluster observations.

The standard procedure was to start all observations using the thin Lexan filter. If the source was bright enough then other filters were used, usually Aluminium/Parylene (Al/P) and Boron (Bor). As clusters are relatively weak and extended sources, only a few were observed with a second filter.

## 2.2 Data Analysis

Images of 16" and 64" pixel size for each exposure were created from standard Final Observation Tapes using software written in Leicester. Each image was inspected for cluster emission and for any serendipitous sources, usually bright stars with high UV flux. Where possible any serendipitous sources were removed from the image to avoid confusion with the extended cluster emission.

The 16" images were convolved with a gaussian mask of 16" FWHM (*i.e.* the central point spread function). Surface brightness profiles were determined from these smoothed images for all clusters centred on the peak of emission or the known optical centre of the cluster for the most diffuse sources. These profiles were analysed using two different techniques, which are described below.

An  $H_0$  of  $50 \text{ km s}^{-1} \text{ Mpc}^{-1}$  and  $q_0$  of 0.5 were assumed throughout this analysis.

### 2.2.1 Surface Brightness Profile Fitting

The surface brightness profile,  $S(r)$ , of the X-ray emission from gas held in a cluster can be described using a modified King profile of

$$S(r) = S_0 \left( 1 + \left( \frac{r}{a} \right)^2 \right)^{\frac{1}{2} - 3\beta} \quad (2.1)$$

where  $a$  is the core radius,  $\beta$  is the density slope parameter and  $S_0$  is the central surface brightness. Such models were fitted to the LE surface brightness profiles, using a  $\chi^2$  minimisation technique, in which the background rate was an additional free variable. This analysis allowed the determination of the central surface brightness, the core radius,  $\beta$  and the total integrated count rate for each cluster.

Surface brightness profile fitting is a relatively unsophisticated method for analysing imaging data. It only provides information on the extent of the emission and little on the state of the gas, *i.e.* gas temperature or density. The determination of these properties requires a more complex method, such as deprojection.

## 2.2.2 Deprojection

The surface brightness deprojection technique was first used for X-ray cluster analysis by Fabian and collaborators in Cambridge and is extensively discussed in Fabian *et al.* (1981), Stewart *et al.* (1984b) and Arnaud (1987 & 1988a).

The analysis is performed by taking a series of three-dimensional ‘shells’ and working out the contribution of each ‘shell’ to each ‘ring’ in the two-dimensional surface brightness profile. Taking  $S_i$  as the surface brightness in the  $i^{\text{th}}$  ring in counts  $\text{s}^{-1} \text{ arcmin}^{-2}$  and  $C_j$  as the count emissivity counts  $\text{s}^{-1} \text{ cm}^{-3}$  for the  $j^{\text{th}}$  shell, then

$$S_i = \sum_{j=1}^i A_{ij} C_j \quad (2.2)$$

where  $A_{ij}$  is a matrix of geometrical factors. Shells within the  $i^{\text{th}}$  ring do not contribute (*i.e.*  $A_{ij} = 0$ ), so the matrix is triangular. Assuming the outer ring includes no emission from beyond that radius then the contribution to each bin within it can be calculated. Repeating this process for each successive inward ring allows  $C_j$  to be determined uniquely.

The values of  $C_j$  obtained can be used to determine the density and temperature in each shell if the gravitational potential (and hence the pressure) is assumed. The temperature in each bin can be determined directly from  $C_j$  by comparison with expected count emissivity for a given emission model (*e.g.* Raymond & Smith 1977) folded through the detector response. So assuming the gas is in hydrostatic equilibrium the pressure is given as

$$\frac{dP}{dr} = -\rho \frac{d\phi}{dr} \quad \text{and} \quad P = \frac{\rho kT}{\mu m_H} \quad (2.3)$$

where  $\phi$  is the gravitational potential of the cluster,  $P$  is the pressure,  $\rho$  is the density,  $T$  is the temperature,  $\mu$  is the mean particle mass and  $m_H$  is the mass of hydrogen. The pressure in the outer shell must be positive as there will be some undetected gas beyond that radius. Therefore this outer pressure must also be assumed. From the temperature and pressure, the density can be derived using Equation 2.3. For this analysis a King potential was used as the gravitational potential and the outer pressure was varied to find an overall emission-weighted temperature which agreed with that obtained by the ME.

It should be noted that if the emissivity *and* the temperature were known for each shell (*i.e.* spatially resolved spectra) then the cluster potential could be derived directly. A crude attempt to do this can be made with the LE data as the ratio of the filter count rates depends on the temperature of the emission. So with profiles from two different filters, it should be possible to determine the temperature independently. However the ratio of the thin Lexan and Boron or Aluminium/Parylene filters was not a strong function of temperature, so any small statistical fluctuation in the count rate in either filter had a large effect on the derived temperature. Because of this instability in the solution, this method was not useful for any of the LE data.

One of the major problems with the deprojection technique is the estimation of errors in the derived parameters. Because of the nature of the assumptions that go into the analysis it is impossible to give definitive errors on mass flow rate or temperature. However using a Monte Carlo method limits on the parameters can be calculated. The method used in this analysis follows that outlined in Arnaud (1987). Two hundred regenerations of the original count profile were made, perturbing each bin by a random increment related to the number of counts in each bin. Each regeneration was deprojected individually and an ensemble of results was produced. From this ensemble the mean and variance of the parameters could be determined. As Arnaud points out, the statistical distribution of the mass flow rates is not gaussian, so the error on it cannot be quoted as a variance. Instead he uses the 10, 50 and 90% percentiles as the limits. This approach was used in this analysis. It should be stressed that the limits derived using this technique, especially for mass flow rate, are *NOT* errors, but are rather the extremes of the calculated values for a particular potential.

## 2.3 Results

The exposure time, X-ray position and estimated cluster count rate from integration of the surface brightness profile for each LE exposure are given in Table 2.2. The count rates in Table 2.2 were used in the spectral fitting of the ME data described in Chapter 3. For the brightest clusters (Virgo, Coma and Perseus) estimating the count rate was difficult due to the extent of these clusters, so no estimated count rate is given. The X-ray positions are accurate to  $\sim 15''$  for the brighter clusters. The only cluster image that was noticeably asymmetric was A1367. The LE image of A1367 shows the highly diffuse core seen in the *EINSTEIN* image (Bechtold *et al.* 1983) with two strong point sources. Therefore no surface brightness fitting or deprojection was attempted for this source.

Five LE upper limits for clusters are given in Table 2.2. Of these five, three (A22, A140 and A2315) had serendipitous AGN within the field of view of the ME giving a significant 2–10 keV flux. Another, A98, was detected by *EINSTEIN* (Henry *et al.* 1981) below the upper limit in the LE. The upper limit on the ME flux is also consistent with the flux seen in the IPC. As there are

Cluster	Date	Pointing Position (1950)	X-ray Position (1950)	Filter	Exposure (seconds)	Count Rate (count s <sup>-1</sup> )
A22*	330/83	00 18 12 -25 59 00	-	3LX	7177.3	< 0.01
A98	205/84	00 43 44 +20 14 47	-	3LX	60183.2	< 0.01
A119	331/84	00 53 48 -01 34 29	00 53 35.3 -01 30 47	3LX	28014.9	0.09 ± 0.03
A133	224/83	01 00 18 -22 04 00	01 00 14.1 -22 09 04	3LX 3LX	L1 17408.8 L2 19575.7	0.07 ± 0.02 0.10 ± 0.02
A140*	327/84	01 02 04 -24 16 50	-	3LX	13361.5	< 0.01
A193*	361/84	01 22 25 +08 24 32	01 22 28.0 +08 26 20	3LX	23841.9	0.05 ± 0.02
A262	224/84	01 49 51 +35 54 15	01 49 46.7 +35 53 42	3LX	18146.6	0.12 ± 0.03
A376	12/85	02 42 32 +36 37 37	02 42 58.3 +36 41 58	3LX	22263.2	0.09 ± 0.02
AWM7	258/84	02 51 23 +41 25 26	02 51 11.8 +41 21 39	3LX	16560.3	0.14 ± 0.02
A400	13/85	02 54 52 +05 48 22	02 55 03.0 +05 49 32	3LX	38937.2	0.14 ± 0.02
A3122*	2/84	03 16 12 -44 16 34	03 16 12.7 -44 24 53	3LX AL/P	4774.5 2364.0	0.05 ± 0.02 0.04 ± 0.02
Perseus (A426)	-	Several pointings (See Chapter 5)	03 16 27.7 +41 19 49	3LX 3LX AL/P AL/P BOR BOR	L1 50308.6 L2 8627.0 L1 9295.6 L2 9577.5 L1 9997.9 L2 13321.3	- - - - - -
0336+096	264/84	03 35 57 +09 48 22	03 35 52.1 +09 48 10	3LX	34983.9	0.18 ± 0.02
A478	276/84	04 10 48 +10 22 18	04 10 40.4 +10 20 06	3LX	19357.8	0.03 ± 0.01
0422-086*	48/85	04 23 15 -08 40 42	04 23 26.2 -08 40 10	3LX	26442.8	0.04 ± 0.01
A496	49/86	04 30 00 -13 16 00	04 31 18.2 -13 21 25	3LX	21670.7	0.06 ± 0.02
3C129	271/85	04 46 14 +45 00 42	04 46 30.0 +44 56 56	3LX	23969.6	0.06 ± 0.02
A576	306/84	07 17 24 +55 50 59	07 17 09.1 +55 49 05	3LX	20192.6	0.09 ± 0.03
0745-191	304/85	07 45 27 -19 08 30	07 45 18.1 -19 10 14	3LX	40309.9	0.017 ± 0.005
A754	323/85	09 05 46 -09 24 44	09 06 55.5 -09 29 22	3LX	23705.5	0.07 ± 0.03
Hydra-A	324/85	09 17 09 -12 04 42	09 15 41.4 -11 53 02	3LX	26113.1	0.07 ± 0.02
A1060	4/84	10 34 30 -27 16 06	10 34 22.3 -27 15 58	3LX	21007.5	0.19 ± 0.02
A1318*	335/84	11 33 58 +55 16 14	-	3LX	14910.2	< 0.01
A1367	5/84	11 41 53 +20 06 59	Highly Diffuse	3LX AL/P	12290.3 16102.5	0.20 ± 0.05 0.07 ± 0.03

Table 2.2: Log of LE observations. The count rates are for the thin Lexan filter. Clusters marked with a \* were not observed by *EINSTEIN*. 0.01 count s<sup>-1</sup> corresponds to approximately  $7 \times 10^{-12}$  erg cm<sup>-2</sup> s<sup>-1</sup> in the band 0.1–2.0 keV for a cluster of temperature 3 keV and a column of  $0.3 \times 10^{21}$  cm<sup>-2</sup>.

Cluster	Date	Pointing Position (1950)	X-ray Position (1950)	Filter	Exposure (seconds)	Count Rate (count s <sup>-1</sup> )
Virgo	-	Several Pointings (See Chapter 5)	12 28 16.9 +12 40 02	3LX 3LX AL/P BOR BOR	L1 36083.8 L2 43684.6 L1 24889.7 L1 12039.9 L2 42702.7	- - - - -
Coma (A1656)	-	Several Pointings (See Chapter 5)	12 57 18.8 +28 13 24	3LX	51171.9	-
Centaurus (A3526)	20/84	12 46 00 -41 02 02	12 46 02.8 -41 02 28	3LX	81565.8	0.24 ± 0.03
A3558*	52/86	13 22 15 -31 06 25	Out of FOV	-	-	-
A3562	176/84	13 29 24 -31 25 56	13 30 47.7 -31 24 52	3LX	38987.9	0.08 ± 0.01
A3571*	29/84	13 44 58 -32 35 02	13 44 31.8 -32 38 08	3LX AL/P	8477.5 4226.4	0.21 ± 0.04 0.18 ± 0.03
A1795	17/85	13 46 48 +26 51 27	13 46 32.5 +26 50 22	3LX	46466.6	0.17 ± 0.03
A1837	23/85	13 59 17 -10 54 28	13 58 53.9 -10 54 08	3LX	16651.5	0.02 ± 0.01
A2052	68/85	15 14 26 +07 13 44	15 14 16.7 +07 12 12	3LX	32459.4	0.18 ± 0.02
A2142	55/86	15 56 12 +27 22 00	15 56 15.7 +27 22 40	3LX AL/P	17468.8 4575.0	0.07 ± 0.01 0.04 ± 0.02
A2147	93/84	15 58 56 +16 05 00	15 59 44.1 +16 07 28	3LX	31563.9	0.08 ± 0.03
A2199	208/84	16 26 54 +39 39 43	16 26 54.8 +39 39 41	3LX AL/P BOR	4910.8 6912.2 4889.6	0.30 ± 0.05 0.13 ± 0.03 0.05 ± 0.02
Ophiuchus	250/84	17 09 35 -23 19 58	17 09 25.8 -23 18 28	3LX	17082.7	0.12 ± 0.03
A2315	215/84	19 01 09 +69 52 43	-	3LX	13733.8	< 0.01
Cygnus-A	305/85	19 57 37 +40 33 03	19 57 45.3 +40 35 55	3LX	17876.4	0.035 ± 0.010
2059-247	304/84	20 59 09 -24 45 49	20 59 09.0 -24 45 49	3LX	18819.1	0.006 ± 0.002
A3825* A3827	152/85	21 56 04 -60 19 58	21 55 06.3 -60 34 18 21 58 26.3 -60 10 46	3LX	10889.9	0.012 ± 0.004 0.011 ± 0.004
S1101 (Sers159-03)	161/84	23 11 16 -42 59 50	23 11 09.7 -43 00 08	3LX AL/P	5156.6 1594.3	0.07 ± 0.02 0.04 ± 0.02
A2589*	171/84	23 21 23 +16 32 37	23 21 26.7 +16 29 28	3LX	15781.3	0.08 ± 0.02
A4059*	338/84 200/84	23 54 26 -35 02 14 23 55 23 -35 01 40	23 54 24.8 -35 02 21	3LX	28334.8 (combined)	0.12 ± 0.02

Table 2.2: contd. Log of LE observations

no clusters that were detected in the ME but not in the LE (at some level), it can be concluded that the detection rate for clusters in the LE was not greatly affected by the insensitivity to low surface brightness emission.

### 2.3.1 Results from Surface Brightness Fitting

The results from fitting modified King models to the surface brightness profiles of all the available clusters are given in Table 2.3. Figure 2.5 shows fits for A478, A754, A1795 and A3571 as examples. The data in all but a few cases were too poor to allow the parameter,  $\beta$  to be constrained so fixed values of 0.5, 0.7 and 1.0 were adopted to determine any variation in core radius,  $a$ , and central surface brightness,  $S_0$ . Table 2.4 gives the cases where  $\beta$  was included as a free parameter, but the limits on  $\beta$  are poor compared with those determined with the *EINSTEIN* IPC (Jones & Forman 1984).

### 2.3.2 Problems with Surface Brightness Fitting

The surface brightness fitting was particularly affected by the insensitivity of the LE to low surface brightness. Fitting the central emission only, caused the core radius for a cluster with a moderate or large cooling flow to be severely underestimated (*e.g.* A1795 and Perseus). This is seen in the analysis of *EINSTEIN* IPC profiles where the outer emission is well determined (Jones & Forman 1984). By fitting this outer emission separately Jones & Forman determine a strong central excess within 300 kpc for A1795. This type of analysis was not possible using the LE data.

Figure 2.6 shows a clear anti-correlation between the core radius in arcmin and central surface brightness, for a given value of  $\beta$ . This trend is caused by a selection effect due to the relatively low dynamic range of count rates measured in the LE. Lines corresponding to a count rate 0.01 and 1 count  $s^{-1}$  are plotted in Figure 2.6. These lines provide the upper and lower limits to the sources detected in the LE. The range of the count rates can account for the narrow distribution seen in Figure 2.6, although some underlying correlation could exist. Figure 2.7 shows the results for core radius in kpc against the central surface brightness. The same anti-correlation is seen, but with a larger scatter.

### 2.3.3 Results from Deprojection Analysis

The parameters used in the deprojection analysis of the surface brightness profiles are given in Table 2.5 and the results are given in Table 2.6. These results are for images using the thin Lexan filter which gave better a signal-to-noise for all cases. The analysis of data from the Aluminium/Parylene

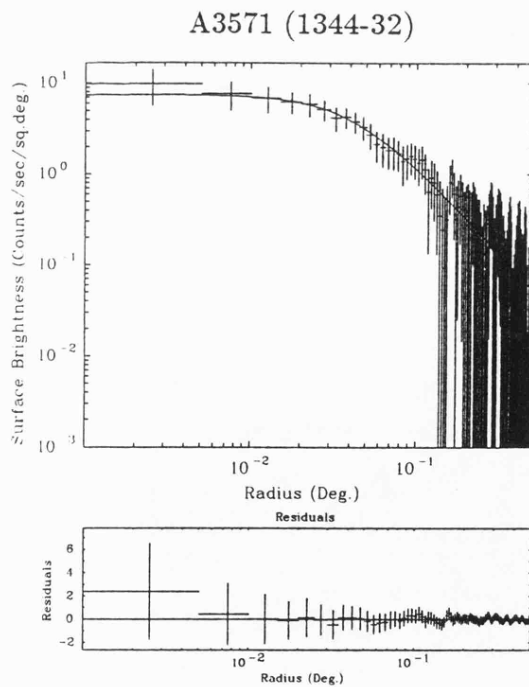
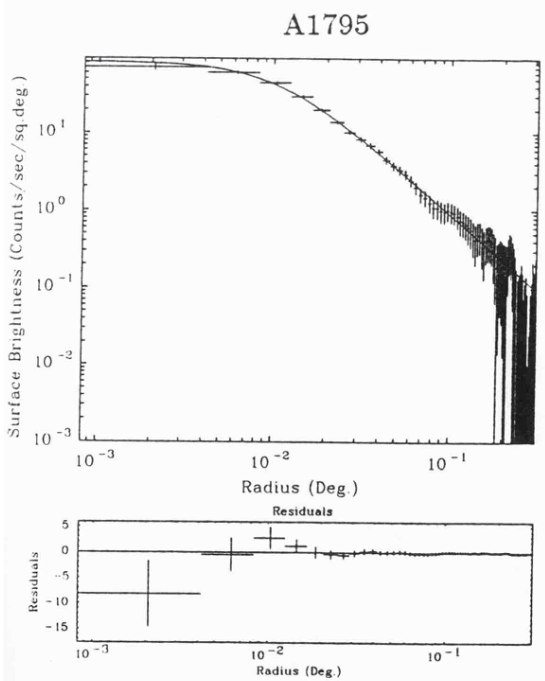
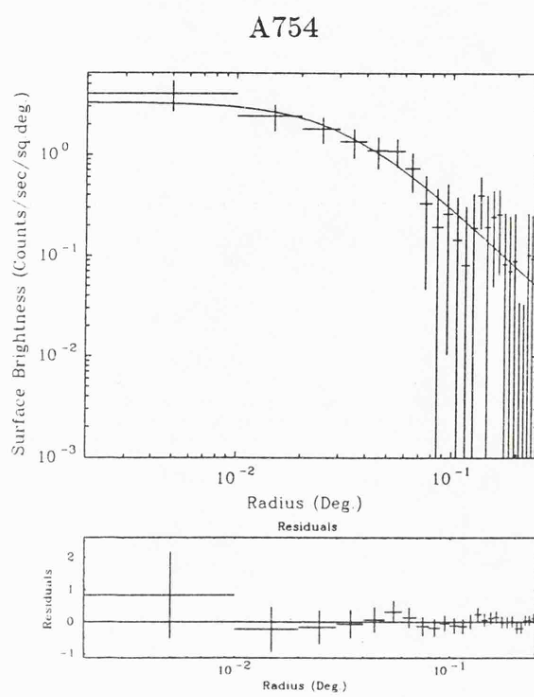
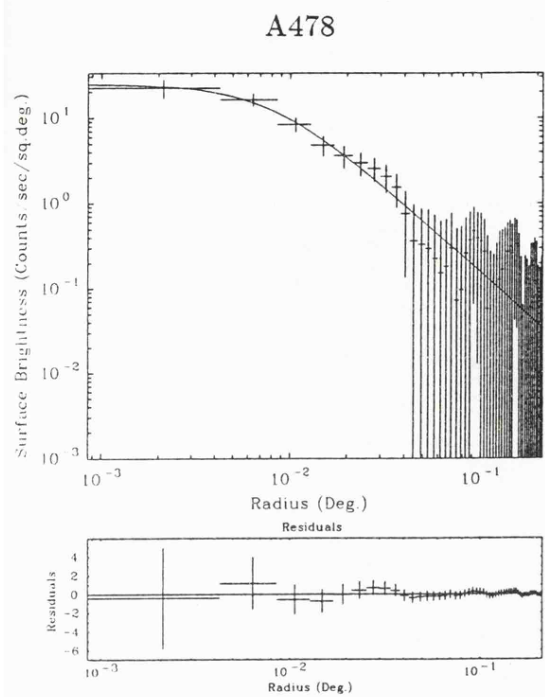


Figure 2.5: Examples of King model fitting: A478, A754, A1795 and A3571

Cluster	Central Surface Brightness (cnts s <sup>-1</sup> D <sup>2</sup> -1) for $\beta = 0.5$	Core Radius (arcmin.) for $\beta = 0.5$	Core Radius (kpc) for $\beta = 0.5$	$\chi^2$ for fit	Central Surface Brightness (cnts s <sup>-1</sup> D <sup>2</sup> -1) for $\beta = 0.7$	Core Radius (arcmin.) for $\beta = 0.7$	Core Radius (kpc) for $\beta = 0.7$	$\chi^2$ for fit	Central Surface Brightness (cnts s <sup>-1</sup> D <sup>2</sup> -1) for $\beta = 1.0$	Core Radius (arcmin.) for $\beta = 1.0$	Core Radius (kpc) for $\beta = 1.0$	$\chi^2$ for fit
A119	0.50 - 3.01	3.37 - 19.27	258. - 1476.	36.6 (50)	0.40 - 2.27	6.10 - 26.44	467. - 2024.	32.5 (50)	0.48 - 2.09	9.91 - 37.5	759. - 2871.	37.5 (50)
A133	11.4 - 60.5	0.35 - 2.04	37. - 214.	32.5 (50)	6.54 - 46.3	0.69 - 3.47	73. - 365.	46.8 (50)	4.86 - 38.0	1.02 - 5.06	107. - 632.	57.5 (50)
A193	0.35 - 2.93	3.08 - 27.35	258. - 2294.	45.4 (50)	0.19 - 2.24	4.91 - 38.5	412. - 3229.	44.8 (50)	0.21 - 1.92	8.49 - 50.5	712. - 4235.	44.6 (50)
A376	0.27 - 5.59	1.16 - 106.	99. - 8019.	23.4 (50)	0.25 - 4.43	1.57 - 134.	134. - 1209.	23.6 (50)	0.17 - 3.92	1.64 - 163.	140. - 1387.	23.7 (50)
AWM7	0.56 - 9.26	1.58 - 38.1	47. - 1127.	38.9 (80)	0.37 - 6.95	2.30 - 46.2	68. - 1367.	39.4 (80)	0.38 - 5.83	3.03 - 56.3	91. - 1665.	39.7 (50)
A400	0.19 - 12.5	2.95 - 168.	119. - 6782.	14.7 (50)	0.17 - 9.59	3.61 - 184.	146 - 7428.	14.7 (50)	0.16 - 8.08	4.46 - 210.	180. - 8477.	14.6 (50)
A3122	<148.	<3.03	<393.	17.1 (50)	<113.	0.11 - 3.45	14. - 448.	17.9 (50)	<98.2	0.21 - 4.67	27. - 606.	19.0 (50)
Perseus	>26.8	1.28 - 4.06	41. - 130.	118. (90)	11.8 - 39.3	2.44 - 6.78	78. - 217.	174. (90)	6.55 - 21.4	4.78 - 9.96	153. - 319.	237. (90)
0336+09	7.15 - 58.0	0.33 - 1.90	20. - 1115.	72.0 (80)	4.31 - 47.6	0.56 - 2.94	33. - 179.	106. (80)	3.10 - 41.3	0.79 - 3.95	48. - 240.	126. (80)
A478	7.59 - 84.3	0.14 - 1.68	22. - 263.	12.2 (50)	<65.4	0.30 - 2.72	47. - 426.	15.5 (50)	<56.1	0.46 - 3.97	72. - 622.	19.5 (50)
0422-08	0.16 - 3.63	1.52 - 31.6	103. - 2144.	67.6 (50)	0.22 - 2.58	5.42 - 39.9	368. - 2708.	63.5 (50)	0.04 - 2.14	9.34 - 80.5	633. - 3427.	61.3 (50)
A496	3.70 - 29.5	0.46 - 3.42	26. - 190.	8.41 (40)	2.94 - 23.5	0.78 - 4.85	43. - 270.	9.20 (40)	1.50 - 20.8	1.17 - 6.65	65. - 370.	11.2 (40)
0745-19	<57.1	0.11 - 1.55	20. - 277.	12.2 (80)	<44.7	0.19 - 2.31	34. - 413.	13.3 (50)	<39.5	0.31 - 3.19	55. - 571.	15.7 (50)
A754	<12.7	0.38 - 9.63	35. - 885.	8.85 (25)	0.17 - 9.72	0.52 - 10.4	48. - 955.	9.08 (25)	0.22 - 8.34	0.63 - 13.6	58. - 1249.	9.41 (25)
Hydra-A	7.73 - 41.3	0.40 - 1.66	36. - 151.	11.1 (40)	6.74 - 33.2	0.73 - 2.46	66. - 223.	10.1 (40)	6.17 - 29.5	1.10 - 3.45	100. - 313.	13.5 (40)
A1060	0.53 - 8.11	1.51 - 40.0	30. - 793.	19.4 (70)	0.29 - 6.20	2.25 - 51.8	45. - 1028.	21.9 (70)	0.30 - 5.29	3.15 - 66.2	62. - 1315.	23.7 (70)
Virgo	12.6 - 17.5	2.72 - 6.00	12. - 26.	107. (71)	10.5 - 19.0	5.28 - 8.82	23. - 39.	144. (71)	9.47 - 16.0	7.98 - 12.1	35. - 53.	183. (71)
Centaurus	1.37 - 5.71	2.07 - 18.2	39. - 345.	57. (92)	1.18 - 4.14	5.03 - 23.5	95. - 446.	66. (92)	1.08 - 3.47	7.44 - 30.2	141. - 573.	74. (92)
Coma	5.47 - 8.51	5.82 - 10.4	235. - 420.	38.9 (100)	5.02 - 7.71	8.56 - 13.8	346. - 557.	38.5 (100)	4.74 - 7.21	11.8 - 18.1	476. - 731.	47.3 (100)
A3562	<26.6	<4.41	<367.	6.16 (40)	<31.2	0.01 - 5.83	1. - 485.	5.26 (40)	<19.1	0.08 - 7.62	7. - 634.	5.25 (40)
A3571	2.02 - 25.7	0.67 - 10.1	45. - 685.	17.8 (80)	0.22 - 20.4	1.16 - 14.0	79. - 950.	20.8 (80)	<39.9	<20.2	<1371.	24.1 (80)
A1796	55.0 - 118.	0.48 - 0.82	51. - 88.	10.7 (50)	43.6 - 87.9	0.92 - 1.45	99. - 155.	56.3 (50)	36.7 - 73.1	0.14 - 2.20	15. - 236.	143. (50)
A2052	9.48 - 50.9	0.47 - 2.28	28. - 138.	51.9 (80)	8.50 - 38.7	0.89 - 4.50	54. - 272.	103. (80)	6.82 - 34.5	1.39 - 7.66	84. - 464.	139. (80)
A2142	4.87 - 44.3	0.46 - 5.59	72. - 874	22.3 (50)	3.55 - 34.2	0.77 - 7.58	120. - 1286.	29.3 (50)	2.49 - 29.1	1.16 - 10.6	181. - 1658.	34.3 (50)
A2199	16.5 - 100.	0.57 - 2.66	31. - 143.	13.1 (80)	12.6 - 76.6	1.07 - 4.28	58. - 230.	22.7 (80)	13.1 - 73.5	1.85 - 6.33	99. - 970.	39.2 (50)
Ophiuchus	1.83 - 14.3	1.63 - 13.9	79. - 677.	36.0 (80)	1.43 - 11.0	70. - 536.	2.38 - 19.4	43.0 (80)	0.84 - 9.54	3.40 - 25.9	166. - 1262.	48.7 (80)
S1101	1.34 - 159.	0.12 - 1.48	11. - 140.	9.99 (35)	3.09 - 128.	0.27 - 2.20	26. - 208.	11.0 (35)	3.19 - 113.	0.42 - 3.04	40. - 288.	13.2 (35)
A4059	5.79 - 41.3	0.46 - 2.89	38. - 240.	29.4 (80)	4.17 - 31.5	0.81 - 4.43	67. - 368.	43.5 (80)	3.57 - 27.7	1.21 - 6.26	101. - 521.	55.9 (80)

Table 2.3: Results from King fits to surface brightness profiles. The errors quoted are 90% confidence.

Cluster	Central Surface Brightness (counts s <sup>-1</sup> sq.deg. <sup>-1</sup> )	Core Radius (arcmin.)	Core Radius (kpc)	$\beta$	$\chi^2$ for fit
A133	14.4 - 91.9	0.24 - 3.39	25. - 356.	0.25 - 0.67	27.7 (50)
Perseus	47.3 - 113.	1.28 - 2.19	41. - 70.	0.43 - 0.65	156. (98)
0336+096	15.0 - 148.	0.17 - 1.74	10. - 106.	0.22 - 0.55	47.3 (80)
Centaurus	12.7 - 282.	0.19 - 1.13	4. - 21.	0.23 - 0.41	70.8 (100)
Coma	4.56 - 11.6	7.73 - 73.2	312. - 2955.	0.50 - 1.02	37.1 (100)
A1795	51.3 - 121.	0.56 - 1.27	60. - 136.	0.42 - 0.73	9.12 (50)
A2052	16.7 - 120.	0.25 - 2.04	15. - 124.	0.27 - 0.67	24.7 (80)
A2199	20.4 - 126.	0.70 - 5.64	38. - 303.	0.33 - 0.84	13.1 (50)
A4059	8.37 - 84.9	0.33 - 8.30	27. - 690.	0.25 - 0.75	25.0 (80)

Table 2.4: Results from King fits to surface brightness profiles with  $\beta$  free. The errors quoted are 90% confidence.

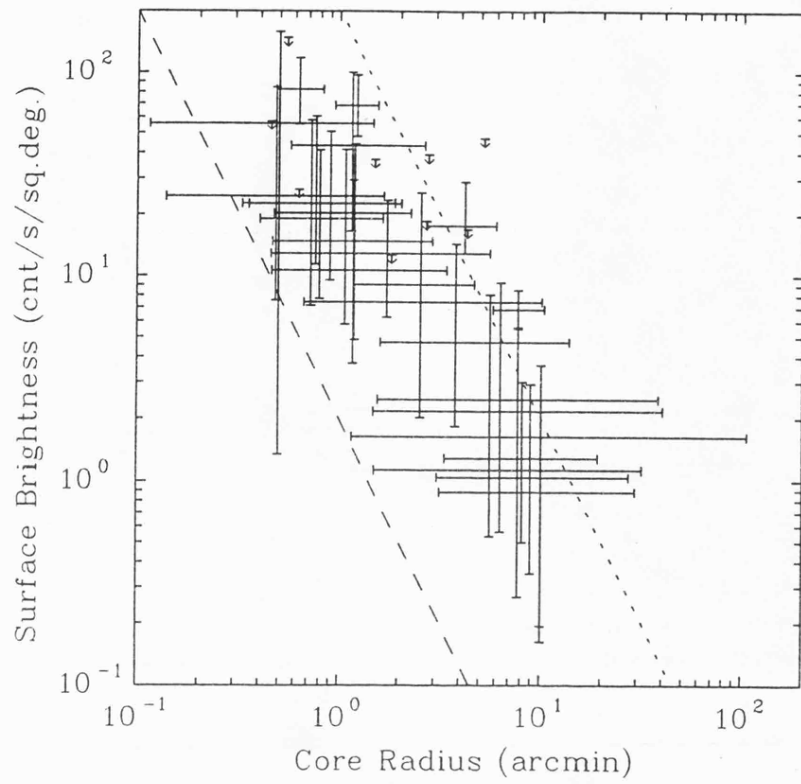


Figure 2.6: Central surface brightness against core radius in arcmin. The long dashed line represents an integrated LE count rate of 0.01 and the short dashed line represents  $1 \text{ count s}^{-1}$ .

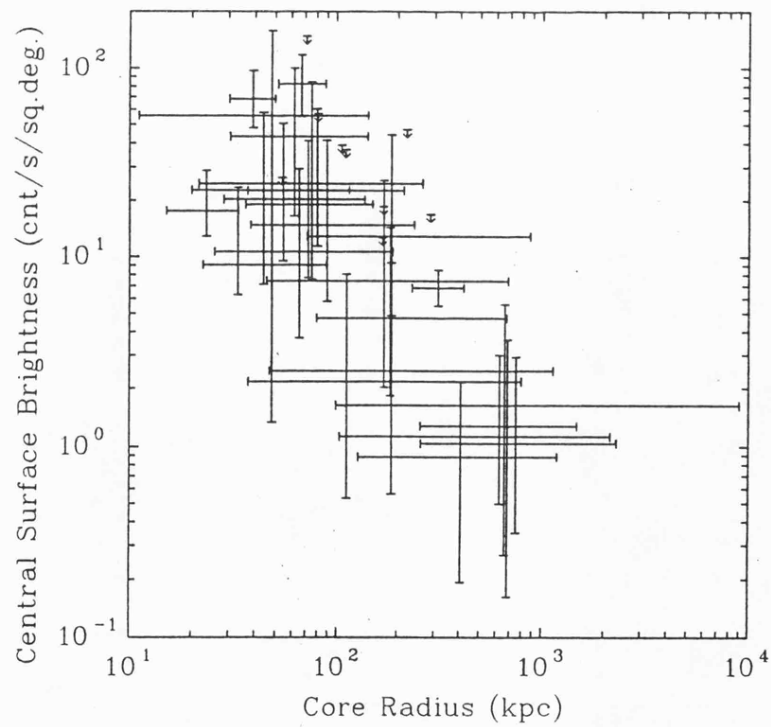


Figure 2.7: Central surface brightness against core radius in kpc

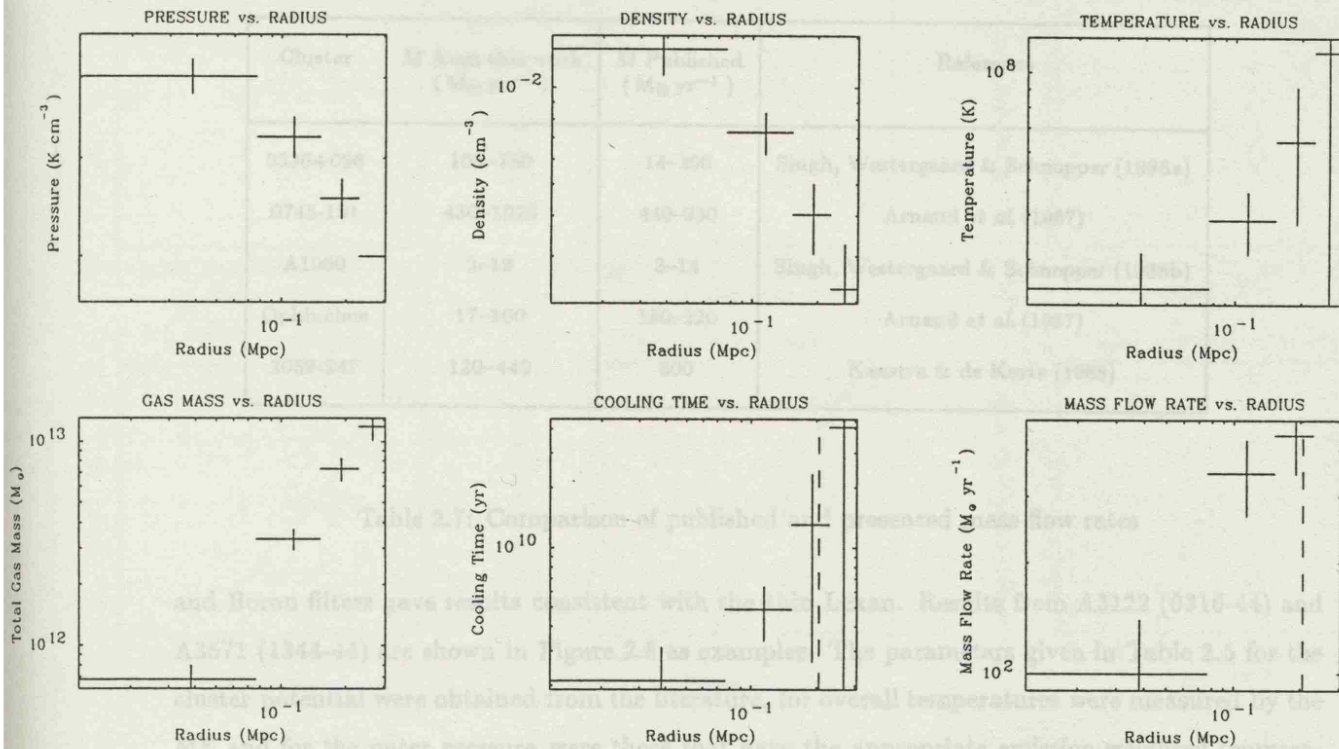
Cluster	Redshift	Number Of Bins	Bin Size (arcsec.)	Outer Radius (kpc)	Velocity Dispersion (kms s <sup>-1</sup> )	Core Radius (Mpc)	Overall Temperature (keV)	Outer Pressure (10 <sup>4</sup> K cm <sup>-3</sup> )
A119	0.044	3	124.	379.3	778.	0.5	5.1	10.
A133	0.0604	9	23.	322.8	700.	0.4	4.0	20.
A193	0.0482	4	108.	504.5	700.	0.4	4.0	6.
A262	0.0164	5	21.	44.3	415.	0.4	2.4	10.
A376	0.0489	3	56.	189.4	800.	0.4	5.1	30.
AWM7	0.017	5	40.	88.5	830.	0.4	3.5	20.
A400	0.0232	6	145.	525.7	423.	0.5	2.2	4.
A3122	0.0746	4	38.	267.1	820.	0.4	4.0	40.
Perseus	0.0184	17	36.	321.3	1100.	0.2	5.5	45.
0336+09	0.0349	5	40.	176.4	700.	0.4	3.1	38.
A478	0.09	7	30.	464.7	1100.	0.2	6.8	22.
0422-08	0.039	4	105.	400.7	600.	0.4	3.0	7.
A496	0.032	6	54.	364.9	657.	0.4	4.7	22.
3C129	0.022	4	93.	203.7	750.	0.4	5.6	10.
A576	0.0381	4	90.	335.8	914.	0.5	3.8	10.
0745-19	0.1028	5	26.	333.1	1200.	0.4	8.5	120.
A754	0.0528	6	36.	288.1	1048.	0.4	8.9	35.
Hydra-A	0.0522	9	36.	440.4	800.	0.4	3.9	18.
A1060	0.0114	7	46.	98.2	676.	0.2	3.3	13.
Virgo	(15 Mpc)	24	36.	63.7	500.	0.2	2.5	50.
Coma	0.0232	14	72.	664.5	800.	0.4	6.8	10.
Centaurus	0.0109	14	32.	135.5	586.	0.4	3.6	32.
A3562	0.0478	6	18.	134.5	800.	0.4	3.8	40.
A3571	0.039	7	36.	255.1	900.	0.4	7.7	55.
A1795	0.0616	11	30.	529.7	821.	0.3	5.0	22.
A1837	0.0376	5	72.	379.0	500.	0.4	2.4	6.
A2052	0.0348	8	40.	293.1	576.	0.3	3.6	25.
A2142	0.0899	6	45.	589.2	1241.	0.4	11.0	40.
A2147	0.0365	3	96.	245.5	1132.	0.4	4.4	20.
A2199	0.0309	11	34.	311.0	807.	0.2	4.7	20.
Ophiuchus	0.028	9	36.	384.8	1000.	0.4	9.0	20.
Cygnus-A	0.057	5	72.	562.9	800.	0.2	4.2	12.
2059-24	0.188	5	36.	801.3	1000.	0.4	9.0	30.
A3825	0.0744	4	72.	576.9	800.	0.4	5.0	5.
A3827	0.0993	4	72.	749.6	800.	0.4	7.0	7.
S1101	0.0544	5	25.	171.3	550.	0.4	2.8	35.
A2589	0.0421	5	32.	168.9	602.	0.4	3.6	28.
A4059	0.0478	13	28.	203.9	700.	0.4	3.5	30.

Table 2.5: Parameters used in deprojection analysis

Cluster	Redshift	Central Density ( $10^{-3} \text{ cm}^{-3}$ )	Central Temperature ( $10^7 \text{ K}$ )	Central Cooling Time ( $10^9 \text{ yr}$ )	Cooling Radius (kpc)	Mass Flow Rate 10,50 and 90 % Percentiles ( $M_{\odot} \text{ yr}^{-1}$ )	Gas Mass in 200kpc ( $10^{12} M_{\odot}$ )
A119	0.044	2.34±0.51	3.25±1.17	14.6±9.3	90.9±38.4	0.0, 23.2, 38.0	3.59±1.50
A133	0.0604	10.4±2.8	2.02±0.99	2.64±2.75	174.5±58.2	98.0, 127.7, 163.3	3.62±0.27
A193	0.0482	1.56±0.48	5.13±3.09	32.1±37.7	-	0.0, 0.0, 17.4	2.63±0.94
A262*	0.0164	12.2±3.8	0.73±0.38	0.87±1.38	34.4±2.1	7.9, 15.6, 29.2	-
A376	0.0489	5.33±1.40	3.71±1.39	7.17±4.75	95.2±35.5	8.8, 25.5, 47.8	-
AWM7*	0.017	8.92±2.58	1.65±0.94	2.79±3.69	66.3±8.9	8.2, 25.4, 41.8	-
A400*	0.0232	1.76±0.59	2.21±1.41	18.9±24.7	81.3±67.4	0.0, 8.2, 32.0	2.45±0.98
A3122	0.0746	13.1±2.3	2.48±0.64	2.11±1.01	205.3±95.3	334.4, 429.6, 565.2	7.86±0.92
Perseus	0.0184	42.0±2.6	3.22±0.21	0.73±0.07	191.6±8.3	338.4, 392.9, 416.6	6.59±0.18
0336+09	0.0349	17.8±1.0	1.36±0.08	0.90±0.11	131.1±14.4	104.5, 142.4, 181.4	-
A478	0.09	18.0±2.0	5.25±0.91	2.28±0.54	266.0±85.5	215.8, 582.5, 1012.2	8.42±1.10
0422-08	0.039	4.33±0.32	1.26±0.13	3.41±0.61	123.5±46.5	41.2, 56.4, 83.4	3.71±1.37
A496*	0.032	9.81±1.53	1.84±0.38	2.24±0.89	176.7±51.7	73.6, 120.6, 214.5	4.13±0.63
3C129	0.022	7.75±2.23	3.55±1.70	5.08±4.52	124.0±32.0	27.8, 61.1, 94.7	4.50±1.40
A576	0.0381	2.63±0.94	4.24±2.44	18.2±19.3	37.5±39.8	0.0, 24.5, 97.7	3.52±0.97
0745-19	0.1028	19.8±2.7	5.20±0.83	2.08±0.49	228.2±37.8	429.5, 702.0, 1020.2	11.9±2.1
A754	0.528	6.11±2.16	5.53±3.77	9.51±12.5	94.1±47.8	2.6, 24.4, 52.0	3.44±0.65
Hydra-A	0.0522	12.6±1.9	1.96±0.40	1.83±0.70	223.7±63.0	233.5, 315.6, 489.0	5.62±0.59
A1060*	0.0114	8.77±2.17	1.33±0.75	2.23±3.30	67.0±22.3	2.0, 8.5, 18.7	-
Virgo	(15 Mpc)	165.0±4.0	0.474±0.017	0.029±0.002	48.9±1.4	5.6, 9.9, 13.2	-
Coma	0.0232	2.74±0.58	5.64±2.03	16.9±11.9	43.0±23.3	0.0, 2.3, 5.0	2.25±0.06
Centaurus	0.0109	22.1±1.7	1.00±0.08	0.49±0.10	79.0±20.4	10.0, 17.7, 25.2	-
A3562	0.0478	9.50±3.71	3.19±1.93	4.48±4.83	100.4±24.6	12.3, 45.3, 65.2	-
A3571	0.039	8.09±3.05	5.89±4.59	7.84±12.9	134.7±63.2	6.7, 71.3, 149.5	4.44±0.70
A1795*	0.0616	16.8±0.9	2.34±0.34	1.50±0.13	266.3±16.4	470.1, 512.2, 556.1	6.83±0.12
A1837	0.0376	3.10±0.82	1.66±0.89	7.71±9.38	130.9±77.4	4.6, 18.3, 92.8	6.09±1.27
A2052	0.0348	12.3±0.7	1.21±0.78	1.14±0.16	148.6±25.7	68.4, 89.9, 113.6	3.03±0.40
A2142	0.0899	8.51±1.10	7.35±1.18	5.77±1.32	203.5±30.8	179.3, 243.8, 312.2	8.39±0.80
A2147	0.0365	3.57±0.96	6.06±3.78	15.2±24.5	126.0±63.2	0.0, 53.8, 88.1	4.28±0.60
A2199*	0.0309	14.1±3.5	2.93±1.17	2.36±1.75	181.1±32.5	103.4, 149.7, 204.1	4.00±0.35
Ophiuchus	0.028	15.7±4.2	4.39±3.58	3.11±7.40	130.3±52.0	17.3, 75.2, 158.6	5.00±0.60
Cygnus-A	0.057	6.12±0.72	2.09±0.36	3.87±0.99	129.1±55.5	51.2, 73.3, 113.1	5.35±0.75
2059-24	0.188	6.30±1.23	6.37±3.19	7.96±8.94	203.8±60.7	121.8, 241.6, 442.2	9.85±2.39
A3825	0.0744	1.25±0.45	4.79±3.22	40.9±55.5	-	0.0, 0.0, 9.83	2.40±1.25
A3837	0.0993	1.05±0.37	8.28±6.09	67.3±96.4	-	0.0, 0.0, 0.0	3.50±1.64
S1101	0.0544	16.2±4.0	1.51±0.71	1.31±1.49	133.4±13.8	158.5, 251.4, 365.3	-
A2589	0.0421	8.29±2.49	2.34±1.27	3.85±4.01	115.3±21.9	14.7, 45.9, 80.3	-
A4059	0.0478	9.97±2.83	2.41±2.00	3.53±8.47	155.1±27.5	79.6, 123.9, 172.7	-

Table 2.6: Results from deprojection of surface brightness profiles. The clusters marked by \* have outer pressures to match the IPC profile. The errors quoted are  $1\sigma$  variation.

## Example of Deprojection Analysis - A3122 (0316-44)



## Example of Deprojection Analysis - A3571 (1344-32)

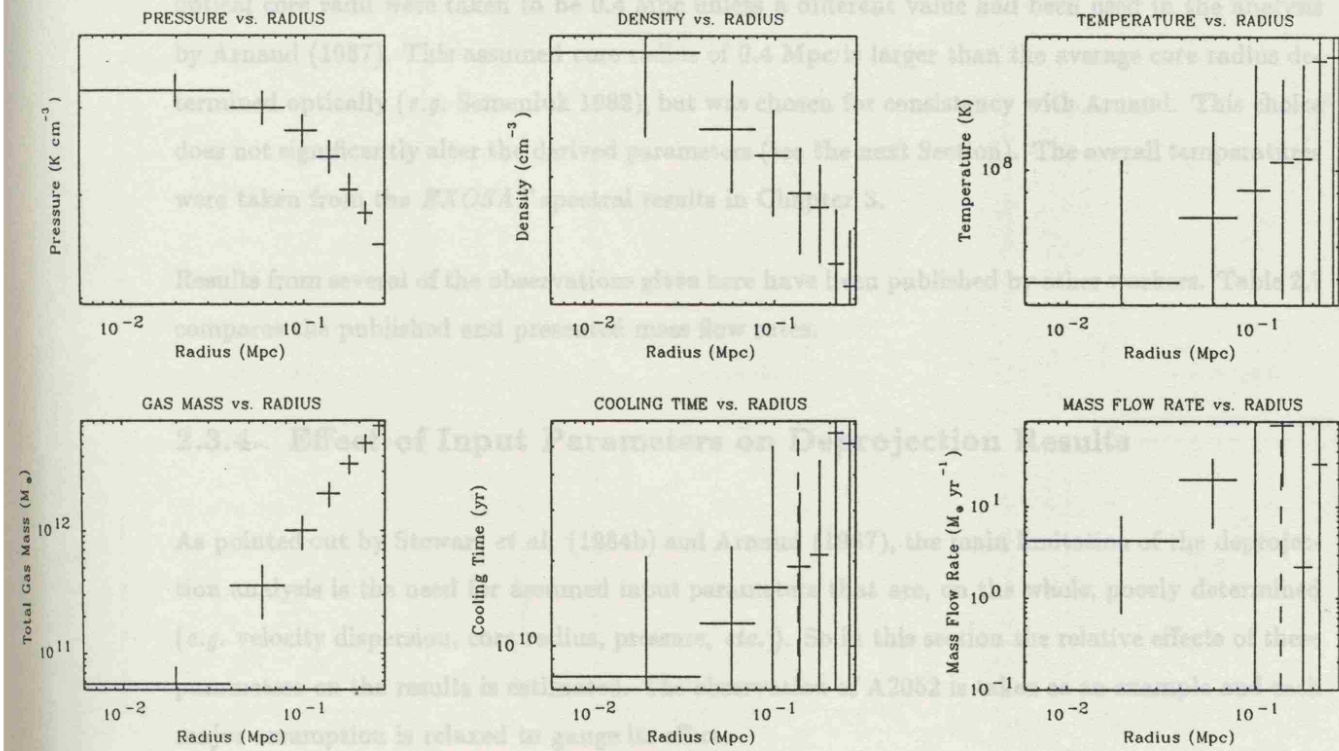


Figure 2.8: Examples of deprojection analysis: A3122 and A3571. The dashed lines represent the cooling radii.

Cluster	$\dot{M}$ from this work ( $M_{\odot} \text{ yr}^{-1}$ )	$\dot{M}$ Published ( $M_{\odot} \text{ yr}^{-1}$ )	Reference
0336+096	105–180	14–200	Singh, Westergaard & Schnopper (1988a)
0745-191	430–1020	440–930	Arnaud <i>et al.</i> (1987)
A1060	2–19	3–14	Singh, Westergaard & Schnopper (1988b)
Ophiuchus	17–160	150–220	Arnaud <i>et al.</i> (1987)
2059-247	120–440	800	Kaastra & de Korte (1988)

Table 2.7: Comparison of published and presented mass flow rates

and Boron filters gave results consistent with the thin Lexan. Results from A3122 (0316-44) and A3571 (1344-44) are shown in Figure 2.8 as examples. The parameters given in Table 2.5 for the cluster potential were obtained from the literature, for overall temperatures were measured by the ME and for the outer pressure were those that gave the appropriate emission-weighted temperature. For clusters without an optical velocity dispersion measurement the velocity dispersion,  $\sigma$ , was estimated from the relation between X-ray temperature and  $\sigma$  discussed in Chapter 5. The optical core radii were taken to be 0.4 Mpc unless a different value had been used in the analysis by Arnaud (1987). This assumed core radius of 0.4 Mpc is larger than the average core radius determined optically (*e.g.* Semeniuk 1982), but was chosen for consistency with Arnaud. This choice does not significantly alter the derived parameters (see the next Section). The overall temperatures were taken from the *EXOSAT* spectral results in Chapter 3.

Results from several of the observations given here have been published by other workers. Table 2.7 compares the published and presented mass flow rates.

### 2.3.4 Effect of Input Parameters on Deprojection Results

As pointed out by Stewart *et al.* (1984b) and Arnaud (1987), the main limitation of the deprojection analysis is the need for assumed input parameters that are, on the whole, poorly determined (*e.g.* velocity dispersion, core radius, pressure, *etc.*). So in this section the relative effects of these parameters on the results is estimated. The observation of A2052 is taken as an example and each major assumption is relaxed to gauge its effect.

The outer pressure is the parameter about which least is known as there is no direct method to measure it. As such the outer pressure allows the greatest freedom in the search for a satisfactory solution. The outer pressure is varied to find the best overall emission-weighted temperature for a given potential. Its principal effect is on the temperature (*i.e.* higher pressure gives higher

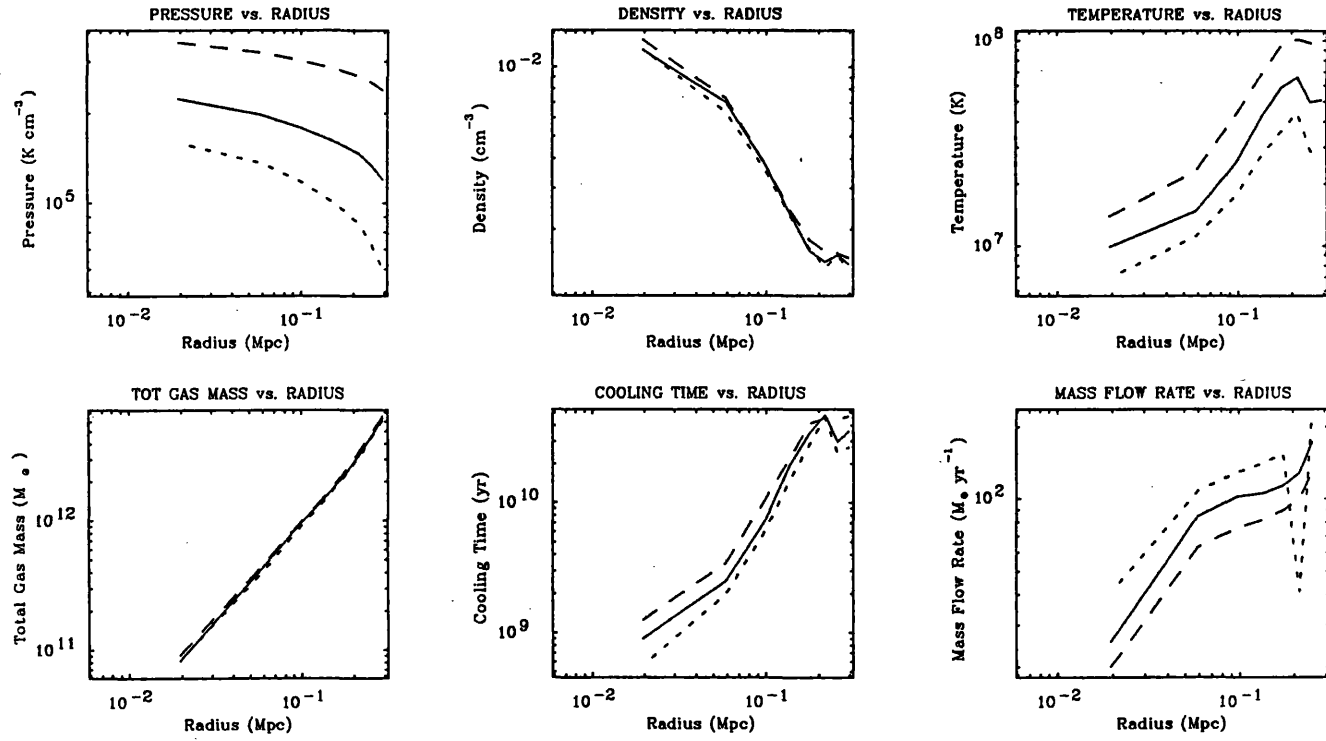


Figure 2.9: Examples of varying the outer pressure on results for A2052. The solid line is for an outer pressure of  $1.2 \times 10^4 \text{ K cm}^{-3}$ . The short dashed line is for  $0.6 \times 10^4 \text{ K cm}^{-3}$  and the long dashed line is for  $2.4 \times 10^4 \text{ K cm}^{-3}$ .

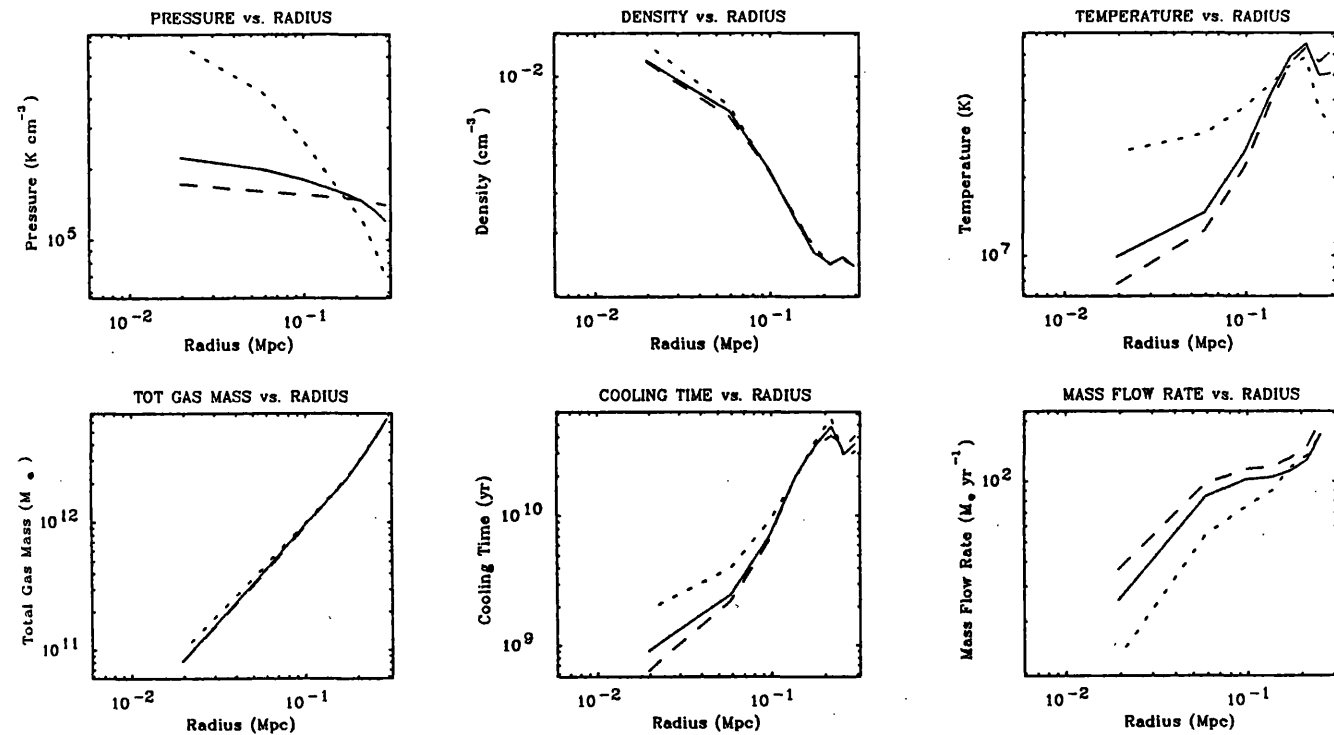


Figure 2.10: Examples of varying the core radius on Results for A2052. The solid line is for a core radius of 0.3 Mpc. The short dashed line is for 0.07 Mpc and the long dashed line is for 0.7 Mpc.

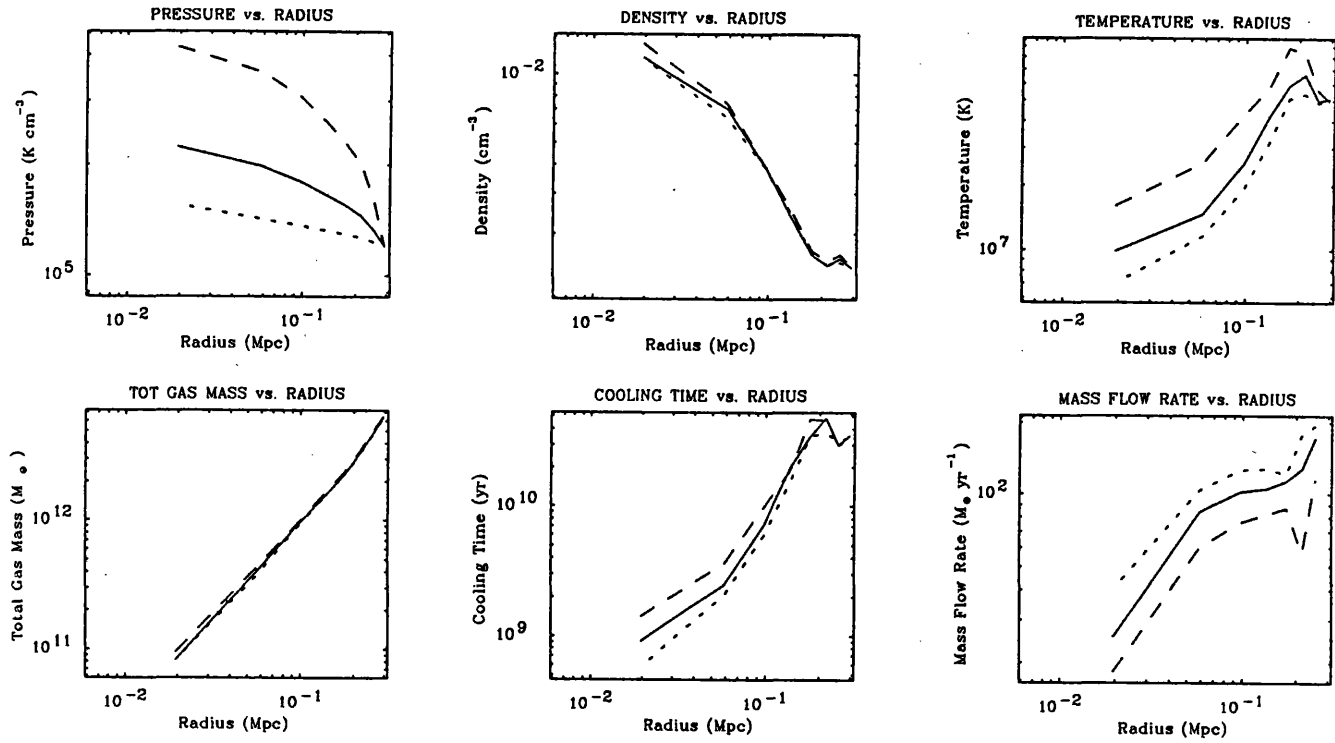


Figure 2.11: Examples of varying the velocity dispersion on Results for A2052. The solid line is for a velocity dispersion of  $576 \text{ km s}^{-1}$ . The short dashed line is for  $300 \text{ km s}^{-1}$  and the long dashed line is for  $1000 \text{ km s}^{-1}$ .

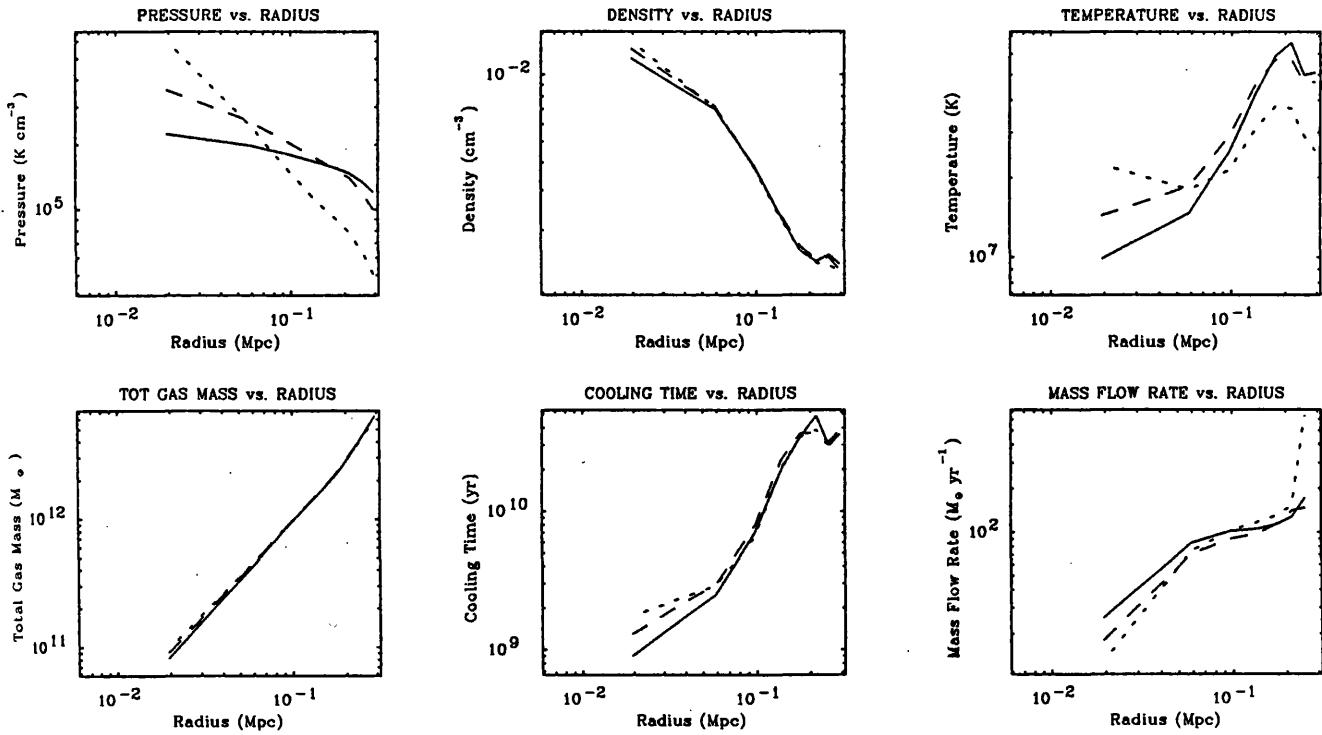


Figure 2.12: Examples of varying the assumed potential on Results for A2052. The solid line is a King Model with a velocity dispersion of  $576 \text{ km s}^{-1}$  and a core radius of  $0.3 \text{ Mpc}$ . The short dashed line is a de Vaucouleurs model with an effective radius of  $0.3 \text{ pc}$ . The long dashed line is a Hubble model with a velocity dispersion of  $200 \text{ km s}^{-1}$  and a core radius of  $0.3 \text{ Mpc}$ .

temperature) as would be expected for the simple gas law. Figure 2.9 shows the deprojection of A2052 for the outer pressure which gave an overall temperature in agreement with the ME result, and pressures of half and double that value.

The depth and form of the potential are related to the optical core radius and velocity dispersion. For consistency with Stewart *et al.* (1984b) and Arnaud (1987) a King model was used which is parameterised by a core radius (*i.e.* 'width') and a velocity dispersion (*i.e.* 'depth'). To determine the effect of varying the core radius, the profile for A2052 was deprojected using core radii of 0.07, 0.3 and 0.7 Mpc. The results for these three core radii are shown in Figure 2.10. To determine the effect of varying the velocity dispersion, the profile for A2052 was deprojected using velocity dispersions of 300, 576 (the published value) and 1000  $\text{kms}^{-1}$ . Figure 2.11 shows the results for these three cases. Finally, the form of the potential can be changed to determine how this assumption affects the analysis. Figure 2.12 gives this results for King, de Vaucouleurs and Hubble mass models. The analysis indicates that the density and mass flow rate are insensitive to the assumptions about the potential. However the temperature is strong affected by these assumptions. Some combinations of input parameters can be excluded if they result in an overall temperature above or below that determined by the ME. These uncertainties prevented any constraints being put on the radial variation of temperature

This analysis demonstrates the robustness of the density and mass flow rate determinations. While it shows the temperature is dependent on the assumptions made, it illustrates the value of the ME spectra in constraining the overall temperature.

### 2.3.5 Problems with Deprojection Analysis

A number of clusters were analysed using only four or five radial bins due to low number of counts from the source in the profile. The derived results are still useful as the central density and mass flow rate can be determined.

The main problem with the LE data (as with the HRI data on *EINSTEIN*) was that the analysis was restricted to the inner parts of the cluster because of the high detector background. This particularly affects A262 and A1060, where the outer bin used is within the cooling radius (*i.e.* all the gas detected has a cooling time less than  $2 \times 10^{10}$  yr). In many cases the outer radius is less than 250 kpc (the average X-ray core radius in Jones & Forman 1984). Reliable gas masses cannot then be determined as only a small fraction of the total emission is included in the analysis.

The radius limit also causes problems when choosing the outer pressure, as the gas at larger radii is not taken into account when the emission-weighted temperature is calculated. If only cooler, central emission is used to calculate the emission-weighted temperature then the cluster

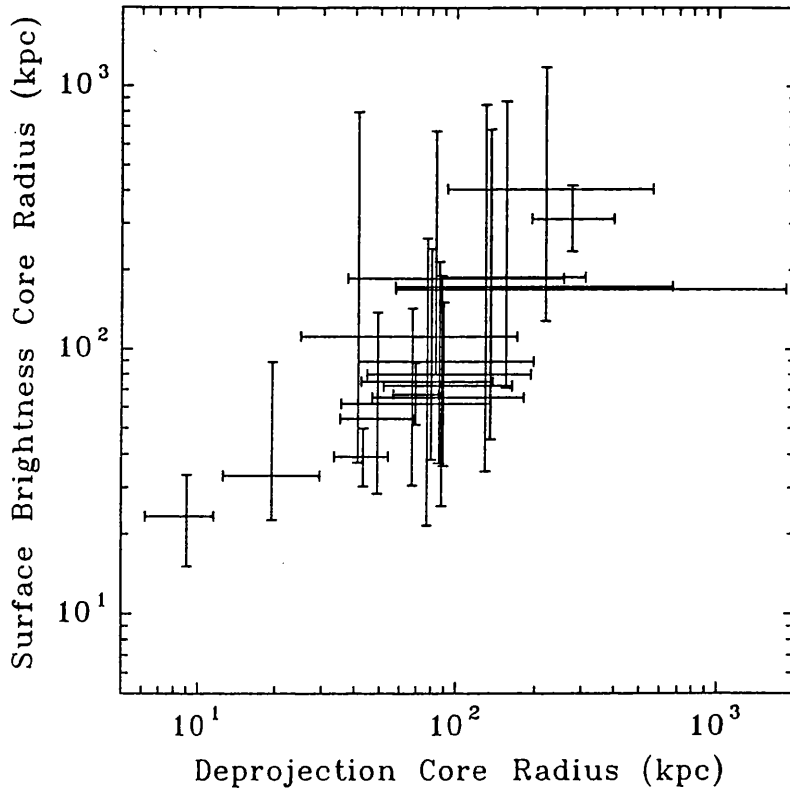


Figure 2.13: Comparing core radii obtained from fitting surface brightness and density profiles

temperature will be underestimated. To match this underestimated temperature with the measured cluster temperature, a higher outer pressure will be used. This higher pressure will in turn lower the implied mass flow rate. This chain of events leads to a possible systematic *underestimation* of the mass flow rate. Where possible this problem was avoided by fitting the *EINSTEIN* IPC profile of the clusters. In most cases this gives data out to twice the radius in the LE. The outer pressure for the LE was then chosen to match the pressure profile found for the IPC result. These cases are noted in Table 2.6.

### 2.3.6 Fitting Profiles to Derived Densities

The deprojection analysis provides a density profile which is insensitive to assumptions about the cluster potential and outer pressure. From the King model the density profile is

$$\rho = \rho_0 \left(1 + \left(\frac{r}{a}\right)^2\right)^{-\frac{3\beta}{2}} \quad (2.4)$$

where the core radius,  $a$ , and density parameter,  $\beta$ , are the same as those in Equation 2.1. Therefore it should be possible to parameterise the density profile in a similar way to the surface brightness profile.

The core radius, central density and  $\beta$  parameter can be determined using a  $\chi^2$  minimisation technique. The problems encountered in the surface brightness fitting were compounded by the fewer bins available (*e.g.* typically 5–10, rather than 50–80). This meant that a statistically meaningful determination of all three parameters was impossible. So again  $\beta$  was fixed at 0.5, 0.7 and 1.0.

The results of the fits to density profiles with more than 4 bins are given in Table 2.8.

The core radii obtained from this method agree with those from the surface brightness fitting. Figure 2.13 compares the results for the determined core radii and shows the large errors associated with these values.

## 2.4 Comparison with *EINSTEIN* Results

Observations of nearly 200 clusters were made with the IPC and in a few cases HRI detectors on *EINSTEIN*. Results from these observations are presented a number of papers (Jones & Forman 1984 (JF); Abramopoulos & Ku 1983 (AK); Stewart *et al.* 1984b; Arnaud 1987 & 1988a). Of the 44 clusters in Table 2.2, 33 were observed by *EINSTEIN*.

Figure 2.14 compares the core radii obtained from the surface brightness fitting results quoted by JF and AK. There is only a loose agreement between the *EXOSAT* and *EINSTEIN* values (and between JF and AK). These differences can be attributed to the differences in fitting procedures. AK used a similar technique to the one used here with a floating background and including the central emission, but they fixed  $\beta$  at a value given by the ratio of velocity dispersion to X-ray temperature. This assumption is often incorrect (Mushotzky 1984 and see Section 6.3.2), so comparing the *EXOSAT* or JF results with those from AK is difficult. JF used an iterative process where central points are left out of the fit until an acceptable fit was obtained. Any central excess due to cooling is not included thus giving larger values of core radius than the values presented here. JF also left  $\beta$  as a free parameter and obtained values between 0.5–0.8 in all cases. Such a fitting method was impossible for the LE due to the insensitivity to the low surface brightness emission at large radii.

There is, however, much better agreement between the *EINSTEIN* and *EXOSAT* results for the deprojection analysis. Figures 2.15 and 2.16 show LE results for mass flow rate and central density plotted against results from Arnaud (1988a). To check for systematic differences between the two analysis techniques several IPC and HRI profiles of clusters with LE profiles were analysed using the same software. Figure 2.17 shows the results for LE plus HRI and LE plus IPC analysis of A2199 and A1060. The consistency of the results from all 3 detectors can be seen. Similar agreement was seen in all other cases where LE and *EINSTEIN* data were available. The agreement between the LE and *EINSTEIN* results is excellent considering the different bandpasses and characteristics of the two telescopes. The LE had a much smaller effective area than the IPC (10 cm<sup>2</sup> compared to 120 cm<sup>2</sup>), however as most LE exposures were significantly longer than those of the IPC (10–15,000s compared to 2–3,000s). Therefore the total number of counts per image is only a factor of 2–3 smaller in the LE. The LE results are also consistent with those obtained with the HRI. The

Cluster	Central Density ( $10^{-3} \text{ cm}^{-3}$ ) for $\beta = 0,5$	Core Radius (kpc) for $\beta = 0,5$	$\chi^2$ for fit	Central Density ( $10^{-3} \text{ cm}^{-3}$ ) for $\beta = 0,7$	Core Radius (kpc) for $\beta = 0,7$	$\chi^2$ for fit	Central Density ( $10^{-3} \text{ cm}^{-3}$ ) for $\beta = 1,0$	Core Radius (kpc) for $\beta = 1,0$	$\chi^2$ for fit
A133	4.74-20.1	45.-192.	4.50 (9)	4.05-15.0	79.-280.	7.80 (9)	3.65-12.0	125.-392.	10.6 (9)
A262	5.60-17.1	7.-102.	0.20 (5)	3.78-94.0	23.-130.	0.76 (5)	3.69-21.1	25.-158.	0.54 (5)
AWM7	3.92-9.63	>33.4	1.35 (5)	3.80-9.39	>52.	1.42 (5)	3.72-9.23	>75.	1.48 (5)
A400	0.46-1.86	>427.	2.74 (6)	0.48-1.77	>558.	2.78 (6)	0.49-1.72	>707.	2.81 (6)
0336+09	10.1-13.1	57.-73.	10.2 (5)	16.7-24.2	50.-84.	0.11 (5)	16.2-23.2	69.-112.	0.90 (5)
A478	11.9-33.5	42.-137.	2.89 (7)	10.4-27.7	77.-211.	7.35 (7)	9.21-23.8	122.-301.	12.0 (7)
A496	5.15-17.2	47.-180.	3.99 (9)	4.65-13.8	78.-259.	6.61 (8)	4.32-11.9	121.-355.	8.91 (8)
0745-19	9.32-54.9	43.-261.	1.33 (11)	8.03-43.9	71.-358.	2.57 (11)	7.31-37.6	110.-485.	3.98 (11)
A754	2.83-8.26	57.-1826.	1.47 (6)	2.37-11.5	>86.	1.91 (6)	2.09-9.96	>89.	2.24 (6)
Hydra-A	7.86-22.7	52.-163.	2.95 (9)	7.20-18.7	84.-234.	6.15 (9)	6.62-16.4	126.-326.	10.2 (9)
A1060	2.02-16.9	25.-170.	1.88 (7)	2.89-9.38	18.-244.	2.50 (7)	2.23-12.2	48.-310.	2.98 (7)
Centaurus	17.1-32.1	13.-29.	10.2 (14)	15.7-27.0	20.-44.	23.9 (14)	7.49-10.4	64.-85.	90.5 (14)
A3562	3.85-20.7	16.-375.	0.24 (6)	3.56-18.0	34.-444.	0.26 (6)	3.40-11.6	56.-533.	0.28 (6)
A3571	3.09-9.54	57.-665.	0.53 (7)	2.83-8.74	64.-838.	0.63 (7)	2.69-8.43	106.-1015.	0.72 (7)
A1795	16.0-24.1	56.3-85.3	3.64 (11)	14.4-20.8	90.-129.	12.7 (11)	13.0-18.4	132.-184.	38.8 (11)
A2052	11.0-18.2	35.-68.	3.61 (8)	10.4-16.7	53.-96.	9.43 (8)	9.99-15.7	75.-132.	17.99 (8)
A2142	5.23-14.5	86.-308.	5.54 (6)	4.74-12.6	140.-449.	8.67 (6)	4.36-11.1	209.-632.	11.47 (6)
A2199	7.11-26.7	35.-135.	0.71 (11)	6.30-20.3	63.-191.	2.81 (11)	5.81-16.6	98.-263.	5.55 (11)
Ophiuchus	5.36-29.2	37.-254.	2.21 (9)	4.58-23.2	59.-338.	2.83 (9)	4.29-20.0	77.-441.	3.32 (9)
Cygnus-A	4.60-13.7	38.-186.	0.76 (5)	4.32-10.7	82.-259.	1.68 (5)	4.18-9.71	134.-348.	2.84 (5)
2059-24	2.85-14.8	73.-491.	1.74 (5)	2.56-11.7	138.-705.	2.98 (5)	2.31-10.3	218.-989.	4.13 (5)
A2589	3.68-18.5	31.-341.	0.44 (5)	3.20-15.9	36.-453.	0.71 (5)	2.93-10.2	60.-576.	0.93 (5)
S1101	6.80-12.8	37.-124.	0.85 (5)	10.5-31.3	47.-147.	0.34 (5)	10.2-28.8	68.-189.	0.35 (5)
A4059	4.96-20.1	41.-196.	0.26 (6)	4.67-17.1	64.-254.	0.58 (6)	4.50-14.8	93.-324.	0.96 (6)

Table 2.8: Results from King model fits to density profiles

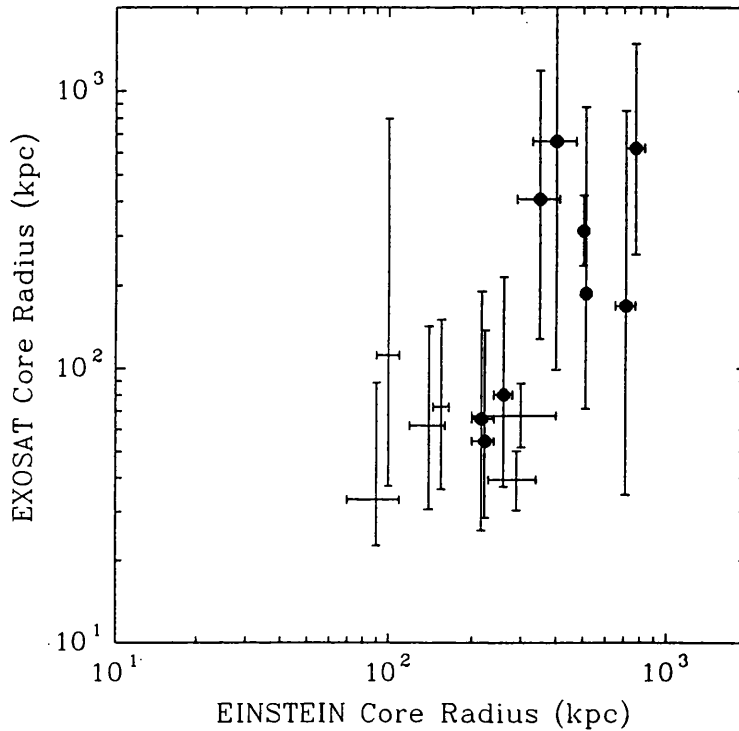


Figure 2.14: Results for core radius from *EXOSAT* and *EINSTEIN*. The filled circles mark results from Abramopoulos & Ku (1983) and the other points are from Jones and Forman (1984).

resolution and number of counts per image again show the LE was (for long exposures) as good as most HRI observations (which tended to be short).

## 2.5 Summary

The *EXOSAT* LE provided a substantial body of information about the distribution of gas and the state of the core regions in the clusters observed. A number of clusters observed by *EXOSAT* have no previous imaging observations and the LE shows evidence for large cooling flows in several of them. The LE results from the deprojection analysis compare very well with those from *EINSTEIN*. These results demonstrate the versatility of the deprojection technique as opposed to surface brightness fitting. The deprojection method is non-parametric and robust allowing it to be used successfully on data from instruments. Surface brightness fitting is sensitive to instrument resolution and response and requires an assumed surface brightness model.

The implications of these results in terms of other cluster properties are to be discussed in Chapter 6.

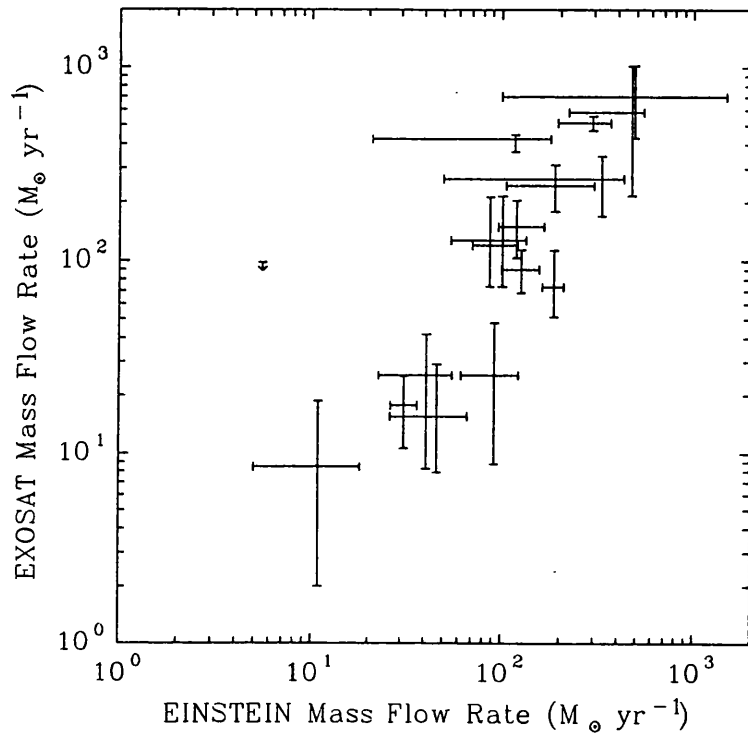


Figure 2.15: Results for mass flow rate from *EXOSAT* and *EINSTEIN*. The *EINSTEIN* results are from Arnaud (1988a).

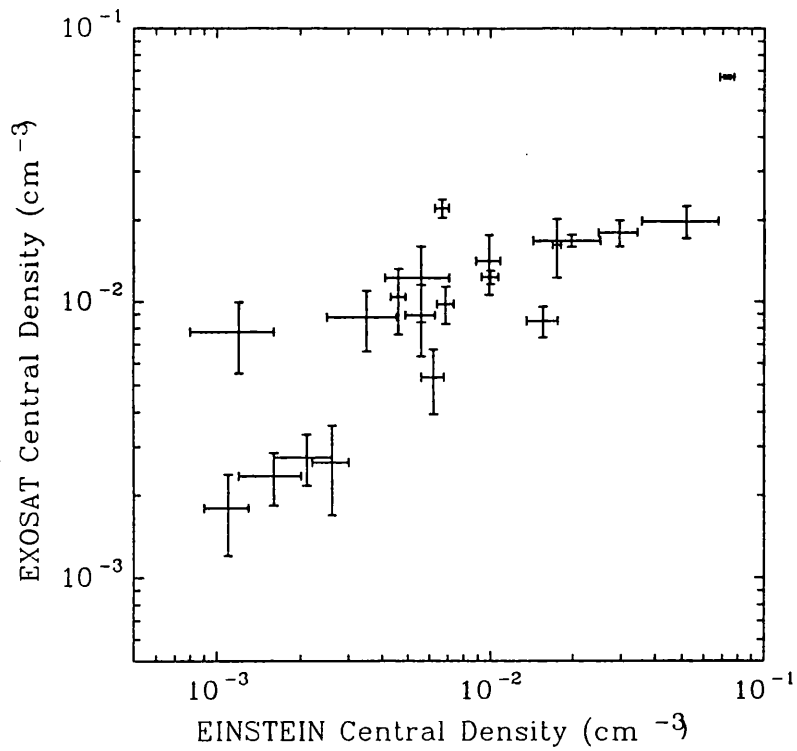
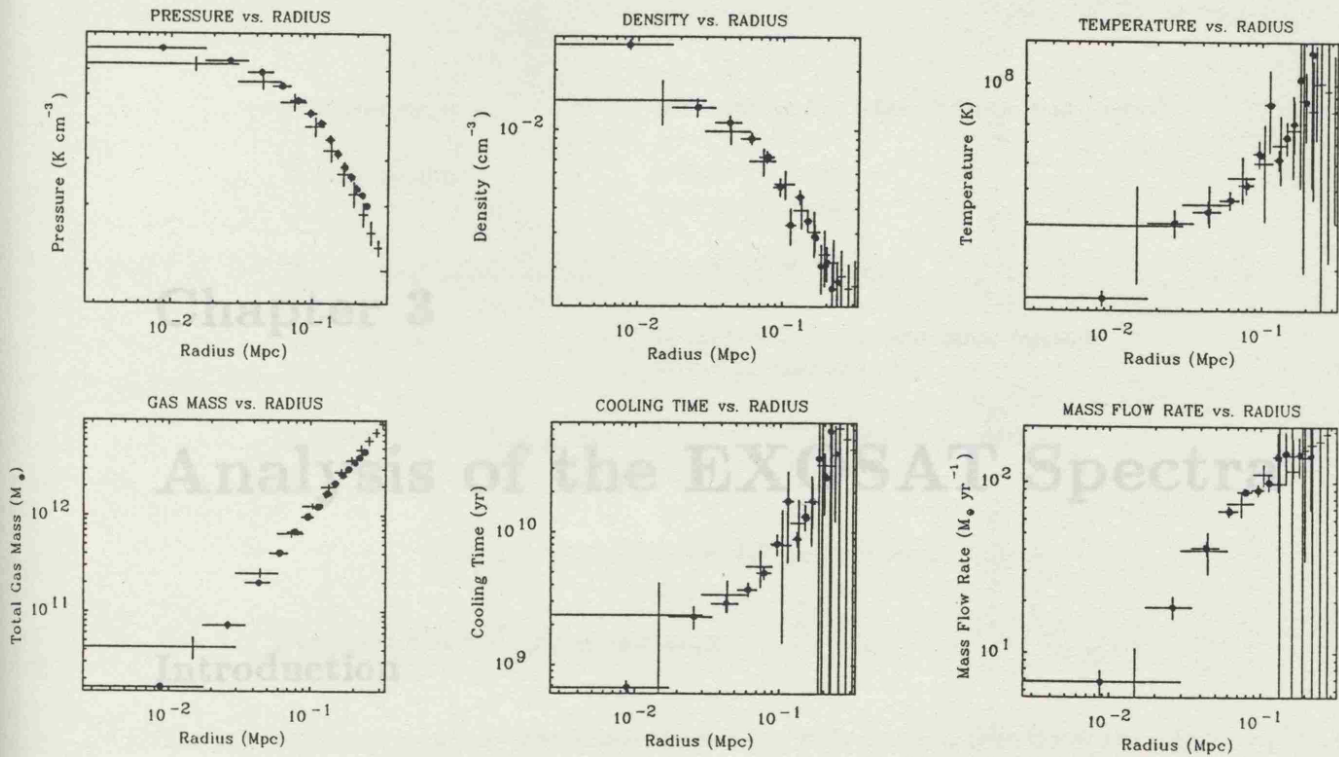


Figure 2.16: Results for central density from *EXOSAT* and *EINSTEIN*. The *EINSTEIN* results are from Arnaud (1988a).

## LE and HRI Deprojection Analysis of A2199



## LE and IPC Deprojection Analysis of A1060

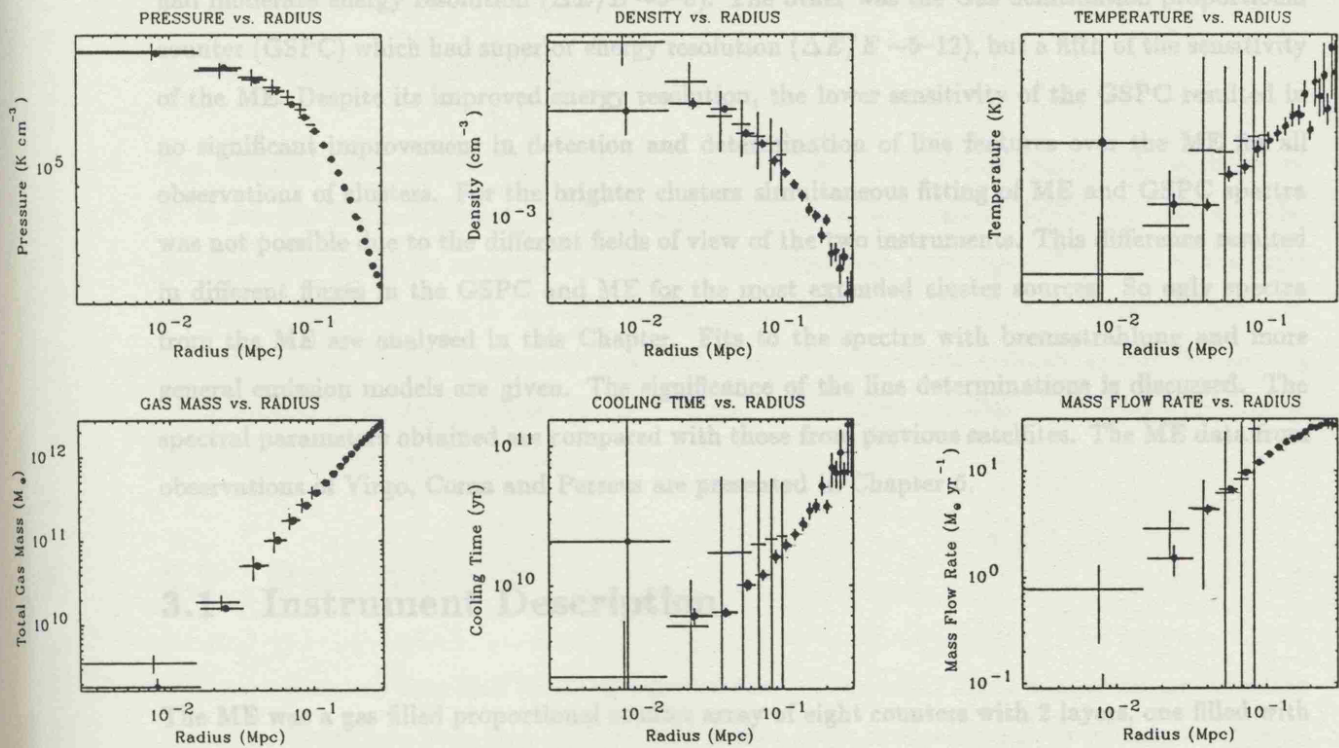


Figure 2.17: Example of LE & HRI for A2199 and LE & IPC deprojection for A1060. The HRI and IPC points are marked with filled circles.

## Chapter 3

# Analysis of the EXOSAT Spectra

### Introduction

*EXOSAT* carried two instruments which gave high quality spectral in the 1–20 keV energy range information. The most sensitive was the Medium Energy proportional counter array (ME) which had moderate energy resolution ( $\Delta E/E \sim 3-8$ ). The other was the Gas Scintillation proportional counter (GSPC) which had superior energy resolution ( $\Delta E/E \sim 5-12$ ), but a fifth of the sensitivity of the ME. Despite its improved energy resolution, the lower sensitivity of the GSPC resulted in no significant improvement in detection and determination of line features over the ME for all observations of clusters. For the brighter clusters simultaneous fitting of ME and GSPC spectra was not possible due to the different fields of view of the two instruments. This difference resulted in different fluxes in the GSPC and ME for the most extended cluster sources. So only spectra from the ME are analysed in this Chapter. Fits to the spectra with bremsstrahlung and more general emission models are given. The significance of the line determinations is discussed. The spectral parameters obtained are compared with those from previous satellites. The ME data from observations of Virgo, Coma and Perseus are presented in Chapter 5.

### 3.1 Instrument Description

The ME was a gas filled proportional counter array of eight counters with 2 layers, one filled with argon and carbon dioxide and the other with xenon and carbon dioxide. These eight counters were grouped in pairs to form four quadrants. These quadrants could be mechanically offset using two hydraulic pistons at the centre of the array (see Figure 3.1). A summary of the ME performance is given in Table 3.1 and the instrument is described in detail in Turner, Smith & Zimmerman (1981).

Effective Area	1600 cm <sup>2</sup> at 4 keV for all 8 counters aligned
Energy Range	1-30 keV Argon 5-50 keV Xenon
Energy Resolution ( $\Delta E/E$ )	$51/\sqrt{E_{\text{keV}}}$ % Argon
Field of View	45 arcmin FWHM, triangular response with 5 arcmin flat top
Average Steady Background	4 counts s <sup>-1</sup> per detector Argon (in 2-10 keV band)

Table 3.1: Performance of ME proportional counters

### 3.1.1 Performance during mission

The ME performed very well throughout the mission with only one detector of the original eight failing in the third year of operation. The highly elliptical orbit of *EXOSAT* resulted in a background in the counters for the majority of the orbit.

### 3.1.2 Observing Strategy

The standard procedure for observations was to have two quadrants on source and two offset by 2° to monitor the background. During the observations, at intervals of 10,000 to 15,000 seconds, the quadrants would be exchanged so source and background were collected in each of the eight detectors. This procedure is hereafter referred to as “nodding”. This array “nodding” was performed for most of the observations presented here. Data were also collected during the slewing of the spacecraft as it moved onto the next source. These slew data allowed the background to be determined for observations without a “nod”.

## 3.2 Data Analysis

The raw count data were read from the standard Final Observation Tapes using software written in Leicester. These data were then used to create a time series to identify periods of high background and serendipitous sources during slew. Having excluded any periods of unstable background, the data were summed into pulse height spectra for each detector in each section of the observation.

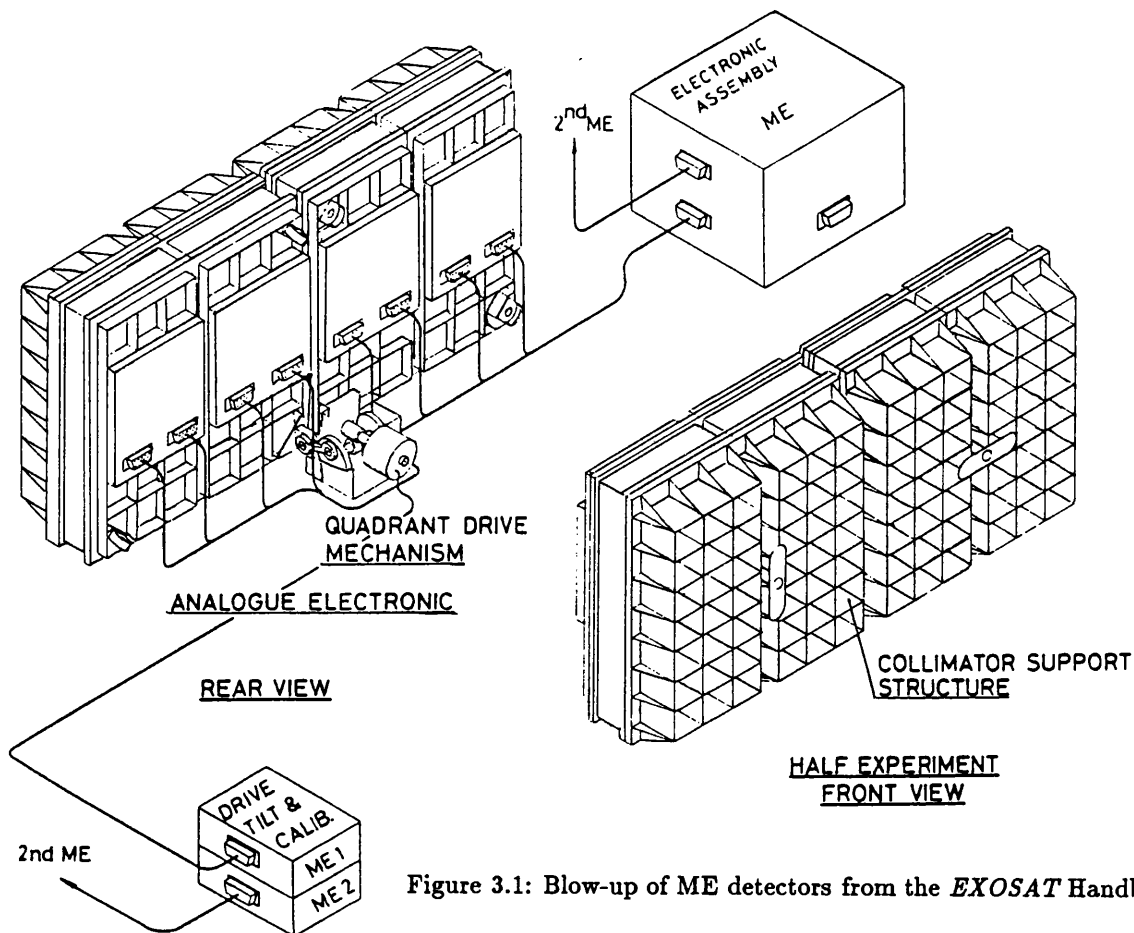


Figure 3.1: Blow-up of ME detectors from the *EXOSAT* Handbook

### 3.2.1 Background Subtraction

The next step in the analysis of ME data was the subtraction of a background from the source data obtained. The background was caused predominately by particle induced decays within the detector, but included a small contribution from the diffuse X-ray background. As mentioned above the *EXOSAT* orbit gave a stable background, which meant that background data from many hours, or even days, before or after the observation could be subtracted successfully. This situation should be compared with satellites in Low Earth Orbit where the background can be highly variable making the process of background subtraction much more complicated.

Most cluster observations contained an array “nod”, so the offset background data were subtracted from the source data for each of the eight detectors to give the source spectrum. A small correction, referred to as the difference spectra (Parmar & Izzo 1986), was added to compensate for the difference in the background for the offset detectors. In the cases where no “nod” was made the best section of slew data was used as a background, providing a source spectrum for only four detectors. Slews were relatively short resulting in poorer background subtractions than those for “noded” observations. Table 3.2 gives the type of subtraction used for each of the observations.

For all but three of the observations, a count rate of greater than  $0.3 \text{ counts s}^{-1} \text{ half}^{-1}$  was observed in the argon chamber. None of these three (A98, A140 and A1318) had any significant flux detected

Cluster	Date	Offset (arcmin.)	Exposure H1 (sec.)	Exposure H2 (sec.)	Subtraction Used	Detectors Used	2-10 keV Count Rate Channels 8 to 38 (cnt s <sup>-1</sup> half <sup>-1</sup> )	Channels fitted
A98	220/84	4.0	-	60000. (17000.)	SLEW	5678	0.11 ± 0.04	-
A119	331/84	4.2	13440.	15010.	NOD	1234678	2.53 ± 0.04	8-35
A133	224/83	5.1	10850.	7980.	NOD	12345678	1.33 ± 0.04	8-27
A140	336/84	2.8	7000.	7000.	NOD	1458	0.10 ± 0.03	-
A193	361/84	3.0	13600.	12350.	NOD	12345678	1.13 ± 0.03	7-31
A262	224/84	1.2	7930. (6170.)	11500. (3220.)	SLEW	12345678	2.20 ± 0.05	8-32
A376	12/85	6.5	9440.	9010.	NOD	12345678	0.80 ± 0.04	8-30
AWM7	258/84	2.6	8880.	9600.	NOD	1234568	7.79 ± 0.05	8-35
A400	13/85	2.5	23660.	25040.	NOD	123478	0.73 ± 0.04	8-32
A3122	2/84	7.2	-	8480. (5820.)	SLEW	5678	1.64 ± 0.06	8-28
0336+096	264/84	2.8	19840.	23500.	NOD	123468	4.14 ± 0.05	6-35
A478	276/84	3.0	10500.	9700.	NOD	12345678	5.28 ± 0.04	8-37
0422-086	48/85	4.2	3680.	10200.	NOD	1245678	1.38 ± 0.06	8-28
A496	49/86	20.6	11760.	13710.	NOD	1245678	2.51 ± 0.04 4.45 ± 0.07(cor)	8-35
3C129	271/85	4.6	8960.	16500.	NOD	1245678	7.15 ± 0.04	8-40
A576	306/84	6.0	13000.	10500.	NOD	12345678	1.50 ± 0.03	8-32
0745-191	304/85	2.8	20790.	22340.	NOD	1245678	4.46 ± 0.03	8-39
A754	323/85	15.2	8890.	16500.	NOD	1245678	4.76 ± 0.04 6.60 ± 0.06(cor)	8-40
Hydra-A	324/85	23.5	9600.	20500.	NOD	1245678	1.04 ± 0.04 1.94 ± 0.07(cor)	8-33
A1060	4/84	1.6	-	29080. (5000.)	SLEW	5678	3.81 ± 0.06	7-35
A1318	335/84	-	10240.	10560.	NOD	1458	-0.01 ± 0.05	-
A1367	5/84	-	-	34130. (5000.)	SLEW	5678	2.90 ± 0.06	7-30
Centaurus	20/84	0.6	29120. (16000.)	29120. (16000.)	SLEW	12468	10.67 ± 0.10	8-37
A3558	52/86	37.8	18480.	17500.	NOD	12468	0.69 ± 0.04 3.40 ± 0.19(cor)	-
A3562	176/84	17.3	-	41260. (5000.)	SLEW	58	2.17 ± 0.06 3.17 ± 0.09(cor)	8-30
A3571	29/84	6.2	-	14860. (3000.)	SLEW	5678	9.14 ± 0.07	8-34
A1795	17/85	3.7	14230.	25220.	NOD	124568	4.34 ± 0.03	8-35
A1837	47/85	2.7	8320.	9590.	NOD	1234578	0.47 ± 0.05	6-30
A2052	68/85	2.7	10300.	11650.	NOD	3456	2.43 ± 0.05	8-29
A2142	55/86	1.8	12340.	13400.	NOD	1245678	5.79 ± 0.04	8-45
A2147	93/84	11.4	-	16620. (4500.)	SLEW	5678	2.16 ± 0.07 2.71 ± 0.09(cor)	7-35
A2199	208/84	0.5	10320.	8200.	NOD	12345678	5.93 ± 0.04	8-36
Ophiuchus	250/84	2.5	3360.	7300.	NOD	1234568	33.64 ± 0.09	8-37
Cygnus-A	320/85	3.2	9760.	10500.	NOD	1245678	5.95 ± 0.05	7-40
2059-24	329/84	2.5	8350.	10360.	NOD	12345678	0.60 ± 0.04	8-37
A3825 & A3827	152/85	19.3	6240.	5500.	NOD	13478	1.14 ± 0.07	-
A2589	171/84	3.2	-	15880. (3780.)	SLEW	5678	1.33 ± 0.07	8-35
S1101 (Sers159-03)	161/84	0.8	-	11200. (8000.)	SLEW	5678	0.83 ± 0.05	8-28
A4059	338/84	0.1	11320.	11160.	NOD	12345678	1.66 ± 0.04	8-37

Table 3.2: Log of ME observations. Slew exposures are in brackets. The count rates are for Argon channels 5 to 38 per half array. The count rates marked '(cor)' have a correction for mispointing in the ME collimator of greater than 1.3.

in the LE.

The argon data were used in the spectral fitting, taking data from channels 7 or 8 (corresponding to bin centres of 1.53 or 1.88 keV) out to at least channel 27 (6.81 keV) and often to channel 35 (9.22 keV), depending on the flux and quality of the background subtraction. The bin ranges used are given in Table 3.2. The low count rates and high background in the xenon chamber resulted in few significant detections of clusters using xenon data. The xenon data were therefore excluded from the analysis of all sources except Perseus (Chapter 4) and Cygnus-A (Section 3.4).

Before fitting, the spectra from each detector were summed to give a single spectrum. A number of observations had detectors excluded because of high background or confusing sources in the offset quadrants. Table 3.2 shows which detectors were used in the fitting. All observations performed after 1985 day 232 did not include detector 3, which was switched off due to detector failure.

### 3.2.2 Collimator Corrections

Several of the observations presented here were not correctly positioned on the centre of the cluster. The ME collimator had a triangular response of  $45' \times 45'$  FWHM and a  $5'$  'flat-top' so any observation with an offset of greater than  $5'$  was corrected for the collimator response. This was done by taking the collimator profiles from the ME calibration data and calculating the relative effective area for each offset observation. The maximum correction factor used was 4.9 for A3558 which was offset by  $38'$ .

As clusters are extended sources there was also some underestimation of the flux due to lower response at large radii. Most clusters have a half-power width (*i.e.* the radius containing half the emitted flux) of a few arcmin so any correction will be negligible. However for nearby clusters, such as Virgo and Coma, the extension is significant compared with the  $45' \times 45'$  FWHM field of view of the ME, hence the ME gave a substantial underestimate for the flux.

Each ME detector had a collimator with a slightly different profile, so for extended sources the relative normalisations of the flux in the detectors differed. This effect could be seen in the brightest clusters when all detectors were fitted separately. The effect was most obvious in detector 7 where the collimator response was much narrower than the others. For AWM7, Ophiuchus and Centaurus, which are all nearby and bright, detector 7 was excluded from the fit to avoid any systematic errors from this effect.

### 3.2.3 Spectral Fitting

The background subtracted spectra were fitted in conjunction with LE filter count rates given in Chapter 2 using a  $\chi^2$  minimisation technique. The predicted model spectrum was generated and convolved with the detector response matrix to give an expected count rate in each channel. These were compared with the measured count rates and the deviations were calculated. This procedure was repeated with modified model parameters until the deviations were minimised.

The models used were a bremsstrahlung model, with and without an iron line fixed at 6.67 keV, and a more complex emission model from Raymond & Smith (1977). The Raymond & Smith (RS) model includes lines from the principal elements such as oxygen, carbon, silicon and iron. The majority of the lines from these heavy elements are emitted at energies below 1.5 keV and were hence outside the energy range of the ME. The most prominent line is the K- $\alpha$  complex of iron around 6.7 keV. For the spectra presented in this Chapter, the ME data were sufficient to constrain only the iron abundance. All other elemental abundances above helium were set to 0.5 of the solar value relative to hydrogen. This value is consistent with the few determinations of these abundances made with the SSS (Mushotzky & Szymkowiak 1988).

All fits included galactic absorption using the cross sections from Morrison & McCammon (1983). The galactic column density was either allowed as a free parameter or was fixed at the value found by radio measurements of the HI column from Stark *et al.* (1988).

## 3.3 Results

The results for the bremsstrahlung and RS fits are given in Tables 3.3 and 3.4 respectively and Figure 3.2 shows examples of the fitted photon spectra for RS models to 4 clusters.

### 3.3.1 Comparing Bremsstrahlung and Raymond & Smith Models

Although there are substantial differences between a bremsstrahlung model with a fixed 6.67 keV line and the RS model, once the model spectrum was convolved with the ME detector response matrix these differences were less obvious. The results from these fits can be compared to determine whether the more physically realistic RS model gave a significantly better fit than the bremsstrahlung model.

The derived temperatures compare well and are shown in Figure 3.3. The reduced  $\chi^2$  for the two models are shown in Figure 3.4 with the 97.5% confidence limit of 1.57 (for 30 degrees of freedom). From a sample of 32, at 97.5% confidence it can be expected that no result will exceed the confidence

Cluster	Temperature (keV)	Equivalent Width (keV)	Column Density ( $\times 10^{21}$ cm $^2$ )	Galactic Column ( $\times 10^{21}$ cm $^2$ )	2-10 keV Flux ( $\times 10^{-11}$ ergs cm $^{-2}$ s $^{-1}$ )	$\chi^2$ for fit
A119	$5.40^{+1.04}_{-0.78}$	< 0.88	$0.10^{+0.70}_{-0.06}$	0.36	3.00	27.41 (25)
A133	$3.94^{+1.56}_{-0.88}$	< 1.65	$0.07^{+0.40}_{-0.05}$	0.40	1.41	19.81 (17)
A193	$4.51^{+1.72}_{-1.49}$	$1.00^{+0.96}_{-0.94}$	$0.10^{+2.06}_{-0.08}$	0.42	1.32	18.74 (22)
A262	$2.39^{+0.37}_{-0.30}$	$2.47^{+1.32}_{-1.32}$	$0.18^{+0.63}_{-0.05}$	0.49	2.32	16.50 (22)
A376	$3.75^{+1.82}_{-0.99}$	< 1.53	$0.27^{+1.03}_{-0.10}$	0.58	1.01	17.82 (20)
AWM7	$3.64^{+0.24}_{-0.20}$	$0.84^{+0.22}_{-0.24}$	$0.62^{+0.59}_{-0.25}$	0.88	9.02	35.76 (25)
A400	$2.34^{+0.80}_{-0.53}$	< 5.18	< 0.32	0.85	0.79	18.91 (22)
A3122	$4.42^{+2.44}_{-1.42}$	$1.50^{+1.30}_{-1.30}$	$0.16^{+1.33}_{-0.09}$	0.40	1.91	22.34 (19)
0336+09	$3.10^{+0.29}_{-0.28}$	$0.58^{+0.46}_{-0.43}$	$0.69^{+1.28}_{-0.25}$	1.40	4.61	23.75 (27)
A478	$7.31^{+1.17}_{-1.00}$	$0.25^{+0.17}_{-0.18}$	$1.01^{+1.63}_{-0.63}$	1.30	6.51	40.05 (30)
0422-09	$2.98^{+0.88}_{-0.65}$	< 2.62	$0.38^{+0.72}_{-0.15}$	0.60	1.59	18.61 (18)
A496	$4.75^{+1.02}_{-0.78}$	< 0.72	$0.70^{+2.38}_{-0.12}$	0.45	5.34	18.46 (25)
3C129	$5.66^{+0.87}_{-0.68}$	$0.36^{+0.20}_{-0.19}$	$6.79^{+2.48}_{-2.29}$	5.76	8.93	36.71 (30)
A576	$3.65^{+0.97}_{-0.53}$	< 1.72	$0.54^{+13.68}_{-0.50}$	0.62	1.70	20.87 (22)
0745-19	$9.48^{+1.83}_{-1.54}$	$0.24^{+0.15}_{-0.15}$	$2.41^{+1.97}_{-1.16}$	4.61	5.70	32.79 (29)
A754	$8.95^{+1.71}_{-1.45}$	< 0.37	$0.51^{+1.87}_{-0.12}$	0.42	8.43	35.61 (30)
Hydra-A	$3.88^{+1.08}_{-1.41}$	< 1.49	$0.51^{+10.07}_{-0.22}$	0.47	2.43	26.80 (23)
A1060	$3.35^{+0.42}_{-0.36}$	< 0.80	$0.25^{+0.80}_{-0.05}$	0.50	4.35	15.28 (26)
A1367	$3.66^{+0.56}_{-0.45}$	< 0.38	$0.07^{+0.28}_{-0.04}$	0.20	3.46	17.91 (22)
Centaurus	$3.77^{+0.45}_{-0.52}$	$0.85^{+0.50}_{-0.48}$	$0.31^{+1.78}_{-0.08}$	0.80	11.13	28.37 (27)
A3562	$3.90^{+1.02}_{-0.84}$	< 2.18	$0.31^{+0.25}_{-0.14}$	0.45	3.56	17.30 (20)
A3571	$8.36^{+0.58}_{-1.42}$	$0.34^{+0.22}_{-0.26}$	$0.23^{+0.43}_{-0.05}$	0.42	12.18	36.95 (25)
A1795	$5.32^{+0.47}_{-0.42}$	$0.41^{+0.22}_{-0.21}$	$0.10^{+0.13}_{-0.04}$	0.11	5.28	29.75 (25)
A1837	$2.61^{+2.66}_{-1.07}$	< 8.05	< 0.55	0.48	0.49	27.89 (22)
A2052	$3.52^{+0.70}_{-0.55}$	$0.95^{+0.75}_{-0.77}$	$0.14^{+1.58}_{-0.05}$	0.27	2.59	24.02 (19)
A2142	$11.58^{+2.17}_{-1.55}$	< 0.20	$0.34^{+0.85}_{-0.12}$	0.38	7.46	33.27 (36)
A2147	$4.60^{+2.18}_{-1.22}$	< 2.06	$0.32^{+1.75}_{-0.11}$	0.35	3.24	23.58 (23)
A2199	$4.90^{+0.40}_{-0.37}$	$0.37^{+0.24}_{-0.23}$	$0.08^{+0.07}_{-0.03}$	0.09	7.10	30.62 (28)
Ophiuchus	$9.87^{+0.84}_{-0.73}$	$0.22^{+0.07}_{-0.08}$	$1.81^{+0.77}_{-0.66}$	1.97	43.52	56.40 (27)
S1101	$2.93^{+1.06}_{-0.75}$	< 2.09	$0.08^{+0.35}_{-0.06}$	0.20	0.94	16.77 (19)
A2589	$3.81^{+2.28}_{-1.22}$	< 3.00	$0.17^{+2.12}_{-0.10}$	0.46	1.59	13.01 (19)
A4059	$3.59^{+0.78}_{-0.57}$	< 1.73	$0.10^{+0.28}_{-0.04}$	0.11	1.86	17.54 (27)

Table 3.3: Results from bremsstrahlung model fits. The equivalent width for a fixed 6.67 keV line is given. The number of degrees of freedom for the fit is shown in brackets.

Cluster	Temperature (keV)	Iron Abundance (relative to solar)	Column Density ( $\times 10^{21}$ cm $^2$ )	Galactic Column ( $\times 10^{21}$ cm $^2$ )	2-10 keV Flux ( $\times 10^{-11}$ ergs cm $^{-2}$ s $^{-1}$ )	$\chi^2$ for fit
A119	5.09 $^{+0.97}_{-0.75}$	0.28 $^{+0.26}_{-0.25}$	0.23 $^{+1.33}_{-0.14}$	0.36	3.02	27.04 (25)
A133	3.75 $^{+1.99}_{-0.88}$	< 1.06	0.28 $^{+0.99}_{-0.26}$	0.40	1.43	24.60 (17)
A193	4.24 $^{+1.59}_{-0.85}$	0.57 $^{+0.64}_{-0.54}$	0.30 $^{+3.78}_{-0.28}$	0.42	1.34	20.74 (22)
A262	2.42 $^{+0.31}_{-0.27}$	1.31 $^{+0.94}_{-0.72}$	0.16 $^{+0.89}_{-0.05}$	0.49	2.34	12.73 (22)
A376	5.05 $^{+3.20}_{-1.91}$	< 0.70	0.24 $^{+0.94}_{-0.09}$	0.58	1.01	17.51 (20)
AWM7	3.57 $^{+0.24}_{-0.20}$	0.43 $^{+0.28}_{-0.25}$	0.59 $^{+0.45}_{-0.09}$	0.88	9.08	53.50 (25)
A400	2.11 $^{+1.31}_{-0.53}$	< 4.57	< 0.75	0.85	0.79	21.07 (22)
A3122	4.06 $^{+2.31}_{-1.12}$	0.81 $^{+0.96}_{-0.71}$	0.28 $^{+1.93}_{-0.16}$	0.40	1.94	23.70 (19)
0336+09	3.05 $^{+0.28}_{-0.25}$	0.35 $^{+0.25}_{-0.23}$	0.61 $^{+1.10}_{-0.19}$	1.40	4.65	23.37 (27)
A478	6.80 $^{+1.08}_{-0.99}$	0.27 $^{+0.14}_{-0.16}$	1.04 $^{+1.87}_{-0.68}$	1.30	6.54	32.39 (30)
0422-09	2.93 $^{+0.86}_{-0.64}$	< 1.63	0.34 $^{+0.95}_{-0.11}$	0.60	1.60	19.22 (18)
A496	4.66 $^{+0.95}_{-0.78}$	< 0.51	0.61 $^{+2.08}_{-0.11}$	0.45	5.37	20.44 (25)
3C129	5.63 $^{+0.74}_{-0.59}$	0.20 $^{+0.11}_{-0.11}$	6.18 $^{+2.27}_{-1.85}$	5.76	9.00	39.23 (33)
A576	3.65 $^{+0.79}_{-0.56}$	0.43 $^{+0.48}_{-0.41}$	< 8.84	0.62	1.72	17.57 (22)
0745-19	8.54 $^{+1.89}_{-1.43}$	0.29 $^{+0.14}_{-0.16}$	2.87 $^{+1.99}_{-1.40}$	4.61	5.71	32.08 (29)
A754	8.67 $^{+1.80}_{-1.55}$	< 0.37	0.48 $^{+1.89}_{-0.11}$	0.42	8.48	38.47 (30)
Hydra-A	3.85 $^{+0.96}_{-0.93}$	< 0.41	< 6.03	0.47	2.44	27.24 (23)
A1060	3.29 $^{+0.40}_{-0.33}$	< 0.46	0.21 $^{+0.61}_{-0.05}$	0.50	4.35	17.04 (26)
A1367	3.54 $^{+0.46}_{-0.46}$	< 0.29	0.20 $^{+0.33}_{-0.13}$	0.20	3.44	20.39 (22)
Centaurus	3.61 $^{+0.41}_{-0.36}$	0.47 $^{+0.28}_{-0.26}$	0.28 $^{+1.24}_{-0.08}$	0.80	11.22	31.81 (29)
A3562	3.75 $^{+0.95}_{-0.77}$	< 1.18	0.29 $^{+0.28}_{-0.13}$	0.45	3.62	16.63 (20)
A3571	7.59 $^{+1.22}_{-0.94}$	0.38 $^{+0.17}_{-0.18}$	0.24 $^{+0.50}_{-0.05}$	0.42	12.26	27.16 (25)
A1795	5.05 $^{+0.39}_{-0.46}$	0.25 $^{+0.14}_{-0.12}$	0.11 $^{+0.10}_{-0.03}$	0.11	5.30	28.98 (25)
A1837	2.38 $^{+0.86}_{-0.78}$	< 11.26	< 5.81	0.48	0.50	27.01 (22)
A2052	3.43 $^{+0.64}_{-0.50}$	0.53 $^{+0.52}_{-0.43}$	0.30 $^{+0.89}_{-0.13}$	0.27	2.62	28.78 (19)
A2142	10.98 $^{+1.99}_{-1.71}$	< 0.36	0.33 $^{+0.99}_{-0.13}$	0.38	7.48	29.34 (36)
A2147	4.36 $^{+2.23}_{-1.10}$	< 1.13	0.53 $^{+1.86}_{-0.19}$	0.35	3.27	25.67 (23)
A2199	4.71 $^{+0.41}_{-0.35}$	0.21 $^{+0.13}_{-0.13}$	0.07 $^{+0.06}_{-0.03}$	0.09	7.12	30.74 (28)
Ophiuchus	8.99 $^{+0.84}_{-0.71}$	0.29 $^{+0.07}_{-0.08}$	2.04 $^{+0.87}_{-0.70}$	1.97	43.63	36.75 (27)
S1101	2.99 $^{+1.17}_{-0.71}$	< 1.53	0.04 $^{+0.25}_{-0.04}$	0.20	0.95	16.54 (19)
A2589	3.66 $^{+2.20}_{-1.12}$	< 2.04	0.15 $^{+2.22}_{-0.09}$	0.46	1.61	13.02 (19)
A4059	3.46 $^{+0.63}_{-0.58}$	< 0.92	0.16 $^{+0.23}_{-0.08}$	0.11	1.88	19.84 (27)

Table 3.4: Results from Raymond & Smith model fits

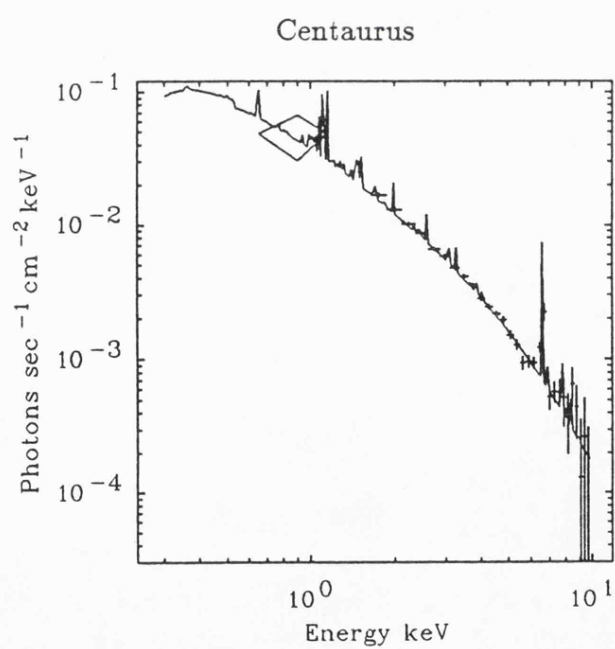
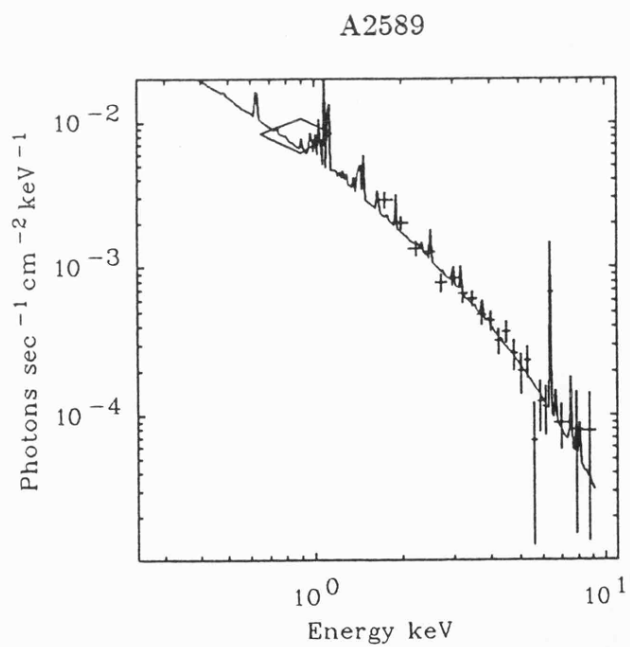
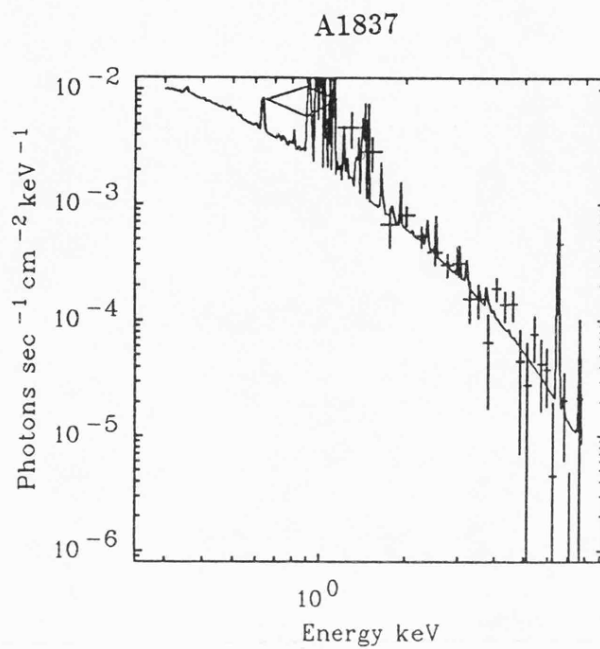
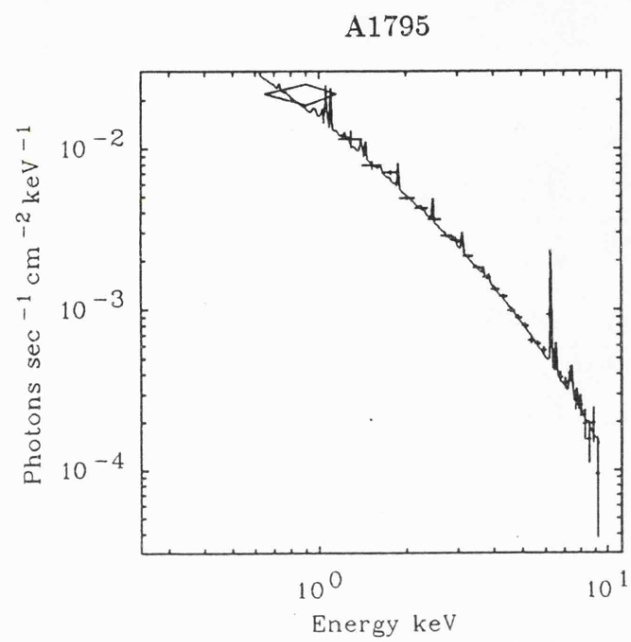


Figure 3.2: Examples the photon spectra of fitted Raymond & Smith models to A1795, A1837, A2589 and Centaurus

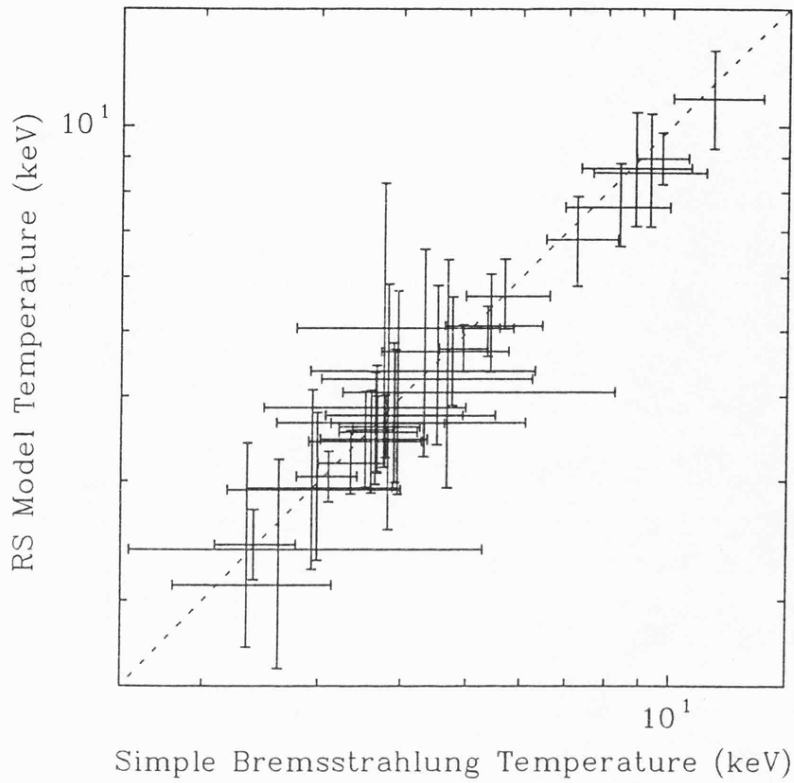


Figure 3.3: Plot of temperatures from bremsstrahlung model fits against those from RS model fits.

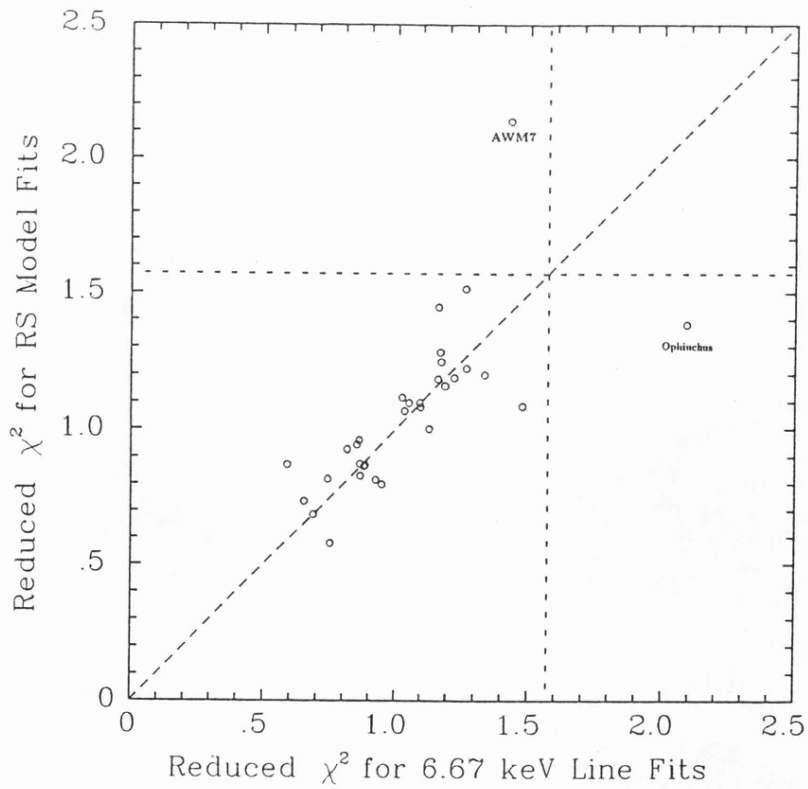


Figure 3.4: Plot of reduced  $\chi^2$  for bremsstrahlung and RS models. The large dashed line represents equal values. The short-dashed lines are the 90% confidence values of  $\chi^2$ .

limit. However for each model one result did exceed this limit. For the bremsstrahlung model, Ophiuchus gave an unacceptable fit due to the strength of the iron K- $\beta$  line at 7.9 keV. The high temperature and flux of Ophiuchus gave a significant detection of the line. So when a model with two lines was used an acceptable fit was obtained (see Table 3.6). For the RS model, AWM7 gave a poor fit due to the unusually low line energy (6.45 keV) obtained for this observation. This low line energy was not due to any background flaring. However the line energy is consistent with being 6.67 keV at the 90% limit.

It can be seen that both models gave statistically acceptable fits to the data although for high temperature, high flux observations the Raymond & Smith model gave a marginally better fit due to the presence of the K- $\beta$  line.

### 3.3.2 Iron Lines

As mentioned above, the principal spectral feature for clusters in the 2–10 keV band is line emission from iron. As the lines detected in the *EXOSAT* spectra are of great astrophysical interest it is important to determine their statistical significance.

#### Significance of Line Detections

The spectra were fitted with and without a line at 6.67 keV. From the improvement in  $\chi^2$  between the fits the significance of the line detection can be calculated using the F-test (Bevington 1969). The values of the F-statistic are given in Table 3.5. In all, 24 of the sample clusters show a line detection at a confidence level of greater than 90%, corresponding to an F-statistic of greater than 4.35 (for 20 degrees of freedom), illustrating the sensitivity of the ME. A similar procedure was followed with the Raymond & Smith code by setting the iron abundance to zero in order to determine the change in  $\chi^2$ . The results obtained were similar to those from the test for the 6.67 keV line.

#### Line Energies

The effective line energy of the iron K- $\alpha$  complex increases with temperature as the relative contribution of the lines changes, so the assumption of a fixed 6.67 keV energy is not strictly correct. However the energy resolution of the ME was poor, so only for the brighter sources could reasonable limits be set on the line energy.

Table 3.6 gives the results for fitting a single free line and two lines (one free line and another fixed at 7.9 keV) to the spectra with a flux greater than  $5 \times 10^{-11}$  erg cm $^{-2}$  s $^{-1}$ . The improvement in  $\chi^2$

Cluster	F-statistic and probability for a better fit with a 6.67 keV line than without a line	F-statistic and probability for a better fit with a free column than the galactic column	F-statistic and probability for a better fit with a free line energy than a fixed 6.67 keV line	F-statistic and probability for a better fit with two lines (free+7.9) than a free single line
A119	9.78 >99.5%	2.07 >75%	-	-
A133	4.94 >95%	1.72 >75%	-	-
A193	11.73 >99.5%	2.34 >75%	-	-
A262	35.72 >99.9%	4.03 >90%	-	-
A376	0.04 <50%	2.11 >75%	-	-
AWM7	71.08 >99.9%	1.50 >75%	2.95 >90%	0.61 >50%
A400	3.09 >90%	9.03 >99%	-	-
A3122	9.35 >99.5%	0.93 >50%	-	-
0336+09	16.58 >99.9%	3.23 >90%	-	-
A478	25.47 >99.9%	0.39 <50%	8.28 >99%	0.17 <50%
0422-09	3.06 >90%	1.21 >50%	-	-
A496	5.75 >97.5%	0.88 >50%	-	-
3C129	33.28 >99.9%	1.32 >50%	0.47 >50%	0.05 <50%
A576	5.33 >95%	0.08 <50%	-	-
0745-19	22.54 >99.9%	8.73 >99%	3.03 >90%	0.85 >50%
A754	6.03 >97.5%	0.04 <50%	-	-
Hydra-A	0.09 <50%	0.06 <50%	-	-
A1060	3.25 >90%	3.10 >90%	-	-
A1367	0.00 <50%	3.37 >90%	-	-
Centaurus	22.35 >99.9%	1.42 >75%	0.57 >50%	0.98 >50%
A3562	7.69 >99%	3.24 >90%	-	-
A3571	21.77 >99.9%	1.39 >75%	12.72 >99.5%	4.22 >95%
A1795	33.17 >99.9%	0.25 <50%	1.39 >75%	0.02 <50%
A1837	4.59 >95%	3.77 >90%	-	-
A2052	16.92 >99.9%	0.44 <50%	-	-
A2142	2.28 >75%	0.05 <50%	5.93 >97.5%	-
A2147	6.02 >97.5%	0.05 <50%	-	-
A2199	21.68 >99.9%	0.48 >50%	1.35 >50%	0.03 <50%
Ophiuchus	37.15 >99.9%	0.24 <50%	7.24 >97.5%	3.07 >90%
S1101	0.03 <50%	2.63 >75%	-	-
A2589	6.16 >97.5%	1.80 >75%	-	-
A4059	9.26 >99.5%	0.20 <50%	-	-

Table 3.5: Values for F-statistic and probability of better fit for the addition of a single fixed line to the fit, allowing the line energy to vary and including 2 lines to the fit (for the brighter clusters). The values for the iron line energies are given in Table 3.6

Cluster	$\chi^2$ for line at 6.67 keV	K- $\alpha$ Line Energy for single line fit (keV)	K- $\alpha$ Equivalent Width for single line fit (keV)	$\chi^2$ for single line fit	K- $\alpha$ Line Energy for two line fit (keV)	K- $\alpha$ Equivalent Width for two line fit (keV)	$\chi^2$ for two line fit
AWM7	35.76 (25)	$6.50^{+0.25}_{-0.23}$	$0.83^{+0.25}_{-0.24}$	31.69 (24)	$6.44^{+0.32}_{-0.27}$	$0.79^{+1.57}_{-0.26}$	30.83 (23)
A478	40.05 (30)	$7.16^{+0.53}_{-0.49}$	$0.38^{+0.25}_{-0.23}$	30.91 (29)	$7.01^{+0.95}_{-0.81}$	$0.47^{+0.44}_{-0.41}$	30.72 (28)
3C129	36.71 (30)	$6.76^{+0.40}_{-0.37}$	$0.36^{+0.22}_{-0.21}$	36.10 (29)	$6.74^{+0.51}_{-0.48}$	$0.35^{+0.23}_{-0.21}$	36.04 (28)
0745-19	32.79 (29)	$6.97^{+0.55}_{-0.51}$	$0.27^{+0.18}_{-0.18}$	29.48 (28)	$6.74^{+0.82}_{-0.70}$	$0.24^{+0.18}_{-0.22}$	28.55 (27)
Centaurus	28.37 (27)	$6.80^{+0.58}_{-0.47}$	$0.90^{+0.57}_{-0.55}$	27.74 (26)	$6.68^{+0.71}_{-0.58}$	$0.75^{+0.67}_{-0.59}$	26.65 (25)
A3571	36.95 (25)	$7.18^{+0.51}_{-0.42}$	$0.52^{+0.28}_{-0.26}$	23.79 (24)	$6.81^{+0.79}_{-0.71}$	$0.35^{+0.37}_{-0.28}$	19.96 (23)
A1795	29.75 (25)	$6.87^{+0.48}_{-0.45}$	$0.43^{+0.25}_{-0.24}$	28.06 (24)	$6.78^{+0.61}_{-0.62}$	$0.40^{+0.28}_{-0.26}$	28.03 (23)
A2142	33.27 (36)	$7.79^{+3.78}_{-1.66}$	< 0.46	28.33 (35)	unconstrained	-	-
A2199	30.62 (28)	$6.88^{+0.56}_{-0.55}$	$0.39^{+0.27}_{-0.26}$	29.11 (27)	$6.88^{+0.65}_{-0.70}$	$0.39^{+0.29}_{-0.29}$	29.07 (26)
Ophiuchus	56.40 (27)	$6.94^{+0.42}_{-0.22}$	$0.26^{+0.08}_{-0.08}$	43.73 (26)	$6.70^{+0.41}_{-0.32}$	$0.23^{+0.09}_{-0.09}$	38.77 (25)

Table 3.6: Results for line fits to spectra with fluxes greater than  $5 \times 10^{-11} \text{ erg cm}^{-2} \text{ s}^{-1}$

between fitting a fixed line, a free line and two lines can be seen. In several cases the line energy for a single line fit was overestimated due to blending with the K- $\beta$  line at 7.9 keV.

### Equivalent Widths

The equivalent widths of the K- $\alpha$  and K- $\beta$  lines change with temperature. Figure 3.5 shows the measured equivalent width of the 6.67 keV line versus temperature and the expected equivalent width for a 0.4 solar abundance plasma shown by a smooth curve. All the points are consistent with a constant abundance apart from A400.

At low temperatures it appears that the measured equivalent widths are quite large. This is largely due to the low level of the continuum above the line energy ( $>7$  keV). The poor statistics for these energies made determining an equivalent width difficult. There is also a large uncertainty in the expected equivalent width from different emission model codes due to poorly determined atomic transition rates (Rothenflug & Arnaud 1985). Therefore great care is required in interpreting the results for low temperature clusters.

The upper limits on the equivalent width of the K- $\beta$  line were all above 0.5 keV and so provided no useful information on the ratio of K- $\alpha$  to K- $\beta$  equivalent widths.

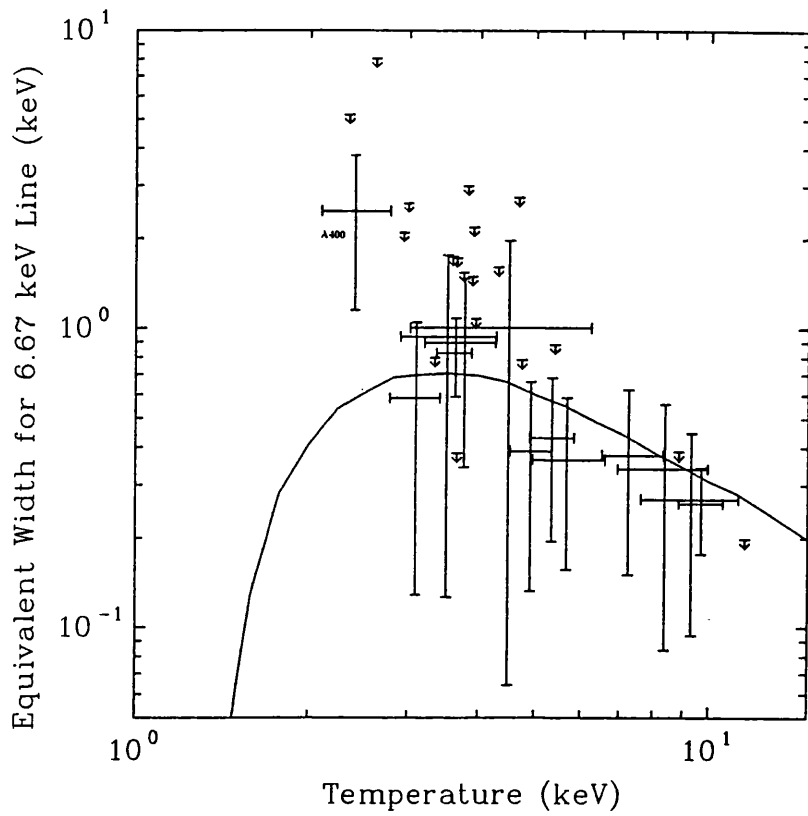


Figure 3.5: Equivalent width for 6.67 keV line plotted against temperature. The solid line is the equivalent width expected for a 0.4 solar abundance plasma from the RS code.

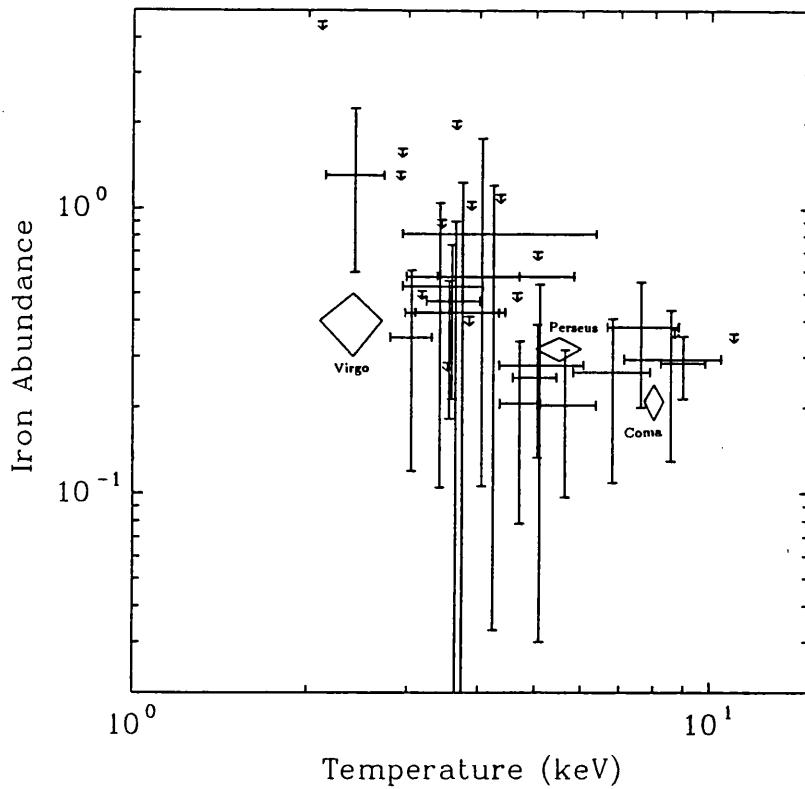


Figure 3.6: Iron abundance plotted against temperature from Raymond & Smith model. The results for Virgo, Coma and Perseus are from Chapter 4.

## Raymond & Smith Abundances

The Raymond & Smith model fits gave an iron abundance directly and these results are plotted in Figure 3.6. Again the abundances at low temperatures appear quite high but this was due to the effects mentioned above.

### 3.3.3 Column Densities

The derived column densities can be compared with the expected galactic values, estimated from measurements of 21 cm line emission of atomic hydrogen in the line of sight through the galaxy (Heiles 1975; Stark *et al.* 1988). The results show a good agreement (see Figure 3.7) and in all but two cases the galactic value was within the 90% confidence limit of the measured value, the exceptions being A400 and 0745-191. Any deviations in column density can also be investigated by fixing the column density at the galactic value and calculating the increase in  $\chi^2$  over that obtained by using a free column density, from which an F-statistic can be determined.

The values of F-statistic are given in Table 3.5 and show that only for A400 and 0745-191 were statistically improved fits achieved with a free column (at the 90% confidence level). As the LE was sensitive to the absorption, the low values of column density obtained for these two clusters could be due either to an underestimation of the galactic column or to an excess in the low energy count rate. The 21 cm observations are known to be reliable, so the latter explanation is more likely. An excess in the LE could have been due to emission from a cooling flow, to some other spectral component in the cluster, or to the poor sensitivity of the LE leading to an overestimate of the count rate. In the case of 0745-191 there is a cooling flow of  $400\text{--}1000 M_{\odot} \text{ yr}^{-1}$  and the image was quite compact due to its large redshift. So the excess can be explained by cooling emission. However in the case of A400 there was only a small amount of cooling ( $<30 M_{\odot} \text{ yr}^{-1}$ ) and the LE image showed that the cluster emission was highly diffuse and weak. Therefore the excess in the LE was probably due to the poorly defined background level.

It can be concluded that the column densities derived from the joint LE/ME fits agreed well with those expected from the galactic estimates. The only significant evidence for excess low energy emission from cooling gas is from 0745-191, which is known to have a large cooling flow.

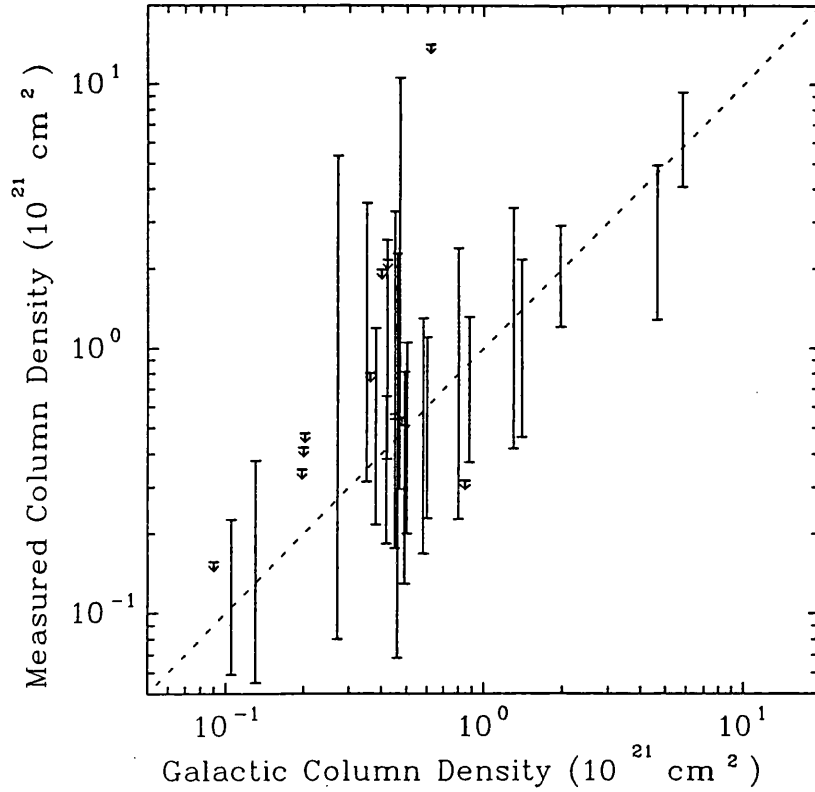


Figure 3.7: Plot of galactic column density and measured column density. The dashed line represents equal galactic and measured columns.

### 3.4 Individual Clusters

Several observations were not included in the analysis of the sample for the following reasons:

**A3558** The observation of A3558 was mistakenly positioned on the centre of the HEAO-1 error box position. This resulted in the cluster being offset by 38 arcmin in the ME field of view. Thus the measured flux in the ME was low and the cluster fell outside the LE field of view. The best fit spectrum gave a temperature of  $3.7_{-1.0}^{+2.0}$  keV and a 2–10 keV flux of  $4.2 \times 10^{-11} \text{ erg cm}^{-2} \text{ s}^{-1}$  corrected for the collimator offset (by a factor of 4.9). As there was no LE count rate for this observation it was not included in the analysis of the sample.

**A2029** The region of sky around A2052 contains a number of X-ray bright clusters. One of those clusters, A2029, was detected in two of the offset quadrants. This complicated the background subtraction, but gave two cluster spectra in one observation. The spectrum of A2029 gave a temperature of  $8.9_{-2.0}^{+3.4}$  keV, a 2–10 keV flux of  $8.6 \times 10^{-11} \text{ erg cm}^{-2} \text{ s}^{-1}$  (including a correction of 1.2 for the offset of the cluster in the ME field of view) and an abundance of less than 0.5. These results were not included in the analysis as no LE count rate was available.

**Cygnus-A** As reported by Arnaud *et al.* (1987), the *EXOSAT* data show evidence for a non-thermal source at the centre of the cluster containing Cygnus-A. Fitting a Raymond & Smith model to the data gave a temperature of  $10.3_{-2.1}^{+4.1}$  keV, an iron abundance of  $0.55_{-0.22}^{+0.35}$

and a  $\chi^2$  of 50.6 with 37 degrees of freedom. This temperature is relatively high compared to other clusters of a similar luminosity. Given the evidence from HEAO-1 of a non-thermal source mentioned in Arnaud *et al.* (1987) the addition of a second component was warranted. Therefore the spectrum was fitted with Raymond & Smith model and a power law with a photon index of 1.7 (*i.e.* a canonical AGN spectrum, Turner 1988). Fixing the galactic column density at the value given by Stark *et al.* of  $3.28 \times 10^{21} \text{ cm}^2$  a significantly improved fit was obtained. The  $\chi^2$  of 39.4 with 36 degrees of freedom gave an F-statistic of 9.7 which is significant at the 99.5% level. The fit gave a lower temperature of  $5.0_{-1.4}^{+4.6}$  and an iron abundance of  $0.40_{-0.21}^{+0.38}$ . The intrinsic column of the power law was determined as  $1.4_{-0.8}^{+1.7} \times 10^{23} \text{ cm}^2$ . This is a moderately high value for AGN, but gives extrapolated LE and HRI count rates in agreement with the upper limits in Arnaud *et al.* (1987). The unabsorbed 2–10 keV fluxes for the cluster and power law were  $6.03 \times 10^{-11} \text{ erg cm}^{-2} \text{ s}^{-1}$  and  $3.73 \times 10^{-11} \text{ erg cm}^{-2} \text{ s}^{-1}$  respectively. Due to the complexity of this source it was left out of the analysis of the sample.

**2008-56** The only published *EXOSAT* result which is not presented in this thesis is of 2008-569 reported in Piro & Fusco-Femiano (1988). The data for the cluster were obtained from one offset quadrant of an observation of another target (RR Tel). The spectrum obtained gave a temperature of  $5.3_{-0.9}^{+1.1}$  keV. But the flux was poorly determined due to the uncertainties in the cluster position in the ME field of view. As this observation had no LE data it was not included in the sample.

**2059-25** 2059-25 was the most distant cluster detected by *EXOSAT*, at a redshift of 0.188. The cluster is reported by White *et al.* (1981) to show a soft spectrum in the *EINSTEIN* IPC, which they interpret as the cluster being at an early stage of evolution. For the *EXOSAT* observation, Kaastra & de Korte (1988) quote a temperature of  $>5$  keV and a luminosity of  $2.8 \times 10^{45} \text{ erg cm}^{-2} \text{ s}^{-1}$  for this source. So 2059-25 is a high luminosity cluster, but is by no means unusual compared with other nearby clusters. The best fit Raymond & Smith temperature was  $7.0_{-2.2}^{+6.9}$  keV (assuming an iron abundance of 0.35) with a 2–10 keV flux of  $7.4 \times 10^{-12} \text{ erg cm}^{-2} \text{ s}^{-1}$ . Due to the large redshift this cluster was omitted from the analysis of the sample to avoid any possible bias from evolutionary effects.

**A3825/7** Piccinotti *et al.* (1982) associate the source 1H2159-60 with a cluster. Two Southern Abell clusters, A3825 and A3827, fell within in the ME field of view and both were detected in the LE (see Table 2.2). The ME spectrum gave a temperature of  $5.6_{-1.7}^{+6.6}$  keV and a 2–10 keV flux of  $1.4 \times 10^{-11} \text{ erg cm}^{-2} \text{ s}^{-1}$  (with no correction for the collimator response). The clusters are of similar optical richness (77 and 100) and redshifts (0.0744 and 0.0993), so the ME spectrum could not be confidently associated with either cluster. Therefore this observation was not included in the analysis. This *EXOSAT* result implies that the Piccinotti identification is confused.

Cluster	Paper	Published Temperature (keV)	Published Iron Abundance (solar)	Presented Temperature (keV)	Presented Iron Abundance (solar)
0336+096	1	$2.9 \pm 0.3$	$0.4 \pm 0.2$	$3.05^{+0.28}_{-0.25}$	$0.35^{+0.25}_{-0.23}$
0745-191	2	$8.6^{+1.1}_{-0.9}$	$0.33^{+0.11}_{-0.11}$	$8.54^{+1.89}_{-1.43}$	$0.29^{+0.14}_{-0.16}$
A1060	3	3.2	–	$3.29^{+0.40}_{-0.33}$	<0.46
Cygnus-A	2	$4.1^{+5.6}_{-1.5}$	$0.59^{+0.68}_{-0.35}$	$5.0^{+4.6}_{-1.4}$	$0.40^{+0.38}_{-0.21}$
Ophiuchus	2	$9.4^{+1.5}_{-1.2}$	$0.26^{+0.14}_{-0.13}$	$8.96^{+0.82}_{-0.74}$	$0.28^{+0.07}_{-0.07}$
2008-569	4	$5.3^{+1.1}_{-0.9}$	$0.57^{+0.20}_{-0.27}$	Omitted	–
2059-247	5	>6.0	–	$7.0^{+6.9}_{-2.2}$	0.35 (fixed)

1. Singh, Westergaard & Schnopper (1986)
2. Arnaud *et al.* (1987)
3. Singh, Westergaard & Schnopper (1988a)

4. Piro & Fusco-Femiano (1988)
5. Kaastra & de Korte (1988)

Table 3.7: Summary of previously published *EXOSAT* results

### 3.5 Comparison with Published *EXOSAT* Results

Results from a few of these *EXOSAT* ME observations have been published. A summary of these results is given in Table 3.7. The agreement between the results is good, apart from Cygnus-A where the temperature presented here is higher than that obtained by Arnaud *et al.* (1987). This difference is due to a smaller estimate of the power law contribution in this analysis (see above).

### 3.6 Comparison with Previous X-ray Observations

The two principal datasets that can be compared with the ME data are from the A-2 instrument on HEAO-1 and the MPC on *EINSTEIN*. The data from HEAO-1 were kindly communicated to me by Richard Mushotzky and the MPC data by Keith Arnaud.

#### 3.6.1 HEAO-1

The HEAO-1 A-2 detectors had a much larger field of view than the ME ( $1.5^\circ \times 3.0^\circ$ ) and an energy range of 2–30 keV. Figure 3.8 shows the *EXOSAT* temperature against the HEAO-1 value. There appears to be significant disagreement between the results for only one cluster, A2147. This is likely to be due to flux from the nearby cluster, A2151, which was included in the large field of view of HEAO-1. There is also marginal evidence for a systematic underestimation of the temperature by HEAO-1 at low temperatures. This is probably be due to the differences in the models and fitting techniques used.

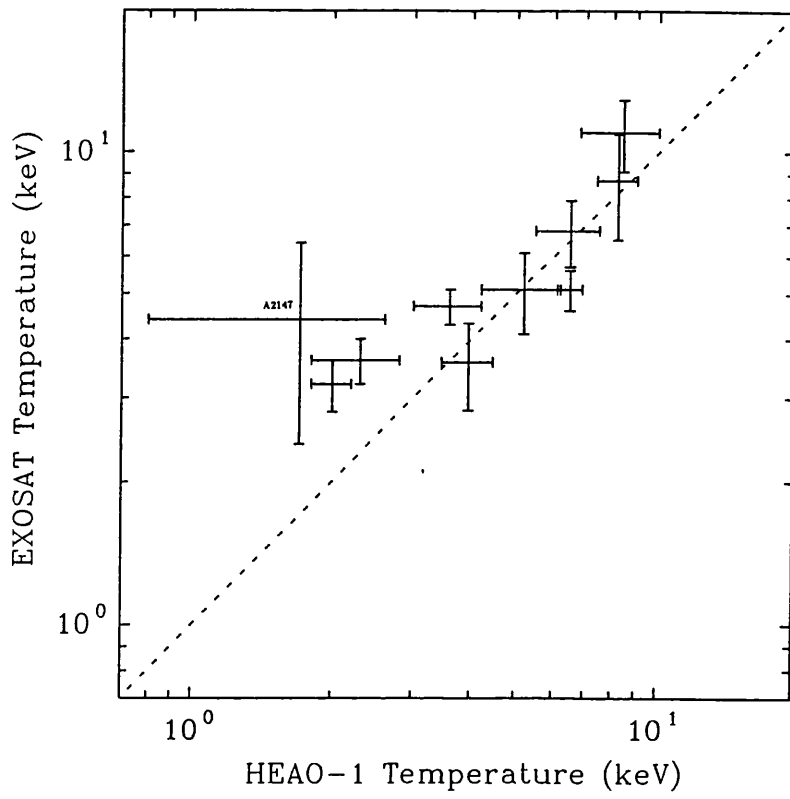


Figure 3.8: Plot comparing temperatures determined by *EXOSAT* and HEAO-1

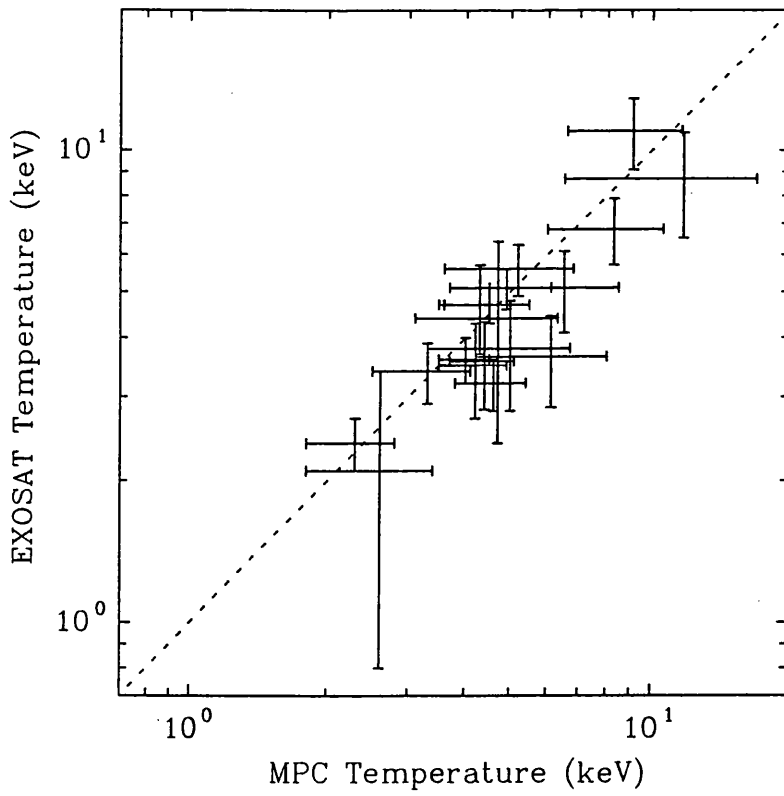


Figure 3.9: Plot comparing temperatures determined by *EXOSAT* and *EINSTEIN* MPC

HEAO-1 results showed evidence of secondary, hard spectral components in A1060 and Centaurus (Mitchell & Mushotzky 1980). The ME spectra showed no evidence of any hard component in A1060, Centaurus or any other cluster (apart from Cygnus-A and Perseus). So it can be concluded that two component models mentioned in Mitchell & Mushotzky are not a common phenomenon.

### 3.6.2 MPC

The MPC had a field of view of identical size to that of the ME ( $45' \times 45'$  FWHM). The effective area was  $\sim 600 \text{ cm}^2$  and the energy range was 2–20 keV. However the MPC had only 8 energy bins for each spectrum so it had poor sensitivity to iron lines. The background subtraction was relatively difficult due to the low earth orbit of *EINSTEIN* and the lack of any simultaneous background detector. However recent analysis by Arnaud (1988b) has produced a reliable background model providing subtractions for fluxes as low as 0.5 mcrab.

Figure 3.9 shows an excellent agreement between the temperatures determined by *EXOSAT* and MPC. The *EXOSAT* temperatures are better determined in all cases.

## 3.7 Conclusions

The *EXOSAT* 0.1–10 keV spectra were well fitted by isothermal bremsstrahlung models. There was no significant evidence for excess hard or soft emission. Iron lines were detected at greater than 90% significance in 24 of the 32 clusters observed. The smaller field of view of the ME reduced the problems of confusion that affected previous proportional counters.

These *EXOSAT* spectra form the largest dataset of cluster temperatures and iron abundances presently available. The implications of these results are discussed in Chapter 5 & 6.

## Chapter 4

# EXOSAT observations of the Virgo, Coma and Perseus Clusters

### Introduction

As the closest rich clusters, Virgo, Coma and Perseus have been intensively observed at all wavelengths. Their proximity means that they extend from 3 to 10 degrees over the sky. The relatively small field of view of the ME experiment on *EXOSAT* ( $45' \times 45'$  FWHM) made possible the study of the variation of temperature and abundance for sources extended on  $\sim 10$  arcmin scales. This Chapter gives a brief explanation of the techniques used and the problems encountered with the ME analysis. The results from multiple pointed observations with the ME and deep LE images of Virgo, Coma and Perseus are presented and the implications of these results are discussed.

### 4.1 Analysis of Highly Extended Sources with the ME

The ME provided a unique opportunity to measure the radial variation of temperature and iron abundance in extended sources utilising the small field of view of the ME collimators. Despite this relatively small field of view it should be noted that for any observation of an extended source, emission from a large range of radii was detected. Therefore the simple approach that the temperature measured from the central pointing represents the *actual* central temperature is incorrect. Instead the “mean” radius of the emission over the whole field of view of the collimator, and along the line of sight through the cluster, should be considered. This approach requires *a priori* knowledge of the the surface brightness profile. For the three clusters presented here the cluster surface brightness profiles have all been well determined using the *EINSTEIN* IPC

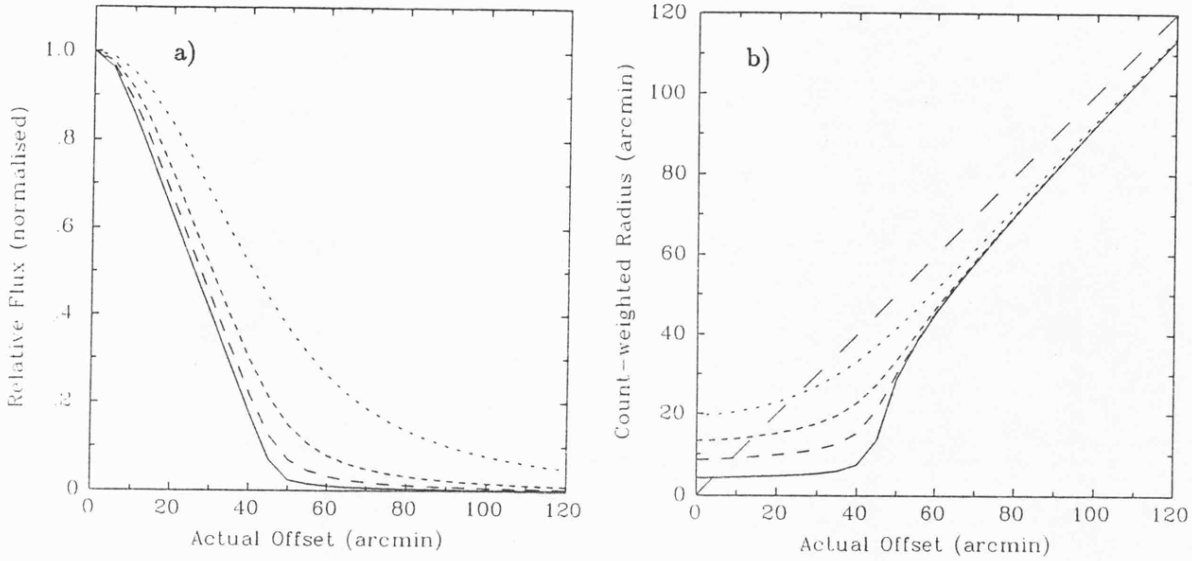


Figure 4.1: a) Predicted flux for the ME against offset angle and b) count weighted radius against offset angle. Both are plotted for the case a roll angle of  $0.0^\circ$ , a  $\beta$  parameter of 0.6 and a core radius 1' (solid line), 4' (large dashed), 10' (medium dashed) and 30' (fine dashed).

out to 30–60 arcmin. So for the two dimensional case (ignoring projection effects) it is possible to calculate the “mean” or “count-weighted” radius for a given surface brightness model, offset position and orientation by summing the expected flux over the ME field of view. Figure 4.1a shows the variation in expected flux with offset for clusters with modified King profiles of core radii of 1, 4, 10 and 30 arcmin and a  $\beta$  parameter of 0.6. The “mean” or “count-weighted” radius determined is shown in Figure 4.1b for the same four cases plotted against the actual offset. The most striking feature of Figure 4.1b is that the “count-weighted” radius tends to a constant value for small offsets. This demonstrates the effect mentioned above that the temperature measured at the centre is *not* the central temperature. Also, for the least extended case, the “count-weighted” radius does not vary substantially until the centre of the emission is outside the collimator. So for highly ‘peaked’ emission and more distant clusters, little, or no variation in the temperature can be expected for offsets less than 45 arcmin.

If any temperature variation exists, then it should appear in the mean temperature measured at different radii. However the “true” variation will be smeared out by the averaging over the field of view and by projection effects. So great care should be taken when interpreting any temperature variation if apparent.

An additional complication to the ME analysis is that the collimators had slightly different widths and alignments (as mentioned in Section 3.2.2). The variation in collimator width means that for an extended source, narrow collimators detected less flux than wide ones. To avoid any systematic error that could be introduced by the change in the normalisation of the flux, all detectors that showed deviation from the mean value were excluded from the analysis. This required the exclusion

of detector 7 (which was the narrowest collimator) from all pointings near the centre of Virgo, Coma and Perseus and detector 6 from two observations of Perseus.

The misalignment of the collimators was corrected for by calculating the average pointing direction of the collimators for each pointing and roll angle. The correction of  $\sim 6$  arcmin from the satellite pointing direction made a significant difference to the offsets of pointings close to the centre of a cluster. The overall uncertainties in the collimator profiles and alignments made determining the surface brightness profile from the relative detector-to-detector ratios impossible. The ME data were fitted without including any LE data as the uncertainties in the LE background subtraction for such extended sources are large.

A correction for the flux outside the field of view of the collimator was made in order to derive the total luminosity of the cluster. To do this the surface brightness profile was integrated out to a large radius (*e.g.*  $5^\circ$ ) without including any correction for the collimator response. This integrated flux could then be compared with the expected central flux for the ME for the same surface brightness profile. The ratio of the two gave the correction required to convert the measured flux to the total flux.

## 4.2 Virgo

Virgo is the nearest cluster of galaxies to our own Local Group and as such has been extensively studied optically (*e.g.* Bingelli, Tammann & Sandage 1987). The Virgo cluster is a highly complex, dynamically young, spiral rich cluster and shows substantial substructure. A single giant elliptical, M87, lies near (but is not coincident with) the cluster centre and has a large X-ray halo surrounding it which extends as much as  $3^\circ$  from the galaxy itself. Although X-ray emission is seen from the other principal galaxies in the cluster (*e.g.* M86 and M49), these galaxies have luminosities 20 to 30 times smaller than M87 (Forman *et al.* 1979).

### 4.2.1 Previous X-Ray Results

Virgo was the first extra-galactic X-ray source to be identified. Early observations from *UHURU* (Kellogg *et al.* 1975) and *OSO-8* (Smith *et al.* 1979) indicated a two component spectrum comprising thermal emission at 2–3 keV and a “hard tail”. Later *ARIEL-V* results suggested that these two components were not coincident (Davison 1978; Lawrence 1978). *HEAO-1* observations (Lea *et al.* 1981) also showed marginal evidence for a variation in intensity of the hard component over a period of six months.

The only previous imaging results came from *EINSTEIN* which provided a number of high qual-

Reference	Date	Pointing Position (1950)	Offset (arcmin)	Exposure H1 (s)	Exposure H2 (s)	Count Rate (cnt s <sup>-1</sup> half <sup>-1</sup> )	Channels fitted
1983 A	194/83	12 18 30 +13 00 00	145.4	5450	20720	Background	-
Offset Q4		12 25 39 +13 52 10	86.8	-	5450	0.76±0.05	6-31
1983 B	194/83	12 21 30 +13 00 00	102.5	7700	4350	1.27±0.04	6-38
Offset Q4		12 28 39 +13 52 10	77.9	-	7700	0.66±0.04	6-31
1983 C	194/83	12 24 00 +13 00 00	67.8	4750	2140	2.99±0.06	6-36
1983 D	195/83	12 27 00 +13 00 00	31.8	4300	7450	11.49±0.06	6-35
1983 E	195/83	12 30 00 +13 00 00	35.8	2670	3450	7.65±0.07	6-35
1983 F	196/83	12 33 00 +13 00 00	73.5	17830	-	0.88±0.06	6-30
1983 G	196/83	12 36 00 +13 00 00	115.6	23610	22720	Background	-
1983 M87	199/83	12 28 46 +12 40 12	9.0	13790	21270	20.87±0.06	6-40
1984 D	147/84	12 21 33 +09 57 52	184.8	13310	8320	Background	-
1984 C	148/84	12 26 21 +11 23 44	75.9	12320	-	0.97±0.06	6-30
1984 B	148/84	12 27 35 +11 54 43	40.9	8800	9280	5.94±0.05	6-38
1984 A	148/84	12 28 45 +12 36 12	7.9	4960	3200	21.25±0.08	6-40
1984 B'	148/84	12 25 26 +13 04 39	50.7	9440	7520	4.43±0.05	6-38
1984 C'	149/84	12 22 19 +13 31 31	103.4	14650	14080	0.97±0.04	6-34
1984 D'	149/84	12 20 06 +13 50 01	140.6	13440	11200	Background	-
1984 M87	361/84	12 28 56 +12 41 09	9.8	21470	21000	17.40±0.06	6-40
Offset Q1&4		12 22 03 +12 00 28	102.6	21000	21470	0.42±0.05	6-26
Offset Q2&3		12 26 14 +14 24 21	103.5	"	"	0.77±0.05	6-26

Table 4.1: Log of *EXOSAT* observations of Virgo. The count rates are quoted for Argon channels 6 to 38 (or approximately 1.5 to 10 keV).

ity images from the HRI and IPC detectors. Fabricant & Gorenstein (1983) presented surface brightness data from the IPC out to 100 arcmin (or 440 kpc) from which they estimated the total gravitational mass around M87 assuming hydrostatic equilibrium. Analysis of the HRI, IPC and FPCS data by Stewart *et al.* (1984a) shows a cooling flow of 2–10  $M_{\odot} \text{ yr}^{-1}$  in M87 with the flow rate increasing with radius. The SSS data also shows evidence for cooler emission at the centre of the cluster (Lea, Mushotzky & Holt 1982).

#### 4.2.2 *EXOSAT* Observations

The Virgo cluster was observed a number of times during the *EXOSAT* mission. Table 4.1 gives a log of these observations. On two occasions the observations were made by ‘stepping’ across the cluster. Figure 4.2 gives a schematic map of the pointings and the positions of the principal galaxies in the Virgo cluster. A preliminary analysis of these *EXOSAT* data was presented in Edge, Stewart & Smith (1986). The calculated “count-weighted” radii for the pointings range from 10 arcmin to 95 arcmin. This corresponds to range of radii of 44 to 420 kpc at the assumed distance of Virgo of 15 Mpc (Mould, Aaronson and Huchra 1980).

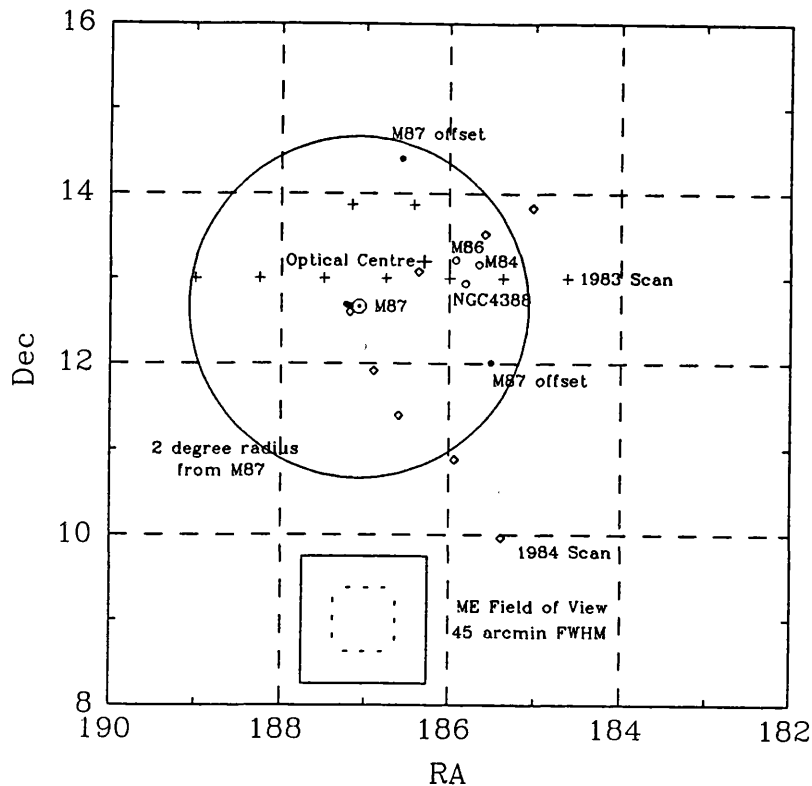


Figure 4.2: Schematic map of the *EXOSAT* pointings on Virgo. The principal galaxies are plotted with open circles. The 1983 scan positions are marked by crosses, the 1984 pointing positions by diamonds and the 1984 M87 pointing positions with filled circles.

#### LE data

The LE observations provided a number of deep images centred on M87 and relatively short exposure images of the offset areas. The offset images showed no significant detections of any of the sources mentioned by Forman *et al.* (1979). The upper limits for M84 and M86 which are the brightest sources given in Forman *et al.*, were  $0.01 \text{ count s}^{-1}$  in the thin Lexan filter. These are consistent with the IPC fluxes. Neither of these sources was near the centre of the field of view for the observations, so the point spread function and vignetting contributed significantly to the uncertainty in the count rate. Figures 4.3 and 4.4 show low and high resolution LE images of M87 in the thin Lexan filter. The high resolution image shows the features seen in the HRI image of M87 (Schreier, Gorenstein & Feigelson 1982); a point source associated with the active nucleus in M87 and asymmetric emission on a scale of a few arcmin similar to that seen in the radio. This X-ray emission is thought to arise from an inverse Compton process between the high energy electrons and radio photons. The Boron image also shows these features, but the signal-to-noise was not sufficient to allow any reliable ratio of the count rates (which was moderately sensitive to the X-ray spectrum) to be obtained. However, a very steep spectrum for the inverse Compton emission can probably be ruled out, since the features were seen in the Boron filter image, which is sensitive to higher energies than the Lexan filter. The low resolution image shows symmetrical emission out to large radii as seen in the IPC.

The exposure times and results from deprojection analysis of surface brightness profiles are given

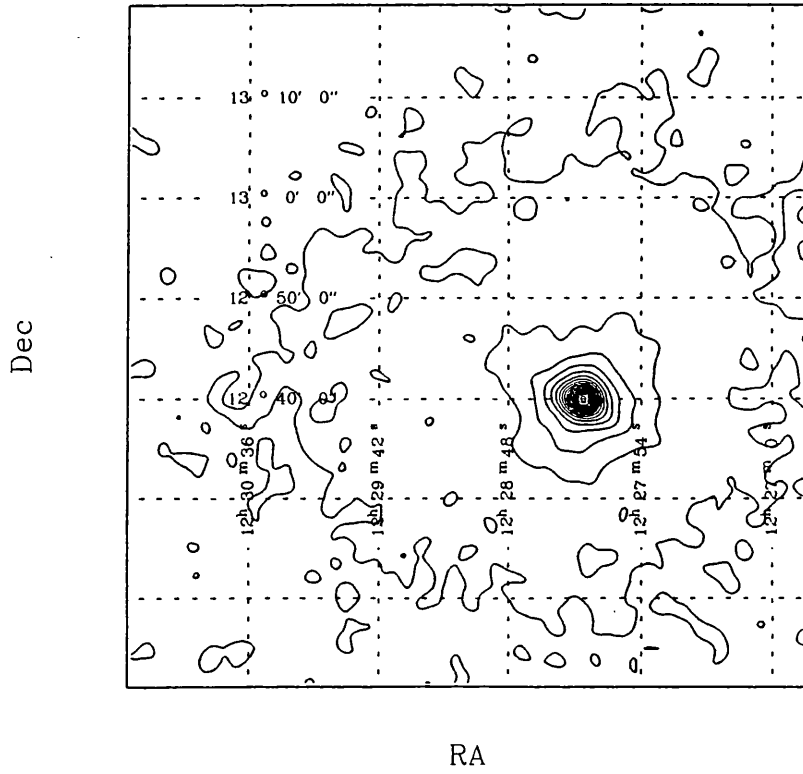


Figure 4.3: Low resolution 3LX LE image of M87 convolved with a gaussian of  $1.5'$ .

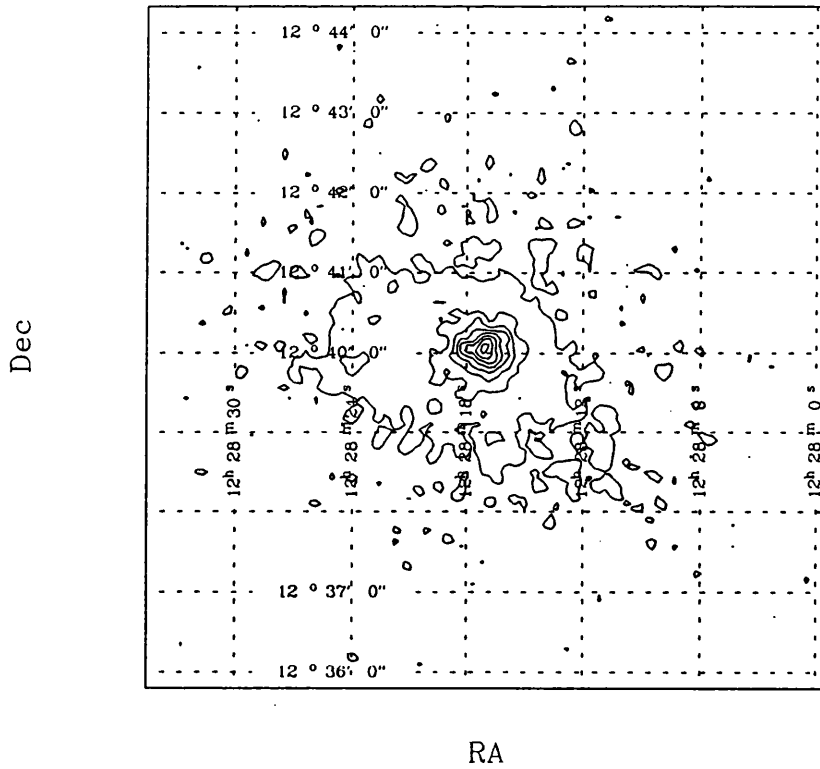


Figure 4.4: High resolution 3LX LE image of M87 convolved with a gaussian of  $5''$ .

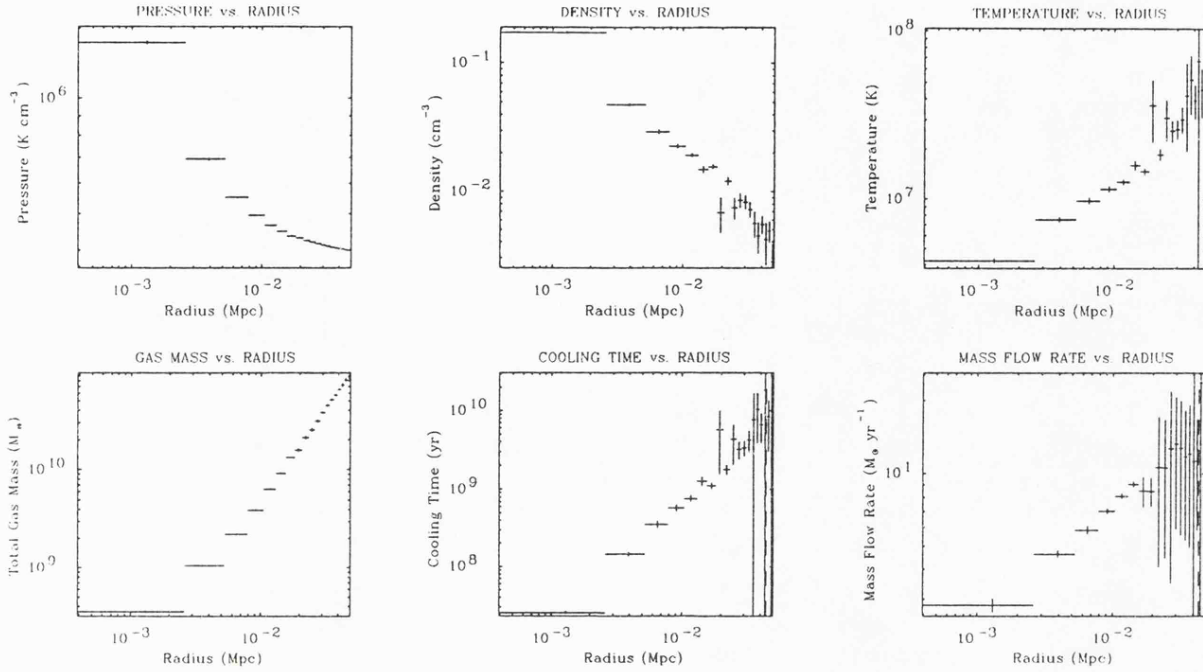


Figure 4.5: Plots of parameters derived from the deprojection analysis of LE images of Virgo

in Tables 2.2 and 2.6 in Chapter 2. Figure 4.5 shows the parameters derived from the deprojection analysis. The results for the mass flow rate and density agree well with those obtained by Stewart *et al.* (1984a) from the HRI, IPC and FPCS data but do not improve on them. The high signal-to-noise of these images allowed a simultaneous fit to the thin Lexan and Boron profiles to be attempted. As mentioned in Section 2.2.2 the filter ratio should provide the temperature at each radius, which would allow the mass to be determined directly. In practice however, the Lexan-Boron filter ratio was not sensitive enough to the temperature for this technique to provide limits on the temperature profile.

### ME data

The first 'stepping' manoeuvre was made during the performance and verification (PV) phase in 1983 when the observing procedures and gain settings were being adjusted. To add to the problems of the PV stage, there were short periods of background flaring due to solar activity which introduced additional uncertainties. The gain problems affected detectors 2,3,6 and 7 and so these 4 detectors were excluded from the analysis. This did not affect the 1984 observations.

**Background Subtraction** The background subtraction for the observations was difficult due to the highly extended cluster emission. Emission was detected out to radii of at least 3 degrees, so for the 'stepped' observations a small amount of emission could have been measured in the furthest offset pointings (4 and 4.5 degrees), which were used as background. This would not

Reference	Detectors Used in Fit	Offset (arcmin)	Raymond and Smith Temperature (keV)	Iron Abundance (relative to Solar)	2-10 keV Flux ( $\text{erg cm}^{-2} \text{s}^{-1}$ )	$\chi^2$ for Fit
1983 A	78 offset	86.8	$2.51^{+0.60}_{-0.41}$	0.4 (fixed)	$1.32 \times 10^{-11}$	26.7 (24 d.o.f.)
1983 B	1458	102.5	No simple fit	See text	$\sim 1.5 \times 10^{-11}$	-
	78 offset	77.9	$2.64^{+0.70}_{-0.56}$	0.4 (fixed)	$1.11 \times 10^{-11}$	24.2 (11 d.o.f.)
1983 C	1458	67.8	No simple fit	See text	$\sim 3.3 \times 10^{-11}$	-
1983 D	148	31.8	$2.44^{+0.09}_{-0.08}$	$0.51^{+0.18}_{-0.17}$	$1.06 \times 10^{-10}$	35.9 (27 d.o.f.)
1983 E	1458	35.8	$2.39^{+0.13}_{-0.11}$	$0.68^{+0.30}_{-0.18}$	$7.10 \times 10^{-11}$	33.2 (27 d.o.f.)
1983 F	14	73.5	$1.75^{+0.29}_{-0.24}$	0.4 (fixed)	$0.73 \times 10^{-11}$	24.3 (23 d.o.f.)
1983 M87	1458	9.0	$2.50^{+0.04}_{-0.04}$	$0.39^{+0.06}_{-0.06}$	$1.87 \times 10^{-10}$	39.2 (32 d.o.f.)
1984 C	1234	75.9	$2.61^{+0.62}_{-0.53}$	0.4 (fixed)	$0.89 \times 10^{-11}$	19.7 (23 d.o.f.)
1984 B	1234568	40.9	$2.56^{+0.10}_{-0.09}$	$0.24^{+0.17}_{-0.17}$	$5.64 \times 10^{-11}$	46.5 (30 d.o.f.)
1984 A	1234568	7.9	$2.67^{+0.14}_{-0.13}$	$0.25^{+0.11}_{-0.15}$	$1.99 \times 10^{-10}$	38.2 (30 d.o.f.)
1984 B'	1234568	50.7	$2.81^{+0.18}_{-0.15}$	$0.37^{+0.25}_{-0.22}$	$4.43 \times 10^{-11}$	32.2 (30 d.o.f.)
1984 C'	12345678	103.4	$2.65^{+0.60}_{-0.34}$	$1.22^{+1.28}_{-0.92}$	$0.89 \times 10^{-11}$	26.9 (26 d.o.f.)
1984 M87	1234568	9.8	$2.39^{+0.08}_{-0.07}$	$0.31^{+0.09}_{-0.08}$	$1.74 \times 10^{-10}$	29.5 (30 d.o.f.)
	1278 offset	102.6	$2.11^{+1.24}_{-0.58}$	0.4 (fixed)	$0.31 \times 10^{-11}$	17.2 (19 d.o.f.)
	3456 offset	103.5	$2.91^{+0.97}_{-0.56}$	0.4 (fixed)	$0.72 \times 10^{-11}$	13.1 (19 d.o.f.)

Table 4.2: Results of the spectral fits to ME data from Virgo. The quoted errors are 90% confidence.

affect the background subtraction for the central pointings, but may have added a small bias into the outer pointings. Cross checking with slew data gave an upper limit to this excess emission of  $3 \times 10^{-12} \text{ erg cm}^{-2} \text{ s}^{-1}$ . The extension meant that the offset quadrants for the central pointings which were pointing 2 degrees away from M87 detected a moderate count rate ( $0.5 \text{ count s}^{-1}$ ). This made a “nod” subtraction for these long pointings impossible. Consequently slew data were used as a background for these observations.

**Spectral Fitting** The spectra were fitted with the multi-element plasma model of Raymond & Smith (1977) with the iron, silicon and all other heavy element abundances as three independent free parameters. In order to reduce the number of free parameters, the column density for all fits was fixed at the galactic value of  $0.25 \times 10^{21} \text{ cm}^2$  (Stark *et al.* 1988). This value is consistent with the upper limit of  $0.70 \times 10^{21} \text{ cm}^2$  from the best signal to noise spectrum. A 1% systematic error was added in quadrature to the statistical error in the data to allow for calibration and systematic effects.

**Results** The results of the spectral fits are given in Table 4.2. The best spectrum was obtained for the 1984 M87 observation. The best fit gave an abundance of  $1.3^{+0.8}_{-0.5}$  for silicon and  $0.4^{+0.3}_{-0.2}$  for the other abundances, which are consistent with the value of  $1.0 \pm 0.6$  obtained with the SSS for

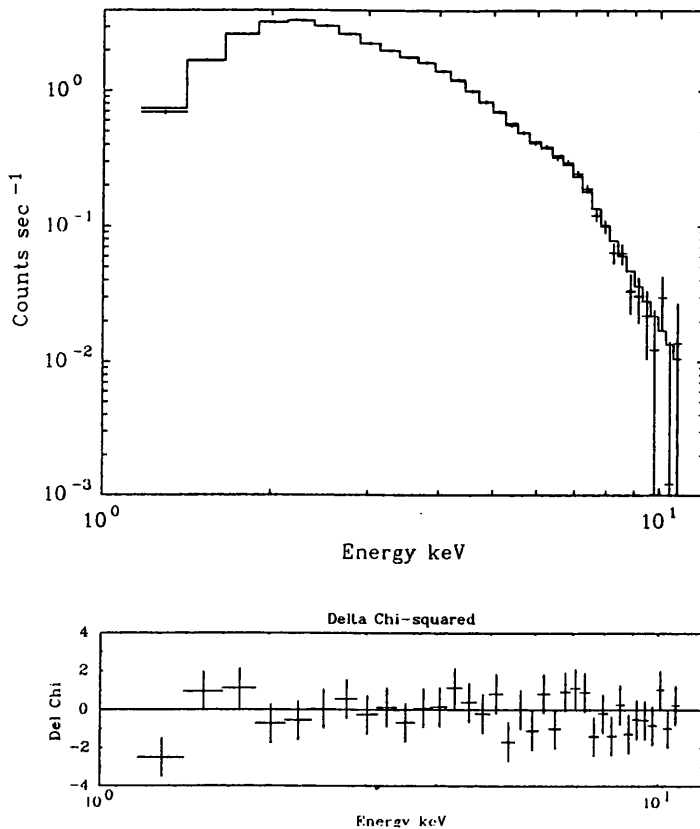


Figure 4.6: Best fit to the argon count spectrum for the 1984 M87 observation

all abundances (Lea, Mushotzky & Holt 1982). These values were fixed and used for all the other fits. Figures 4.6 and 4.7 show the best fits to the count spectra for 1984 M87 data for the central and offset pointings.

The 1984 M87 observation also provided limited information on the “hard tail” emission seen by other instruments above 10 keV. The poor sensitivity of the ME to energies above 10 keV made the detection of any excess hard emission difficult, but an upper limit could be determined. The data from 10 to 20 keV were fitted with a power law with a photon index of 1.7 and fixed thermal component determined from the data below 10 keV. The upper limit to the normalisation of the power law was 0.006. This is consistent with the lower values of the power law seen in HEAO-1 observations (Lea *et al.* 1981). The poorer signal-to-noise of the other observations prevented any other limits for the “hard tail” being determined.

All the fits, bar two, gave a good fit to a single Raymond & Smith model. The two poorly fit spectra both contain M84, M86 and NGC 4388 in the field of view (observations B and C in 1983). These two spectra gave RS fits with temperatures of 2.5 and 2.6 keV, iron abundances of 5.4 and 2.0 and reduced chi-squareds of 1.37 and 2.10 respectively. These iron abundances are much larger than expected and indicate excess emission above 5 keV. The offset detectors for these two observations showed no excess emission, implying that the detected flux was from a source in the field of view rather than a background flare. *EINSTEIN* IPC observations show that both M84, M86 and NGC 4388 are soft X-ray sources with M84 and NGC 4388 being a point-like sources and M86 having extended emission (Forman *et al.* 1979). M84 is a narrow emission line source and has a two-sided radio jet (Laing & Bridle 1987) indicating nuclear activity, possibly from a region obscured by the dust belt seen in M84 (similar to that in Centaurus-A). NGC 4388 has a Seyfert

2 type nucleus (Phillips & Malin 1982). Several Seyfert 2s have been detected in X-rays and all have heavily cut-off spectra (Turner 1988). Fitting the two spectra with a bremsstrahlung and power law with an intrinsic column density gave much better fits (*i.e.*  $\chi^2_{red}$  of 0.95 and 1.07) and reduces the implied iron abundance by a factor of two. The best fit intrinsic column density was  $2 \times 10^{23} \text{ cm}^{-3}$  for a fixed power law index of 1.7. The ratio of the power law normalisations is 1:2 between observations B and C. Figure 4.8 shows the best fit photon spectrum for observation C for the single RS fit and RS and power law fit. The contribution of the cut-off power law can be seen above 5 keV. The ‘hard’ emission is unlikely to have come from M86 which is believed to thermal emission as it is extended. However it could have originated from either M84 or NGC 4388. Unfortunately the fits could not definitely distinguish whether M84 or NGC 4388 was the source, although the ratio of the power law components in the two fits favours NGC 4388. The implied unabsorbed 2–10 keV luminosity for either M84 or NGC 4388 was  $\sim 3 \times 10^{42} \text{ erg cm}^{-2} \text{ s}^{-1}$ . These X-ray properties are consistent with those seen in other low luminosity AGN.

These data indicate that there is a “hard” source in Virgo which is not associated with M87. The field of view HEAO-1 included M84, M87 and NGC 4388 so the “hard tail” detected could be due to a combination of these sources. This scenario is consistent with results from ARIEL-V scans of Virgo (Davison 1978) where the ‘mean’ position of hard emission was shown to lie between M84 and M87.

Figures 4.9–4.11 show the flux, temperature and iron abundance plotted against radius from M87. Figure 4.9 shows scatter at large radii which can be interpreted as an asymmetry in the cluster gas. Any excess seen cannot be attributed to a point sources at M84 and M86 alone. The asymmetry is also seen in the optical distribution (Binggelli, Tammann & Sandage 1987) where the galaxies are centred to the north-west of M87. So it appears that the gas at large radii reacts to the potential well of the cluster as a whole rather than to M87 alone. The asymmetry made it difficult to determine a surface brightness profile that correctly described the data at radii greater than  $\sim 60'$ . Fabricant & Gorenstein (1983) determined the surface brightness from the IPC at four offset positions and give a much steeper profile to the south and west of M87 (as is seen here). Correcting for the emission outside the collimator gave a total 2–10 keV flux of  $2.80 \times 10^{-10} \text{ erg cm}^{-2} \text{ s}^{-1}$ .

### 4.2.3 Implications of the *EXOSAT* results

The temperature and abundance profiles show no obvious trend over almost an order of magnitude in radius, indicating an isothermal, homogeneous gas distribution out to  $\sim 0.5$  Mpc. The resolution of the ME does not allow the temperature profile within the central  $\sim 5$  arcmin to be determined because of the large field-of-view. This temperature profile is inconsistent with the model for pressure confinement of the gas around M87 by hot ( $T \sim 10$  keV) intracluster gas proposed by

Binney & Cowie (1981). Calculating the gravitational mass, as shown in Section 1.1.2 for a constant temperature of  $2.4 \pm 0.3$  keV from 5 to 100 arcmin and a  $\beta$  parameter of  $0.6 \pm 0.1$ , gives the limits seen in Figure 4.12. Plotting the optically determined masses for M87 from the stellar velocity dispersion (Sargent *et al.* 1978) and from the globular cluster velocity dispersion (Mould, Oke & Nemec 1987; Cohen 1988) shows that the mass determined from the X-ray results extrapolates well to smaller scales. The two component mass models from Stewart *et al.* (1984a), which fit the IPC, HRI and FPCS data, agree with the X-ray and optical data. The total mass within 0.5 Mpc is  $8.4 \times 10^{13} M_{\odot}$ .

Binggelli, Tammann & Sandage (1987) note that there is substantial morphological segregation in velocity and structure. The velocity dispersion of the E and S0 galaxies is  $573 \text{ km s}^{-1}$  whereas for spiral and irregular galaxies it is  $800 \text{ km s}^{-1}$ . They interpret this segregation as evidence for infall of spirals and irregulars demonstrating the relative ‘youth’ of the cluster. Calculating the value of  $\beta$  (see Section 6.3.2) for these two velocity dispersions gives 0.79 and 1.55 for a temperature of 2.4 keV. The former value is consistent with the imaging data at large radii (Fabricant & Gorenstein 1983). This suggests that the elliptical and lenticular galaxies provide a better measure of the virial mass than the spirals and irregulars. Such velocity segregation could affect other clusters and cause similar overestimation of the velocity dispersion if all galactic types are used the determination.

#### 4.2.4 Summary

- The gas in the Virgo cluster is isothermal over a wide range of radii.
- Hard emission was detected from the region of M84, M86 and NGC 4388 which could be due to a heavily cut-off active nucleus in M84 or NGC 4388.
- The gravitational mass within 0.5 Mpc is  $8.4 \times 10^{13} M_{\odot}$ .

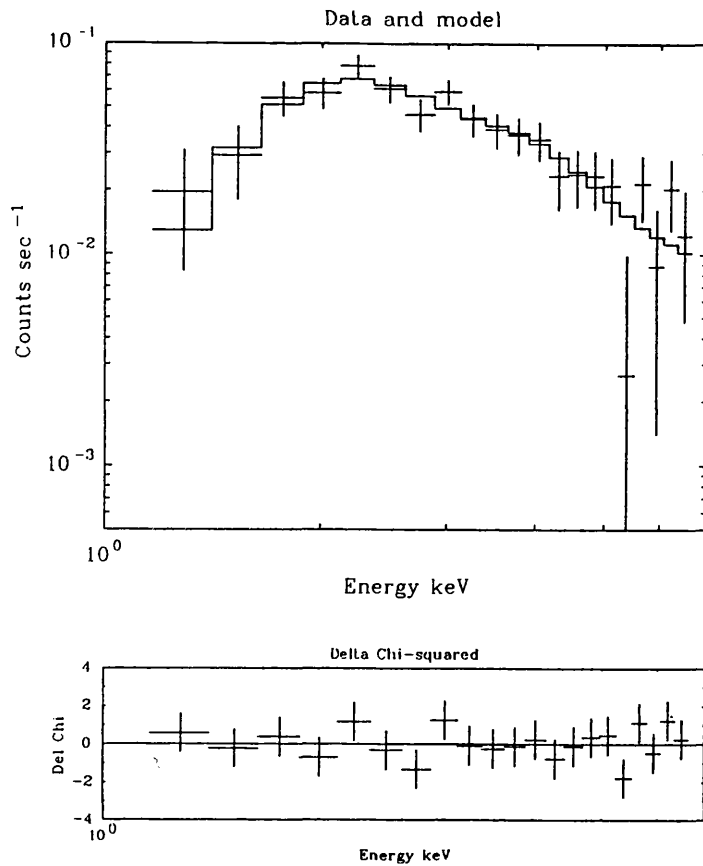


Figure 4.7: Best fit to argon count spectrum for offset quadrants 2 and 3 of the 1984 M87 observation

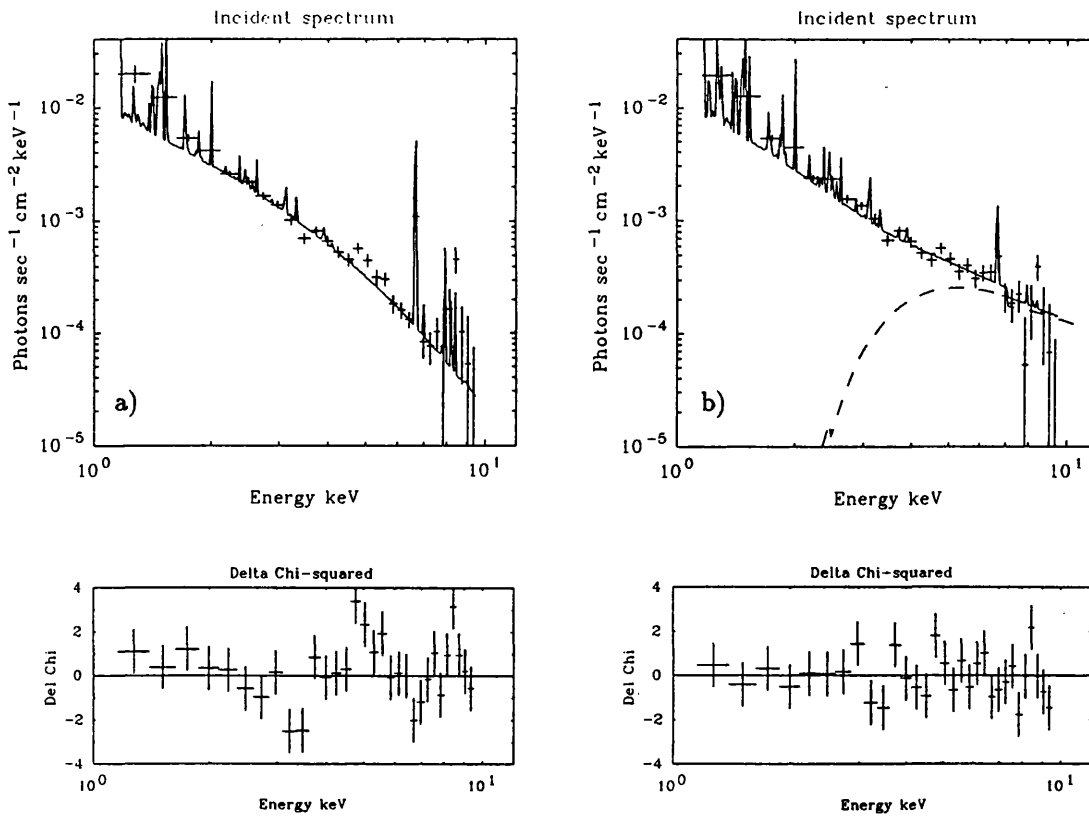


Figure 4.8: Best fit photon spectrum to 1983 Observation C with (a) and without (b) a power law component. The dashed line in b. is the power law component.

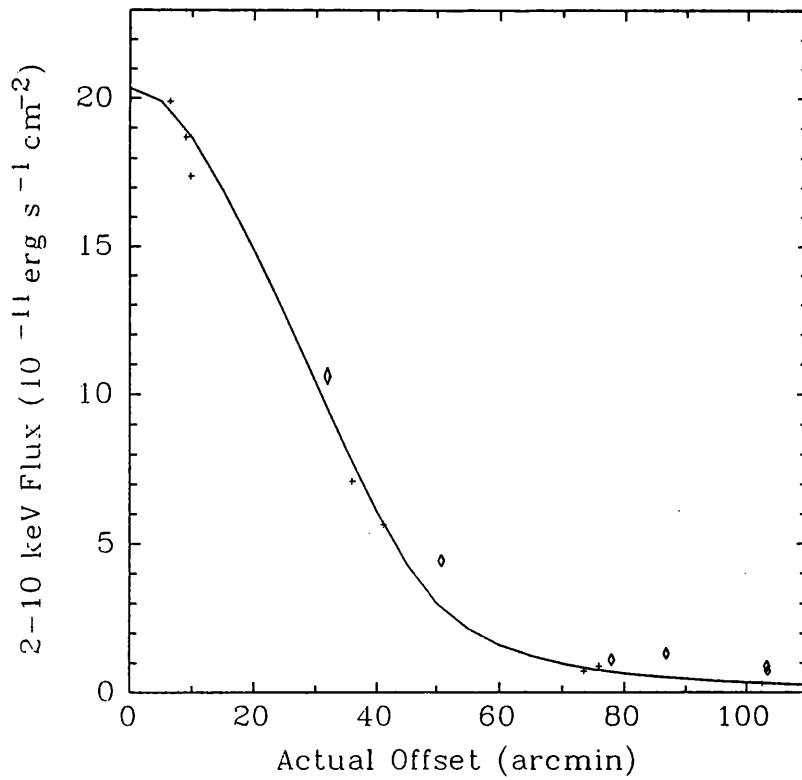


Figure 4.9: 2-10 keV flux against offset angle from M87 for the Virgo pointings. The crosses mark the fluxes from pointing south and east of M87 and diamonds those to the north and west (*i.e.* toward the cluster centre and M84). The solid line gives the expected flux with offset for a modified King model surface brightness profile with a core radius of  $10'$  and a  $\beta$  of 0.6 folded through the ME field of view.

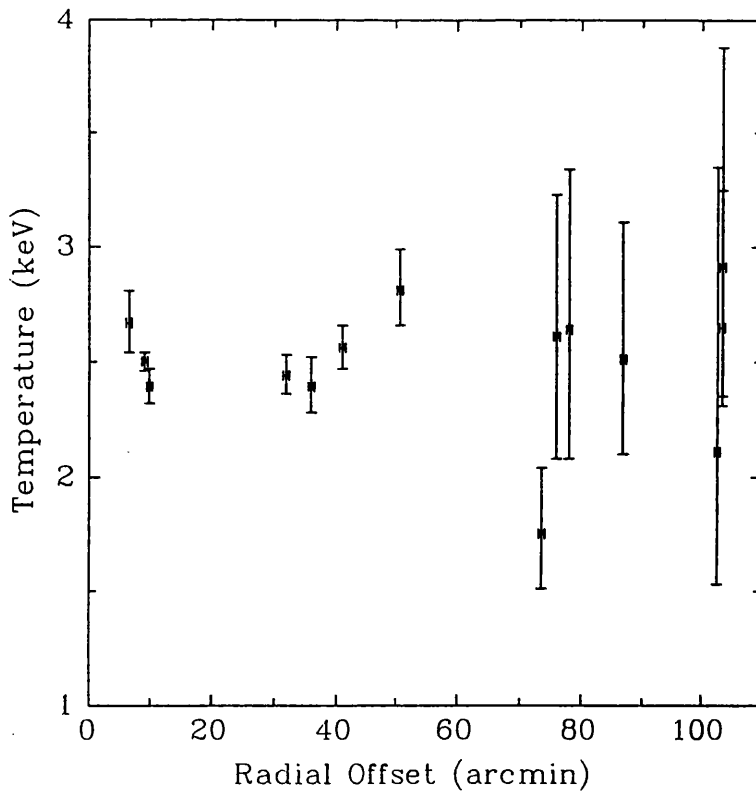


Figure 4.10: Measured temperature against offset angle from M87 for Virgo

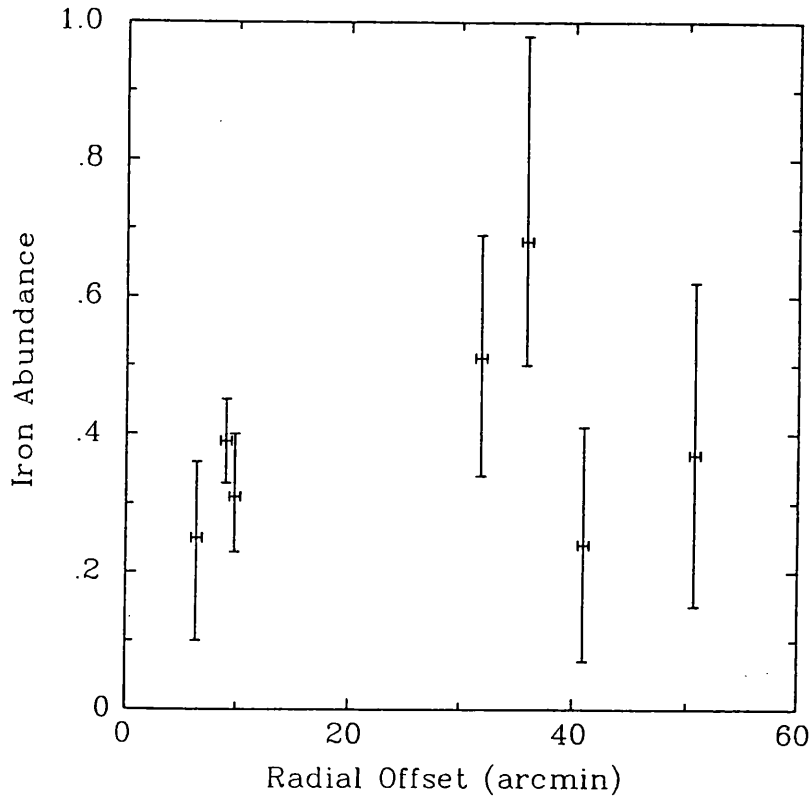


Figure 4.11: Iron abundance against offset angle from M87 for Virgo

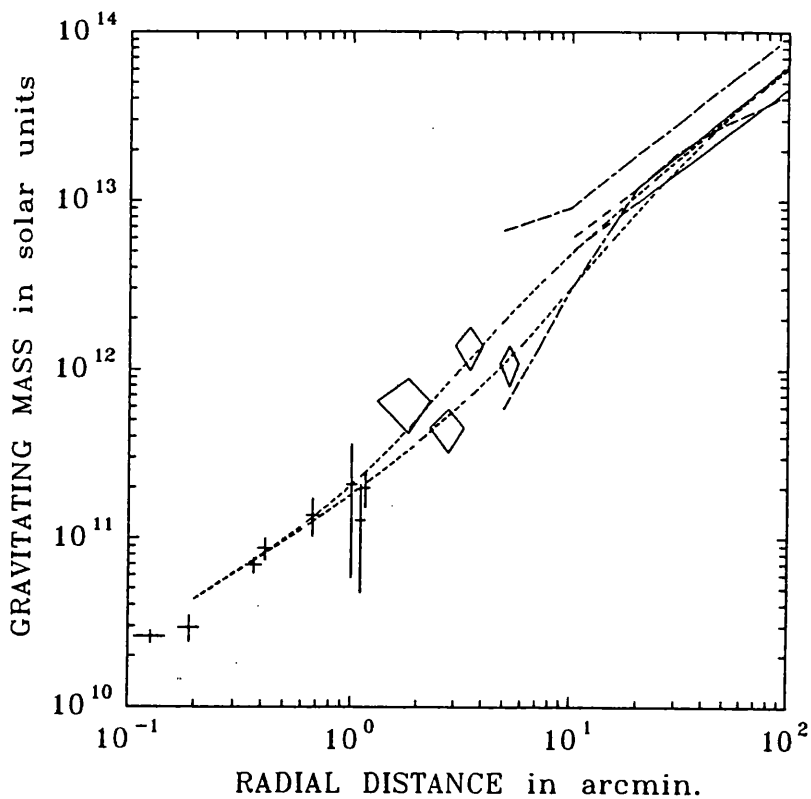


Figure 4.12: Total gravitational mass for the Virgo cluster plotted against radius. The solid lines are the X-ray determined limits from this work. The large dashed lines are the X-ray limits from Fabricant & Gorenstein (1983). The crosses and diamonds are optical measurements from Sargent *et al.* (1978) and Mould, Oke & Nemec (1987) respectively. The dashed lines are two-component mass models from Stewart *et al.* (1984a) which agree with the FPCS line ratios. The two best fit models for Stewart *et al.* (for galactic core radii of 10 kpc and 40 kpc) are plotted.

## 4.3 Coma

Coma is the archetypal evolved cluster without a dominant galaxy. Detailed studies suggest some asymmetry within the velocity structure (Pryor & Geller 1984; Mellier *et al.* 1988), but the overall relaxed nature of the cluster is evident. Coma is dominated by two giant elliptical galaxies NGC 4874 and NGC 4889 and has a low spiral fraction (13%).

### 4.3.1 Previous X-Ray Results

All early survey instruments detected Coma and it has been widely studied by preceding missions. It is bright, at a high galactic latitude ( $+88^\circ$ ) and has no additional components to its spectrum (*c.f.* Perseus). UHURU, OSO-8 and HEAO-1 gave temperatures of 8.7, 8.9 and 8.0 keV respectively, but ARIEL-V gave 6.0 keV. The HEAO-1 spectrum was studied in detail by Henriksen & Mushotzky (1986) and was purported to show a strongly non-isothermal spectrum. This conclusion has been disputed by Hughes *et al.* (1988) who point to poor calibration of the HEAO-1 detectors and inadequate treatment of systematic errors as the factors which lead to the rejection of an isothermal fit.

The *EINSTEIN* IPC results for Coma were presented by Abramopoulos, Chanan & Ku (1981). They fitted the surface brightness profile with models where elements were not homogeneously distributed within the ICM. This analysis gave results consistent with iron being concentrated at the centre of the cluster which was interpreted as settling of heavy elements. As has been pointed out by Hughes, Gorenstein & Fabricant (1988), for this settling to occur requires times substantially greater than the Hubble time making these models highly implausible. Hughes *et al.* (1988) have fitted the same IPC data with isothermal and adiabatic models and find evidence for an isothermal core of at  $\sim 15$  arcmin and reject polytropic models in the cluster core. Data from the FPCS on *EINSTEIN* set an upper limit for the cooling rate over the whole cluster of  $150 M_\odot \text{ yr}^{-1}$  (Canizares, Markert & Donahue 1988).

The Japanese satellite *Tenma* observed Coma and gave an isothermal temperature of  $8.2 \pm 0.3$  keV (Okumura *et al.* 1988). These *Tenma* data have been fitted, in conjunction with the *EINSTEIN* IPC data, with a more complex model by Hughes *et al.* (1988) which combines an isothermal core with an outer polytropic region. The *EXOSAT* data have been analysed by Hughes, Gorenstein & Fabricant (1988) which again requires a hybrid isothermal-polytropic model. This analysis is discussed in more detail below.

The *EXOSAT* LE images have been studied by Branduardi-Raymont *et al.* (1985a). They found 8 point sources in the LE within a few square degrees of Coma. This represents a higher sky density

Reference	Date	Pointing Position (1950)	Offset (arcmin)	Exposure H1 (s)	Exposure H2 (s)	Count Rate (cnt s <sup>-1</sup> half <sup>-1</sup> )	Channels fitted
1983 Centre	197/83	12 57 29 +28 11 24	4.4	25320	24410	22.44±0.04	6-50
1984 East Offset Q4	359/84	13 00 58 +28 11 24 12 54 02 +27 33 47	48.1 63.0	11520 -	10320 11520	3.38±0.05 1.33±0.08	6-35 6-35
1984 Centre Offset Q4	359/84	12 57 29 +28 11 24 12 50 27 +27 33 47	7.4 102.2	7200 -	4320 7200	22.94±0.07 0.37±0.08	6-50 6-23
1984 West	360/84	12 54 00 +28 11 24	45.2	10240	10080	4.58±0.05	6-40
1984 South	360/84	12 57 29 +27 29 24	49.3	21360	9920	3.25±0.04	6-40

Table 4.3: Log of *EXOSAT* observations of Coma. The count rates are quoted for Argon channels 6 to 38 (or approximately 1.5 to 10 keV).

than found for AGN at lower galactic latitudes. This is interpreted as evidence of a population of AGN with very soft spectra which are detected due to the combination of the low column density ( $0.1 \times 10^{21} \text{ cm}^{-2}$ ) in the line of sight and the low energy response of the LE (around 0.05keV).

### 4.3.2 *EXOSAT* Observations

Coma was observed twice by *EXOSAT* and Table 4.3 lists the details for those observations. Figure 4.13 gives a schematic map of the pointings. The range of “count-weighted” radii for these pointings was 11 to 100 arcmin. This corresponds to a range of projected radii of 0.44 to 4.04 Mpc from the centre of Coma.

### LE Data

Only the thin Lexan filter was used for these observations. The 8 serendipitous AGN seen by Branduardi-Raymont *et al.* (1985a) were detected in the 4 images around the cluster. These point sources were subtracted from the central image and the resulting LE image is shown in Figure 4.14.

The X-ray centre of 12 57 18.8 +28 13 24 from the LE image agrees well with that given by Abramopoulos, Chanan & Ku (1981) of 12 57 19 +28 13 07 from the *EINSTEIN* IPC data. It appears that the ‘peak’ in the X-rays is not coincident with any of the bright galaxies given in Kent & Gunn (1982). Figure 4.15 shows the central cooling time is close to the Hubble time ( $2 \times 10^{10} \text{ yr}$ ). A conservative upper limit of  $20 M_{\odot} \text{ yr}^{-1}$  can be put on the cooling rate for this central region.

The total exposure time and deprojection results for the LE image are given in Chapter 2. Figure 4.15 shows plots of the results from the deprojection analysis.

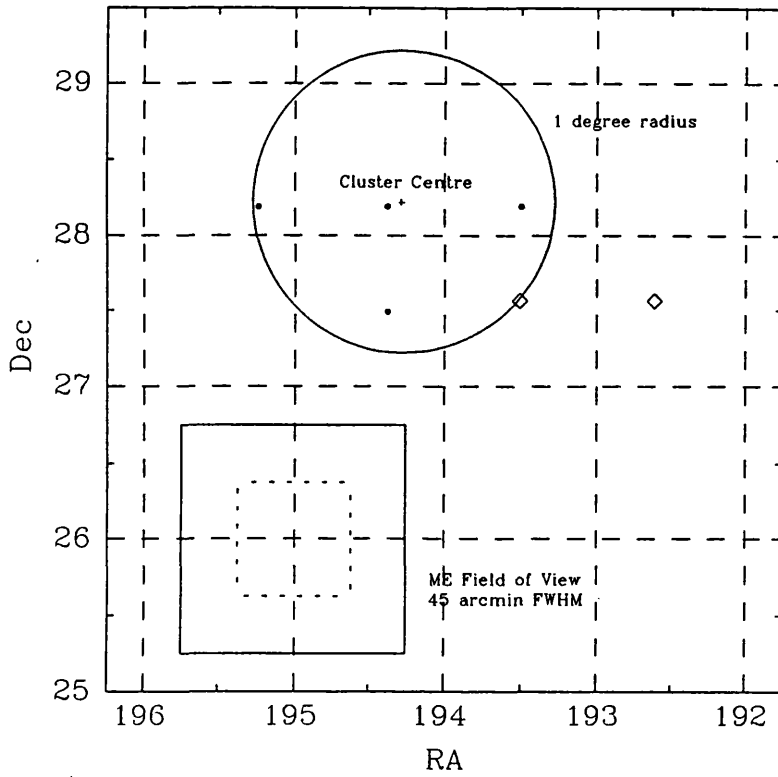


Figure 4.13: Schematic map of the *EXOSAT* pointings on Coma. The pointing positions are marked with filled circles and the offset positions where flux was detected are marked with diamonds.

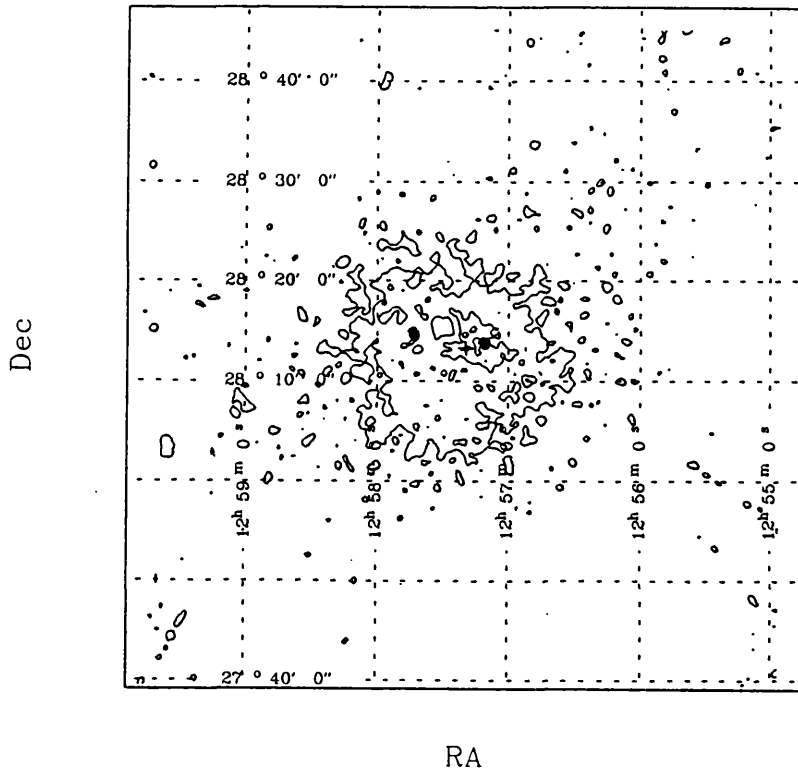


Figure 4.14: LE image of Coma in the 3LX filter convolved with a gaussian of  $16''$ . The filled circles mark the positions of NGC 4874 & 4889. The cross marks the X-ray centre.

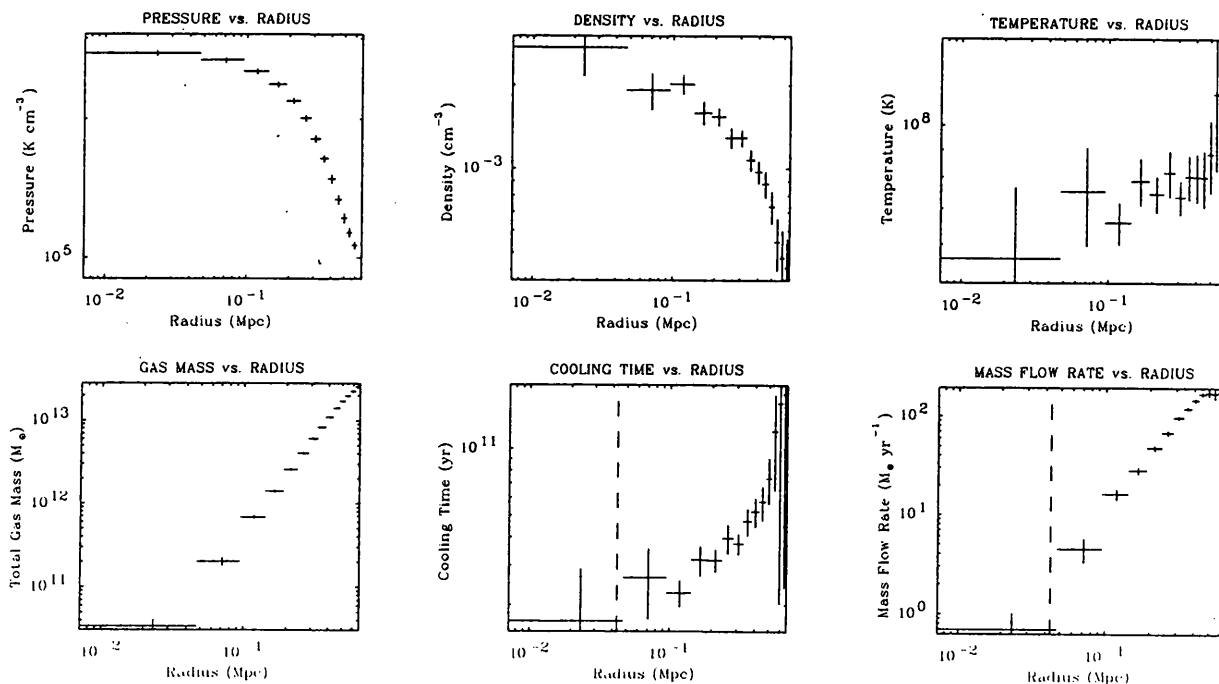


Figure 4.15: Plots of results from deprojection of LE images of Coma. The dashed line marks the cooling radius.

### ME data

The 1983 observation was affected by the same calibration problems as the 1983 Virgo observations so data from detectors 2,3,6 and 7 were omitted from the analysis.

**Background Subtraction** The background for the 1983 observation was taken for the offset quadrants which were checked for flux using data from the preceding observation of Virgo mentioned above.

The background for the 1984 multiple pointing observations was taken from the offset data in the southern pointing which had the longest relative exposure and was furthest from the cluster centre. This background allowed the flux in the offset detectors to be determined. There was significant flux found in one offset (quadrants 1 and 4 in the eastern observation) and a marginal detection in another (quadrants 1 and 4 in the central observation). The latter implies that a small amount of flux was subtracted from the 1983 data using a “nod” subtraction as the 1984 and 1983 pointings were coincident. However this flux was less than 1% of the central value and should not greatly affect the results obtained.

The background subtraction method used by Hughes, Gorenstein & Fabricant (1988) on the 1984 data was similar, but they used the offset data of each pointing instead of the southern one. Although this method gave similar results it was more vulnerable to oversubtraction due to flux in the offset quadrants.

Reference	Detectors Used in Fit	Offset (arcmin)	Raymond and Smith Temperature (keV)	Iron Abundance (relative to Solar)	2-10 keV Flux ( $\text{erg cm}^{-2} \text{s}^{-1}$ )	$\chi^2$ for Fit
1983 Centre	1458	4.4	$7.92^{+0.52}_{-0.46}$	$0.21^{+0.07}_{-0.07}$	$2.60 \times 10^{-10}$	44.8 (40 d.o.f.)
1984 East	12346	48.1	$5.98^{+1.21}_{-0.90}$	$0.50^{+0.28}_{-0.28}$	$4.28 \times 10^{-11}$	33.2 (27 d.o.f.)
			$6.71^{+1.03}_{-0.77}$	0.21 (fixed)	$4.25 \times 10^{-11}$	39.5 (28 d.o.f.)
East Offset	78	63.0	$3.59^{+1.08}_{-0.65}$	$0.94^{+0.92}_{-0.71}$	$1.34 \times 10^{-11}$	18.1 (27 d.o.f.)
			$4.23^{+1.58}_{-1.06}$	0.21 (fixed)	$1.31 \times 10^{-11}$	21.2 (28 d.o.f.)
1984 Centre	1234568	7.4	$7.97^{+0.74}_{-0.66}$	$0.21^{+0.10}_{-0.09}$	$2.67 \times 10^{-10}$	41.4 (40 d.o.f.)
Centre Offset	78	102.2	$1.87^{+1.66}_{-0.72}$	0.21 (fixed)	$0.25 \times 10^{-11}$	17.1 (16 d.o.f.)
1984 West	1234568	45.2	$7.24^{+1.21}_{-0.92}$	$0.33^{+0.20}_{-0.22}$	$5.23 \times 10^{-11}$	38.5 (32 d.o.f.)
			$7.59^{+0.89}_{-0.72}$	0.21 (fixed)	$5.22 \times 10^{-11}$	40.3 (33 d.o.f.)
1984 South	1234568	49.3	$6.11^{+1.08}_{-0.79}$	$0.29^{+0.24}_{-0.25}$	$3.48 \times 10^{-11}$	30.3 (32 d.o.f.)
			$6.28^{+0.75}_{-0.61}$	0.21 (fixed)	$3.47 \times 10^{-11}$	30.9 (33 d.o.f.)

Table 4.4: Results of spectral fits to ME data from Coma. The quoted errors are 90% confidence.

**Spectral Fitting** As with the Virgo data, the signal-to-noise for the best central pointing was sufficient to constrain the silicon and other elemental abundances, in addition to iron. The column was fixed at the galactic value of  $0.1 \times 10^{21} \text{cm}^2$  (Stark *et al.* 1988) and a 1% systematic error was included in all the fits.

**Results** Table 4.4 gives the results of the fits to the data. The silicon and other abundances were obtained from fits to the 1983 data which gave best fit values of  $2.2^{+2.7}_{-1.7}$  for silicon and  $0.7^{+1.4}_{-0.6}$  for the others. These best fit values were used for the other fits. Figures 4.16 and 4.17 show the best fits to the count spectra for the 1983 observation and the eastern offset quadrant observations. Figures 4.18–4.20a show the variation of flux, temperature and iron abundance with radius.

The variation of measured flux with offset angle was close to that predicted from the measured surface brightness from the IPC (Hughes *et al.* 1988). The best fit profile had a core radius of 8.5 arcmin and a  $\beta$  parameter of 0.63, instead of a core radius of 7.6' for the same  $\beta$ , as found by Hughes. There was little evidence of the non-symmetric emission seen in the inner regions in the IPC image as the fluxes at 3 similar radii (but different offset directions) were in good agreement. This indicates that at the largest scales the cluster is symmetric, but at smaller scales there is subclustering and hence asymmetry. This scenario agrees with results for subclustering from optical results (Fitchett & Webster 1987) and N-body simulations (White 1976; West, Oemler and Dekel 1988). Correcting for the emission outside the collimator gave a total 2–10 keV flux of  $3.24 \times 10^{-10} \text{erg cm}^{-2} \text{s}^{-1}$ .

The strong temperature gradient seen in the results is of great significance. Given the reliability of

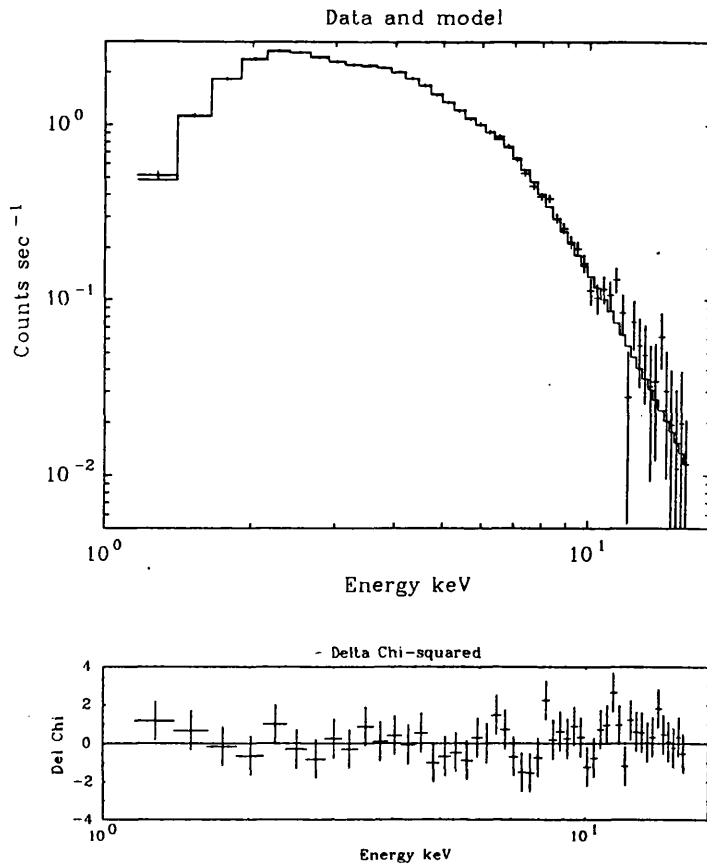


Figure 4.16: Best fit to argon count spectrum for the 1983 Coma central observation

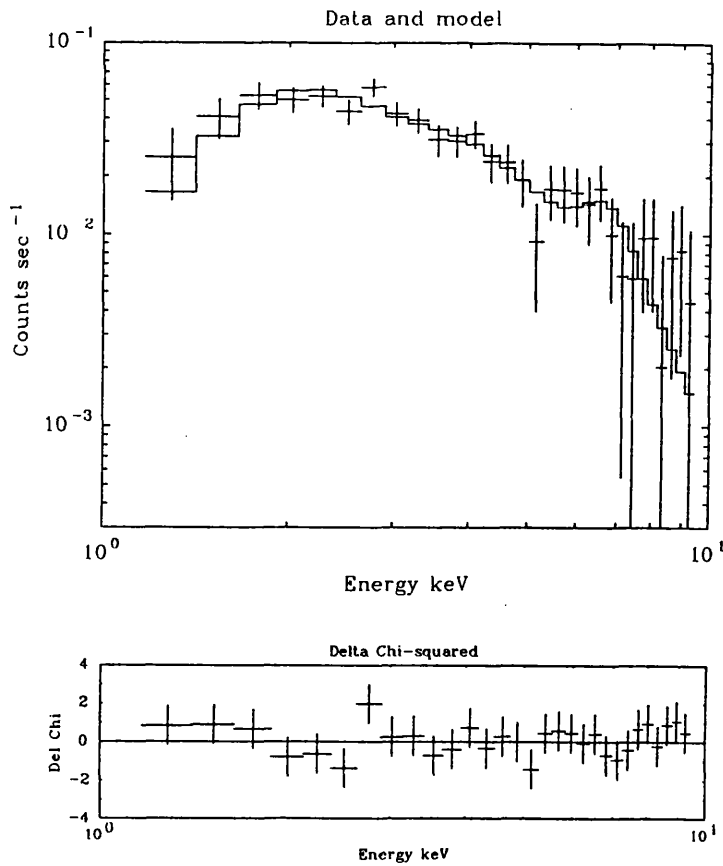


Figure 4.17: Best fit to argon count spectrum for the offset quadrant 4 of the 1984 Coma eastern observation

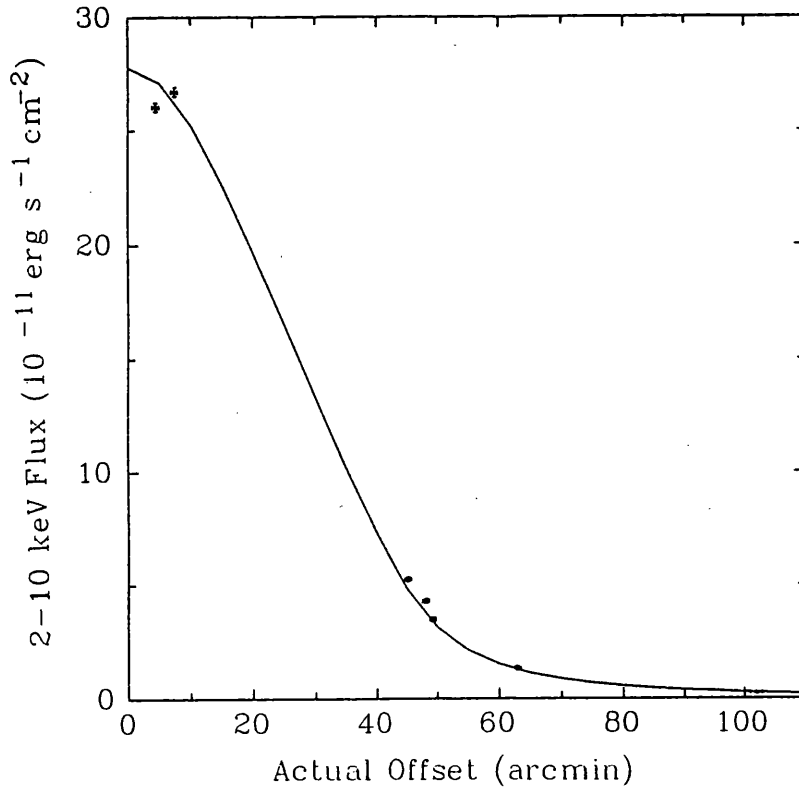


Figure 4.18: 2-10 keV flux against offset angle from the centre of Coma. The solid line gives the expected flux with radius for a modified King model with a core radius of 8.5' and a  $\beta$  of 0.63

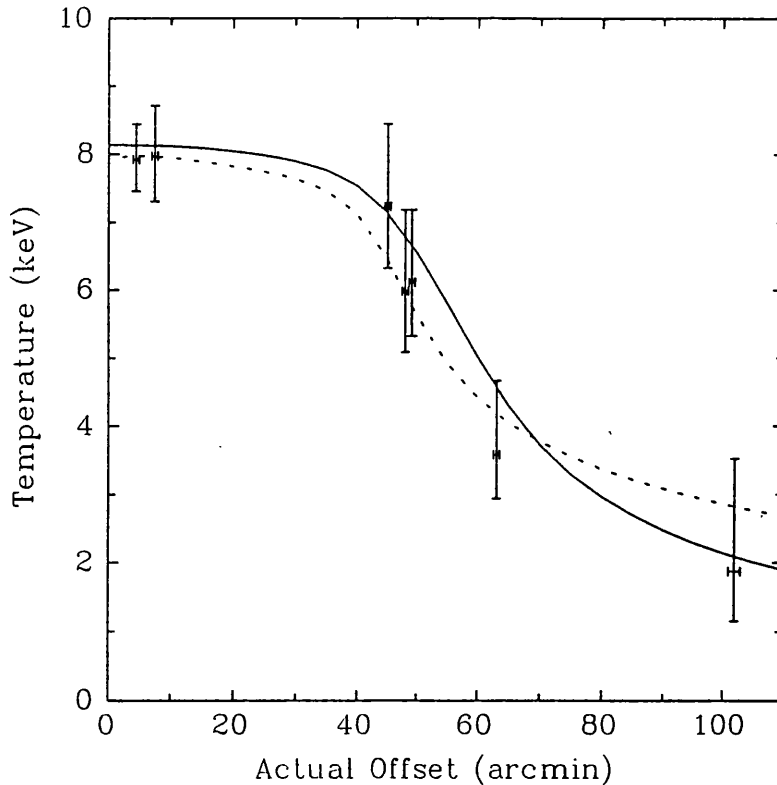


Figure 4.19: Measured temperature against offset radius. The solid line gives the expected temperature with radius for a hybrid model with a central temperature of 8.5 keV, an isothermal radius of 23' and a polytropic index of 1.55. The dashed line gives the temperature with radius for a polytropic model with a central temperature of 12 keV and polytropic index of 1.3. Both models assume a surface brightness profile of 8.5' and a  $\beta$  of 0.63.

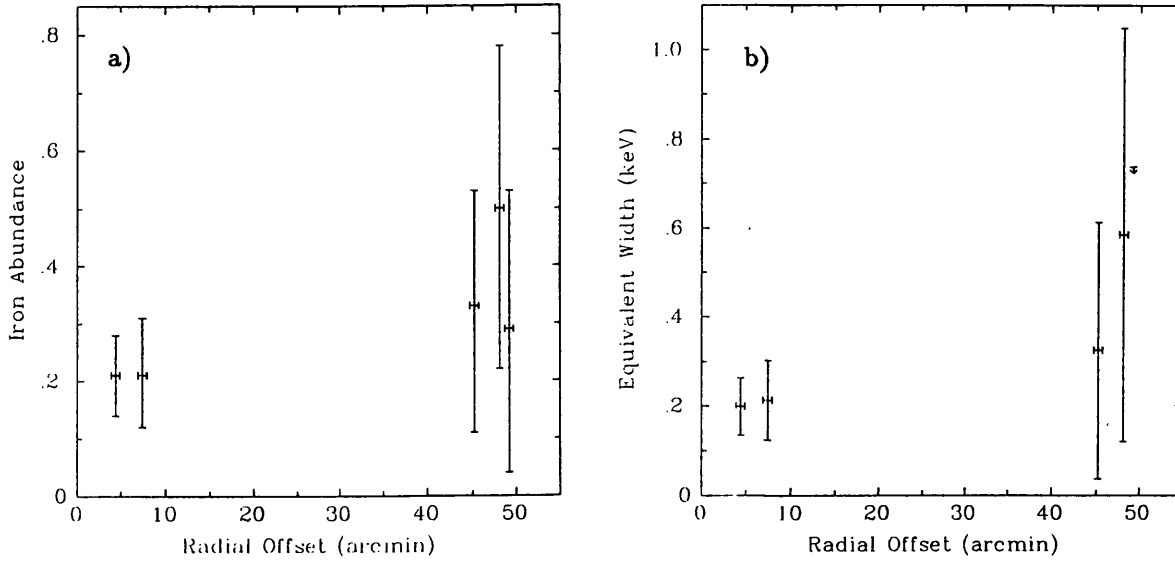


Figure 4.20: a) Iron abundance against offset radius for Coma and b) Equivalent width of the 6.67 keV line against radius for Coma

the ME and the stability of the background it is difficult to imagine any systematic instrumental effect which could account for such an effect. To test for any soft contamination from individual cluster galaxies or background AGN (Branduardi-Raymont *et al.* 1985a), the offset spectra above 4 keV were fitted, but no substantial change in the best fit temperature was found. Therefore it can be concluded that the temperature variation is intrinsic to the intra-cluster gas.

Henriksen & Mushotzky (1986) state that an isothermal fit to the HEAO-1 spectrum of Coma is statistically unacceptable and they propose a polytropic model. The ME data are consistent with a polytropic model (Figure 4.19) with a central temperature of 12 keV and a polytropic index of 1.3. However Hughes *et al.* (1988) find that the polytropic models of Henriksen & Mushotzky are inconsistent with the IPC surface brightness profile and the *Tenma* spectrum.

The proposed temperature profile of Hughes *et al.* (1988) with an isothermal core and a polytropic exterior was taken and the expected “emission-weighted” temperature in the ME was calculated for a range of radii. The best fit model of Hughes, Gorenstein & Fabricant with a central temperature of 8.5 keV, isothermal radius of 23 arcmin and polytropic index of 1.55 is plotted in Figure 4.19 and is consistent with the temperatures obtained. As the imaging IPC data favour an isothermal core, the hybrid isothermal-polytropic model is the preferred description of the data.

The increase in measured abundance with radius is significant in two of the offset pointings (eastern and eastern offset) at the 95% level using the F-test between the fits with the abundance fixed at the central value and those with the abundance allowed to be free. To check that the increased abundance was not an artifact of the Raymond & Smith code, a simple bremsstrahlung model with a line was fitted. Figure 4.20b shows the equivalent width of the fitted line against offset radius, and the same trend is seen. The high abundance in the eastern pointings could have been caused

Reference	Offset (arcmin)	Leicester Temperature (keV)	Leicester Iron Abundance	Leicester 2-10 keV Flux ( $\text{erg cm}^{-2} \text{s}^{-1}$ )	Hughes Temperature	Hughes Iron Abundance	Hughes 2-10 keV Flux ( $\text{erg cm}^{-2} \text{s}^{-1}$ )
1984 Centre	7.4	$7.97^{+0.74}_{-0.66}$	$0.21^{+0.10}_{-0.09}$	$2.67 \times 10^{-10}$	$8.50^{+0.31}_{-0.37}$	$0.20^{+0.04}_{-0.04}$	$27.2 \times 10^{-10}$
1984 West	45.2	$7.24^{+1.21}_{-0.92}$	$0.33^{+0.20}_{-0.22}$	$5.23 \times 10^{-11}$	$7.65^{+0.81}_{-0.71}$	$0.09^{+0.09}_{-0.11}$	$4.94 \times 10^{-11}$
1984 East	48.1	$5.98^{+1.21}_{-0.90}$	$0.50^{+0.28}_{-0.28}$	$4.28 \times 10^{-11}$	$7.78^{+1.27}_{-0.98}$	$0.27^{+0.24}_{-0.19}$	$3.78 \times 10^{-11}$
1984 South	49.3	$6.11^{+1.08}_{-0.79}$	$0.29^{+0.24}_{-0.25}$	$3.48 \times 10^{-11}$	$6.82^{+0.79}_{-0.66}$	$0.23^{+0.12}_{-0.20}$	$2.85 \times 10^{-11}$

Table 4.5: Comparison of the results for Coma obtained here and by Hughes, Gorenstein & Fabricant (1988)

by the background subtraction as they were the first observations in the series and the background was the last. Despite the stability of the ME background and the fact that no flaring was seen, this is the most likely source of error.

#### Comparison with Hughes, Gorenstein & Fabricant analysis

The values obtained here for the 1984 observation should be compared with those given in Hughes, Gorenstein & Fabricant (1988) who analyse the same data. Table 4.5 gives the direct comparison of the sets of the results showing several differences. The abundances and the fluxes for the offset data are lower in the Hughes analysis. This could be caused by too much background flux being subtracted from the source or some variation in the background. Also the central temperature is substantially higher in the Hughes analysis although the abundance is close to the one presented here. This may be, in part, to the different Raymond & Smith models and fitting procedures used. However despite these differences the basic trend for the temperature to decrease with radius is seen.

The *overall* agreement of these two sets of analysis of the same data is good, but the abundances and fluxes in the Hughes results seem to be underestimated for the offset data.

#### 4.3.3 Implications of EXOSAT Results

Optical studies of Coma have shown that if the mass distribution is assumed to follow the light distribution, then the mass can be well constrained from the optical light profile and velocity dispersion (Kent & Gunn 1982). However if this assumption is relaxed then many more mass models can be fitted and the mass becomes poorly constrained (The & White 1986). The X-ray data can, however, provide an independent measure of the mass distribution, which is not dependent

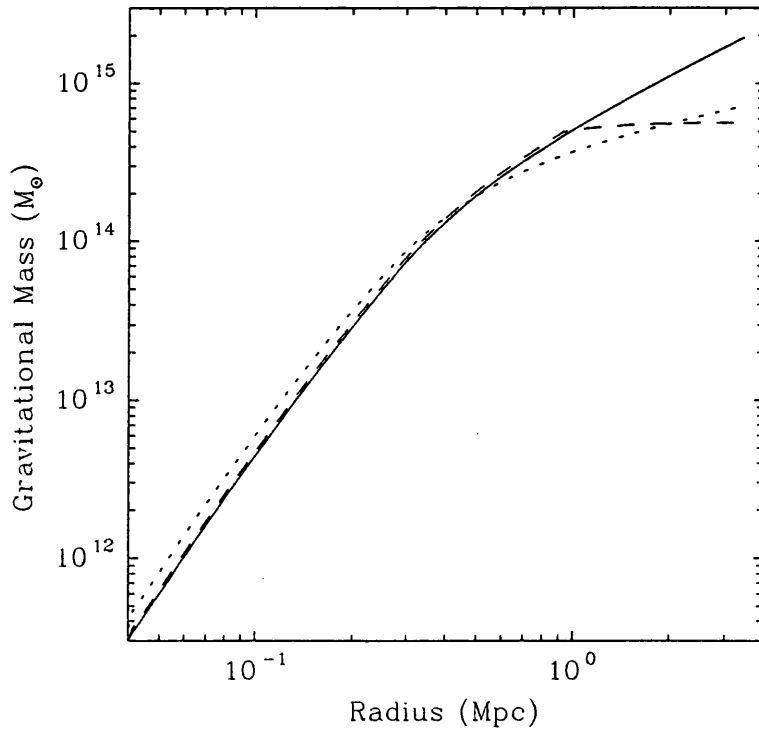


Figure 4.21: Calculated gravitational mass plotted against radius. The solid line gives the mass expected for an isothermal case of a temperature of 8.0 keV. The long-dashed line is for the best fit hybrid model and the short dashed line is for the best fit polytropic model

on the assumptions about galactic orbits or mass-to-light which affect the optical studies. The full implications of the X-ray results on models for the mass distribution in Coma are discussed in Hughes (1989). Hughes takes general optical mass models and the well determined gas density profile to determine the expected temperature profile for cases where the mass-to-light ratio is constant and where it varies with radius. From this analysis Hughes concludes that mass-follows-light models are the preferred solutions to the data and quotes a mass-to-light ratio of  $165 \pm 25$ .

The mass profile can be determined from the X-ray results by using the hydrostatic equilibrium assumption (see Chapter 1). Taking an isothermal core out to 23 arcmin and a polytrope of  $\gamma$  of 1.55 beyond that, a core radius of 8.5 arcmin and a  $\beta$  of 0.63, the gravitational mass with radius is plotted in Figure 4.21. The mass beyond the isothermal core reaches a 'plateau' level of  $8.5 \times 10^{14} M_{\odot}$ , indicating a 'break' in the mass profile. This profile is similar to those given by Hughes (1989) and The & White (1986, 1988a & b).

The iron abundance for Coma is 50% lower than the value of 0.32 of solar abundance determined from the *EXOSAT* sample (Section 6.2) and is the only cluster observed by *EXOSAT* that is inconsistent with the sample mean. This low abundance is interpreted by Hughes, Gorenstein & Fabricant (1988) as evidence for a large fraction of primordial gas ( $\sim 90\%$ ) which dilutes the enriched gas which was ejected or stripped from galaxies.

#### 4.3.4 Summary

- The temperature profile determined from the ME data shows unambiguous evidence of a non-isothermal gas distribution. The cluster appears to have an isothermal core and an adiabatic outer region.
- There is an apparent ‘break’ in the mass profile at 1 Mpc where the cluster mass reaches a constant value.
- The gravitational mass within 1 Mpc is  $8.5 \times 10^{14} M_{\odot}$ .

## 4.4 Perseus

As the brightest extra-galactic source (barring periods of outburst in AGN, *e.g.* Cen-A), Perseus presents an excellent opportunity to study cluster emission in detail. However, Perseus is a particularly difficult cluster to study due to its low galactic latitude and the presence of a powerful active nucleus in the cD galaxy, NGC 1275, which has a substantial X-ray luminosity.

### 4.4.1 Previous X-Ray Results

Perseus has been extensively observed at energies from 0.1 to 100 keV. The earliest survey missions identified Perseus as an X-ray source and emission from the active nucleus in NGC 1275 was deduced from the hard energy tail detected above 10 keV by OSO-7 and HEAO-1 (Rothschild *et al.* 1981; Primini *et al.* 1981). This high energy, power law emission is known to vary on timescales of years by factors of a few. This power law component affects the measured temperatures from these survey instruments causing them to overestimate the cluster temperature. The temperatures from UHURU, OSO-8, HEAO-1 and ARIEL-V are 7.5, 6.8, 6.4 and 6.0 keV respectively for a single temperature fit to the data. Adding a power law source to the fit would lower these temperatures.

Images from *EINSTEIN* IPC and HRI showed a strong cooling flow centred NGC 1275 and elongated emission in the East-West direction (Branduardi-Raymont *et al.* 1981; Fabian *et al.* 1981). The SSS detector on *EINSTEIN* detected a cool  $\sim 1$  keV component which showed strong emission lines from silicon, sulfur and iron (Mushotzky *et al.* 1981). The Japanese satellite *Tenma* observed Perseus with GSPC detectors (Okumura *et al.* 1988) which provided excellent energy resolution around the 6.7 keV iron line and also detected a low energy silicon line.

Recently two Space Shuttle missions have flown experiments with which Perseus was observed. The first, SPARTAN-1 (Ulmer *et al.* 1987), used a very narrow collimator ( $3^\circ \times 5'$ ) to scan the cluster and isolate the emission from the central region. Their data show a large difference in temperature and abundance between the inner 5 arcmin and the region of 5–20 arcmin. The other mission was the coded mask telescope on SPACELAB-2 (Eyles *et al.* 1989). The 3–20 keV images obtained have a resolution of 15 arcmin so it should be possible to measure the temperature profile directly. However due to the difficulty in analysing such complex data the results obtained so far have not been conclusive.

From the previous results on Perseus two points should be noted. Firstly the power law source contributes a significant fraction of the measured 2–10 keV flux. Therefore it must be fitted simultaneously with the overall cluster emission to the data otherwise single component thermal fits will tend to overestimate the temperature. Secondly the cooling flow will make some contribution

Reference	Date	Pointing Position (1950)	Offset (arcmin)	Exposure H 1 (s)	Exposure H 2 (s)	Count Rate (cnt s <sup>-1</sup> half <sup>-1</sup> )	Detectors Used in Fit	Channels fitted
1983 NGC 1275	205/83	03 16 30 +41 20 11	5.2	9940 (8370)	- -	low channels affected by flare	14	13-46 Ar
1984 Centre	24/84	03 16 30 +41 20 11	5.3	-	34690	67.21±0.08	568	6-52 Ar
1984 South	24/84	03 16 50 +40 50 00	25.5	-	20440	33.90±0.08	58	6-44 Ar
1984 North	25/84	03 16 30 +42 05 00	49.9	-	25400	3.85±0.07	567	6-37 Ar
1984 West	25/84	03 12 50 +41 20 00	42.1	-	24040	11.83±0.07	578	6-40 Ar
1984 Slew	25/84	-	-	-	(4270)	-	-	-
1985 East	20/85	03 19 01 +41 17 43	27.0	9760	11040	31.77±0.06	1234568	6-55 Ar 16-50 Xe
1985 NGC 1275	21/85	03 16 21 +41 17 44	4.4	13100	17340	68.42±0.06	1234568	6-58 Ar 16-60 Xe

Table 4.6: Log of *EXOSAT* observations of Perseus. The count rates are quoted for Argon channels 6 to 38 (or approximately 1.5 to 10 keV)

to the measured flux with gas emitting over a range of temperatures from  $\sim 10^8$ K to  $\sim 10^6$ K. This will particularly affect the central temperature measured by SPARTAN-1.

Ideally what is required from *EXOSAT* is a determination of the power law slope (which requires data above 10 keV), a measure of the amount of cooling gas and the temperature and iron abundance profiles. The ME data were able to provide information on all of these points. A preliminary analysis of these *EXOSAT* data is presented in Branduardi-Raymont *et al.* (1985b).

#### 4.4.2 *EXOSAT* Observations

Table 4.6 gives details of the *EXOSAT* observations of Perseus. Figure 4.22 shows a schematic map of the pointings across the field of the cluster. The “count-weighted” radii for these pointings range from 8 to 30 arcmin. This corresponds to a range of projected radii at Perseus of 250 to 960 kpc.

#### LE Data

Figure 4.23 shows the thin Lexan image of the centre of Perseus. The strong point source associated with the active nucleus of NGC 1275 and extended emission from the strong cooling flow centred on NGC 1275 can be distinguished.

The count rates for the point source were 23, 19 and 12 ( $\pm 3$ ) counts per 1000s for the thin Lexan, Aluminium/Parylene and Boron filters respectively. The deprojection analysis presented in Chapter 2 required this point source contribution to be subtracted from the surface brightness profile. Figure 4.24 shows the results from the deprojection analysis. The deprojection results

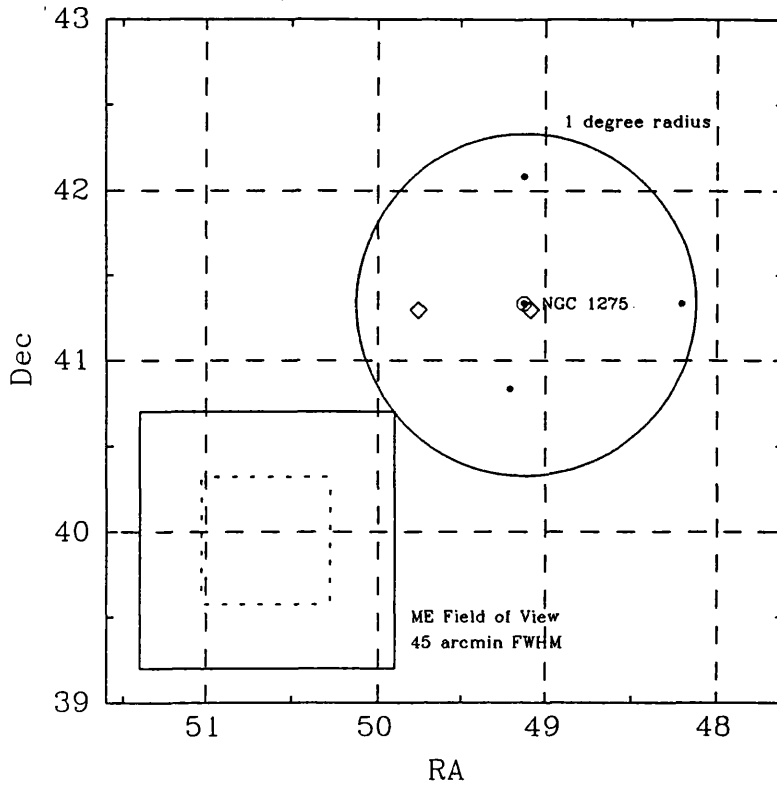


Figure 4.22: Schematic map of *EXOSAT* pointings on Perseus. The 1984 pointing positions are marked with filled circles and the 1985 pointing positions are marked with diamonds

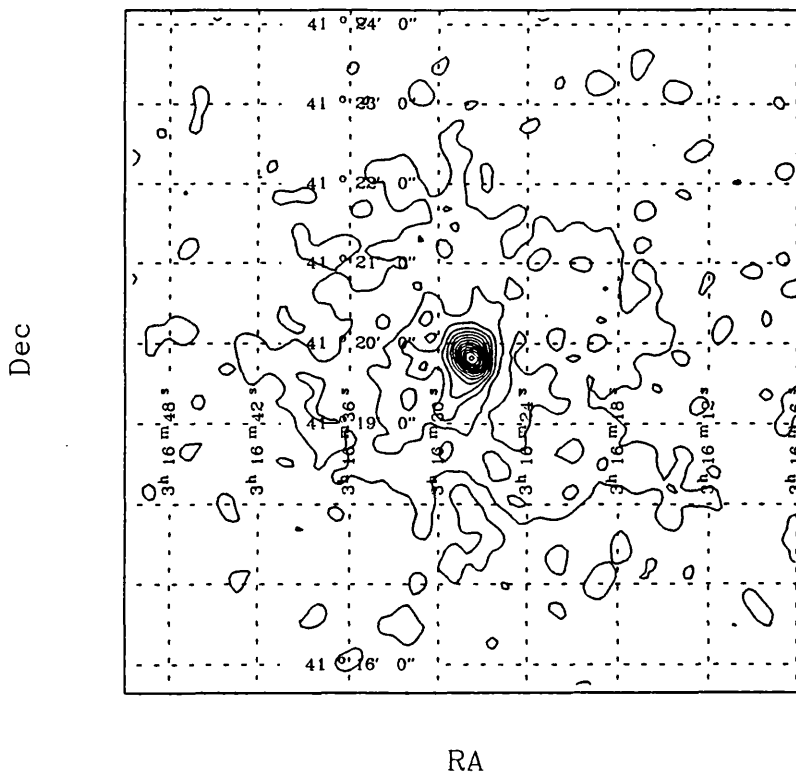


Figure 4.23: LE Image of Perseus in the 3LX filter convolved with a gaussian of 16".

obtained are consistent with those of Fabian *et al.* (1981) and Arnaud (1988a), although the mass flow rate of  $120 M_{\odot} \text{ yr}^{-1}$  quoted by Arnaud is lower than expected from this and other work.

## ME Data

As with the Virgo and Coma observations made in 1983 the poor calibration of detectors 2,3,6 and 7 required these detectors to be omitted from the analysis of the 1983 observation. The observations in 1984 and 1985 provided data for four offset positions around the cluster as well as central pointings.

**Background Subtraction** The background subtraction for 1983 observation was particularly difficult. Firstly there was no “nod” or slew for the observation, and secondly a large fraction of the observation was affected by solar flaring. However the observation following it was of  $\alpha$  ERI which was not detected with the ME so the background was taken from that observation. Unfortunately there was a residual flux at low energies due to the solar flaring and therefore all data below 4 keV were excluded from the analysis. The background for the 1984 data was obtained from a 4700 second slew after the scan pointings. This was the only possible method as no “nods” were made during the observation. No flux was measured by any of the offset detectors in the 1984 data above the level of 0.2 counts per second in the 2–10 keV range. As no flux is expected in the offset detectors a “nod” subtraction was possible for the 1985 pointings. This subtraction method allowed a xenon spectrum for both 1985 observations to be obtained.

**Spectral Fitting** Perseus is known to have a complex X-ray spectrum with thermal cluster emission and non-thermal emission from the active nucleus in NGC 1275. A series of fits were made to the 1985 central pointing, as it had the highest signal-to-noise and covered the largest energy range (1–25 keV) using gradually more complex models. The galactic column density was fixed at a value of  $1.4 \times 10^{21} \text{ cm}^2$  (Stark *et al.* 1988) and for all of these fits a systematic error of 1% was included.

Once the best fit central spectrum was determined, the other spectra were fitted with the same spectrum but with the power law fixed at the value expected for a point source in NGC 1275 offset in the ME detector collimator.

**Results** Table 4.7 gives the results of fits to the 1985 central observation for a series of fits. The fit for a single Raymond & Smith model was unacceptable and showed a strong “hard tail” from NGC 1275 (see Figure 4.25). Fitting a power law with an intrinsic absorption in addition to the the Raymond & Smith model gave an acceptable value for  $\chi^2$  and a power law index and normalisation

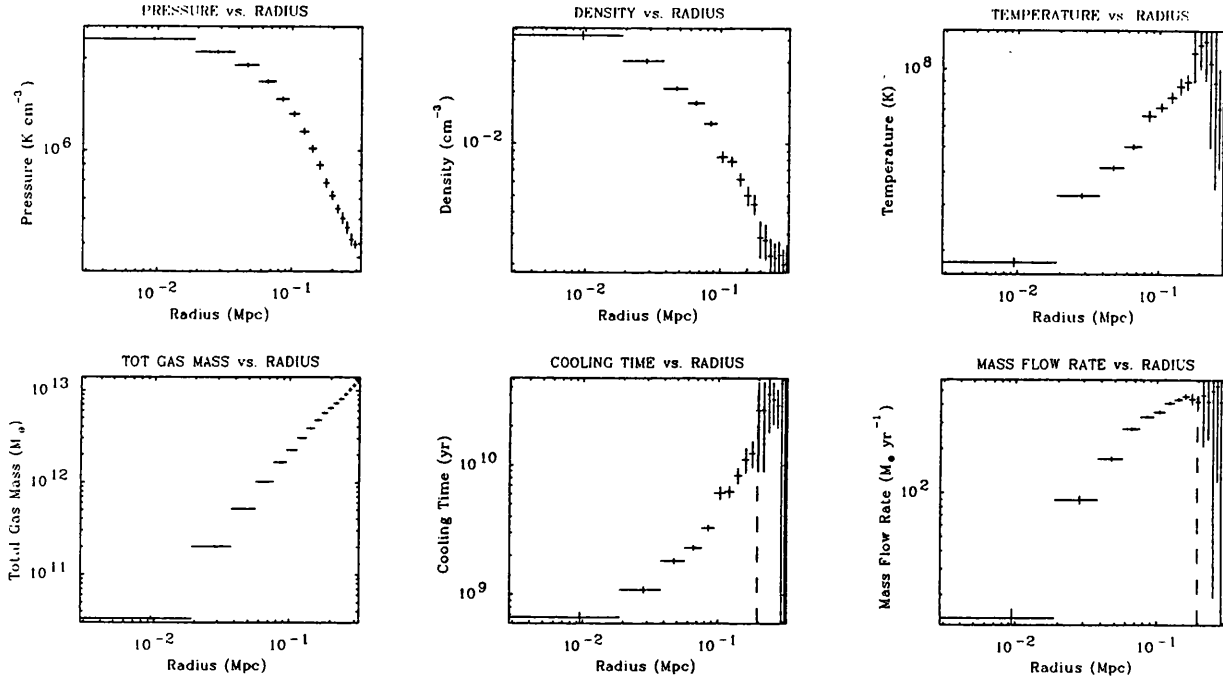


Figure 4.24: Plots of parameters derived from deprojection analysis of LE images of Perseus. The dashed line represents the cooling radius.

Fit Used	Raymond and Smith Temperature (keV)	Silicon and Iron Abundance (relative to Solar)		Power Law and Low Temp Normalisation	Power Law Index	Intrinsic Power Law Column (cm <sup>2</sup> )	2-10 keV Flux for each component (erg cm <sup>-2</sup> s <sup>-1</sup> )	$\chi^2$ for fit
Single RS	6.22 <sup>+0.17</sup> <sub>-0.14</sub>	4.89 <sup>+1.67</sup> <sub>-1.49</sub>	0.25 <sup>+0.04</sup> <sub>-0.04</sub>	-	-	-	7.71 × 10 <sup>-10</sup>	230.9 (93 d.o.f.)
Single RS Plus P. Law	4.83 <sup>+0.23</sup> <sub>-0.25</sub>	1.35 <sup>+0.85</sup> <sub>-0.70</sub>	0.32 <sup>+0.03</sup> <sub>-0.03</sub>	0.035 <sup>+0.062</sup> <sub>-0.005</sub>	1.59 <sup>+0.27</sup> <sub>-0.55</sub>	1.65 <sup>+5.08</sup> <sub>-1.65</sub> × 10 <sup>21</sup>	6.12 × 10 <sup>-10</sup> 1.59 × 10 <sup>-10</sup>	84.45 (90 d.o.f.)
Single RS Plus P. Law	4.79 <sup>+0.18</sup> <sub>-0.18</sub>	1.43 <sup>+0.78</sup> <sub>-0.61</sub>	0.32 <sup>+0.03</sup> <sub>-0.03</sub>	0.035 <sup>+0.077</sup> <sub>-0.025</sub>	1.59 <sup>+0.30</sup> <sub>-0.43</sub>	2.9 × 10 <sup>21</sup> (fixed)	6.12 × 10 <sup>-10</sup> 1.60 × 10 <sup>-10</sup>	84.62 (91 d.o.f.)
Single RS Plus P. Law	4.78 <sup>+0.24</sup> <sub>-0.24</sub>	1.43 (fixed)	0.32 <sup>+0.03</sup> <sub>-0.03</sub>	0.035 <sup>+0.008</sup> <sub>-0.006</sub>	1.59 (fixed)	2.9 × 10 <sup>21</sup> (fixed)	6.12 × 10 <sup>-10</sup> 1.60 × 10 <sup>-10</sup>	84.62 (94 d.o.f.)
Two RS Plus P. Law	4.85 <sup>+0.60</sup> <sub>-0.40</sub> 1.00 (fixed)	1.17 <sup>+2.00</sup> <sub>-1.12</sub>	0.32 <sup>+0.06</sup> <sub>-0.06</sub>	0.034 <sup>+0.008</sup> <sub>-0.011</sub> 0.19 <sup>+1.40</sup> <sub>-0.19</sub>	1.59 (fixed)	2.9 × 10 <sup>21</sup> (fixed)	6.13 × 10 <sup>-10</sup> 1.57 × 10 <sup>-10</sup> 1.66 × 10 <sup>-12</sup>	84.03 (91 d.o.f.)

Table 4.7: Results for spectral fits to ME data from the central Perseus 1985 pointing. The quoted errors are 90% confidence.

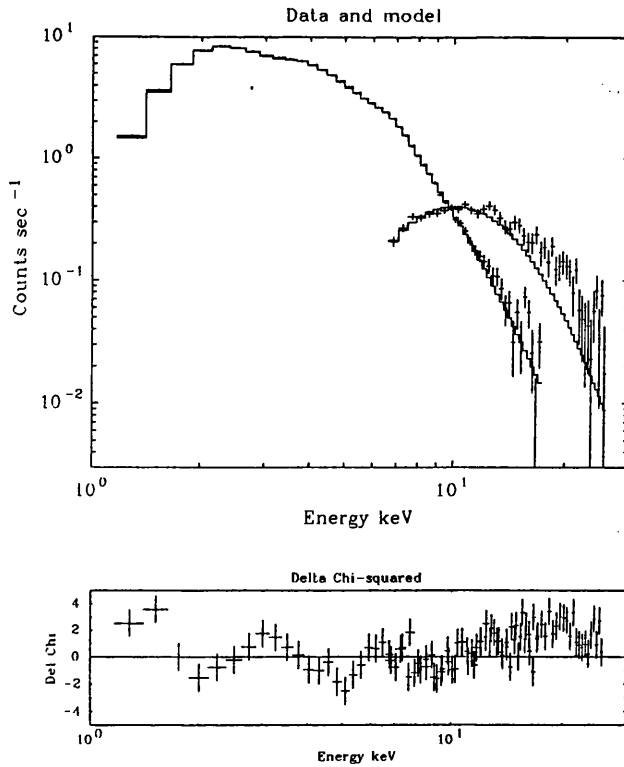


Figure 4.25: Best fit to the argon and xenon count spectra of central Perseus 1985 pointing for single Raymond & Smith model

in agreement with previous hard X-ray measurements (Primini *et al.* 1981; Rothschild *et al.* 1981). The best fit intrinsic column was lower than that predicted by Gorenstein *et al.* (1978) and gave an extrapolated LE count rate a factor of 2 too high. Fixing the intrinsic column at  $2.9 \times 10^{21} \text{cm}^2$  as given in Gorenstein *et al.* (1978) an acceptable fit was obtained and the other parameters, such as temperature and abundance, were unchanged. The derived silicon abundance of 1.4 is close to the value of 0.9 found in the *EINSTEIN* SSS data (Mushotzky *et al.* 1981). The SSS data required the addition of a low temperature component which was attributed to the low temperature cooling gas at the centre of the cluster. Adding this second thermal component into the fit as a 1 keV Raymond & Smith model did not significantly improve the fit and the normalisation was not constrained. Figure 4.26 shows the best fit to the count spectrum for the two component model with fixed intrinsic column. Figure 4.27 shows the best fit photon spectrum split into the two components.

The spectral fitting results for the other pointings are given in Table 4.8. Both the 1984 central and eastern spectra statistically required the addition of the power law component at the 99% level. Unfortunately the limits on the power law normalisation for these fits are not good enough to determine whether there was any variability of the power law component. Previous observations of Perseus indicate variability of  $\sim 100\%$  over timescales of years (Rothschild *et al.* 1981; Arnaud 1988b), as is seen in AGN in general (Turner 1988). However, as the 2–10 keV count rates for the central pointings were so similar (67.2 and 68.4), a limit of  $\sim 20\%$  variability over the 12 months between the two observations could be set. So for simplicity it was assumed that the power law did not change between the observations. Figures 4.28 and 4.29 show the best fits to the eastern and northern pointings. Figures 4.30–4.32 show the variation of cluster flux, temperature and iron

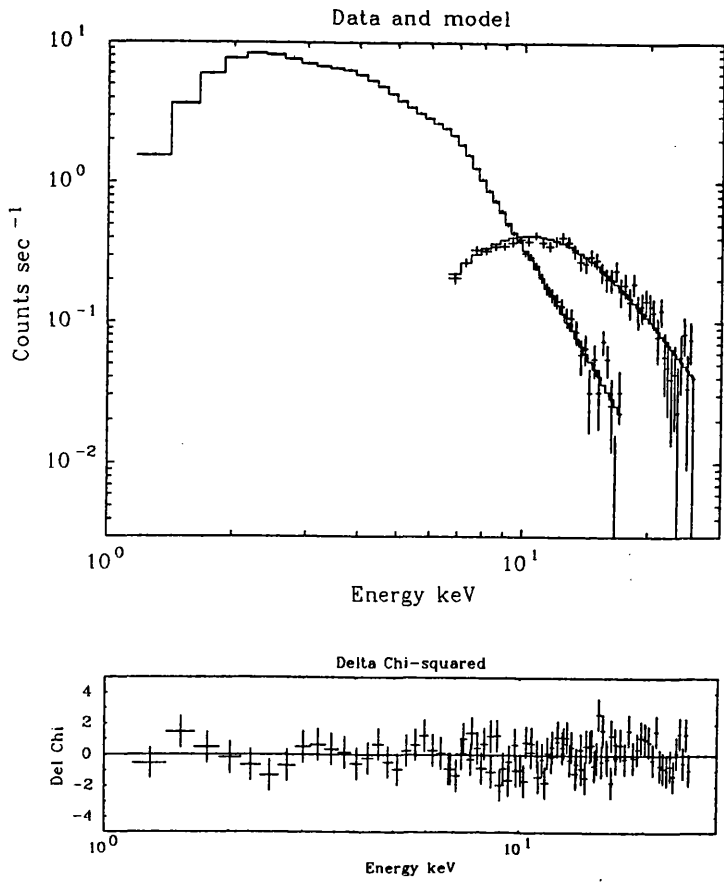


Figure 4.26: Best fit to the argon and xenon count spectra of central Perseus 1985 pointing with two component model

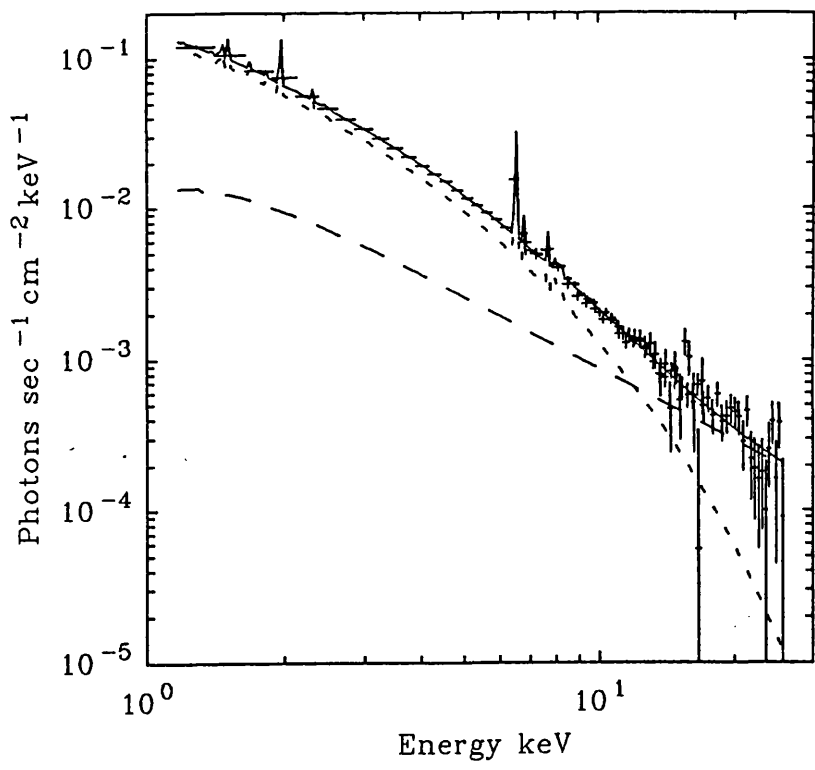


Figure 4.27: Best fit photon spectrum for the two component model split into the two components. The long dashed line shows the absorbed power law component and the short dashed line shows the thermal component

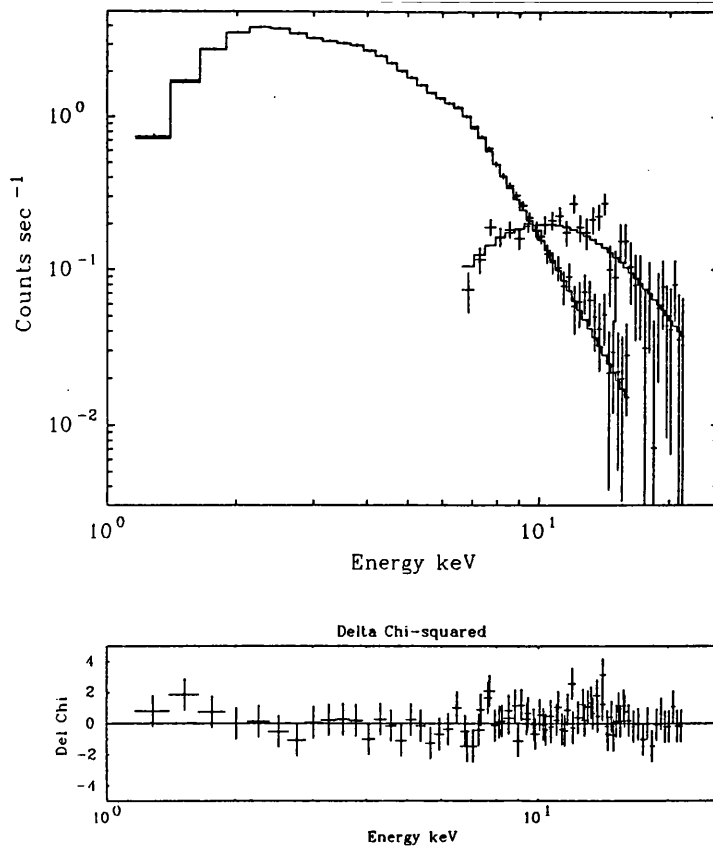


Figure 4.28: Best fit to the argon and xenon count spectra of the eastern Perseus pointing

abundance with radius from NGC 1275.

The 2–10 keV flux against radius agrees with the previously determined surface brightness profile of core radius 8 arcmin and  $\beta$  parameter of 0.6 determined from the *EINSTEIN* IPC profile (Branduardi-Raymont *et al.* 1981). Both the *EINSTEIN* and 2–10 keV profiles appear to be highly ‘peaked’ due to the cooling flow which emits as much as 40% of the total bolometric luminosity of the cluster within the cooling radius of 6–10 arcmin. Correcting for the cluster emission outside the collimator gives a total 2–10 keV flux of  $7.15 \times 10^{-10} \text{ erg cm}^{-2} \text{ s}^{-1}$ .

The temperature profile expected for the cooling flow can be approximated to a low central temperature, which increases to constant value at a radius equivalent to the radius at which the cooling time reaches the Hubble time (*i.e.* the cooling radius). Taking the simplest profile, a linear increase, then the emission-weighted temperature can be calculated for increasing radius. The profiles obtained are close to isothermal for the expected range of cooling radii. Figure 4.31 shows two profiles which are consistent with the temperature data obtained, one with a central temperature of 1 keV, outer temperature of 5.5 keV and a cooling radius of 8 arcmin and the other with a central temperature of 0.5 keV, outer temperature of 6.0 keV and a cooling radius of 10 arcmin. The latter profile gives predicted temperatures for the SPARTAN-1 of 4.0 and 6.0 keV for the inner and outer regions (compared to the measured values of 3.6 and 6.0 keV). So although the *EXOSAT* temperature profile is consistent with an isothermal distribution, it is also consistent with the temperature gradient seen by SPARTAN-1. Similarly the *EXOSAT* abundance was constant with radius, but an increase at the centre seen by SPARTAN-1 is not ruled out due to the poorer spatial resolution afforded by the ME compared to SPARTAN-1. However the high central abundance obtained by SPARTAN-1 could be due, in part, to the fitting of a single temperature

Reference	Detectors Used in Fit	Offset (arcmin.)	Count-Weighted Radius (arcmin.)	Raymond and Smith Temperature (keV)	Iron Abundance (relative to Solar)	2-10 keV Flux (erg cm <sup>-2</sup> s <sup>-1</sup> )	χ <sup>2</sup> for Fit
1983 NGC 1275	14	5.2	5.5	4.92 <sup>+0.31</sup> <sub>-0.29</sub>	0.29 <sup>+0.06</sup> <sub>-0.05</sub>	7.62×10 <sup>-10</sup> (1.54×10 <sup>-10</sup> )	45.5 (31 d.o.f.)
1984 South	58	24.8	6.2	4.77 <sup>+0.23</sup> <sub>-0.21</sub>	0.31 <sup>+0.07</sup> <sub>-0.07</sub>	3.80×10 <sup>-10</sup> (8.07×10 <sup>-11</sup> )	40.33 (36 d.o.f.)
1984 Centre	568	5.8	5.6	4.97 <sup>+0.14</sup> <sub>-0.14</sub>	0.32 <sup>+0.04</sup> <sub>-0.04</sub>	7.75×10 <sup>-10</sup> (1.515×10 <sup>-10</sup> )	39.5 (35 d.o.f.)
1984 West	578	43.1	9.9	5.14 <sup>+0.47</sup> <sub>-0.40</sub>	0.32 <sup>+0.13</sup> <sub>-0.13</sub>	1.19×10 <sup>-10</sup> (1.24×10 <sup>-11</sup> )	37.3 (32 d.o.f.)
1984 North	567	50.3	26.0	5.47 <sup>+1.47</sup> <sub>-1.00</sub>	< 0.60	3.85×10 <sup>-11</sup> (0.0)	25.4 (29 d.o.f.)
1985 NGC 1275	1234568	4.4	5.5	4.79 <sup>+0.18</sup> <sub>-0.18</sub>	0.32 <sup>+0.03</sup> <sub>-0.03</sub>	7.72×10 <sup>-10</sup> (1.60×10 <sup>-10</sup> )	84.6 (91 d.o.f.)
1985 East	1234568	27.0	6.1	4.90 <sup>+0.17</sup> <sub>-0.16</sub>	0.30 <sup>+0.04</sup> <sub>-0.05</sub>	3.64×10 <sup>-10</sup> (7.24×10 <sup>-11</sup> )	69.3 (82 d.o.f.)

Table 4.8: Results for spectral fits to ME data from Perseus. The 2–10 keV flux for the power law component is given in brackets. The quoted errors are 90% confidence.

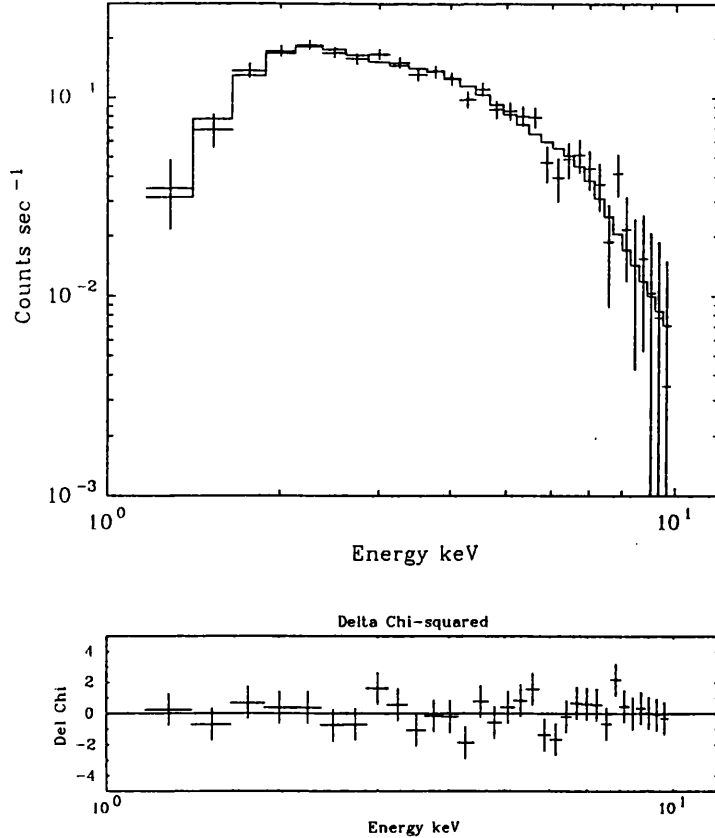


Figure 4.29: Best fit to the argon count spectrum of the northern Perseus pointing

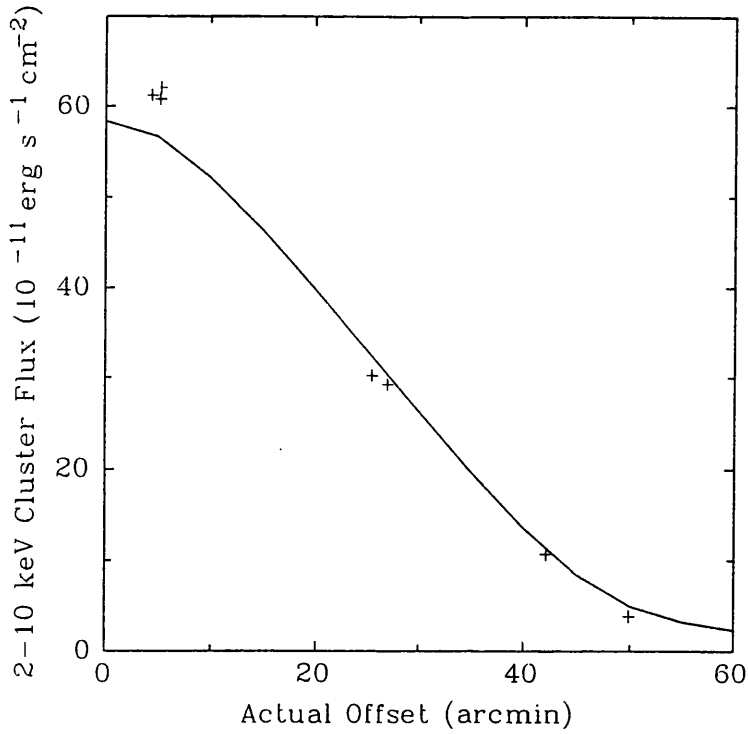


Figure 4.30: 2–10 keV flux from the cluster against offset angle from NGC 1275. The solid line gives the expected flux with radius for a modified King model with a core radius of  $5'$  and  $\beta$  of 0.6

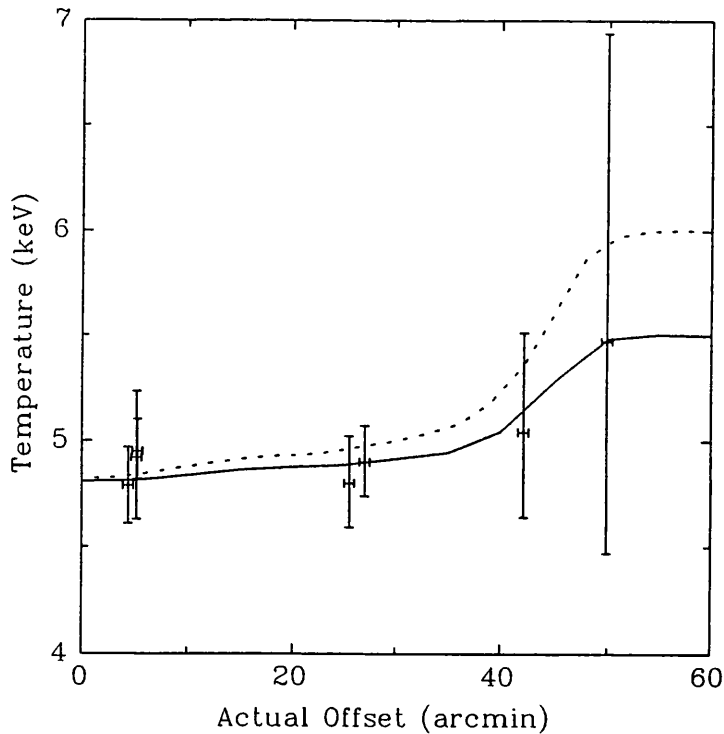


Figure 4.31: Measured temperature against offset radius for Perseus. The solid line gives the expected temperature with radius for a 'cooling core' model with a central temperature of 1 keV, an outer temperature of 5.5 keV and a cooling radius of  $8'$ . The dashed line is the same but for a central temperature of 0.2 keV, an outer temperature of 6 keV and a cooling radius of  $10'$

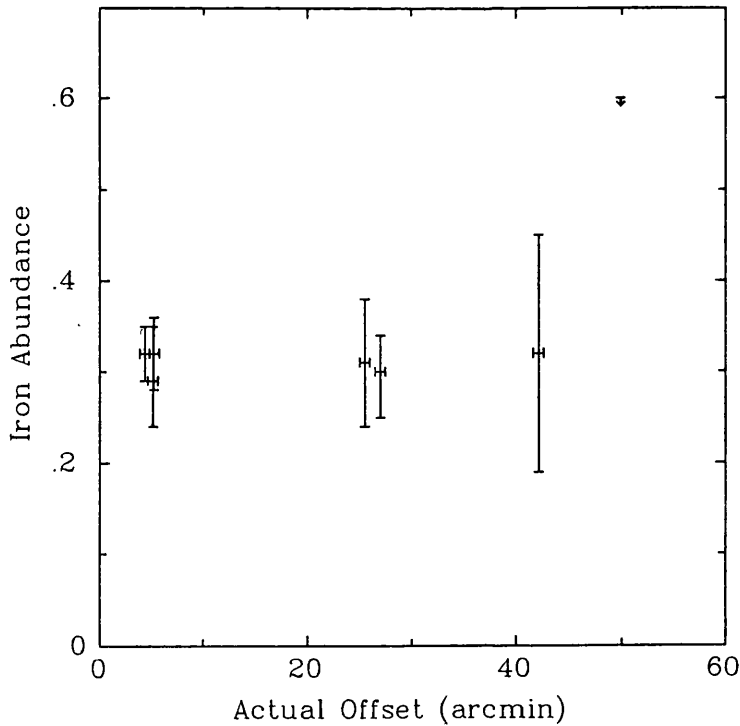


Figure 4.32: Iron abundance against offset radius for Perseus

model to multi-temperature data and the resulting miscalculated line strengths.

These results illustrate the relative insensitivity of the ME to temperature and abundance variations over scales of  $\sim 10$  arcmin, whereas for Coma the temperature varies on larger scales and the ME results show much clearer trends.

#### 4.4.3 Implications of *EXOSAT* Results

Perseus is the most quoted example in discussion of the “Beta Problem” (Kent & Sargent 1983; see Section 6.3.2). The imaging data give  $\beta$  of 0.6, but using a velocity dispersion of  $1181 \text{ km s}^{-1}$  and a temperature of 5.5 keV the calculated value of  $\beta$  is 1.5. This discrepancy has been explained in a number of ways: using the central temperature of the polytropic model given by Cowie, Henriksen & Mushotzky (1987) of 9 keV lowers  $\beta$  to 1.0; Kent & Sargent (1983) suggest highly anisotropic galactic orbits may cause the line of sight velocity dispersion to be overestimated. The *EXOSAT* and SPARTAN-1 results rule out a ‘hot’ core so overestimation of the velocity dispersion by some means is the most compelling explanation. Kent & Sargent point out that the optical data show evidence for predominately radial orbits, but the determination of orbit parameters from the line-of-sight velocity dispersion alone is difficult and model dependent. As the value of  $\beta$  is dependent on the three-dimensional velocity dispersion,  $\sigma_{3D}$ , it will decrease if the orbits are anisotropic, as  $\sigma_{3D}$  will be overestimated in this case. The precise factor for the overestimation of  $\sigma_{3D}$  depends on the model used, but could be as much as  $\frac{1}{\sqrt{2}}$ . This would give a value of  $\beta$  as low as 0.7. Therefore any apparent discrepancy between X-ray and optical results could indicate either the nature of the galactic orbits or the presence of sub-clustering.

The implied gravitational mass within 1 Mpc, assuming an isothermal temperature of 5.5 keV, is  $4.0 \times 10^{14} M_{\odot}$ . The value expected from the Virial theorem from Kent & Sargent is  $5.9 \times 10^{14} M_{\odot}$ . This is higher due to the overestimation of the velocity dispersion discussed above.

#### 4.4.4 Summary

- The temperature profile obtained by *EXOSAT* showed a small increase in temperature with radius which is consistent with the expected ‘cooling core’ models.
- The abundance was apparently constant with radius and the 2–10 keV flux showed an excess toward the centre associated with the cooling flow.
- The power law emission from the active nucleus in NGC 1275 was well constrained and is consistent with the previous high energy observations.
- The high value of  $\beta$  implies that the velocity dispersion is overestimated due to subclustering or to anisotropic galactic orbits.
- The gravitational mass within 1 Mpc is  $4.0 \times 10^{14} M_{\odot}$ .

## 4.5 Conclusions

In all 3 cases presented here the advantage of the small field of view of the ME detector over previous large field of field instruments can be seen. *EXOSAT* provided, for the first time, conclusive evidence for a non-isothermal gas distribution in the Coma cluster. The data also put strong limits on any temperature gradient in Virgo and Perseus. These temperature profiles can be used to improve estimates of the total gravitational mass in these clusters. These observations clearly demonstrate the need for spatially resolved spectra on scales of a few arcmin.

## Chapter 5

# Correlation Analysis of the EXOSAT Sample

### Introduction

The *EXOSAT* sample results from Chapters 2, 3 & 4 are compared with other X-ray, optical and radio properties from the literature. Correlations between these properties are investigated using a least squares fitting technique. The significance and relative importance of these correlations are determined. The astrophysical implications of the correlations are discussed in Chapter 6.

### 5.1 X-ray Results

The results from *EXOSAT* provide an excellent sample for determining the relationships between various cluster properties. Due to the insensitivity of the LE to low surface brightness emission, few reliable core radii or gas masses were obtained, so these have not been included in the analysis. Gas masses derived from deprojection analysis of *EINSTEIN* IPC data (Arnaud 1987) have been used in the analysis to supplement the data from the LE.

The determination of X-ray luminosities from the fluxes in Chapters 3 and 4 required corrections for both the galactic absorption and limited energy range of the observed spectra. The corrections for absorption were calculated from the ratio of the 2–10 keV fluxes with and without absorption. The maximum correction of 1.055 was for 3C129 (column density of  $5.76 \times 10^{21} \text{cm}^2$ ). The proportion of the luminosity emitted below 2 keV and above 10 keV depends on the temperature. To obtain a bolometric luminosity, a temperature dependent correction had to be applied. This factor was calculated from the ratio of the fluxes between 2–10 keV and  $10^{-4}$ – $10^4$  keV. The correction factors used are shown in Figure 5.1 as a function of temperature and were large at low temperatures.

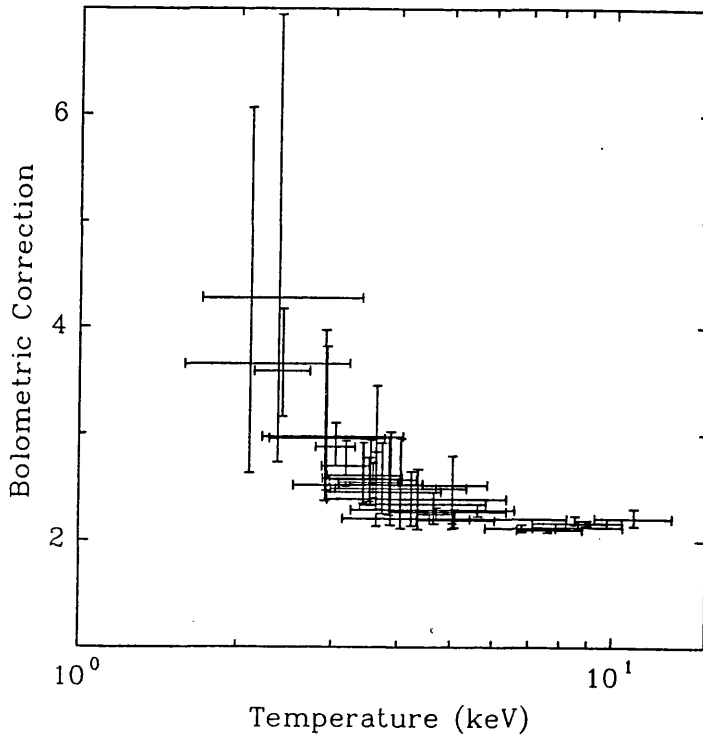


Figure 5.1: Bolometric correction for 2–10 keV flux plotted against temperature

The absorption corrected 2–10 keV and bolometric luminosities are given in Table 5.1, assuming  $H_0$  of  $50 \text{ km s}^{-1} \text{ Mpc}^{-1}$  and  $q_0$  is 0.5.

Figures 5.2a–f show histograms of the distribution of temperature, bolometric luminosity, redshift, iron abundance, flux and mass flow rate measured for the whole sample. A clear excess of objects with temperatures around 3–4 keV and bolometric luminosity of  $3\text{--}6 \times 10^{44} \text{ erg s}^{-1}$  can be seen. The skewed distribution of luminosity and temperature is also present in the redshift and reflects the flux limited nature of the sample.

Despite the large errors on the iron abundance, the range of values is relatively small (compared to the HEAO-1 results from Rothenflug & Arnaud 1985). The data are consistent with a normal distribution with a mean of  $0.32 \pm 0.18$ , apart from the three low temperature clusters with greater than solar abundance, which are discussed in Chapter 3. Performing a  $\chi^2$  test on the data for the difference between the mean value of 0.32 and the measured values gave a total  $\chi^2$  of 42.7, for 35 degrees of freedom. Only Coma, with an abundance of  $0.21 \pm 0.04$ , was significantly different from the mean value and contributes 23.9 to the total  $\chi^2$ . Excluding Coma, the abundances are consistent with a constant value of 0.32.

The fluxes show the distribution expected from the Log-N/Log-S distribution of clusters (Piccinotti *et al.* 1982). Unfortunately, as the EXOSAT sample was not complete (only 18 of the 32 clusters in the HEAO-1 high galactic latitude survey of Piccinotti *et al.* (1982) were observed), a formal

Cluster	Temperature (keV)	Iron Abundance (relative to solar)	2-10 keV Flux ( $\text{erg cm}^{-2} \text{s}^{-1}$ )	Bolometric Correction	2-10 keV Luminosity ( $\text{erg s}^{-1}$ )	Bolometric Luminosity ( $\text{erg s}^{-1}$ )
A119	$5.09^{+0.97}_{-0.75}$	$0.28^{+0.26}_{-0.25}$	$3.02 \pm 0.09 \times 10^{-11}$	$2.19^{+0.10}_{-0.07}$	$2.57 \pm 0.08 \times 10^{44}$	$5.62 \pm 0.35 \times 10^{44}$
A133	$3.75^{+1.99}_{-0.88}$	< 1.06	$1.43 \pm 0.09 \times 10^{-11}$	$2.49^{+0.53}_{-0.35}$	$2.31 \pm 0.14 \times 10^{44}$	$5.75 \pm 1.11 \times 10^{44}$
A193	$4.24^{+1.59}_{-0.85}$	$0.57^{+0.84}_{-0.54}$	$1.34 \pm 0.09 \times 10^{-11}$	$2.34^{+0.30}_{-0.20}$	$1.37 \pm 0.10 \times 10^{44}$	$3.20 \pm 0.48 \times 10^{44}$
A262	$2.42^{+0.31}_{-0.27}$	$1.31^{+0.94}_{-0.72}$	$2.34 \pm 0.09 \times 10^{-11}$	$3.58^{+0.58}_{-0.43}$	$2.63 \pm 0.12 \times 10^{43}$	$9.43 \pm 1.51 \times 10^{43}$
A376	$5.05^{+3.20}_{-1.91}$	< 0.70	$1.01 \pm 0.07 \times 10^{-11}$	$2.21^{+0.59}_{-0.10}$	$1.07 \pm 0.08 \times 10^{44}$	$2.35 \pm 0.42 \times 10^{44}$
AWM7	$3.57^{+0.24}_{-0.20}$	$0.43^{+0.28}_{-0.25}$	$9.08 \pm 0.14 \times 10^{-11}$	$2.57^{+0.37}_{-0.25}$	$1.17 \pm 0.07 \times 10^{44}$	$3.00 \pm 0.45 \times 10^{44}$
A400	$2.11^{+1.31}_{-0.53}$	< 4.57	$0.79 \pm 0.08 \times 10^{-11}$	$4.27^{+1.79}_{-1.64}$	$1.86 \pm 0.17 \times 10^{43}$	$7.93 \pm 3.52 \times 10^{43}$
A3122	$4.06^{+2.31}_{-1.12}$	$0.81^{+0.96}_{-0.71}$	$1.94 \pm 0.15 \times 10^{-11}$	$2.39^{+0.28}_{-0.28}$	$4.82 \pm 0.37 \times 10^{44}$	$1.15 \pm 0.38 \times 10^{45}$
Perseus	$5.5 \pm 0.5$	$0.32 \pm 0.03$	$7.1 \pm 0.4 \times 10^{-10}$	$2.216^{+0.054}_{-0.035}$	$1.0 \pm 0.1 \times 10^{45}$	$2.3 \pm 0.1 \times 10^{45}$
0336+09	$3.05^{+0.28}_{-0.25}$	$0.35^{+0.25}_{-0.23}$	$4.65 \pm 0.12 \times 10^{-11}$	$2.88^{+0.22}_{-0.18}$	$2.47 \pm 0.07 \times 10^{44}$	$7.12 \pm 0.64 \times 10^{44}$
A478	$6.80^{+1.08}_{-0.99}$	$0.27^{+0.14}_{-0.16}$	$6.54 \pm 0.18 \times 10^{-11}$	$2.11^{+0.04}_{-0.04}$	$2.38 \pm 0.39 \times 10^{45}$	$5.04 \pm 0.89 \times 10^{45}$
0422-09	$2.93^{+0.86}_{-0.64}$	< 1.63	$1.60 \pm 0.12 \times 10^{-11}$	$2.96^{+0.86}_{-0.48}$	$1.07 \pm 0.09 \times 10^{44}$	$3.15 \pm 0.73 \times 10^{44}$
A496	$4.66^{+0.95}_{-0.78}$	< 0.51	$5.37 \pm 0.23 \times 10^{-11}$	$2.27^{+0.19}_{-0.11}$	$2.40 \pm 0.42 \times 10^{44}$	$6.70 \pm 1.10 \times 10^{44}$
3C129	$5.63^{+0.74}_{-0.59}$	$0.20^{+0.11}_{-0.11}$	$9.00 \pm 0.28 \times 10^{-11}$	$2.27^{+0.06}_{-0.04}$	$1.89 \pm 0.14 \times 10^{44}$	$4.31 \pm 0.39 \times 10^{44}$
A576	$3.65^{+0.79}_{-0.56}$	$0.43^{+0.48}_{-0.41}$	$1.72 \pm 0.07 \times 10^{-11}$	$2.53^{+0.30}_{-0.23}$	$1.09 \pm 0.05 \times 10^{44}$	$2.76 \pm 0.36 \times 10^{44}$
0745-19	$8.54^{+1.89}_{-1.43}$	$0.29^{+0.14}_{-0.16}$	$5.71 \pm 0.15 \times 10^{-11}$	$2.17^{+0.07}_{-0.02}$	$2.72 \pm 0.70 \times 10^{45}$	$5.90 \pm 1.91 \times 10^{45}$
A754	$8.67^{+1.80}_{-1.55}$	< 0.37	$8.49 \pm 0.21 \times 10^{-11}$	$2.12^{+0.06}_{-0.02}$	$1.04 \pm 0.21 \times 10^{45}$	$2.21 \pm 0.75 \times 10^{45}$
Hydra-A	$3.85^{+0.96}_{-0.93}$	< 0.41	$2.44 \pm 0.24 \times 10^{-11}$	$2.46^{+0.51}_{-0.22}$	$2.93 \pm 0.29 \times 10^{44}$	$7.20 \pm 1.27 \times 10^{44}$
A1060	$3.29^{+0.40}_{-0.33}$	< 0.46	$4.35 \pm 0.12 \times 10^{-11}$	$2.70^{+0.23}_{-0.19}$	$2.45 \pm 0.08 \times 10^{43}$	$6.61 \pm 0.66 \times 10^{43}$
A1367	$3.54^{+0.46}_{-0.46}$	< 0.29	$3.44 \pm 0.12 \times 10^{-11}$	$2.55^{+0.23}_{-0.18}$	$6.92 \pm 0.28 \times 10^{43}$	$1.76 \pm 0.19 \times 10^{44}$
Virgo	$2.4 \pm 0.3$	$0.4 \pm 0.1$	$32.8 \pm 0.2 \times 10^{-10}$	$3.425^{+0.551}_{-0.355}$	$1.1 \pm 0.1 \times 10^{43}$	$3.7 \pm 0.6 \times 10^{43}$
Coma	$8.0 \pm 0.3$	$0.21 \pm 0.04$	$3.2 \pm 0.2 \times 10^{-10}$	$2.133^{+0.004}_{-0.002}$	$7.4 \pm 0.4 \times 10^{44}$	$1.6 \pm 0.1 \times 10^{45}$
Centaurus	$3.61^{+0.41}_{-0.36}$	$0.47^{+0.28}_{-0.26}$	$1.12 \pm 0.03 \times 10^{-10}$	$2.55^{+0.18}_{-0.14}$	$5.77 \pm 0.21 \times 10^{43}$	$1.47 \pm 0.13 \times 10^{44}$
A3562	$3.75^{+0.95}_{-0.77}$	$0.57^{+0.61}_{-0.56}$	$3.62 \pm 0.18 \times 10^{-11}$	$2.49^{+0.42}_{-0.23}$	$3.84 \pm 0.19 \times 10^{44}$	$9.55 \pm 1.34 \times 10^{44}$
A3571	$7.59^{+1.22}_{-0.94}$	$0.38^{+0.17}_{-0.18}$	$1.23 \pm 0.02 \times 10^{-10}$	$2.10^{+0.02}_{-0.02}$	$8.22 \pm 0.15 \times 10^{44}$	$1.73 \pm 0.50 \times 10^{45}$
A1795	$5.05^{+0.39}_{-0.46}$	$0.25^{+0.14}_{-0.12}$	$5.30 \pm 0.09 \times 10^{-11}$	$2.20^{+0.06}_{-0.04}$	$8.91 \pm 0.40 \times 10^{44}$	$1.96 \pm 0.12 \times 10^{45}$
A1837	$2.38^{+0.86}_{-0.78}$	< 11.26	$0.50 \pm 0.08 \times 10^{-11}$	$3.65^{+4.46}_{-1.37}$	$3.08 \pm 0.52 \times 10^{43}$	$1.12 \pm 0.42 \times 10^{44}$
A2052	$3.43^{+0.64}_{-0.50}$	$0.53^{+0.52}_{-0.43}$	$2.62 \pm 0.10 \times 10^{-11}$	$2.61^{+0.34}_{-0.26}$	$1.39 \pm 0.06 \times 10^{44}$	$3.63 \pm 0.26 \times 10^{44}$
A2142	$10.98^{+1.99}_{-1.71}$	< 0.36	$7.48 \pm 0.11 \times 10^{-11}$	$2.21^{+0.10}_{-0.07}$	$2.71 \pm 0.06 \times 10^{45}$	$5.99 \pm 0.32 \times 10^{45}$
A2147	$4.36^{+2.23}_{-1.10}$	< 1.13	$3.27 \pm 0.21 \times 10^{-11}$	$2.29^{+0.39}_{-0.18}$	$1.82 \pm 0.14 \times 10^{44}$	$4.16 \pm 0.62 \times 10^{44}$
A2199	$4.71^{+0.41}_{-0.35}$	$0.21^{+0.13}_{-0.13}$	$7.12 \pm 0.10 \times 10^{-11}$	$2.25^{+0.06}_{-0.05}$	$2.97 \pm 0.43 \times 10^{44}$	$6.67 \pm 1.10 \times 10^{44}$
Ophiuchus	$8.99^{+0.84}_{-0.71}$	$0.29^{+0.07}_{-0.0}$	$4.37 \pm 0.45 \times 10^{-10}$	$2.16^{+0.03}_{-0.02}$	$1.49 \pm 0.23 \times 10^{45}$	$3.22 \pm 0.52 \times 10^{45}$
S1101	$2.99^{+1.17}_{-0.71}$	< 1.53	$0.95 \pm 0.09 \times 10^{-11}$	$2.97^{+1.00}_{-0.59}$	$1.30 \pm 0.13 \times 10^{44}$	$3.85 \pm 1.07 \times 10^{44}$
A2589	$3.66^{+2.20}_{-1.12}$	< 2.04	$1.61 \pm 0.15 \times 10^{-11}$	$2.52^{+0.93}_{-0.39}$	$1.26 \pm 0.12 \times 10^{44}$	$3.17 \pm 0.75 \times 10^{44}$
A4059	$3.46^{+0.63}_{-0.58}$	< 0.92	$1.88 \pm 0.08 \times 10^{-11}$	$2.58^{+0.33}_{-0.25}$	$1.89 \pm 0.14 \times 10^{44}$	$4.89 \pm 0.66 \times 10^{44}$

Table 5.1: Table of derived X-ray luminosities. All errors are 90% confidence.

Log-N/Log-S relationship and luminosity function could not be determined.

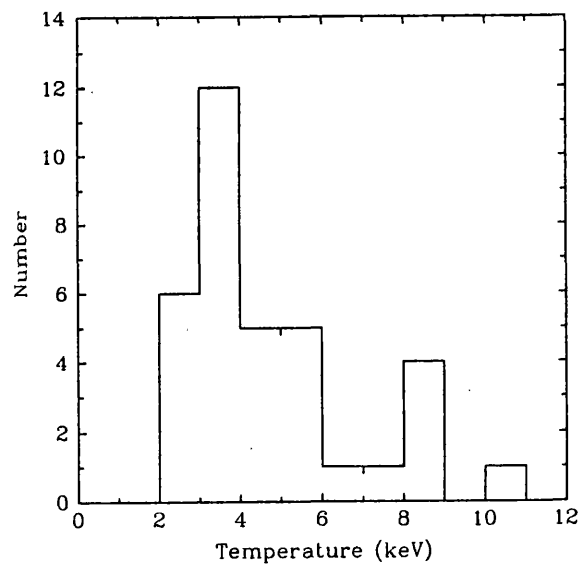
The calculated mass flow rates show a similar distribution to that shown in Arnaud (1988a). The majority of clusters have a mass flow rate of less than  $100 M_{\odot} \text{ yr}^{-1}$ , but there is a 'tail' of values up to  $1000 M_{\odot} \text{ yr}^{-1}$ .

## 5.2 Optical Results

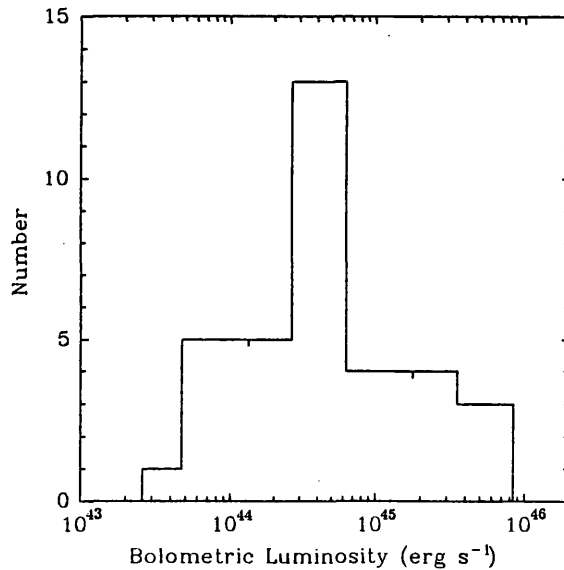
There is a large body of optical data concerning clusters in the literature. However due to the differences in the detectors, telescopes and techniques used, it was difficult to produce a homogeneous body of data for comparison with the *EXOSAT* data. Table 5.2 gives a summary of the optical properties for the clusters in the sample. The Abell richness and distance classes and Bautz-Morgan types are included where known.

The most extensively studied optical property of clusters is the velocity dispersion (Danese, De Zotti & di Tullio 1980; Struble & Rood 1987). The sources for the velocity dispersions are given with Table 5.2. 22 of the 35 clusters in the sample have a velocity dispersion measurement, although only 13 of those are based on more than 35 velocities. Velocity dispersions based on less than 35 velocities are susceptible to sampling errors which all lead to an overestimate of the dispersion (Danese, De Zotti & di Tullio 1980). The two most common sources of error in these determinations are the inclusion of foreground and background galaxies and the presence of subclusters within the cluster. The only way to reduce these errors is to increase the number of measured velocities. This is well illustrated in the case of Centaurus where two velocity systems were resolved only when the number of galaxies was increased to 150 (Lucey, Currie & Dickens 1986a). Another subclustered system observed by *EXOSAT* is A3122 (or 0316-443). Materne & Hopp (1983) present a double-peaked velocity profile and quote a velocity dispersion of  $1481 \text{ km s}^{-1}$  for 33 velocities. This velocity dispersion is greatly overestimated. Including galaxies in the subcluster around the cD galaxy (on which the X-rays are centred), lowers the velocity dispersion to  $820 \text{ km s}^{-1}$  for 23 galaxies, which is the value used in this analysis. Given the high frequency of subclustering observed in clusters (Fitchett 1988) and expected from N-body simulations of clusters (West, Oemler & Dekel 1988), it is likely that other clusters in this sample are subclustered and hence have overestimated velocity dispersions.

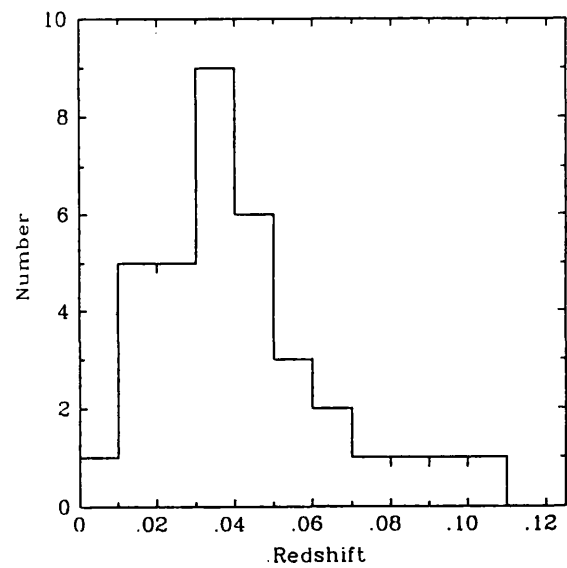
The optical luminosity of clusters has been investigated by observers, usually in terms of the number of galaxies brighter than a certain magnitude limit (Bahcall 1977a & 1981; Dressler 1980b). The Abell catalogue gives a number density,  $N_A$ , for each cluster on which the richness class of a cluster was based.  $N_A$  is defined as the number of galaxies within 3 Mpc of the cluster centre brighter than  $m_3 + 2$ , where  $m_3$  is the magnitude of the third brightest galaxy.  $N_A$  is, however, poorly



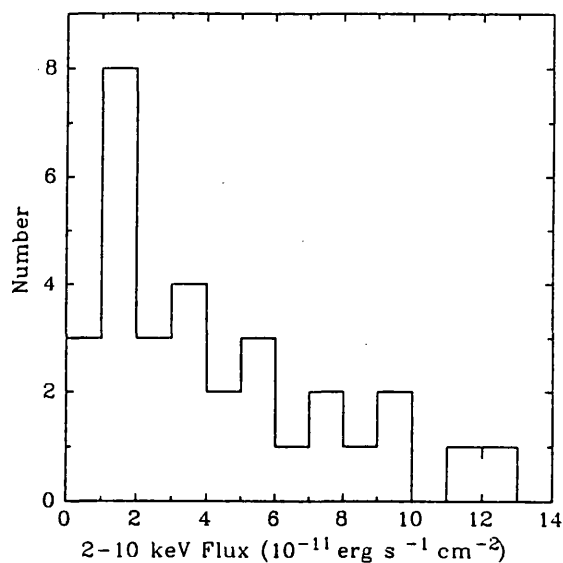
a. Histogram of measured temperatures



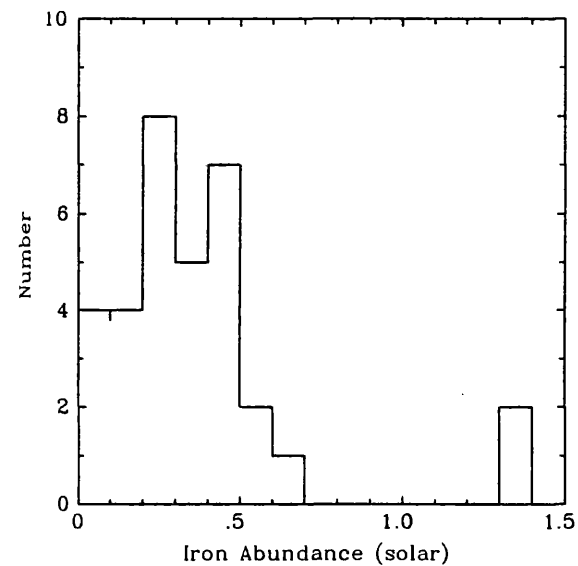
b. Histogram of measured bolometric luminosities



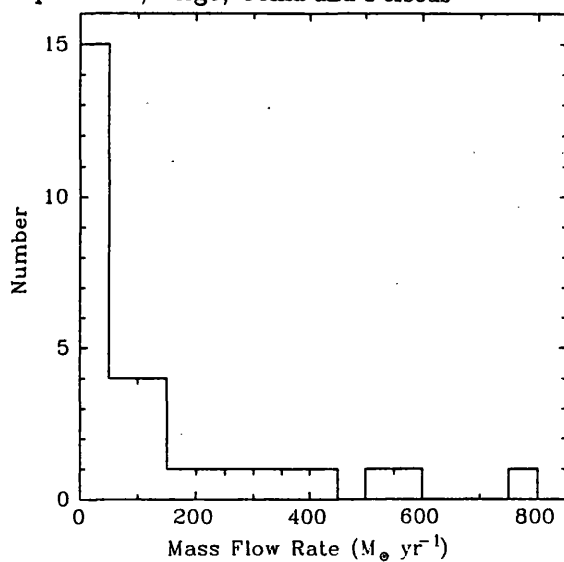
c. Histogram of cluster redshifts



d. Histogram of measured 2-10 keV fluxes, excluding Ophiuchus, Virgo, Coma and Perseus



e. Histogram of measured iron abundances



f. Histogram of measured mass flow rates (including upper limits)

Figure 5.2:

Cluster	Redshift	RS Type	BM Class	D Class	R Class	Abell Number Density	Bahcall Number Density	Velocity Dispersion (km s <sup>-1</sup> )	Optical Luminosity of Central Galaxy (10 <sup>10</sup> L <sub>⊙</sub> )
A119	0.0440(3)	C12	II-III	3	1	69	-	778 <sup>+174</sup> <sub>-122</sub> (23) [1]	13.5±2.7
A133	0.0604(3)	cD	I	4	0	47	-	-	12.0±2.5
A193	0.0482(3)	cDs	II	4	1	58	-	-	15.1±3.1
A262	0.0161(3)	C9	III	1	0	40	11	415 <sup>+63</sup> <sub>-48</sub> (38) [2]	-
A376	0.0489(5)	C7	I-II	3	0	36	-	-	-
AWM7	0.0172(7)	-	-	-	-	-	13	849 <sup>+130</sup> <sub>-89</sub> (33) [3]	-
A400	0.0232(3)	Ic	II-III	1	1	58	-	423 <sup>+96</sup> <sub>-68</sub> (21) [4]	8.1±1.7
A3122	0.0746(10)	cD	I	3	2	116	-	820 <sup>+158</sup> <sub>-100</sub> (23) [5]	-
Perseus	0.0184(3)	cD	II-III	0	2	88	32	1181 <sup>+89</sup> <sub>-73</sub> (108) [6]	-
0336+09	0.0349(3)	cD	-	-	-	-	-	-	-
A478	0.09(1)	cD	-	6	2	104	35	-	-
0422-09	0.039(1)	-	-	-	-	-	-	-	-
A496	0.0320(4)	cD	I	3	1	50	14	657 <sup>+104</sup> <sub>-72</sub> (32) [7]	13.5±2.7
3C129	0.022(1)	-	-	-	-	-	-	-	-
A576	0.0381(5)	Ic	III	2	1	61	22	914 <sup>+128</sup> <sub>-102</sub> (48) [4]	-
0745-19	0.1028(3)	cD	-	-	-	-	-	-	-
A754	0.0528(2)	cDs	I-II	3	2	92	29	1048 <sup>+173</sup> <sub>-133</sub> (38) [8]	21.4±4.3
Hydra-A	0.0522(3)	cD	I	-	-	-	-	-	-
A1060	0.0114(1)	C6	III	0	1	50	11	676 <sup>+61</sup> <sub>-49</sub> (78) [9]	-
A1367	0.0215(3)	F/I+I	II-III	1	2	117	18	813 <sup>+81</sup> <sub>-63</sub> (68) [10]	10.0±2.0
Virgo	0.0038(2)	-	III	-	-	-	10	573 <sup>+35</sup> <sub>-30</sub> (159) [11]	-
Coma	0.0232(3)	B	II	1	2	106	28	880 <sup>+45</sup> <sub>-39</sub> (226) [12]	13.5±2.7
Centaurus	0.0109(2)	-	I-II	0	0	33	13	586 <sup>+41</sup> <sub>-34</sub> (123) [13]	-
A3562	0.0491(3)	-	I	2	2	129	-	-	-
A3571	0.0391(3)	cD	I	2	2	126	-	1070 <sup>+114</sup> <sub>-86</sub> (60) [14]	-
A1795	0.0621(4)	cD	I	4	2	115	27	838 <sup>+110</sup> <sub>-80</sub> (41) [15]	14.5±2.9
A1837	0.0376(3)	cD	I-II	4	1	50	-	-	7.2±1.5
A2052	0.0348(3)	cD	I-II	3	0	41	-	576 <sup>+83</sup> <sub>-60</sub> (61) [7]	11.0±2.2
A2142	0.0899(11)	Bb	II	4	2	89	29	1241 <sup>+321</sup> <sub>-180</sub> (15) [16]	10.7±2.2
A2147	0.0356(10)	F/L+C	III	1	1	52	10	1148 <sup>+187</sup> <sub>-125</sub> (30) [17]	12.0±2.5
A2199	0.0309(3)	cD	I	1	2	88	18	807 <sup>+110</sup> <sub>-80</sub> (70) [18]	21.9±4.4
Ophiuchus	0.028(3)	cD	-	-	-	-	-	-	-
S1101	0.0556(9)	-	III	3	0	28	-	-	-
A2589	0.0421(5)	cD	I	3	0	40	16	602 <sup>+176</sup> <sub>-98</sub> (13) [16]	-
A4059	0.0478(3)	cD	I	2	1	66	-	845 <sup>+276</sup> <sub>-139</sub> (11) [19]	-

Table 5.2: Table of optical parameters from the literature. The redshifts are quoted with the error in the last significant figure in brackets. The velocity dispersions are quoted with 68% confidence errors. The number of galaxies used in the velocity dispersion is given in brackets and the reference is given in square brackets (see next page). The optical luminosity of the central galaxy is taken from Hoessel, Gunn & Thuan (1980).

- |  |   |
|--|---|
| [1] Melnick & Quintana 1981            | [11] Binggeli, Tammann & Sandage 1987                         |
| [2] Danese, De Zotti & di Tullio 1980  | [12] Kent & Gunn 1982   |
| [3] Beers <i>et al.</i> 1984           | [13] Lucey, Dickens & Currie 1986a                            |
| [4] Hintzen <i>et al.</i> 1982         | [14] Quintana & de Souza 1988                                 |
| [5] Materne & Hopp 1983                | [15] Hill <i>et al.</i> 1988                                  |
| [6] Kent & Sargent 1983                | [16] Hintzen & Scott 1979                                     |
| [7] Quintana <i>et al.</i> 1985        | [17] Tarengi <i>et al.</i> 1980                               |
| [8] Jones & Forman 1984                | [18] Gregory & Thompson 1984                                  |
| [9] Richter, Materne & Huchtmeier 1982 | [19] Parker <i>et al.</i> 1986 and Green, Godwin & Peach 1988 |
| [10] Moss & Dickens 1977               |   |

Table 5.2: contd. List of references for velocity dispersions quoted in the table

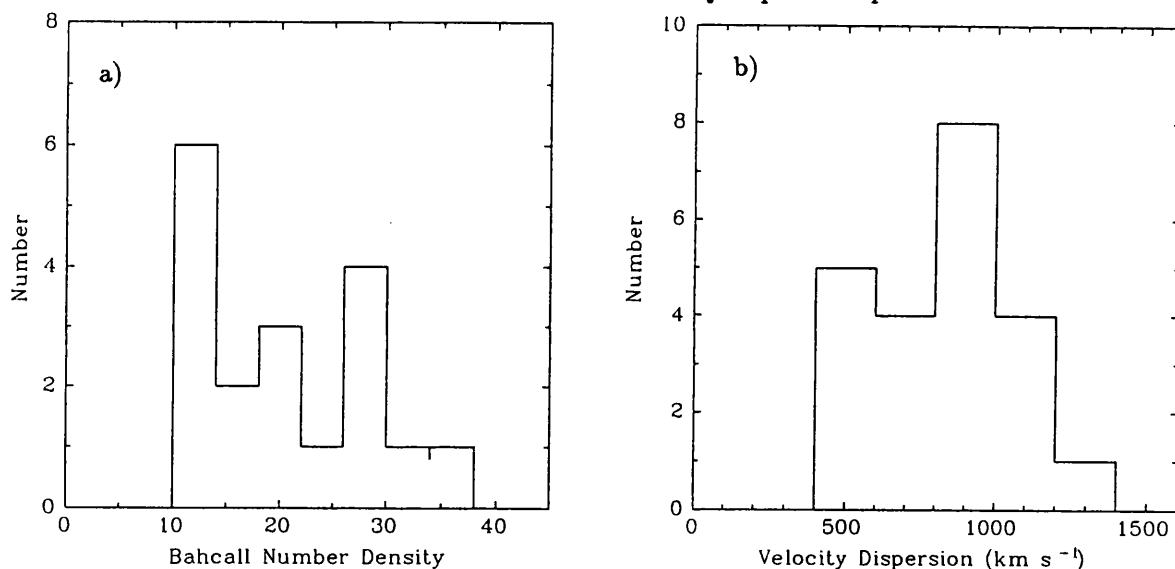


Figure 5.3: a. Histogram of Bahcall Number Densities and b. known Velocity Dispersions

determined due to the large radius used and the difficulty in estimating magnitudes from plates by eye. Bahcall also gives number densities, but based on galaxies within 0.5 Mpc of the cluster centre. These values are less prone to error, but still suffer from the difficulty in estimating magnitudes by eye. The distributions of velocity dispersion and Bahcall number density are shown in Figures 5.3a & b.

The optical luminosity of the brightest cluster member (BCM) has also been shown to be related to the X-ray luminosity and velocity dispersion (Hoessel, Gunn & Thuan 1980; Schombert 1986 & 1988). The relative populations of the three galactic types (ellipticals, lenticulars and spirals) have been determined for a number of clusters (Bahcall 1977b; Melnick & Sargent 1977; Dressler 1980a). These studies show the fraction of spirals is closely related to the X-ray luminosity (Bahcall 1977b) and the galaxy density (Melnick & Sargent 1977). However the quality of optical plate material prevents reliable galaxy classification for redshifts greater than 0.05.

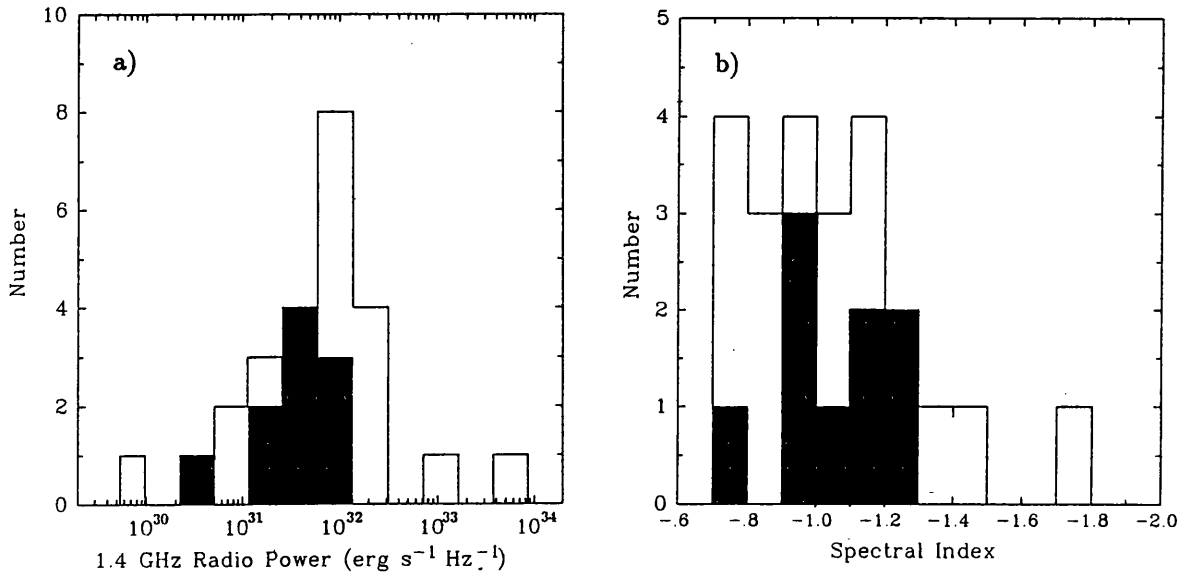


Figure 5.4: a. Histogram of 1.4 GHz radio powers. and b. Radio spectral indices.

The shaded area represents the offset and tailed sources.

### 5.3 Radio Results

A summary of the radio data for the sample is given in Table 5.3. The radio fluxes were taken primarily from the Dixon radio catalogue and from a survey of clusters by Owen *et al.* (1982), but fluxes from studies of individual clusters in the literature were used as well. For simplicity the radio power at 1.4 GHz was used without correction for the spectral slope. For clusters without an entry in the Dixon catalogue or in Owen *et al.* an upper limit of 0.2 Jy was assumed. The values of spectral slope were calculated from as many frequencies as possible. There are two principal types of powerful radio sources in clusters: extended central sources associated with a giant cD galaxy; and ‘head-tail’ sources which are associated with a cluster galaxy passing through the ICM (see Figure 1.2). The type of source is noted in Table 5.3.

The distributions of radio power at 1.4 GHz and spectral index are given in Figures 5.4a & b. The tailed sources have a narrower range of power and index than the central sources. The radio powers appear to have a distribution quite different from that of the X-ray luminosities. The spectral indices show ‘steep’ spectra, with a mean of -1.0–1.1 as seen in M<sup>c</sup>Hardy (1979).

### 5.4 Correlation Analysis

The analysis of large inhomogeneous datasets is not a simple procedure. The determination of the significance of correlations between parameters can be seriously affected by selection effects and indirect correlations with other parameters. This section contains an outline of the statistical

Cluster	Redshift	1.4 GHz Flux (Jy)	1.4 GHz Spectral Power ( $\text{erg s}^{-1} \text{Hz}^{-1}$ )	Spectral Index	Structure	Reference
A119	0.0440(3)	$1.50 \& 1.13 \pm 0.02$	$1.25 \& 0.94 \pm 0.02 \times 10^{32}$	-1.27	Two Tailed Sources	O'Dea & Owen 1985a
A133	0.0604(3)	$0.25 \pm 0.05$	$3.93 \pm 0.79 \times 10^{31}$	-1.49	Central Galaxy	Dixon
A193	0.0482(3)	<0.1	$< 1.0 \times 10^{31}$	-	-	Owen <i>et al.</i> 1982
A262	0.0161(3)	$0.081 \pm 0.004$	$9.04 \pm 0.45 \times 10^{29}$	-	Central Galaxy	Fanti <i>et al.</i> 1982
A376	0.0489(5)	<0.1	$< 1.0 \times 10^{31}$	-	-	Owen <i>et al.</i> 1982
AWM7	0.0172(7)	$0.25 \pm 0.05$	$3.19 \pm 0.64 \times 10^{30}$	-1.22	20' offset from Centre	Dixon
A400	0.0232(3)	$5.59 \pm 0.18$	$1.30 \pm 0.04 \times 10^{32}$	-0.73	Central Galaxy	Owen <i>et al.</i> 1982
A3122	0.0746(10)	(0.82 2.7 GHz)	( $1.97 \times 10^{32}$ )	-	Central Galaxy	Dixon
Perseus	0.0184(3)	$13.0 \pm 0.4$	$1.90 \pm 0.06 \times 10^{32}$	-0.73	Central Galaxy	Owen <i>et al.</i> 1982
0336+09	0.0349(3)	$0.37 \pm 0.02$	$4.96 \pm 0.27 \times 10^{31}$	-1.13	Tailed Source	O'Dea & Owen 1985a
A478	0.09(1)	$0.033 \pm 0.004$	$1.15 \pm 0.19 \times 10^{31}$	-	Central Galaxy	Schnopper <i>et al.</i> 1982
0422-09	0.039(1)	<0.2	$< 1.3 \times 10^{31}$	-	-	-
A496	0.0320(4)	$2.56 \pm 0.19$	$1.13 \pm 0.08 \times 10^{32}$	-1.19	Tailed Source	Owen <i>et al.</i> 1982
3C129	0.022(1)	$8.06 \pm 0.10$	$1.68 \pm 0.02 \times 10^{32}$	-0.74	Central Galaxy	Dixon
A576	0.0381(5)	$0.24 \pm 0.01$	$1.50 \pm 0.06 \times 10^{31}$	-0.98	Tailed Source	Fanti <i>et al.</i> 1982
0745-19	0.1028(3)	$2.4 \pm 0.1$	$1.1 \pm 0.1 \times 10^{33}$	-1.02	Central Galaxy	Dixon
A754	0.0528(2)	$0.44 \pm 0.04$	$5.28 \pm 0.48 \times 10^{31}$	-1.02	Tailed Source	Harris <i>et al.</i> 1984
Hydra-A	0.0522(3)	$45.6 \pm 1.4$	$5.35 \pm 0.16 \times 10^{33}$	-0.93	Central Galaxy	Owen <i>et al.</i> 1982
A1060	0.0114(1)	(0.18 4.85 GHz)	( $1.10 \times 10^{30}$ )	-	20' offset from centre	Andernach <i>et al.</i> 1981
A1367	0.0215(3)	$5.45 \pm 0.17$	$1.09 \pm 0.03 \times 10^{32}$	-0.75	Tailed Source	Elvis <i>et al.</i> 1981
Virgo	0.0038(2)	$\sim 100$	$\sim 2.7 \times 10^{31}$	-0.9	Central Galaxy	Schreier <i>et al.</i> 1982
Coma	0.0232(3)	$3.07 \pm 0.17$	$7.12 \pm 0.39 \times 10^{31}$	-1.37	Central Galaxy	Owen <i>et al.</i> 1982
Centaurus	0.0109(2)	$4.1 \pm 0.1$	$2.1 \pm 0.1 \times 10^{31}$	-0.82	Central Galaxy	Dixon
A3562	0.0491(3)	<0.2	$< 2.1 \times 10^{31}$	-	-	-
A3571	0.0391(3)	<0.2	$< 1.3 \times 10^{31}$	-	-	-
A1795	0.0621(4)	$1.03 \pm 0.07$	$1.68 \pm 0.11 \times 10^{32}$	-0.82	Central Galaxy	Owen <i>et al.</i> 1982
A1837	0.0376(3)	<0.1	$< 6.1 \times 10^{30}$	-	-	Owen <i>et al.</i> 1982
A2052	0.0348(3)	$5.39 \pm 0.17$	$2.81 \pm 0.09 \times 10^{32}$	-1.04	Central Galaxy	Owen <i>et al.</i> 1982
A2142	0.0899(11)	$0.09 \pm 0.02$	$3.13 \pm 0.70 \times 10^{31}$	-0.94	Tailed Source	O'Dea & Owen 1985a
A2147	0.0356(10)	$0.86 \pm 0.04$	$4.69 \pm 0.22 \times 10^{31}$	-0.95	11' offset from centre	Owen <i>et al.</i> 1982
A2199	0.0309(3)	$3.48 \pm 0.17$	$1.43 \pm 0.07 \times 10^{32}$	-1.16	Central Galaxy	Owen <i>et al.</i> 1982
Ophiuchus	0.028(3)	(2.8 0.4 GHz)	( $9.46 \times 10^{31}$ )	(-1.73)	Central Galaxy	Dixon
S1101	0.0556(9)	<0.2	$< 2.7 \times 10^{31}$	-	-	-
A2589	0.0421(5)	$0.15 \pm 0.10$	$1.15 \pm 0.77 \times 10^{31}$	-	10' offset from centre	Owen <i>et al.</i> 1982
A4059	0.0478(3)	$1.09 \pm 0.05$	$1.07 \pm 0.05 \times 10^{32}$	-1.17	Central Galaxy	Dixon

Table 5.3: Table of radio parameters from the literature. The redshifts are quoted with the error in the last significant figure in brackets.

methods used in analysing the sample data.

### 5.4.1 Least Squares Fits

The most commonly used method to obtain the relation between two parameters is the least squares method. For data where X is an independent variable (*i.e.* it is precisely determined) and Y is a dependent variable, a line of the form  $Y=AX+B$  can be determined by minimising the deviations,  $\Delta$ , in Y (where  $\Delta = \sum_{\text{npts}} (Y_i - AX_i - B)^2$ ). However for the sample data all variables have an appreciable error, so the assumption that a variable is independent is incorrect. For any non-perfect correlation the result for a least squares fit with X on Y is different from that with Y on X which may cause some confusion. The ratio of the two gradients obtained for these two fits gives a correlation coefficient,  $r$ . For a perfect correlation  $r$  equals 1 and for a random distribution  $r$  equals 0. In this analysis all correlations have been determined for *both* X on Y and Y on X. The two lines are, where possible, shown on the plots of the data. For data with a range of associated errors (*i.e.* some points are better determined than others) a weighting factor can be included which is inversely proportional to the square of the error.

For all the correlations the logarithmic values of the parameters were used in the fitting, so relationships were determined in the form  $Y = 10^B X^A$ .

### 5.4.2 Rank and Partial Rank Correlation Coefficients

As well as the correlation coefficient determined by the least squares method, it is possible to determine a non-parametric Spearman rank correlation coefficient,  $r_s$ . The  $r_s$  coefficient is related to the relative ordering of the data and so is less affected by outlying points.

Any correlation has a finite probability of arising by chance. If the correlation is random the statistic

$$t = r_s \sqrt{\frac{N-2}{1-r_s^2}} \quad (5.1)$$

will follow "Students" t distribution with N-2 degrees of freedom. From statistical tables (*e.g.* Bevington 1969) the probability of any  $r_s$  occurring by chance can be found.

A correlation between two parameters may result from the correlation of both with a third parameter, *i.e.* the correlation between A and B, is due to separate correlations between A and C, and B and C. To test for this condition partial rank correlation coefficients should be calculated. If

$r_{AB}$ ,  $r_{BC}$  and  $r_{AC}$  are the Spearman rank correlation coefficients for the three correlations, then the partial rank coefficient is

$$r_{AB,C} = \frac{r_{AB} - r_{AC}r_{BC}}{[(1 - r_{AC}^2)(1 - r_{BC}^2)]^{\frac{1}{2}}} \quad (5.2)$$

The D-statistic, which is defined as

$$D_{AB,C} = \frac{1}{2}(N - 4)^{\frac{1}{2}} \ln\left(\frac{1 + r_{AB,C}}{1 - r_{AB,C}}\right) \quad (5.3)$$

is randomly distributed, with a mean of zero and a variance of one, if the correlation between A and B is due only to the correlations between A and C and B and C.

## 5.5 X-ray to X-ray Correlations

From the spectral and imaging X-ray data a correlation matrix was calculated using a weighted least squares fit (see Table 5.4). The correction for the bolometric luminosity made a small difference to the derived correlations between the luminosity (2–10 keV and bolometric) and the other parameters. As the bolometric luminosity reflects the total X-ray luminosity, it was used in all further correlations. The probability that any of the correlations result from data drawn from a random distribution is less than 1% (*i.e.* they are significant at a confidence level of over 99%).

The strongest correlations are between luminosity and gas mass within 0.5 Mpc, and between luminosity and temperature. The mass of gas is the integrated gas density over the volume of the cluster. The X-ray luminosity is the integrated emissivity (proportional to the density squared). Thus the luminosity and gas mass should be related to the power  $\sim 2$ , as is seen. The temperature of the gas in the cluster is proportional to the mass of the cluster. So if the ratio of the gas mass to total mass is constant (or near constant) then the X-ray luminosity and temperature will be well correlated through this ratio. Any scatter in the gas mass to total mass ratio will be apparent in the temperature-gas mass relation, as shown in Figure 5.7. The luminosity-temperature correlation is discussed in more detail in Section 6.1.

These correlations should also be checked for the possibility that they are a result of the flux limit of the sample (*i.e.* they are due to a secondary correlation with redshift). Calculating the partial correlation coefficients for the luminosity, gas mass and redshift triad and the luminosity, temperature and redshift triad gives  $r_{AB,C}$  of 0.909 (for 12 points) and 0.772 (for 35 points). The resulting values of the D-statistic are 4.30 and 5.71. Thus the possibility of a purely secondary correlation can be rejected above the 4 and 5 sigma levels.

	$L_{2-10}$	$L_{\text{Bol}}$	T	z	$M_{0.5\text{Mpc}}$
$L_{2-10}$		$L_{2-10}$ vs. $L_{\text{Bol}}$ $A=1.07\pm 0.02$ $B=-3.51\pm 0.08$ $r=0.998$ $n=35$	$L_{2-10}$ vs. T $A=2.78\pm 0.05$ $B=42.54\pm 0.03$ $r=0.899$ $n=35$	$L_{2-10}$ vs. z $A=1.84\pm 0.04$ $B=47.19\pm 0.05$ $r=0.826$ $n=35$	$L_{2-10}$ vs. $M_{0.5\text{Mpc}}$ $A=2.59\pm 0.07$ $B=10.50\pm 0.09$ $r=0.981$ $n=12$
$L_{\text{Bol}}$	$L_{\text{Bol}}$ vs. $L_{2-10}$ $A=0.94\pm 0.03$ $B=3.02\pm 0.15$ $r=0.998$ $n=35$		$L_{\text{Bol}}$ vs. T $A=2.62\pm 0.10$ $B=43.05\pm 0.08$ $r=0.862$ $n=35$	$L_{\text{Bol}}$ vs. z $A=1.38\pm 0.06$ $B=47.04\pm 0.08$ $r=0.747$ $n=35$	$L_{\text{Bol}}$ vs. $M_{0.5\text{Mpc}}$ $A=2.45\pm 0.16$ $B=12.69\pm 0.18$ $r=0.967$ $n=12$
T	T vs. $L_{2-10}$ $A=0.28\pm 0.05$ $B=-11.73\pm 0.20$ $r=0.868$ $n=35$	T vs. $L_{\text{Bol}}$ $A=0.30\pm 0.05$ $B=-12.73\pm 0.23$ $r=0.847$ $n=35$		T vs. z $A=0.21\pm 0.10$ $B=1.04\pm 0.15$ $r=0.298$ $n=35$	T vs. $M_{0.5\text{Mpc}}$ $A=0.62\pm 0.24$ $B=-7.37\pm 0.28$ $r=0.607$ $n=12$
z	z vs. $L_{2-10}$ $A=0.29\pm 0.01$ $B=-14.23\pm 0.01$ $r=0.822$ $n=35$	z vs. $L_{\text{Bol}}$ $A=0.32\pm 0.01$ $B=-15.68\pm 0.02$ $r=0.833$ $n=35$	z vs. T $A=0.72\pm 0.01$ $B=-1.79\pm 0.01$ $r=0.644$ $n=35$		z vs. $M_{0.5\text{Mpc}}$ $A=0.62\pm 0.03$ $B=-9.42\pm 0.03$ $r=0.589$ $n=12$
$M_{0.5\text{Mpc}}$	$M_{0.5\text{Mpc}}$ vs. $L_{2-10}$ $A=0.38\pm 0.03$ $B=-3.77\pm 0.17$ $r=0.957$ $n=12$	$M_{0.5\text{Mpc}}$ vs. $L_{\text{Bol}}$ $A=0.41\pm 0.05$ $B=-5.26\pm 0.19$ $r=0.960$ $n=12$	$M_{0.5\text{Mpc}}$ vs. T $A=0.74\pm 0.10$ $B=12.66\pm 0.09$ $r=0.667$ $n=12$	$M_{0.5\text{Mpc}}$ vs. z $A=0.55\pm 0.08$ $B=13.98\pm 0.11$ $r=0.65$ $n=12$	

Table 5.4: Table with results for least squares fits to X-ray data in the form  $Y = 10^B X^A$ . The  $3\sigma$  errors in the coefficients are quoted.

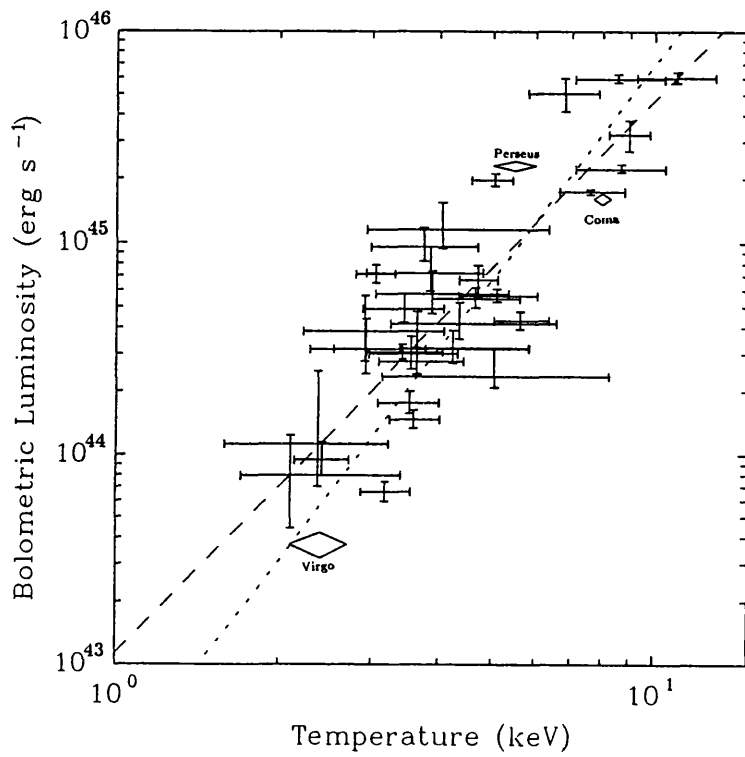


Figure 5.5: Bolometric luminosity plotted against temperature

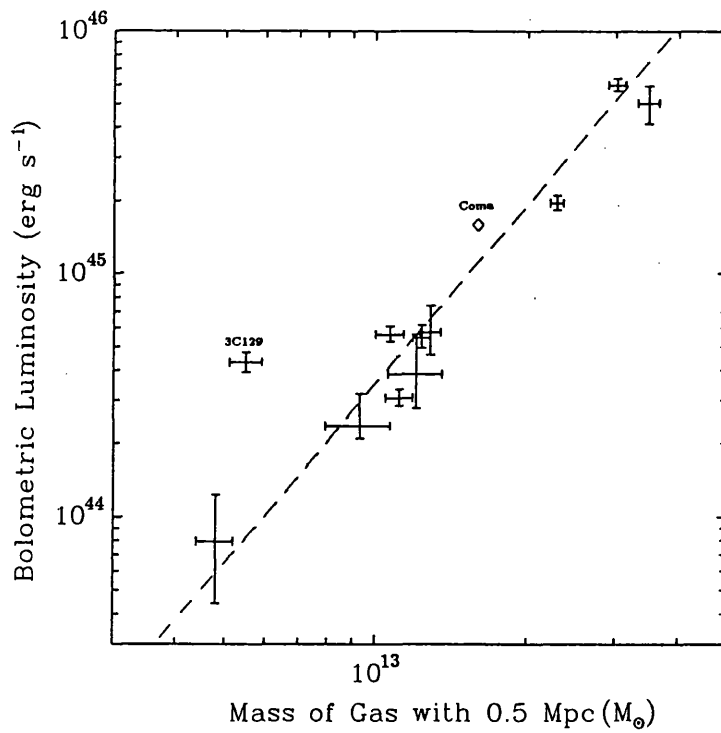


Figure 5.6: Bolometric luminosity plotted against gas mass within 0.5 Mpc obtained from the *EINSTEIN* IPC. The value for the gas mass for 3C129 has been excluded from the correlation analysis.

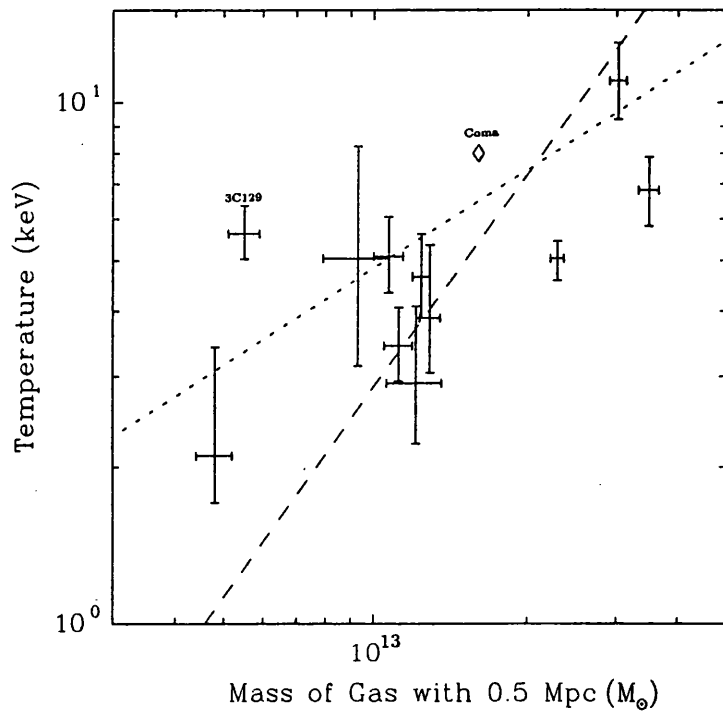


Figure 5.7: Temperature plotted against gas mass within 0.5 Mpc obtained from the *EINSTEIN* IPC. The value for the gas mass for 3C129 has been excluded from the correlation analysis.

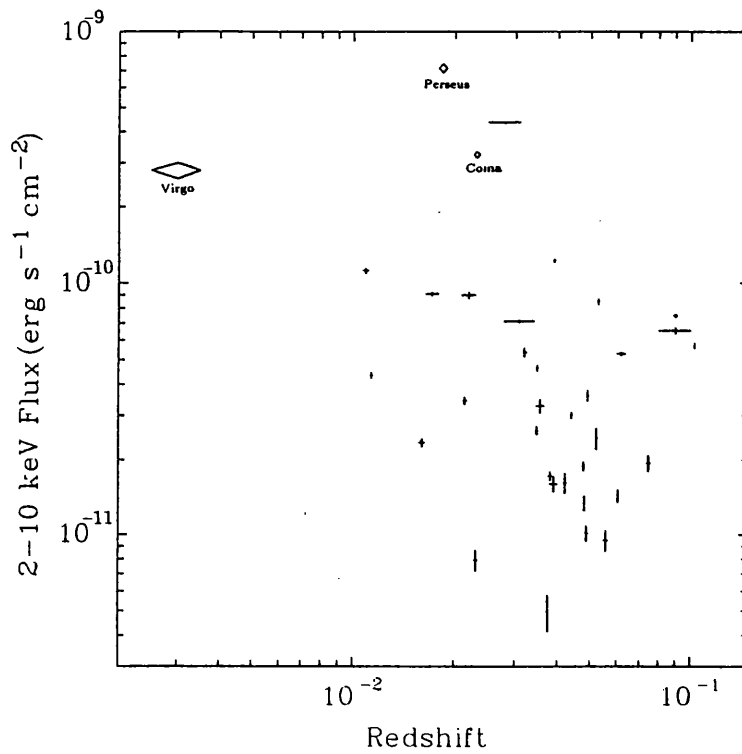


Figure 5.8: 2-10 keV flux plotted against redshift

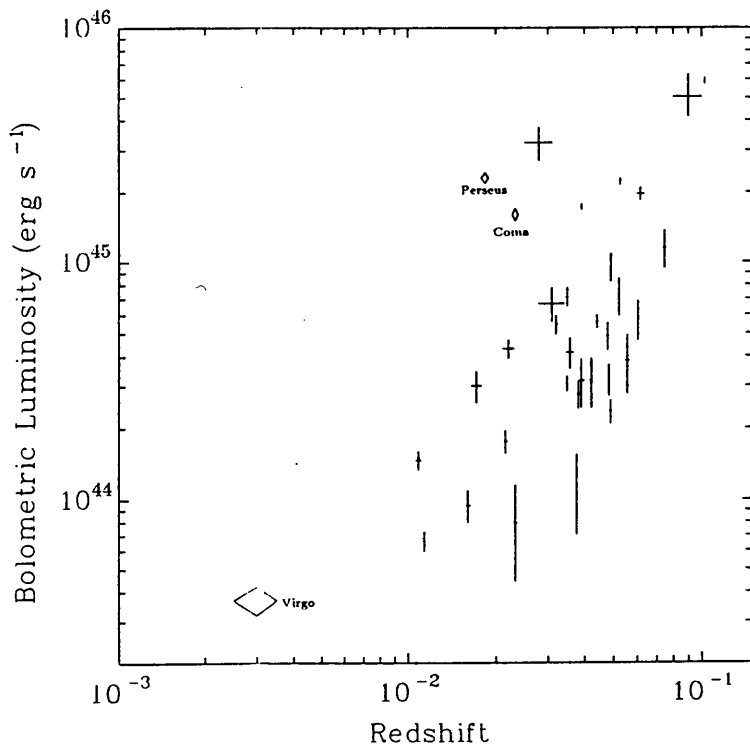


Figure 5.9: Bolometric luminosity plotted against redshift

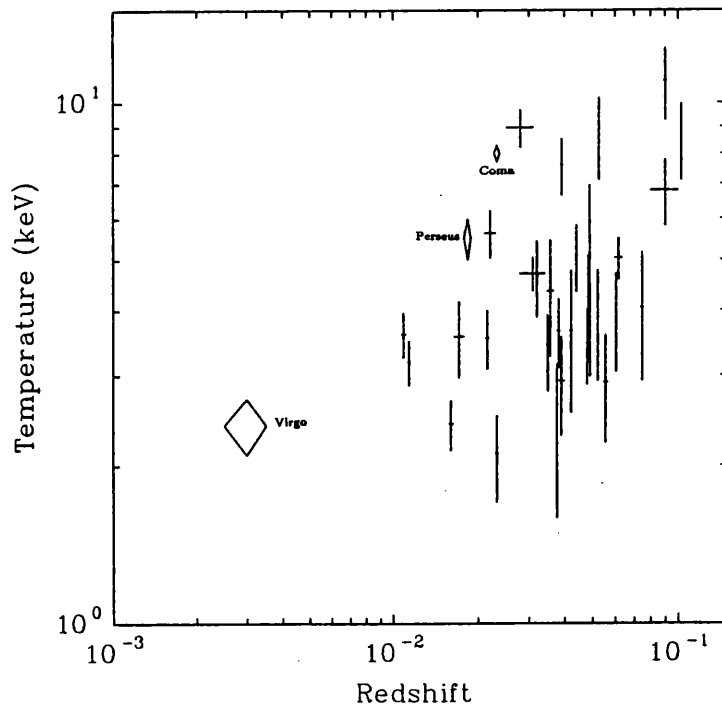


Figure 5.10: Temperature plotted against redshift

## 5.6 X-ray to Optical Correlations

The sample contains clusters of every common optical type and morphology. Clusters have been optically classified in a number of ways. The two most common classifications are the Bautz-Morgan (BM) type, which is a measure of the relative luminosity of the three brightest galaxies, and the Rood-Sastry (RS) type, which depends on the overall structure of the cluster. Figures 5.11–5.16 show bolometric luminosity, temperature and mass flow rate plotted against BM and RS types. The Abell richness class,  $R$ , (related to the total number of galaxies) is indicated in these Figures. Tables 5.5 give the averages of the X-ray parameters for each BM and RS type. There is a clear tendency for BM type Is (clusters with a very dominant galaxy) and RS cDs (clusters with a central dominant galaxy) to have large cooling flows. The average temperatures within individual types show no great differences apart from RS type Is and BM type IIIs being cooler than the average. Abell richness class 2 clusters are hotter than richness class 0 or 1 within each type (*e.g.* for cD clusters  $T_{\text{ave}} = 5.1 \pm 1.5$  for  $R=2$  and  $T_{\text{ave}} = 3.9 \pm 0.5$  for  $R=0$  & 1). However the limited numbers in the sample prevents a detailed analysis of each RS or BM type by richness class to be made as most classes only have 3 or 4 members.

Tables 5.6 and 5.7 give the least squares fit results for bolometric luminosity and temperature verses velocity dispersion, Bahcall number density, optical luminosity of the central galaxy and the percentage of spirals. The tables include the Spearman rank correlation coefficient plus the partial correlation coefficient and D-statistic for an indirect correlation through redshift. Figures 5.17–5.24 show plots of these correlations with the two least squares lines.

All the individual correlations are significant at the 99% confidence level and are not secondary correlations with redshift (*i.e.* the D-statistic is  $> 3\sigma$ ). The most striking correlation is between the bolometric luminosity and the percentage of spirals, which is discussed in Section 6.5. The partial correlation coefficients indicate that the percentage of spirals to temperature correlation is secondary through the correlation with bolometric luminosity.

The correlations found here agree with those found in other studies. Quintana & Melnick (1982) give  $L_{2-10 \text{ keV}} \propto \sigma^{3.81 \pm 0.58}$  for 25 clusters observed by HEAO-1. Abramopoulos & Ku (1983) quote  $L_{0.5-4.0 \text{ keV}} \propto \sigma^{3.16 \pm 0.63}$  and  $L_{0.5-4.0 \text{ keV}} \propto N_{\text{B}}^{2.28 \pm 0.62}$  for *EINSTEIN* IPC and HRI observations. The only X-ray to optical correlation which has not been noted in the literature is that of temperature to central galaxy luminosity. For clusters with a single dominant galaxy (*e.g.* cD clusters) this relation is strong. However for RS type B clusters which contain 2 or more bright galaxies (A2142 and Coma in this sample) the relation does not hold (see Figure 5.23). Therefore A2142 and Coma were not included in the correlation analysis. This correlation has implications on attempts to determine  $q_0$  using the brightest cluster members (BCMs) as standard candles (*e.g.* Hoessel, Gunn & Thuan 1980).

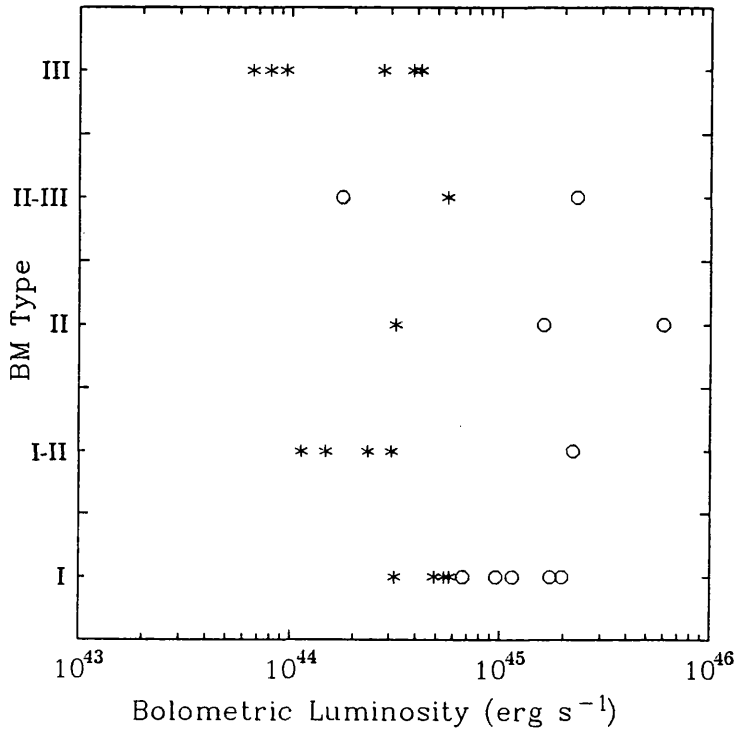


Figure 5.11: Bolometric luminosity plotted against Bautz-Morgan type. Circles represent richness class 2 clusters, asterisks represent richness class 1 or 0 clusters and crosses represent clusters with no richness class.

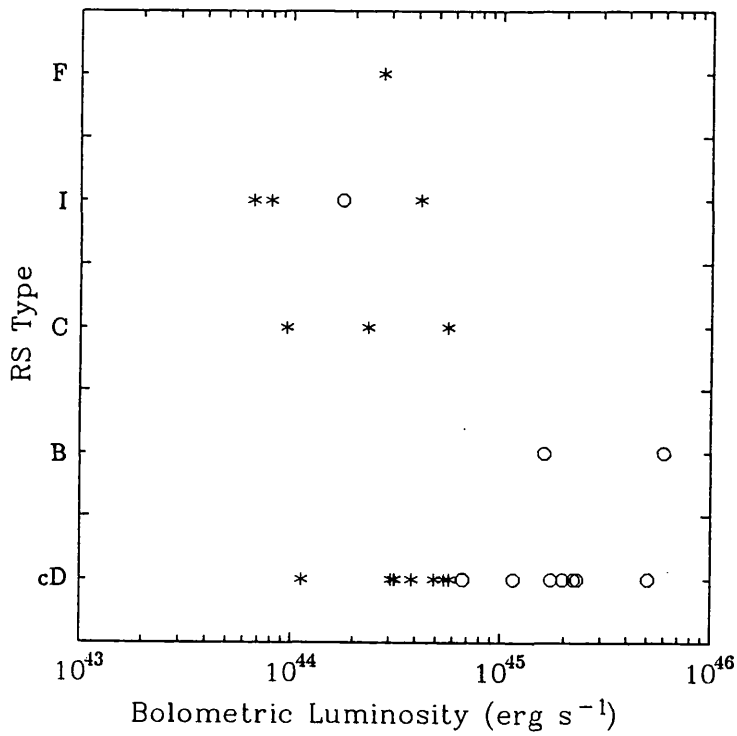


Figure 5.12: Bolometric luminosity plotted against Rood-Sastry type. Marked as Figure 5.11

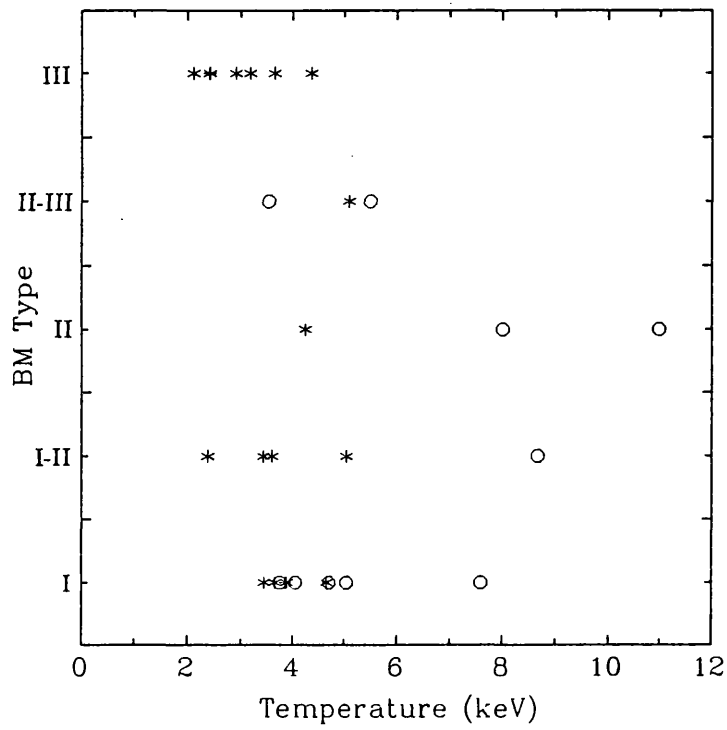


Figure 5.13: Temperature plotted against Bautz-Morgan type. Marked as Figure 5.11

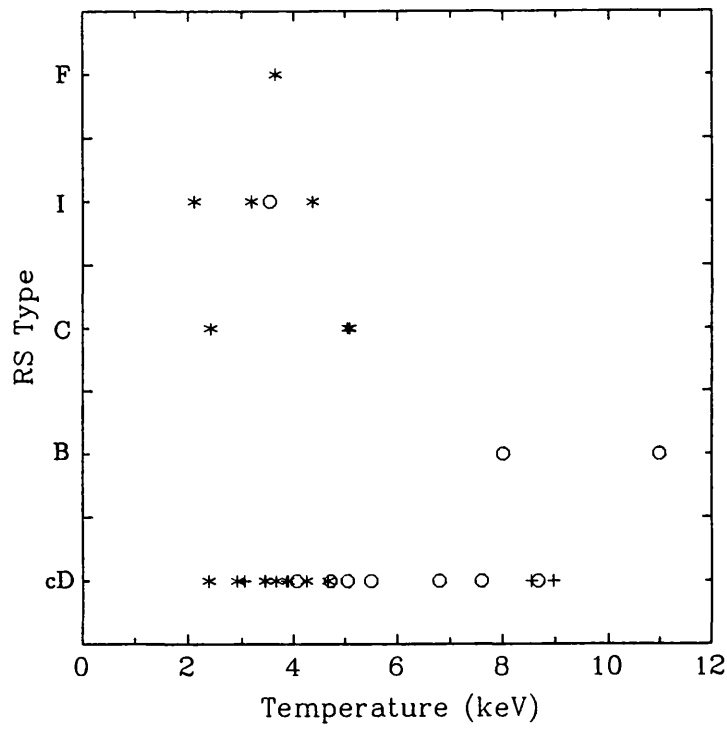


Figure 5.14: Temperature plotted against Rood-Sastry type. Marked as Figure 5.11

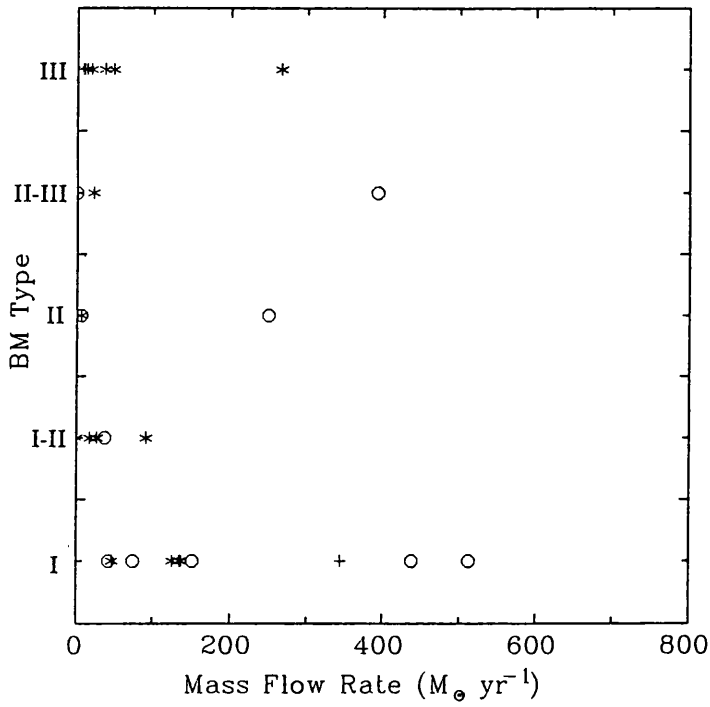


Figure 5.15: Mass flow rate plotted against Bautz-Morgan type. Marked as Figure 5.11

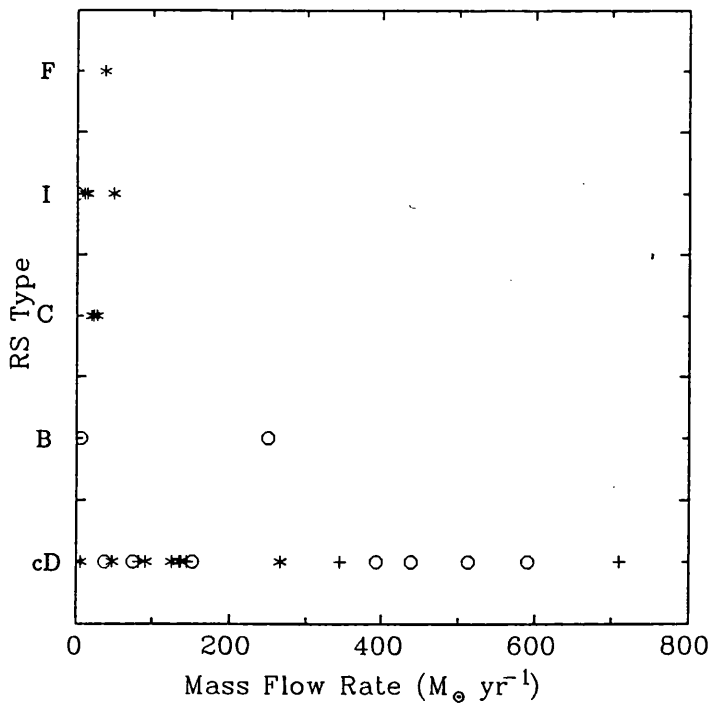


Figure 5.16: Mass flow rate plotted against Rood-Sastry type. Marked as Figure 5.11

B-M Type	Number in Sample	Temperature (keV)	Bolometric Luminosity ( $\text{erg s}^{-1}$ )	Mass Flow Rate ( $M_{\odot} \text{ yr}^{-1}$ )
I	10	Ave= $4.5 \pm 1.2$	Ave= $9.1 \pm 5.5 \times 10^{44}$	Ave= $194 \pm 166$
I-II	5	Ave= $4.6 \pm 2.5$	Ave= $9.2 \pm 5.4 \times 10^{44}$	Ave= $35 \pm 31$
II	3	Ave= $7.74 \pm 3.78$	Ave= $8.5 \pm 11.0 \times 10^{44}$	Ave= $83 \pm 139$
II-III	4	Ave= $4.1 \pm 1.6$	Ave= $7.8 \pm 10.4 \times 10^{44}$	Ave= $69 \pm 117$
III	6	Ave= $3.2 \pm 0.8$	Ave= $1.5 \pm 1.5 \times 10^{44}$	Ave= $60 \pm 95$

R-S Type	Number in Sample	Temperature (keV)	Bolometric Luminosity ( $\text{erg s}^{-1}$ )	Mass Flow Rate ( $M_{\odot} \text{ yr}^{-1}$ )
cD	18	Ave= $5.1 \pm 2.1$	Ave= $1.6 \pm 1.4 \times 10^{45}$	Ave= $209 \pm 208$
B	2	Ave= $9.5 \pm 1.5$	Ave= $3.8 \pm 2.2 \times 10^{45}$	Ave= $125 \pm 125$
C	4	Ave= $3.9 \pm 1.3$	Ave= $2.4 \pm 2.2 \times 10^{44}$	Ave= $20 \pm 7$
I	2	Ave= $2.9 \pm 0.7$	Ave= $1.8 \pm 1.4 \times 10^{44}$	Ave= $25 \pm 17$
F	2	Ave= $4.0 \pm 0.4$	Ave= $3.0 \pm 1.7 \times 10^{44}$	Ave= $30 \pm 30$

Table 5.5: Table of averages of X-ray properties for particular BM and RS types. The errors quoted are  $1\sigma$ .

$N_B$	$\sigma$	$\%_{\text{spiral}}$	$L_{\text{opt}}$
$L_{\text{Bol}}$ vs. $N_B$	$L_{\text{Bol}}$ vs. $\sigma$	$L_{\text{Bol}}$ vs. $\%_{\text{spiral}}$	$L_{\text{Bol}}$ vs. $L_{\text{opt}}$
A=3.16±0.15 B=40.75±0.20 r=0.903 n=17	A=3.99±0.19 B=33.24±0.55 r=0.863 n=21	A=-2.16±0.11 B=47.67±0.14 r=-0.957 n=16	A=2.53±0.22 B=14.09±0.29 r=0.870 n=12
$N_B$ vs. $L_{\text{Bol}}$	$\sigma$ vs. $L_{\text{Bol}}$	$\%_{\text{spiral}}$ vs. $L_{\text{Bol}}$	$L_{\text{opt}}$ vs. $L_{\text{Bol}}$
A=0.25±0.14 B=-9.53±0.65 r=0.859 n=17	A=0.15±0.05 B=-3.01±0.17 r=0.829 n=21	A=-0.35±0.12 B=17.06±0.50 r=-0.960 n=16	A=0.27±0.17 B=-1.13±0.78 r=0.822 n=12
$r_s = 0.846$	$r_s = 0.760$	$r_s = -0.982$	$r_s = 0.828$
$r_{L_{\text{Bol}}N_B,z} = 0.707$	$r_{L_{\text{Bol}}\sigma,z} = 0.683$	$r_{L_{\text{Bol}}\%_{\text{spiral}},z} = -0.976$	$r_{L_{\text{Bol}}L_{\text{opt}},z} = 0.810$
$D_{L_{\text{Bol}}N_B,z} = 3.30$	$D_{L_{\text{Bol}}\sigma,z} = 3.44$	$D_{L_{\text{Bol}}\%_{\text{spiral}},z} = -7.57$	$D_{L_{\text{Bol}}L_{\text{opt}},z} = 3.19$

Table 5.6: Table with results from least squares fits for bolometric luminosity and optical parameters in the form  $Y = 10^B X^A$ .  $L_{\text{bol}}$  is in  $\text{erg s}^{-1}$ ,  $\sigma$  is in  $\text{kms}^{-1}$ ,  $\%_{\text{spiral}}$  is in percent and  $L_{\text{opt}}$  is solar units ( $L_{\odot}$ ). The errors are  $3\sigma$  variation. The Spearman rank correlation coefficients, partial correlation coefficients with redshift and D statistics with redshift are included.

$N_B$	$\sigma$	$\%_{\text{spiral}}$	$L_{\text{opt}}$
T vs. $N_B$	T vs. $\sigma$	T vs. $\%_{\text{spiral}}$	T vs. $L_{\text{opt}}$
A=0.95±0.18 B=-0.52±0.24 r=0.876 n=17	A=1.33±0.27 B=-3.14±0.77 r=0.762 n=21	A=-0.67±0.12 B=1.60±0.16 r=-0.900 n=16	A=0.62±0.36 B=-6.23±0.42 r=0.724 n=12
$N_B$ vs. T	$\sigma$ vs. T	$\%_{\text{spiral}}$ vs. T	$L_{\text{opt}}$ vs. T
A=0.78±0.47 B=0.73±0.31 r=0.793 n=17	A=0.48±0.12 B=2.58±0.08 r=0.774 n=21	A=-0.94±0.38 B=2.08±0.21 r=-0.800 n=16	A=0.80±0.45 B=10.62±0.29 r=0.876 n=12
$r_s = 0.823$	$r_s = 0.760$	$r_s = -0.931$	$r_s = 0.839$
$r_{TN_B,z} = 0.663$	$r_{T\sigma,z} = 0.679$	$r_{T\%_{\text{spiral}},z} = -0.901$	$r_{TL_{\text{opt}},z} = 0.808$
$D_{TN_B,z} = 2.99$	$D_{T\sigma,z} = 3.41$	$D_{T\%_{\text{spiral}},z} = -5.12$	$D_{TL_{\text{opt}},z} = 3.17$

Table 5.7: Table with results from least squares fits for temperature and optical parameters in the form  $Y = 10^B X^A$ . T is in keV and the other parameters are as in Table 5.6.

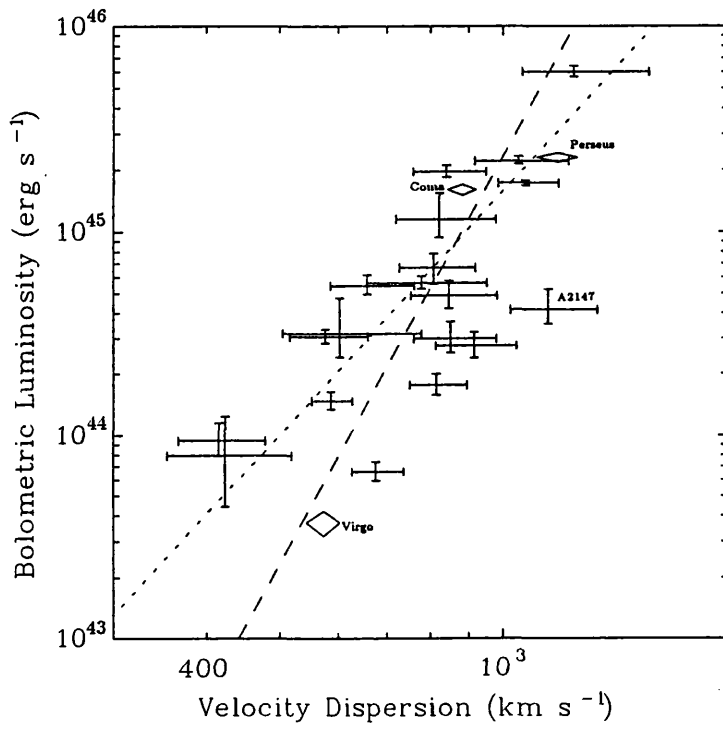


Figure 5.17: Bolometric luminosity plotted against velocity dispersion. The velocity dispersion for A2147 is overestimated (see Section 6.3.2) so is not included in the correlation analysis.

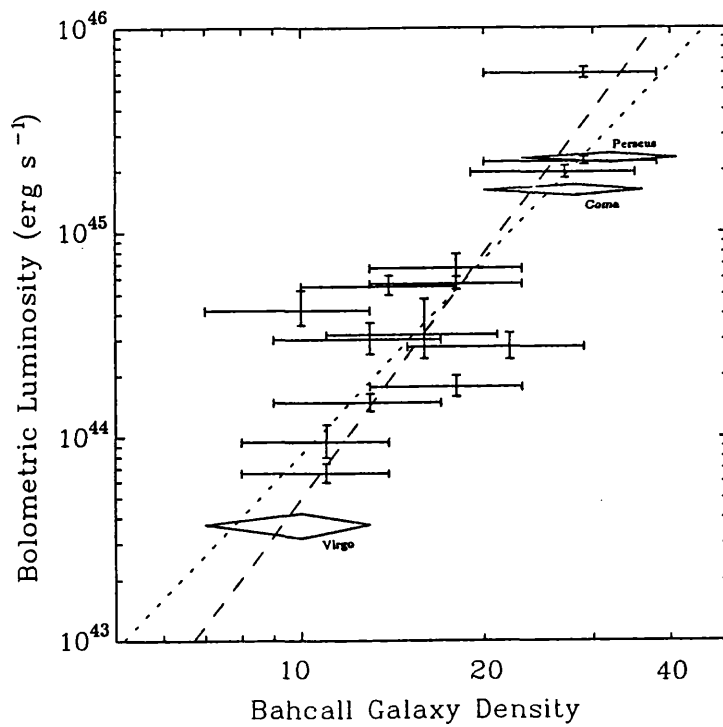


Figure 5.18: Bolometric luminosity plotted against Bahcall number density

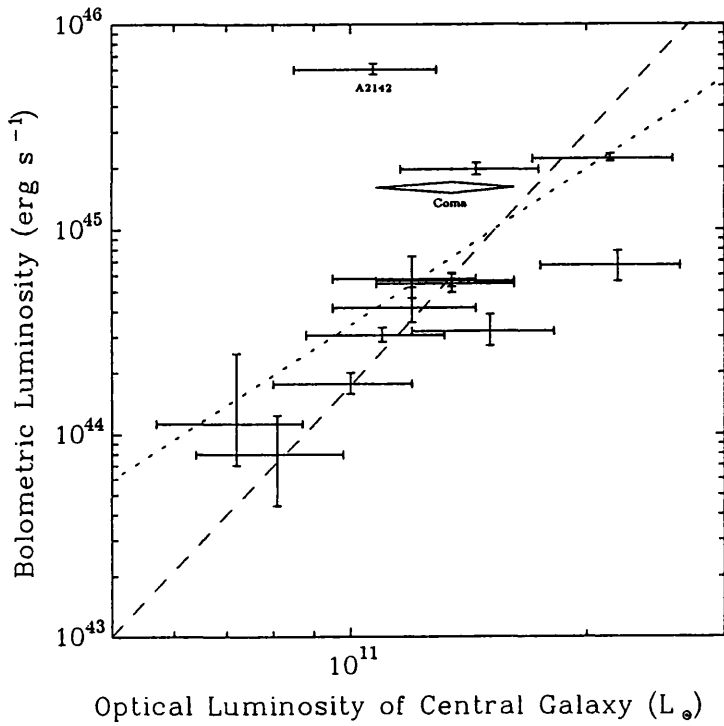


Figure 5.19: Bolometric luminosity plotted against optical luminosity of the brightest galaxy from Hoessel, Gunn & Thuan (1980). A2142 and Coma are not included in the correlation analysis.

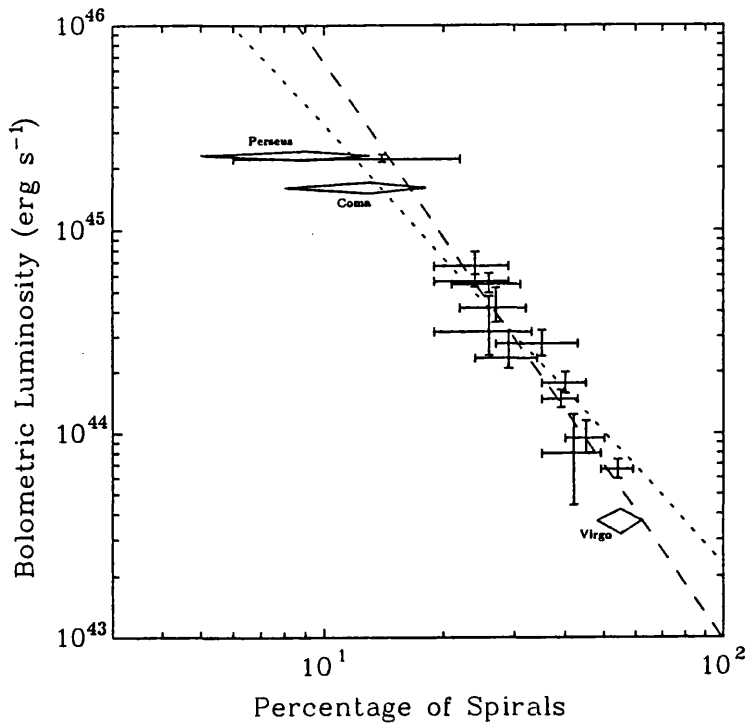


Figure 5.20: Bolometric luminosity plotted against percentage of spiral galaxies

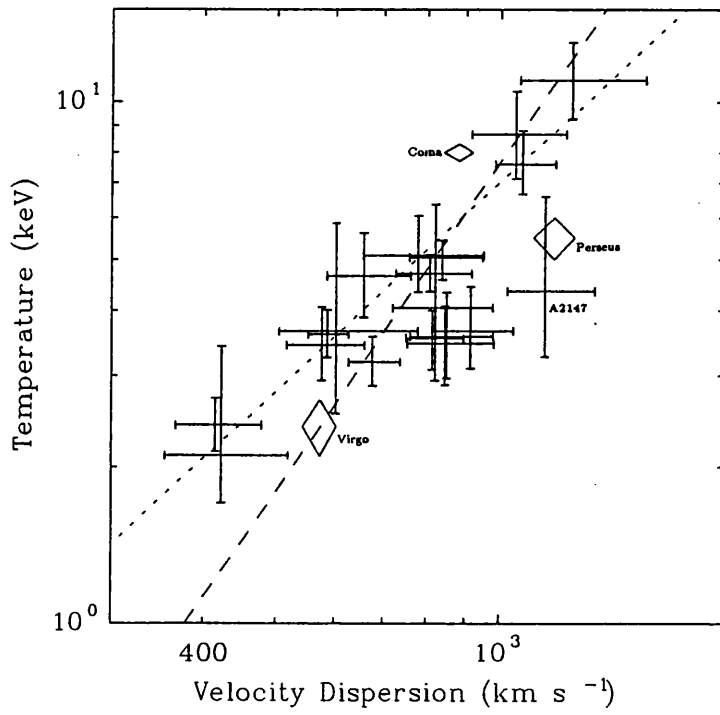


Figure 5.21: Temperature plotted against velocity dispersion. The velocity dispersion for A2147 is not included in the correlation analysis.

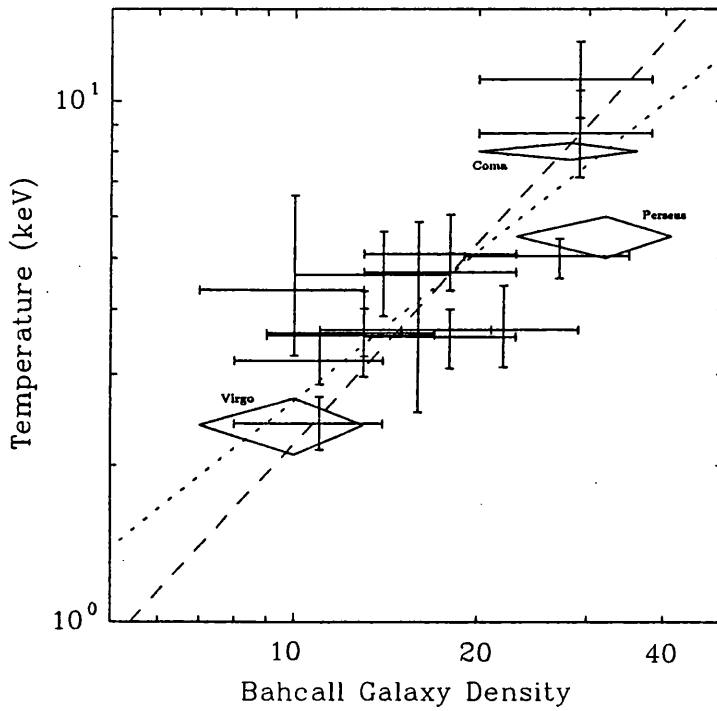


Figure 5.22: Temperature plotted against Bahcall number density

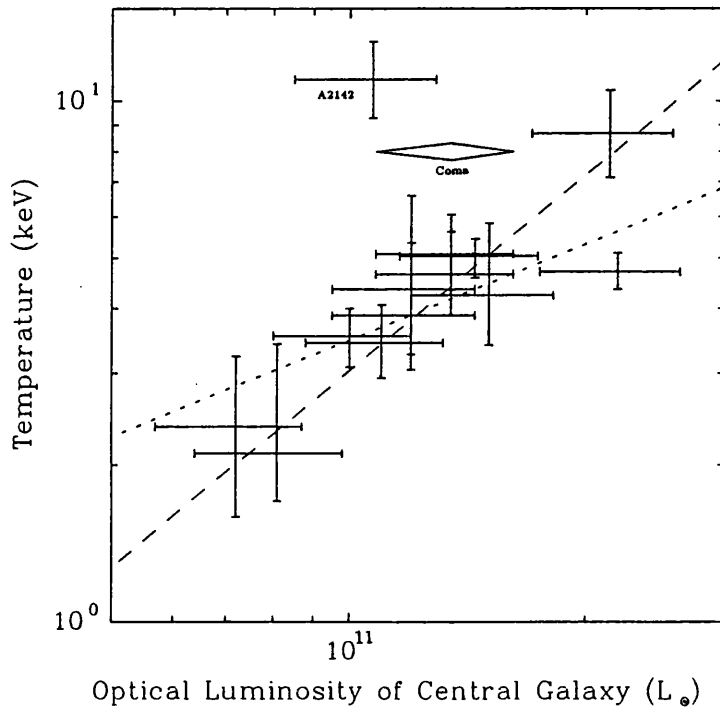


Figure 5.23: Temperature plotted against optical luminosity of the brightest galaxy from Hoessel, Gunn & Thuan (1980). A2142 and Coma are not included in the correlation analysis.

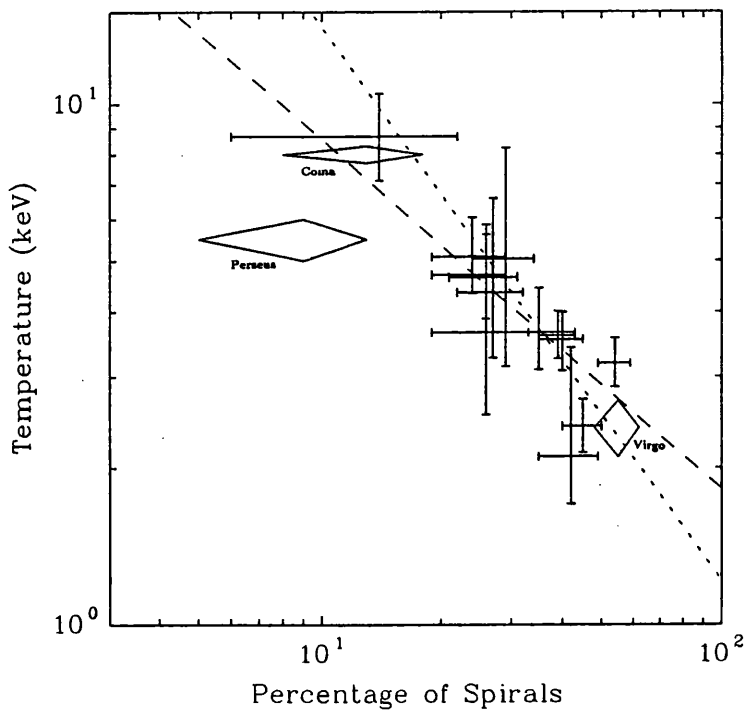


Figure 5.24: Temperature plotted against the percentage of spirals

## 5.7 X-ray to Radio Correlations

Figures 5.25 and 5.26 show the radio power and spectral slope plotted against the bolometric luminosity. A weak trend between the radio and X-ray luminosities can be seen. The Spearman rank correlation coefficient for this relation is 0.41 which is significant at the 98% level. However this correlation is a product of the radio and X-ray flux limits. The partial correlation coefficient for the radio and X-ray luminosity depending on redshift is 0.17, resulting in a D statistic of 0.77. So the relation is likely to be purely a secondary correlation through the dependence of both luminosities on redshift. A similar trend is also seen in the spectral slope against X-ray luminosity, but again the significance is low with a D statistic of 0.59 for an indirect correlation through redshift. However the *general trend* for the most luminous, steep spectrum sources to be found in the brighter X-ray clusters is consistent with models of radio source confinement. The lack of any significant correlation between X-ray and radio powers reflects the different processes behind the production of the two types of emission.

## 5.8 Conclusions

The principal correlations seen in the sample are:-

- The X-ray luminosity and temperature are well correlated:  $L_{\text{bol}} \propto T^{2.6}$
- The velocity dispersion is correlated with both the X-ray luminosity and temperature:  
 $L_{\text{bol}} \propto \sigma^4$  and  $T \propto \sigma^{1.3}$
- The optical luminosity of the central galaxy is related to the X-ray luminosity and temperature:  $L_{\text{bol}} \propto L_{\text{opt}}^{2.5}$  and  $T \propto L_{\text{opt}}^{0.6}$
- The X-ray luminosity is closely related to the percentage of spiral galaxies:  
 $L_{\text{bol}} \propto \%_{\text{spiral}}^{-2.7}$
- The iron abundance is constant at a value of 0.3 solar.
- The radio properties of a cluster are, at best, only loosely related to the X-ray properties.

These correlations are not significantly affected by the flux limited nature of the sample. Although all the cluster properties are inter-related to some degree two *primary* correlations do stand out from the others: temperature verses velocity dispersion and luminosity (*i.e.* gas mass) verses percentage of spirals. The astrophysical implications of these correlations are considered in the next Chapter.

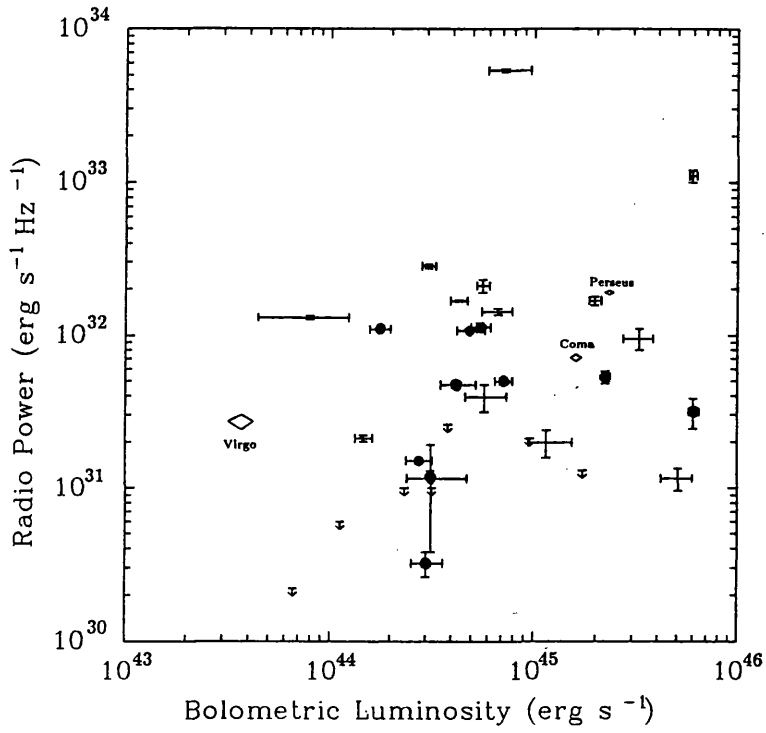


Figure 5.25: 1.4 GHz radio power plotted against bolometric luminosity. The filled circles represent tailed and offset sources.

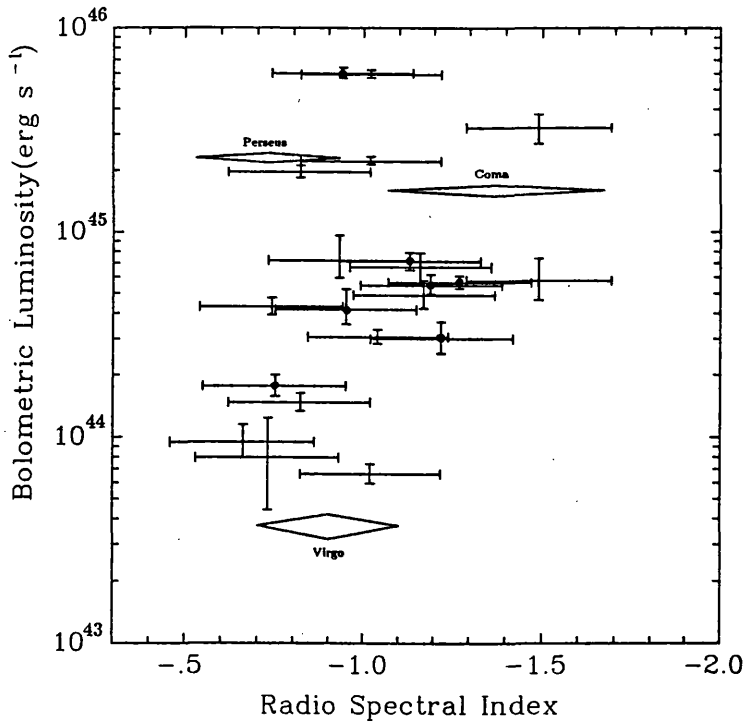


Figure 5.26: Radio spectral index plotted against bolometric luminosity. The filled circles represent tailed and offset sources. A nominal error of 0.2 is assumed for all indices.

## Chapter 6

# Astrophysical Implications of the EXOSAT Sample

### Introduction

The *EXOSAT* sample provides a great deal of information about clusters. These results and correlations with optical properties are reviewed and their implications are discussed below.

### 6.1 Luminosity and Temperature

The two best determined X-ray parameters are the luminosity and temperature. As can be seen from Figure 5.5, there is a strong correlation between them. The relationship between luminosity and temperature found by a least squares fit to the data is  $L \propto T^{2.6 \pm 0.1}$ . This agrees with the relationship  $L \propto T^{2.3 \pm 0.3}$  obtained from HEAO-1 data by Mushotzky (1984). The improvement in the determination of both luminosity and temperature over previous missions (*e.g.* ARIEL-V: Mitchell *et al.* 1979 and HEAO-1: Mushotzky 1984 & 1988) reveals a significant scatter within the correlation. For instance, for clusters with temperatures of 3–4 keV there is a range of ten in bolometric luminosity. This can be understood if the X-ray luminosity is related to the mass of gas (Figure 5.6) and the temperature is related to the total mass (See Section 1.1.2). Thus if the ratio of gas mass to total mass varies, then there will be a range of values of luminosity for any given temperature. To demonstrate this, Figure 6.1 shows the luminosity to temperature plot split into two subsets; low density ( $\rho_0 < 9 \times 10^{-3} \text{ cm}^{-3}$ ) and high density ( $\rho_0 > 9 \times 10^{-3} \text{ cm}^{-3}$ ). For these two subsets a least squares fit gives  $L \approx 3.7 \times 10^{42} T^{3.01 \pm 0.15}$  for the low density clusters and  $L \approx 1.2 \times 10^{43} T^{2.93 \pm 0.15}$  for the high density clusters. So the high density clusters are a factor of three more luminous than the low density ones for the same temperature. Splitting the data into these two groups ‘steepens’ the luminosity to temperature relation. Thus the variation in the ratio

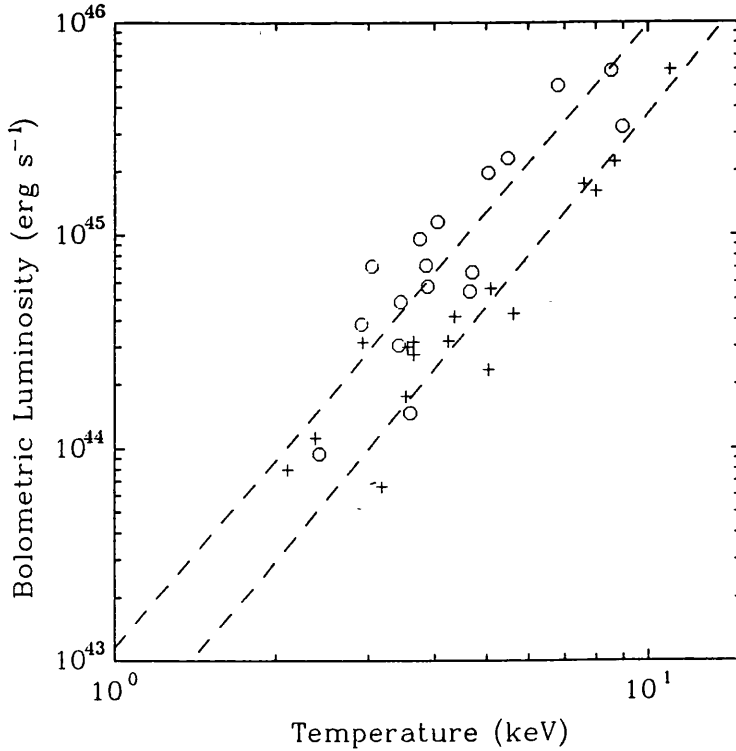


Figure 6.1: Bolometric luminosity plotted against temperature split by measured central density. Circles are high density ( $\rho_0 > 9 \times 10^{-3} \text{ cm}^{-3}$ ), crosses low density ( $\rho_0 < 9 \times 10^{-3} \text{ cm}^{-3}$ ). The two dashed lines are the best fit lines for the two subsets.

of gas mass to total mass causes a bias in the best fit line which should be taken into account if this correlation is used to determine underlying astrophysical properties (Kaiser 1986; Mushotzky 1988).

There is an additional factor to be taken into account: the effect of a cooling flow on the cluster, which could affect the X-ray temperature. As shown below in Section 6.6, a cooling flow can contribute as much as 40% of the bolometric luminosity and could lower the measured temperature, hence distorting the luminosity to temperature relation. To test for any drop in temperature with increasing mass flow rate, temperature is plotted against galaxy number density and against velocity dispersion in Figures 6.2a & b differentiating between clusters with low  $\dot{M}$  ( $< 100 M_{\odot} \text{ yr}^{-1}$ ) and high  $\dot{M}$  ( $> 100 M_{\odot} \text{ yr}^{-1}$ ). There does not appear to be any decrease in temperature with increasing mass flow rate. So it can be concluded that the overall effect of the mass flow rate on the measured temperature was small. For instance, in Chapter 4 the central temperature for Perseus was measured as 4.8 keV, but the outer cluster temperature was 5.5 keV. In this case the  $400 M_{\odot} \text{ yr}^{-1}$  cooling flow lowers the measured temperature by only 15%. This is much smaller than the scatter seen in the luminosity to temperature relation.

The variation in the gas mass to total mass ratio ( $M_{\text{gas}}/M_{\text{tot}}$ ) has significant implications. For instance there may be a population of clusters which have a low value of  $M_{\text{gas}}/M_{\text{tot}}$  and are hence weak X-ray emitters. These clusters would therefore not be included in X-ray surveys and would have been overlooked in X-ray studies despite having similar optical properties to X-ray ‘bright’ clusters. The opposite case is known to occur, where optically ‘poor’ clusters have a high value

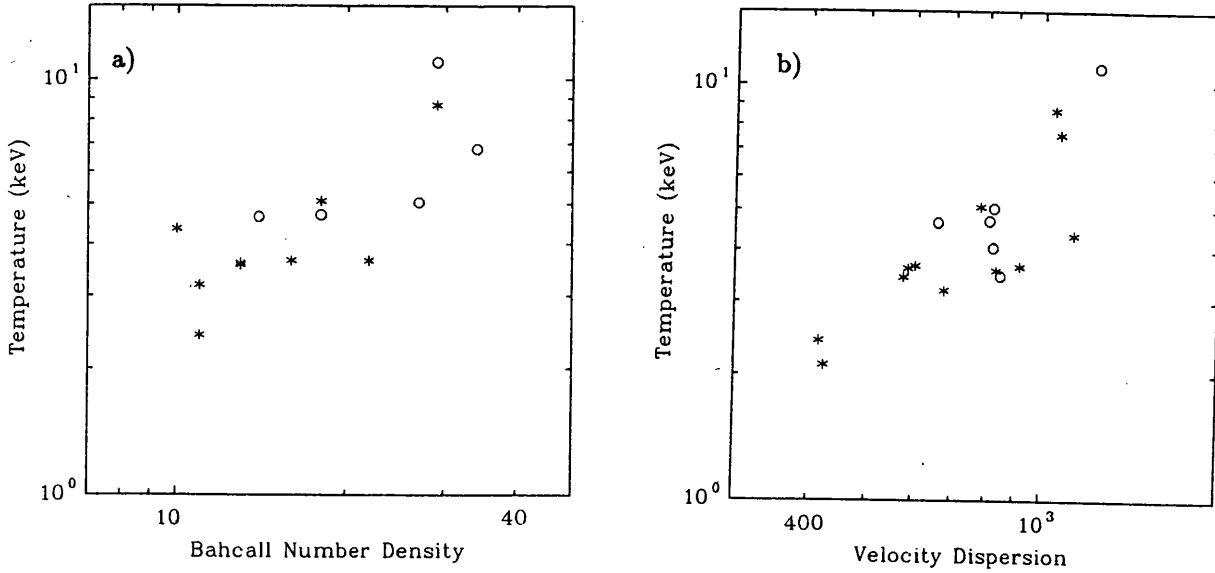


Figure 6.2: a. Temperature plotted against Bahcall number density split on mass flow rate and b. Temperature plotted against velocity dispersion split on mass flow rate. The circles indicate mass flow rates greater than  $100 M_{\odot} \text{ yr}^{-1}$  and the asterisks indicate mass flow rates less than  $100 M_{\odot} \text{ yr}^{-1}$ .

of  $M_{\text{gas}}/M_{\text{tot}}$  and are strong X-ray emitters. Of the thirty five clusters presented here, five are optically classified as ‘poor’. These five clusters all have a high value of  $M_{\text{gas}}/M_{\text{tot}}$ . Figure 6.3 shows the values of  $M_{\text{gas}}/M_{\text{tot}}$  derived from the luminosity and temperature (see Section 6.4), plotted against temperature. A large scatter of values is seen, with a range of a factor of four between highest and lowest. The highest  $M_{\text{gas}}/M_{\text{tot}}$  clusters also have large cooling flows.

## 6.2 Iron Abundances

As shown in Chapter 3, the derived iron abundance shows no significant trend with temperature (Figure 3.6) given the uncertainties in the transition coefficients used in the emission models and in the line measurement for low temperature clusters. Figure 6.4 shows the iron abundance against bolometric luminosity, which again shows no trend.

The average value of the iron abundance is  $0.32 \pm 0.18$  solar (excluding A262, A400 and A1837 because of the uncertainties in the continuum above 6.7 keV). This value is consistent with the 0.4 obtained by Rothenflug & Arnaud (1985) from HEAO-1 data and marginally consistent with the commonly quoted value of 0.5 solar.

The uniform enrichment of the ICM has important implications for the understanding of the formation and evolution of the gas in clusters, and of clusters themselves.

The most widely accepted model for the enrichment of the ICM is hot gas ejection at the epoch of galaxy formation. The model proposed by de Young (1978) for this gas ejection involves a rapid burst of stellar winds and supernovæ from short-lived, massive stars  $10^6$ – $10^7$  yr after the formation

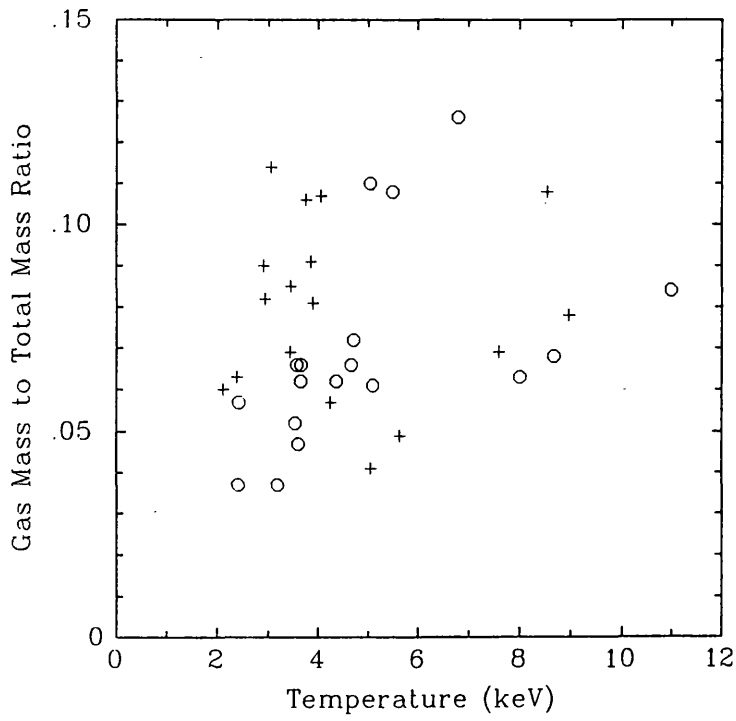


Figure 6.3: Ratio of gas mass to total mass plotted against temperature. The circles mark clusters with Bahcall number densities.

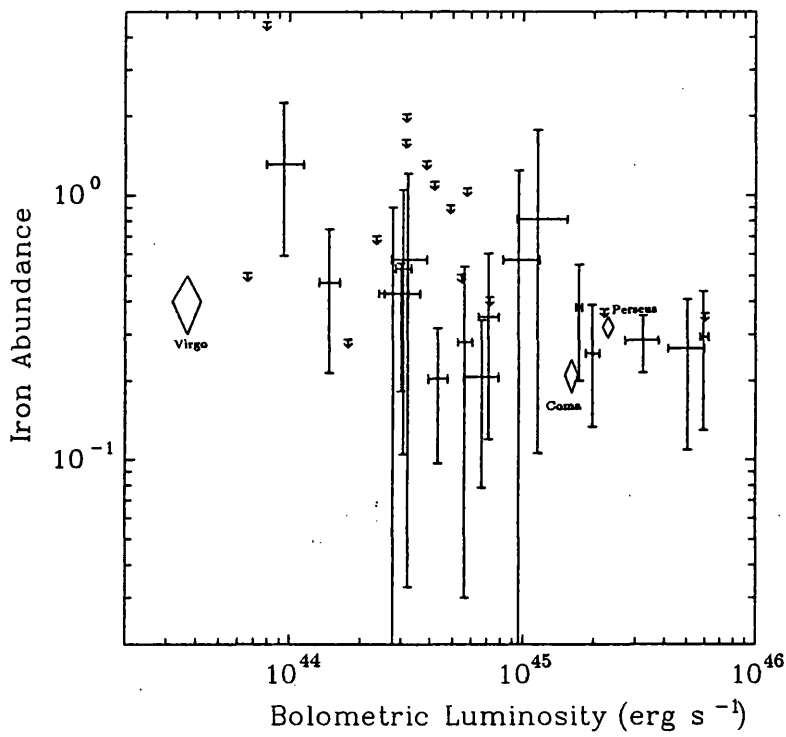


Figure 6.4: Iron abundance plotted against bolometric luminosity

of the galaxy. These stellar winds and supernovæ drive a ‘hot’ galactic wind out of the galaxy and into the ICM. This wind carries supernova ejecta with it thus enriching the ICM. This ejection may also continue (at a lower rate) in a ‘standard’ star formation bursts (Scalo & Struck-Marcell 1986). Assuming a constant ratio of total mass to primordial gas in the ICM for all clusters and a similar abundance for the ejecta for all galaxies, then the heavy element abundance in the ICM will not depend on the mass of the cluster. The calculated ejection velocities are much greater than the escape velocity from the galaxy (*i.e.* 500–1000 km s<sup>-1</sup> compared to 200–300 km s<sup>-1</sup>), so this ejected gas could ‘heat’ the ICM through shocks. This would result in a value of  $\beta < 1$ , which is as observed (Section 6.3.2).

The alternative model for the origin of the ICM which has been investigated is gas stripping. Lea & de Young (1976) have considered ram-pressure stripping, where the gas in the ICM comes mainly from galaxies. The predicted gas masses and abundances for this model are much lower than seen, so stripping cannot account for the ICM alone. Although the process of ram-pressure stripping cannot explain the origin of the ICM, it is still an important influence on the galaxies passing through the ICM (see Section 6.5).

## 6.3 Cluster Mass

The mass of a cluster is reflected in a number of observable properties, *e.g.* the number of galaxies, the velocity dispersion and the X-ray temperature. The correlations in Chapter 5 show these properties are all closely related. Of these three the best determined property is the X-ray temperature.

### 6.3.1 The Distribution of Mass

The most widely used description for the distribution of mass in clusters is the parameterisation of Cavaliere & Fusco-Femiano (1976) which is described in Chapter 1. The description assumes an isotropic distribution of galactic orbits, isothermal gas, no mass segregation and a constant mass-to-light ratio. These assumptions can be relaxed to provide more general models, but the lack of any detailed radial information in velocity dispersion and temperature makes these models difficult to distinguish. The principal parameter in the Cavaliere & Fusco-Femiano description is  $\beta$ , which is the ratio of the specific energy in galaxies to that in gas.

Henriksen & Mushotzky (1985) have identified several potential problems with the Cavaliere & Fusco-Femiano description for clusters. They point out that the gas masses at very large radii (10–20 core radii) will approach the virial mass for low values of  $\beta$  ( $\sim 0.5$ – $0.7$ ). This problem appears to be intractable as little is known about the gas density beyond 3 core radii. If there is a substantial amount of gas beyond 5 core radii it should have been detected using the ME if it is

at a temperature above 1 keV. However, as no scatter is apparent in the correlation between the mass of gas within 0.5 Mpc and the luminosity measured by the ME (see Figure 5.6). Therefore it seems that the gas mass is *not* large beyond a few core radii *or* that it is below 1 keV.

Henriksen & Mushotzky also point out that the published optical and X-ray core radii should agree, but their analysis shows that they do not. However this conclusion is dependent on the quality of the observational data. Very few optical core radii measurements have been made using data from automatic plate measuring machines (*e.g.* Colless 1987; Sharples, Ellis & Gray 1988). Most measurements in the literature are done by eye and are subject to a number of selection effects (*e.g.* Dressler 1978; Semeniuk 1982). The effect of a cooling flow can cause the X-ray core radius to be underestimated due to the central ‘peak’ that is introduced. There are a few cases where the optical and X-ray core radii data are compared directly. For instance, work on A2670 by Sharples, Ellis & Gray (1988) presents both optical data from plate scanning and X-ray data from the *EINSTEIN* IPC. The derived core radii agree. The disagreement then, between optical and X-ray core radii may be a result of the difficulty in obtaining reliable values for either.

Taking these points into account, it can be concluded that the Cavaliere & Fusco-Femiano description is still consistent with the available data. So it has been used as the basis for the interpretation of the sample.

### 6.3.2 Deriving $\beta$

The  $\beta$  parameter mentioned above can be determined in two ways: from the surface brightness profile (hereafter denoted as  $\beta_i$ ) and from the X-ray temperature and optical velocity dispersion (hereafter denoted as  $\beta_s$ ). From the LE surface brightness data it was not possible to determine  $\beta_i$  to any great precision. However analysis of *EINSTEIN* data by Jones & Forman (1984) gave values of  $\beta_i$  between 0.5 and 0.9, with an average value of 0.65 (Figure 6.5a). Mushotzky (1988) notes that the Jones & Forman data contain a tendency for  $\beta_i$  to increase with core radius. From the spectral data the calculated values of  $\beta_s$  have a much larger dispersion (Figure 6.5b) ranging from 0.4 to 1.8, with an average of 0.83. This average value excludes Perseus, which is known to have a high value of  $\beta_s$  (see below), and A2147, which has an overestimated velocity dispersion, possibly due to the inclusion of members of A2151 which is close in redshift (Tarengi *et al.* 1980). Figure 6.5b shows a peak at  $\sim 0.7$  close to the average imaging value. In all, two thirds of the calculated values of  $\beta_s$  are less than 1. These values should be compared with those in Mushotzky (1984) where the average  $\beta_s$  was 1.2 and only a quarter of the values were less than 1 for sample of a similar size. Figure 6.6 shows a comparison of the values of  $\beta_s$  from the spectral and  $\beta_i$  from *EINSTEIN* IPC data (Fabricant & Gorenstein 1983; Jones & Forman 1984; Matilsky, Jones & Forman 1984). Although the agreement of the two values of  $\beta$  is not exact, it is much better than

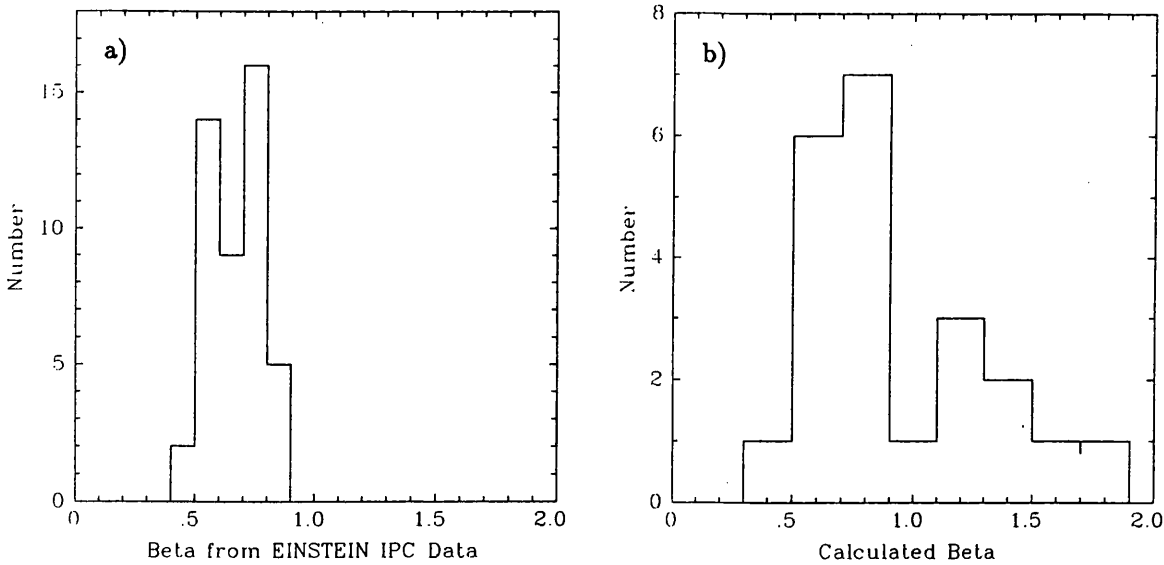


Figure 6.5: Histogram of a.  $\beta_i$  from Jones & Forman and b.  $\beta_s$  from this work

the results quoted in Mushotzky (1984).

Although there is overall consistency in the *EXOSAT* data between the values of  $\beta$  determined from the spectral and imaging data, there are clearly a number of cases where the two values do not agree. Figures 6.7a & b show the calculated values of the  $\beta_s$  plotted against temperature and velocity dispersion. The scatter in Figure 6.7b shows a trend that high values of  $\beta_s$  have high velocity dispersions, possibly indicating an overestimation of the velocity dispersion. Some of this overestimation could be due to the measurement errors mentioned in Section 5.2. The velocity dispersion could also be overestimated through subclustering. Recent work by Fitchett (1988) indicates that subclustering is common in  $\sim 40\%$  of rich clusters. Of the twenty-two clusters here, seven have  $\beta_s > 1$  and Centaurus and A3122 are known to be subclustered. So the fraction of subclustering could be as much as 40% if the overestimation of  $\beta_s$  is due entirely due to subclustering.

The most commonly cited case of the disagreement of  $\beta_i$  and  $\beta_s$  (usually referred to as “the  $\beta$  problem”) is Perseus where the imaging data give  $\beta_i$  of 0.6 and the spectral data give 1.5. The X-ray surface brightness profile, the X-ray temperature and the optical velocity dispersion are all well determined for Perseus so this difference is highly significant. A number of explanations have been put forward to account for this discrepancy, *e.g.* Kent & Sargent (1983) suggest anisotropic galactic orbits and Cowie, Henriksen & Mushotzky (1987) propose a non-isothermal gas distribution. There is evidence that the orbits are predominately radial at large radii (Kent & Sargent 1983), which may reduce  $\beta_s$  by about  $\sim 30\%$ , but not enough to completely explain the difference. An alternative solution is to increase the temperature of the cluster. In the case of Perseus this would imply a temperature of  $\sim 13$  keV which is close to the central temperature predicted by Cowie, Henriksen & Mushotzky (1987) from their polytropic models. However, this temperature is inconsistent with

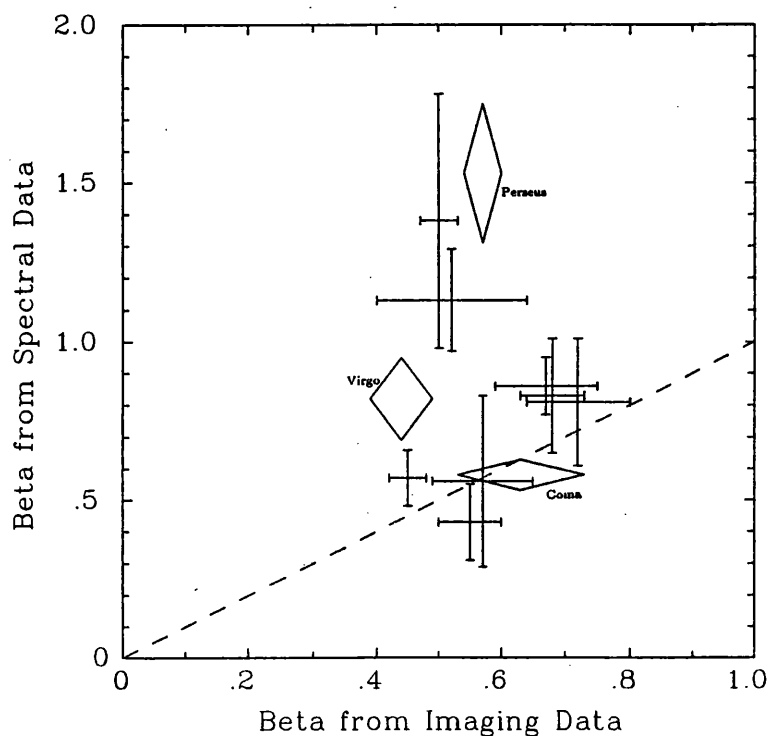


Figure 6.6: Comparison of  $\beta_s$ , derived from *EXOSAT* temperature and to  $\beta_i$  from *EINSTEIN* IPC data

the observed spectrum and is higher than any other cluster temperature, making it extremely unlikely. The value of  $\beta_s$  could also be decreased if the gas is turbulent and had a large amount of energy stored in tangled magnetic fields (Loewenstein & Fabian 1989). The total gas energy is increased thus reducing  $\beta_s$ . However turbulence should apply equally to all clusters so cannot easily explain the fraction of high values of  $\beta_s$ .

To conclude, the *EXOSAT* data presented here appear to indicate a self-consistent picture for the isothermal model. There are cases where the model does not hold, either because one of the assumptions of the model is incorrect or one of the cluster properties is poorly determined. To determine conclusively whether the model describes clusters in general requires spatially resolved spectra and well sampled velocity dispersions (*i.e.* over 300 galaxies) both of which should be available within the next 5 years.

## 6.4 Mass-To-Light verses Luminous-to-Total Mass Ratios

The most popular method of expressing the ratio of 'dark' mass to 'visible' mass is the mass-to-light ratio ( $M/L$ ). The mass-to-light ratio is believed to increase with scale length (Faber & Gallagher 1979) and for most clusters is around  $100\text{--}400 M_\odot/L_\odot$ . However the X-ray results show that the mass of gas in the ICM is comparable to that in galaxies (see Section 6.4.1). Therefore the simple mass-to-light ratio is not a good measure of fraction of the mass that can be accounted for in galaxies *and* the ICM. Instead the ratio of the luminous mass (in galaxies and gas) to total mass

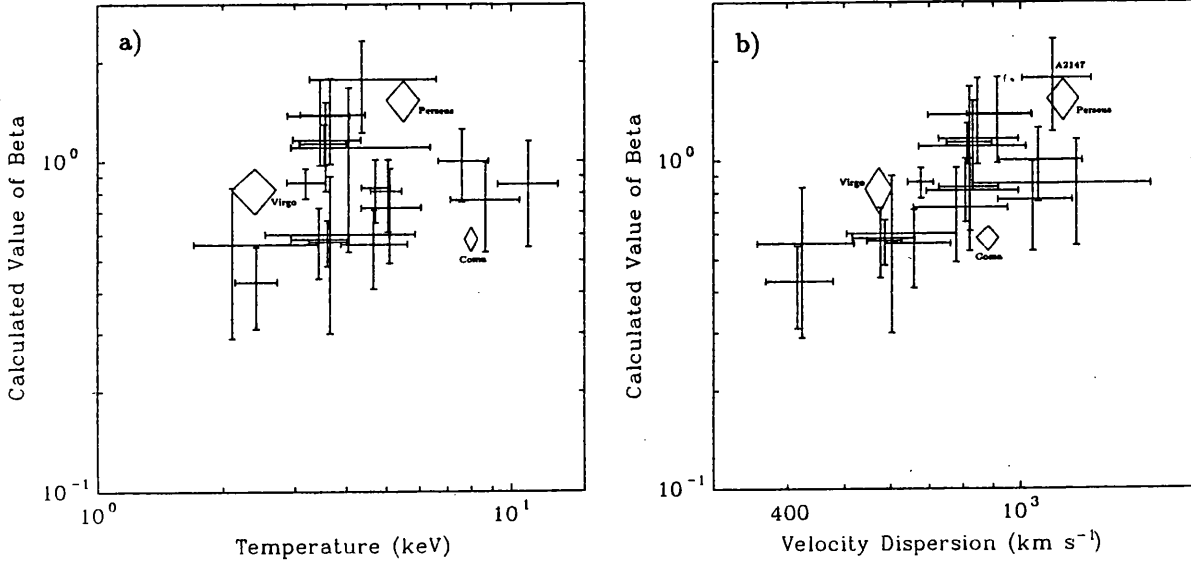


Figure 6.7: a. Derived value for  $\beta$ , plotted against temperature and b. velocity dispersion

$(M_{lum}/M_{tot})$  should be calculated. This ratio gives a much clearer indication of the proportion of ‘dark’ mass in the cluster but the method requires *both* optical and X-ray data.

The lack of any consistent optical dataset for the clusters in this sample makes the determination of the total optical luminosity,  $L$ , and hence  $M/L$ , difficult. The only measure of the optical luminosity available for a significant number of clusters is the Bahcall number density,  $N_B$ .  $N_B$  is defined as the number of galaxies within a projected radius of 0.5 Mpc that have a magnitude  $\leq m_3 + 2$ . However this number of galaxies cannot be used directly to determine the optical luminosity as the number of galaxies between  $m_3$  and  $m_3 + 2$  is not linearly related to the luminosity. To correct for this effect the expected Bahcall number density has been calculated using the ‘universal’ luminosity function from Colless (1988), which is, in terms of the Schechter function:

$$n(L)dL = N^*(L/L^*)^{-\alpha} \exp -L/L^* d(L/L^*) \quad (6.1)$$

where  $L^*$  is the characteristic luminosity and  $N^*$  is the number of galaxies at that luminosity. The total optical luminosity is given as  $L_{opt} = N^* \Gamma(2 - \alpha) L^*$  where  $\Gamma(x)$  is the Gamma function. Calculating  $N_B$  for a series of  $N^*$  gives the result that  $N^* \propto N_B^{1.42}$  for a range of  $N^* = 10-1000$ . The normalisation of this relation was taken from Kent & Gunn (1982) who gave a value of  $N^*$  of 279 and Bahcall (1981) who gave a value of  $N_B$  of 28. Correcting for the different radius gives  $N^*(\text{within } 0.5 \text{ Mpc}) = 0.45 N_B^{1.42}$ . Thus the total luminosity within 0.5 Mpc for  $\alpha=1.25$  and  $M^*=-20.06$  (Colless 1988) gives

$$L_B = 1.81 \times 10^{10} N_B^{1.42} L_{\odot} \quad (6.2)$$

This relation implies that the correlations given in Tables 5.6 and 5.7 should be corrected (*e.g.*  $N_B \propto T^{0.78}$  becomes  $L_B \propto T^{1.1}$ ). Also this effect is not accounted for in Bahcall (1981). Bahcall derives  $N_B \propto \sigma^{1.2}$  which is interpreted as  $M/L \propto \sigma^{0.8}$ . However this relation corrects to  $L_{opt} \propto \sigma^{1.7}$ . This is much closer to the  $L \propto \sigma^2$  expected from the Virial theorem and constant  $M/L$  and agrees with other optical work (Lucey, Currie & Dickens 1986a; Colless 1987).

Taking Equation 1.20 and a constant value of  $\beta$  of 0.7 gives a total cluster mass with 0.5 Mpc of

$$M_{(0.5 \text{ Mpc})} = 3.94 \times 10^{13} T M_{\odot} \quad (6.3)$$

where  $T$  is in keV. If the cluster is non-isothermal, then this calculated mass will be overestimated. This results in lower mass-to-light ratios, as pointed out by Cowie, Henriksen & Mushotzky (1987). However there is little evidence for the polytropic models they propose (Butcher 1989), apart from the case of Coma (see Chapter 4). As Coma appears to have an isothermal core within  $\sim 1$  Mpc, the isothermal estimate should hold for the cluster within 0.5 Mpc.

Taking these values for mass and luminosity gives a mass-to-light ratio  $M/L_B$  of

$$\frac{\text{Mass}}{\text{Galactic Light}} = 2180 T N_B^{-1.42} \quad (6.4)$$

The values of this ratio calculated for the clusters with Bahcall number densities are shown in Figure 6.8.

The relation for the gas mass within 0.5 Mpc and the bolometric luminosity given in Table 5.4 gives

$$M_{\text{gas}} = 5.5 \times 10^{-6} L_{\text{bol}}^{0.41} M_{\odot} \quad (6.5)$$

Thus combining these three values of mass gives

$$\frac{\text{Luminous Mass}}{\text{Total Mass}} = \frac{L_B \times M_{\text{galaxy}}/L_B + M_{\text{gas}}}{M_{(<R)}} \quad (6.6)$$

Assuming a value of the galactic mass-to-light ratio  $M_{\text{galaxy}}/L_B$  of 8, as found for S0 and Es (David *et al.* 1988), give the luminous mass-to-total mass ratios shown in Figure 6.9.

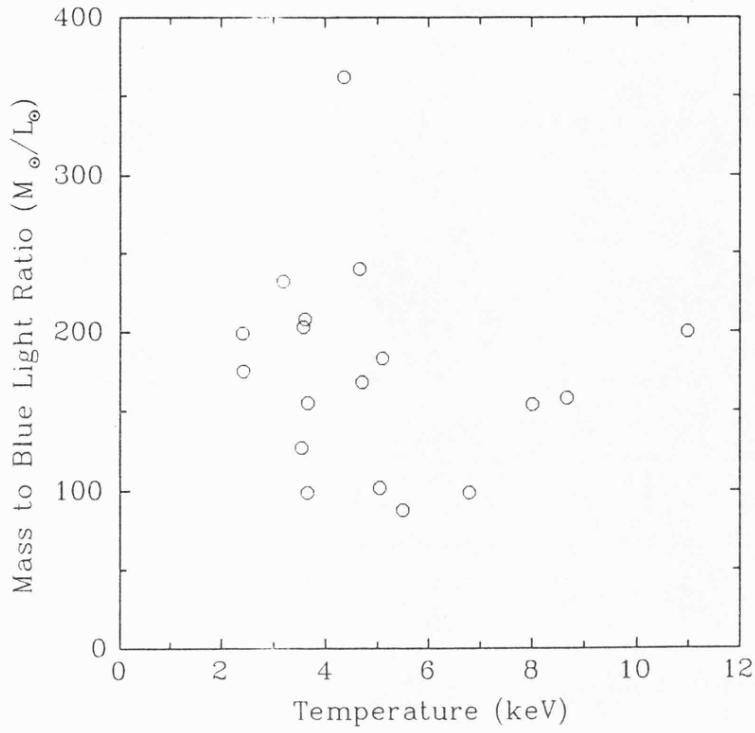


Figure 6.8: Total mass-to-blue light ratio plotted against temperature

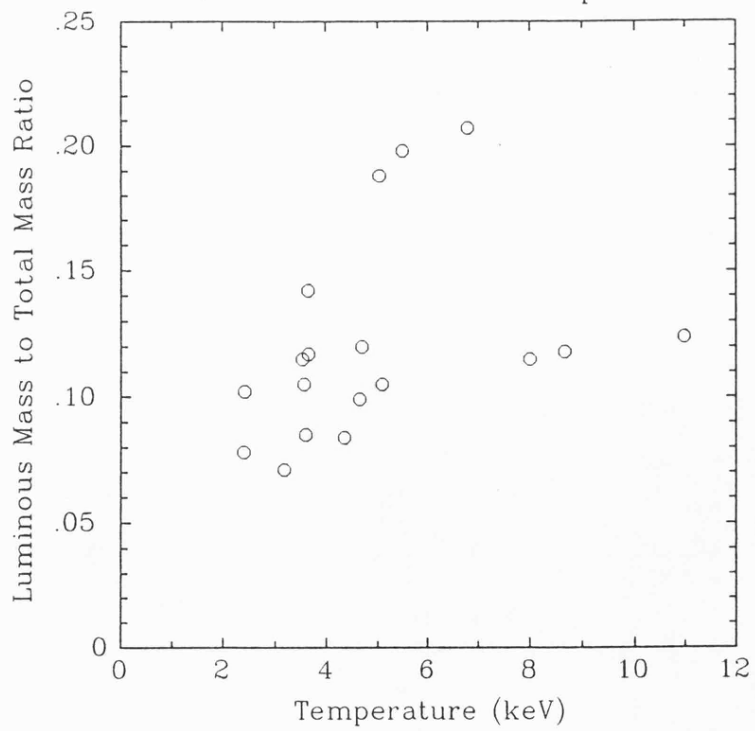


Figure 6.9: Luminous mass-to-total mass ratio plotted against temperature

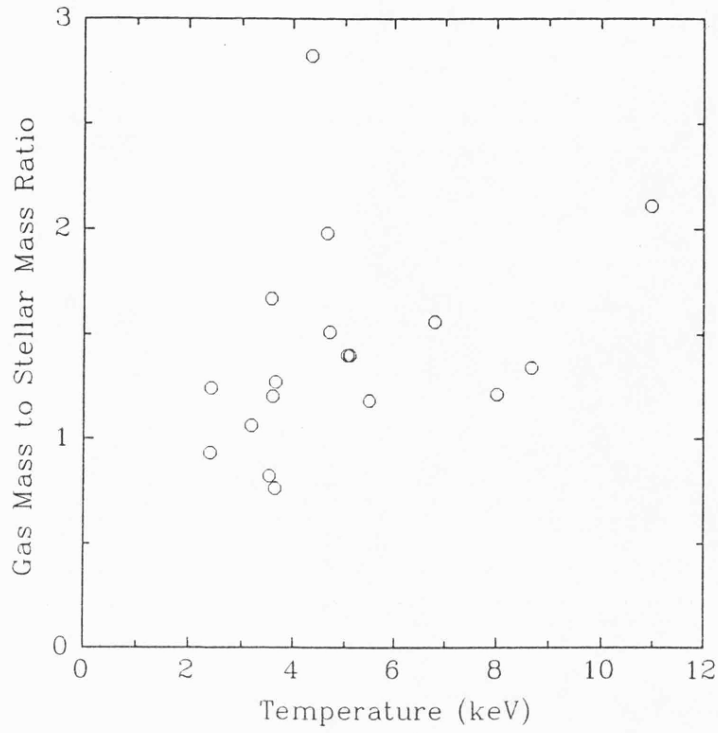


Figure 6.10: Ratio of the gas and stellar masses plotted against temperature

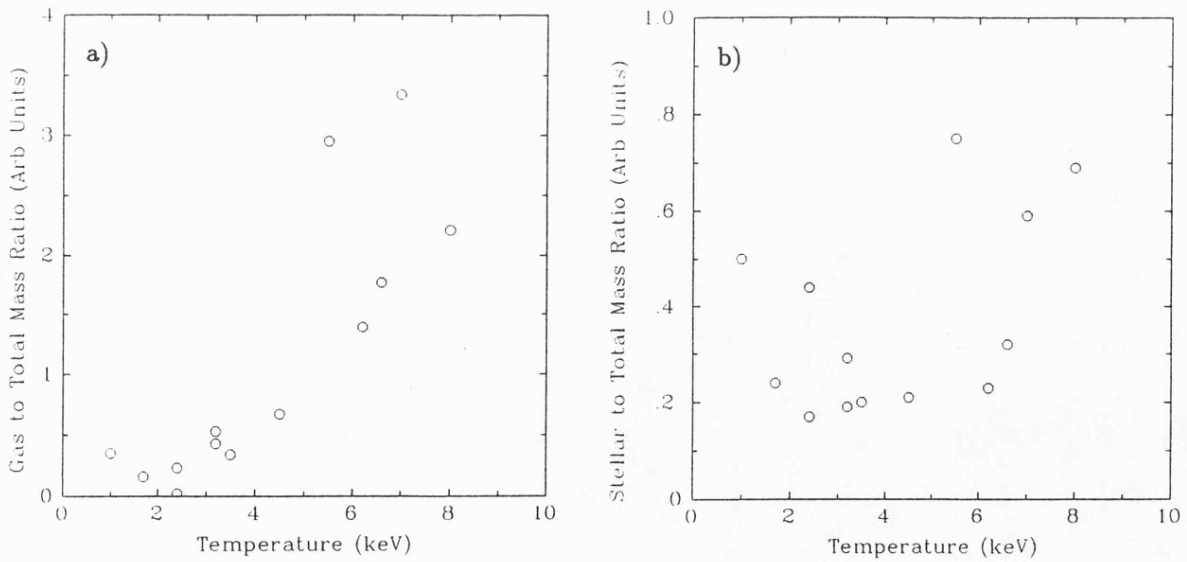


Figure 6.11: a. Ratio of gas mass to total mass plotted against temperature. and b. Ratio of stellar mass to total mass plotted against temperature. For data used in David *et al.* (1988).

### 6.4.1 Gas Mass to Stellar Mass Ratio

Work by David *et al.* (1988) points to a strong correlation between the ratio of gas mass to stellar mass ( $M_{\text{gas}}/M_{\text{star}}$ ) and temperature. David *et al.* attribute this correlation to a variation in the efficiency of galaxy formation. Plotting  $M_{\text{gas}}/M_{\text{star}}$  derived from the *EXOSAT* data shows a similar but weaker trend (Figure 6.10).

However further analysis of the data used by David *et al.* shows that the increase in  $M_{\text{gas}}/M_{\text{star}}$  is due principally to an increase in the proportion of gas in the cluster (Figure 6.11a). If the proportion of stellar mass is constant (Figure 6.11b) then this trend will also appear in the  $M_{\text{gas}}/M_{\text{star}}$ . Comparing Figure 6.11a with Figure 6.3 shows an optical selection effect against ‘poor’ clusters with a low temperature and high gas mass. If the correlation of David *et al.* holds for these clusters, they should have *higher* optical luminosities than the other ‘rich’ clusters. This cannot be the case if they are ‘poor’. Therefore it can be inferred that the  $M_{\text{gas}}/M_{\text{star}}$  correlation does not reflect a decrease in the efficiency of the galaxy formation but an *increase* in the proportion of gas in the ICM. This question requires further optical work on the low temperature clusters to determine  $M_{\text{gas}}/M_{\text{star}}$  for a set of clusters with roughly the same temperature (and mass) but different fractions of gas.

## 6.5 Stripping of Spiral Galaxies

One of the strongest correlations in the analysis is the relation between the bolometric luminosity (and hence gas mass) and the percentage of spiral galaxies. Figure 6.12 shows the percentage of spirals (Sp s) plotted against bolometric luminosity but also includes the percentage of ellipticals (E s) and lenticulars (S0 s). The figure shows similar trends to plots of galactic type and galaxy density shown in Dressler (1980b) and in Kent (1981).

Melnick & Sargent (1977) show that the ratio of Sp s to S0 s decreases toward the centre of a cluster indicating a possible transition of galactic type from Sp to S0, as Sp s pass through a high gas density region. Melnick & Sargent interpret this as evidence of ram-pressure stripping (Gunn & Gott 1972; Salpeter 1988). In the centre of a cluster the gas pressure exceeds  $10^4 \text{ K cm}^{-3}$  (*i.e.* the typical pressure of the inter-stellar medium (ISM) in a spiral galaxy). So if the galaxy moves with respect to the ICM then the ISM will be pushed out of the galaxy. This stripping removes the ISM from the galaxy and hence changes the the star formation pattern and outward appearance of the galaxy (Biermann & Shapiro 1979). This model can also be applied to ellipticals which contain hot gas (Tadepka, Nulsen & Fabian 1984). Other theories have also been put forward. Dressler (1980b) and Kent (1981) propose that the proportion of spirals is related to the collapse of the cluster. If large clusters collapse violently, the haloes of the infalling galaxies will be disrupted.

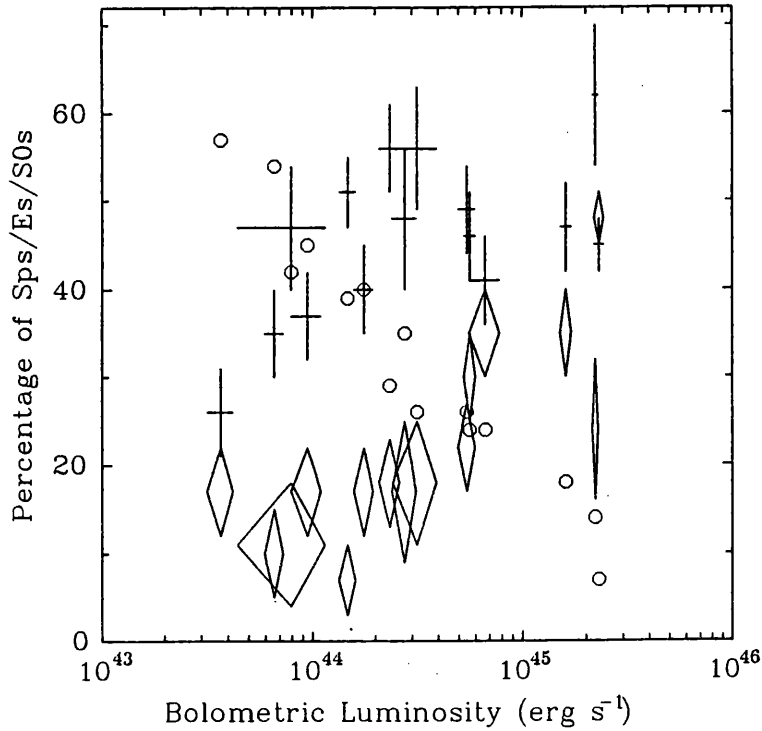


Figure 6.12: Fraction of galactic types plotted against derived bolometric luminosity. Circles are spirals; diamonds are ellipticals; crosses are lenticulars

This stops the formation of the disks that are seen in spirals, resulting in a small fraction of spirals. This effect is weaker in less massive clusters and so a higher fraction of spirals is seen. Miller (1988) suggests that an E is produced by violently disturbing (through tidal and collisional interaction with other galaxies) a Sp, with an S0 being an intermediate step. However the strength of the correlation with gas mass (as opposed to cluster mass/gas temperature) indicates that the effect is environmental. So, tentatively, the favoured mechanism for this effect is ram-pressure stripping of spirals creating lenticulars and ellipticals.

The only direct evidence for gas stripping in a cluster is from M86 in Virgo which is an elliptical (Fabian, Schwartz and Forman 1980). There is a large X-ray and optical 'plume' to the North-West of the galaxy (out of the cluster). There is also some indirect observational evidence for stripping. The wide variety of 'wide-angle' and 'narrow-angle' tail radio sources (O'Dea & Owen 1985a & b) indicate strong interaction between ISM and ICM. From observations of the HI content of individual cluster galaxies in nine clusters, Giovanelli & Haynes (1985) show a clear increase in the HI deficiency with increasing X-ray luminosity and decreasing distance from the centre of the cluster.

## 6.6 Cooling Flows

The presence of a cooling flow in a cluster has a large impact on the evolution of the central galaxy and the cluster itself. Over a Hubble time ( $\sim 2 \times 10^{10}$  yr) as much as  $10^{13} M_{\odot}$  will be deposited in the central 150 kpc of the cluster for a mass flow rate of  $1000 M_{\odot} \text{ yr}^{-1}$ . Only a small percentage

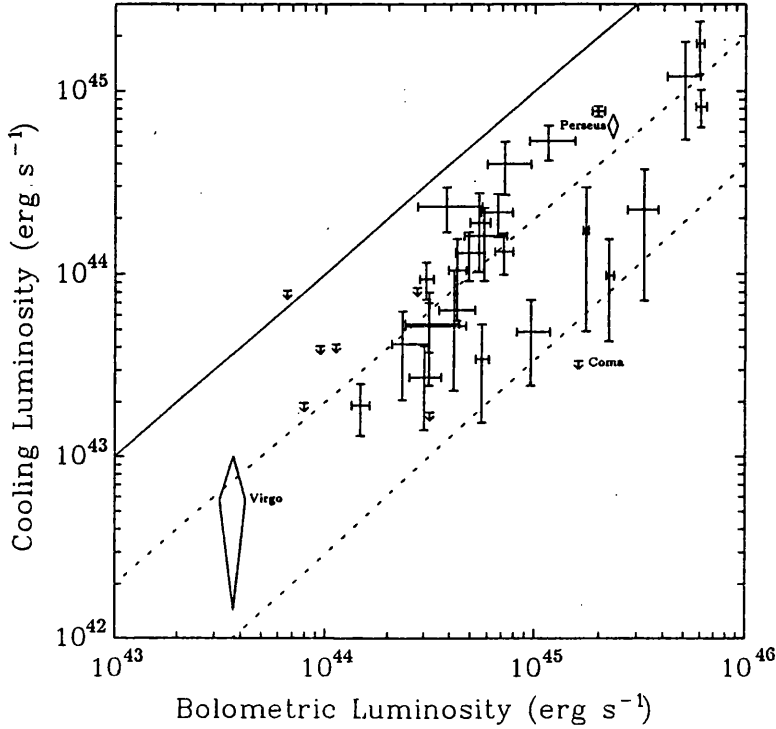


Figure 6.13: Cooling luminosity plotted against derived bolometric luminosity. The solid line represents equal cooling and bolometric luminosities. The dashed lines represent cooling luminosities of 20% and 4% bolometric.

of this mass can be accounted for by observed star formation, so it can be inferred that the gas condenses in a form that is 'dark' (Johnstone, Fabian & Nulsen 1987).

As shown in Chapter 2, all the clusters detected in the LE are found to have central cooling times equal to, or less, than the Hubble time, due to the background limit of the LE detectors. Figure 6.13 shows the calculated bolometric luminosity of the cooling flow for each cluster plotted against the inferred bolometric luminosity from the 2-10 keV flux. The total cooling flow luminosity is taken from Equation 4 in Stewart *et al.* (1984b):-

$$L_{\text{cool}} = 3.0 \times 10^{41} \dot{M} T \text{ ergs s}^{-1} \quad (6.7)$$

where  $\dot{M}$  is in  $M_{\odot} \text{ yr}^{-1}$  and  $T$  is in keV. It can be seen in Figure 6.13 that the ratio of cooling luminosity to cluster luminosity varies substantially, and can be as much as 40%. The fraction of the cooling luminosity that is emitted in the 2-10 keV band (*i.e.* is detected in the ME and is hence included in the bolometric luminosity) depends on the temperature the gas cools from. Therefore a direct comparison of the bolometric and cooling luminosities is incorrect. However the calculation of the contribution of the cooling flow to the measured bolometric luminosity is complicated. Therefore calculation of the ratio of the two is not attempted and a straight line is used *for comparison only*.

## 6.7 Constraints on the Hubble Constant and Cosmology

The X-ray results can be used to put some loose limits on the Hubble constant,  $H_0$ . If  $H_0$  is expressed as  $H_0 = 50h \text{ km s}^{-1} \text{ Mpc}^{-1}$  then

$$M_{\text{gas}} \propto h^{-\frac{5}{2}} \quad \text{and} \quad M_{\text{tot}} \propto h^{-1} \quad (6.8)$$

So the ratio of the gas mass to total mass ( $M_{\text{gas}}/M_{\text{tot}}$ ) is proportional to  $h^{-\frac{3}{2}}$ . This implies that if  $H_0$  is lower than  $50 \text{ km s}^{-1} \text{ Mpc}^{-1}$  then the ratio of the gas mass increases. The limit for this ratio is where the gas mass equals the total mass. As  $M_{\text{gas}}/M_{\text{tot}}$  reaches a maximum  $\approx 0.15$  when  $h=1$ , then if the gas mass equals the total mass  $h$  is 0.31, *i.e.*  $H_0 = 16 \text{ km s}^{-1} \text{ Mpc}^{-1}$ . This is substantially lower than most accepted values of  $H_0$  of 50–100 (Tully 1988; Bartel 1988). However recent work on the Sunyaev-Zel'dovich effect by M<sup>c</sup>Hardy *et al.* (1989) gives a value for  $H_0$  of  $24_{-10}^{+13} \text{ km s}^{-1} \text{ Mpc}^{-1}$  indicating that measurements of the radio decrement are too large or all other determinations of  $H_0$  are biased in some way.

From limits on nucleosynthesis at early epochs the proportion of baryons in the density parameter,  $\Omega$ , is

$$0.01 \leq \Omega_{\text{baryon}} h^2 \leq 0.2 \quad (6.9)$$

So, if  $H_0$  is  $25 \text{ km s}^{-1} \text{ Mpc}^{-1}$ , then  $\Omega_{\text{baryon}}$  would be as much as 0.8, *i.e.* there is a smaller proportion of ‘‘Dark Matter’’ in the Universe. This value of 25 for  $H_0$  also implies that the age of the Universe is doubled and a larger proportion of the mass in clusters of galaxies is in the form of gas. Given the large body of data indicating much larger values of  $H_0$  the probability of such a low value of  $H_0$  seems small, although the result should be considered.

The results presented here are consistent with the standard ‘Cold Dark Matter’ models (Kaiser 1986; Frenk 1988). However they are inconsistent with ‘Hot Dark Matter’ models as the ‘dark’ mass appears to be distributed on the same scale as the ‘visible’ mass which contradicts the predictions of existing HDM theories (Bond & Szalay 1983).

## 6.8 Conclusions

The *EXOSAT* sample has provided the best spectral X-ray dataset for the study of clusters presently available. The basic conclusions that can be drawn from the sample are:-

- The data show strong evidence that the ratio of gas mass to total mass varies between clusters.
- The iron abundance is constant at a value of 0.3 solar for all clusters.
- The mass-to-light ratio in the clusters studied has range of 100-400.
- Five to fifteen percent of the total gravitational mass of a cluster can be accounted for by gas and galaxies.
- The proportion of spiral galaxies in a cluster is strongly influenced by the amount of gas in the ICM.
- Cooling flows can emit as much as 40% of the total bolometric luminosity.
- The results are consistent with Cold Dark Matter models.

# Conclusions

The results from the *EXOSAT* sample represent the largest and most reliable dataset of X-ray results presently available. The data provide a great deal of information about clusters, which can be summarised as:

- The iron abundance in clusters is a constant value.
- The X-ray temperature and luminosity are closely correlated.
- The mass flow rate can produce up to 40% of the bolometric luminosity of a cluster.
- The optical velocity dispersion is strongly correlated with the X-ray properties.
- A third of clusters have overestimated velocity dispersions, possibly through subclustering.
- The ratio of galaxy to gas energies ( $\beta$ ) agrees with imaging determinations for *most* clusters.
- The fraction of spiral galaxies is closely related to the cluster gas mass.
- There is strong evidence for non-isothermal distribution of gas in the Coma cluster indicating a ‘cut-off’ in the mass profile at  $\sim 1$  Mpc.

These results give a much clearer picture of the inter-relation of the optical and X-ray properties and hence the underlying mass distribution in clusters. In particular the long standing controversy about the disagreement of imaging and spectral values of  $\beta$  (see Section 6.3.2) which is not conclusively resolved, but the *EXOSAT* data point strongly to a general agreement with a number of cases with overestimated velocity dispersions. Improved velocity dispersions for the clusters with high  $\beta$  will be crucial in any attempt to answer the “Beta problem” completely.

Despite the clear advances made with *EXOSAT* the limitations of the large field of view proportional counter leave a great many observational and theoretical questions unanswered.

- Are there any very gas poor or rich clusters?
- What is the frequency of non-isothermal temperature distributions?

- Are there abundance gradients?
- How does the Mass-to-Light ratio vary between clusters?
- When and how did the ICM originate?
- How are cluster galaxies affected by the ICM?

## Future Prospects

There are a number of X-ray missions active, due for launch and planned that will provide answers to some of the observational questions.

The joint Japanese/UK satellite, *GINGA*, is presently producing high quality spectra that provide excellent iron abundance and temperature determinations. The collecting area of *GINGA* is a factor five greater than that of *EXOSAT*. *GINGA* can measure iron abundances with 30% accuracy down to 1 mcrab as opposed to 5 mcrab for *EXOSAT*. The capabilities of *GINGA* are well demonstrated in M<sup>c</sup>Hardy *et al.* (1989) where the temperature of the distant cluster A2218 was determined to 20% despite a flux of less than 0.5 mcrab.

*ROSAT* will be launched in 1990 and will provide an imaging all-sky survey in 0.1–2 keV to a limit of  $\sim 10^{-12}$  erg cm<sup>-2</sup> s<sup>-1</sup>. This survey will include approximately 10–20,000 clusters out to a redshift of 1.0. Clusters at moderate ( $z < 0.2$ ) redshifts should be distinguishable from stars and AGN by their extended emission. However diffuse sources can easily be missed in imaging surveys as shown by the *EINSTEIN* Medium Sensitivity Survey which is deficient in clusters due to the nature of the automatic point search algorithm used (Gioia *et al.* 1984). So great care will be needed when the survey data are processed. The catalogue of clusters produced will be an important dataset for further X-ray, optical and radio work. Once the all-sky survey is completed *ROSAT* will perform pointed observations on a number of targets with higher resolution and longer exposures than obtained in the survey. These observations will provide high quality surface brightness profiles for clusters.

A number of missions are scheduled to follow *ROSAT*, *e.g.* *Jet-X* and *ASTRO-D* (both due to be launched in 1993) which will have similar capabilities. They will provide 0.2–8 keV images with arcminute resolution. These missions will both be able to get spatially resolved spectra and hence model independent masses. They will also allow abundance gradients to be studied as the 6.7 keV iron line can be resolved.

Looking further ahead, the missions scheduled for the turn of the century *AXAF* and *XMM* will revolutionise all fields of astrophysics. Their large collecting areas (thousands of cm<sup>2</sup>) combined

with excellent spectral and spatial resolution will give a wealth of information on all classes of X-ray sources. The scientific potential of *AXAF* and *XMM* is vast. For instance, for clusters not only will the iron abundance be determined out to several core radii but the relative abundances of C,S,Si,Ca and other lines can be found which are of great astrophysical interest.

To illustrate just how large an improvement *AXAF* and *XMM* will be, each exposure with *AXAF* or *XMM* will detect about 100 serendipitous sources each with as much spectral information as an *EXOSAT* observation!

There is also a need for more optical data to complement the available X-ray data. Much of the work on X-ray-to-optical correlations and mass-to-light ratios was hampered by the lack of good quality optical data. Plate measuring machines can be used to obtain reliable galaxy distributions and magnitudes. The core radii and optical luminosities for clusters derived from these plate scans can provide a much better comparison for the X-ray data (Sharples, Ellis & Gray 1988).

# References

The following abbreviations for names of journals have been used:

<i>A. Adv. Space Res.</i>	Advanced Astronomy and Space Science Research
<i>Ann. Rev. Astron. Astrophys.</i>	Annual Reviews of Astronomy and Astrophysics
<i>Astrophys. J.</i>	Astrophysical Journal
<i>Astrophys. J. Suppl.</i>	Astrophysical Journal Supplement Series
<i>Astrophys. J. (Letters)</i>	Astrophysical Journal Letters to the Editor
<i>Astr. J.</i>	Astronomical Journal
<i>Astr. &amp; Astrophys.</i>	Astronomy & Astrophysics
<i>Astr. &amp; Astrophys. Suppl.</i>	Astronomy & Astrophysics Supplement Series
<i>Comm. Astrophys. Sp. Sci.</i>	Communications in Astrophysics and Space Science
<i>Mon. Not. R. astr. Soc.</i>	Monthly Notices of the Royal Astronomical Society
<i>Nucl. Instr. Meth.</i>	Nuclear Instrumentation and Methods (in Physics Research A)
<i>Publ. astr. Soc. Japan</i>	Publications of the Astronomical Society of Japan
<i>Sp. Sci. Rev.</i>	Space Science Reviews

- Abell, G.O. 1958. *Astrophys. J. Suppl.*, **3**, 211.
- Abell, G.O., Corwin, H.G. & Olowin, R.P. 1989. *Astrophys. J. Suppl.*, in press.
- Abramopoulos, F., Chanan, G. & Ku, W. 1981. *Astrophys. J.*, **248**, 429.
- Abramopoulos, F. & Ku, W. 1983. *Astrophys. J.*, **271**, 446.
- Andernach, H., Waldthausen, H. & Wielebinski, R. 1980. *Astr. & Astrophys. Supp.*, **41**, 339.
- Arnaud, K.A. 1987. preprint.
- Arnaud, K.A., Johnstone, R.M., Fabian, A.C., Crawford, C.S., Nulsen, P.E.J., Shafer, R.A. & Mushotzky, R.F. 1987. *Mon. Not. R. astr. Soc.*, **227**, 97.
- Arnaud, K.A. 1988a In *Cooling Flows in Galaxies and Clusters*, ed. A.C. Fabian Dordrecht: Reidel.
- Arnaud, K.A. 1988b Private communication.
- Bahcall, N.A. 1977a *Astrophys. J. (Letters)*, **217**, L77.
- Bahcall, N.A. 1977b *Astrophys. J. (Letters)*, **218**, L93.
- Bahcall, N.A. 1981. *Astrophys. J.*, **247**, 787.
- Bahcall, N.A. & Soniera, R.M. 1983. *Astrophys. J.*, **270**, 20.
- Bartel, N. 1988. In *The Impact of VLBI on Astrophysics and Geophysics*, eds. Reid, M.J. & Moran, J.M., p175.
- Bechtold, J., Forman, W., Giacconi, R., Jones, C., Schwartz, J., Tucker, W. & Van Speybroeck, L. 1983. *Astrophys. J.*, **265**, 26.
- Beers, T.C., Geller, M.J., Huchra, J.P., Latham, D.W. & Davis, R.J. 1984. *Astrophys. J.*, **283**, 33.
- Beers, T.C. & Tonry J.L. 1986. *Astrophys. J.*, **300**, 557.
- Bertschinger, E. & Meiksen, A. 1986. *Astrophys. J.*, **306**, L1.
- Bevington, P.R. 1969. *"Data Reduction and Error Analysis for the Physical Sciences"* Pub. McGraw-Hill Book Company.
- Biermann, P. & Shapiro, S.L. 1979. *Astrophys. J. (Letters)*, **230**, L33.
- Binggeli, B., Tammann, G.A. & Sandage, A. 1987. *Astr. J.*, **94**, 251.
- Binney, J. & Cowie, L. L. 1981. *Astrophys. J.*, **247**, 464.
- Birkinshaw, M. 1986. in *NRAO Greenbank Workshop No.16, Radio Continuum Processes in Clusters of Galaxies*, ed. C.P. O'Dea and J.M. Uson, p. 261.
- Blumenthal, G.R., Faber, S.M., Primack, J.R. & Rees, M.J. 1984. *Nature*, **311**, 517.
- Bond, J.R. & Szalay, A.S. 1983. *Astrophys. J.*, **274**, 443.
- Bookbinder, J., Cowie, L.L., Krolik, J.H., Ostriker, J.P. & Rees, M. 1980 *Astrophys. J.*, **237**, 647.
- Bradt, H., Mayer, W., Naranan, S., Rappaport, S. & Spuda, G. 1967. *Astrophys. J. (Letters)*, **161**, L1.
- Branduardi-Raymont, G., Fabricant, D., Feigelson, E., Gorenstein, P., Grindlay, J., Soltan, A. & Zamorani, G. 1981. *Astrophys. J.*, **248**, 55.

- Branduardi-Raymont, G., Mason, K.O., Murdin, P.G. & Martin, C. 1985a  
*Mon. Not. R. astr. Soc.*, **216**, 1043.
- Branduardi-Raymont, G., Kellet, B., Fabian, A.C., McGlynn, T., Manzo, G. & Peacock, A. 1985b  
*A. Adv. Space Res.*, Vol 5, No. 3, p. 129.
- Brinkman, C., Heise, J., den Boggende, A.J.F., Grindlay, J., Gursky, H. & Parsignault, D. 1977.  
*Astrophys. J.*, **214**, 35.
- Butcher, J.A. 1989. Private communication.
- Byram, E.T., Chubb, T.A. & Friedman, H. 1966. *Science*, **152**, 66.
- Canizares, C.R., Clark, G.W., Markert, T.H., Berg, C., Smedira, M., Bardas, D., Schnopper, H. & Kalata, K. 1979. *Astrophys. J. (Letters)*, **234**, L33.
- Canizares, C.R., Clark, G.W., Jernigan, J.G., & Market, T.H. 1982. *Astrophys. J.*, **262**, 33.
- Canizaries, C.R., Markert, T.H. & Donahue, M.E. 1988. In *Cooling Flows in Galaxies and Clusters*, ed. A.C. Fabian Dordrecht: Reidel 1988.
- Carnevali, P., Cavaliere, A. & Santangelo, P. 1981. *Astrophys. J.*, **249**, 449.
- Cavaliere, A. & Fusco-Femiano, R. 1976. *Astr. & Astrophys.*, **49**, 137.
- Cavaliere, A. & Colafrancesco, S. 1988. *Astrophys. J.*, **331**, 660.
- Chiappetti, L. & Giommi, P. 1985. *EXOSAT Express No.11*, 37.
- Cohen, J.G. 1988. *Astr. & Astrophys.*, **95**, 682.
- Colless, M.M. 1987. *Ph. D. Thesis*, University of Cambridge.
- Colless, M.M. 1988. preprint.
- Cowie, L.L. & Binney, J. 1977. *Astrophys. J.*, **215**, 723.
- Cowie, L.L., Fabian, A.C. & Nulsen, P.E.J. 1980. *Mon. Not. R. astr. Soc.*, **191**, 399.
- Cowie, L.L., Hu, E.M., Jenkins, E.B. & York, D.G. 1983. *Astrophys. J.*, **272**, 29.
- Cowie, L.L., Henriksen, M.J. & Mushotzky, R.F. 1987. *Astrophys. J.*, **317**, 593.
- de Souza, R. & Quintana, H. 1988. Private Communication.
- Danese, L., de Zotti, G. & di Tullio, G. 1980. *Astr. & Astrophys.*, **82**, 322.
- David, L.P., Arnaud, K.A., Forman, W. & Jones, C. 1988. preprint.
- Davison, P.J.N. 1978. *Mon. Not. R. astr. Soc.*, **183**, 39p.
- de Korte, P.A.J., Bleeker, J.A.M., den Boggende, A.J.F., Branduardi-Raymont, G., Brinkman, A.C., Culhane, J.L., Gronenschild, E.H.B.M., Mason, I. & M<sup>c</sup>Kechnie, S.P. 1981.  
*Sp. Sci. Rev.*, **30**, 495.
- de Vaucouleurs, G. 1948. *Contrib. Inst. Astrophys. Paris A*, No. 27.
- de Young, D.S 1978. *Astrophys. J.*, **223**, 47.
- Dickens, R.J., Currie, M.J. & Lucey, J.R. 1986. *Mon. Not. R. astr. Soc.*, **220**, 679.
- Dressler, A. 1978. *Astrophys. J.*, **226**, 55.

- Dressler, A. 1980a *Astrophys. J. Suppl.*, **42**, 565.
- Dressler, A. 1980b *Astrophys. J.*, **236**, 351.
- Edge, A.C., Stewart, G.C. & Smith, A. 1986. in *NRAO Greenbank Workshop No.16, Radio Continuum Processes in Clusters of Galaxies*, ed. C.P. O'Dea and J.M. Uson, p. 105.
- Edge, D.O. 1958. *Ph. D. Thesis*, University of Cambridge.
- Eyles, C.J. *et al.* 1989. In preparation.
- Ellis, R.S., Gray, P.M., Carter, D. & Godwin, J. 1984. *Mon. Not. R. astr. Soc.*, **206**, 285.
- Elvis, M., Schreier, E., Tonry, J., Davis, M. & Huchra, J. 1981. *Astrophys. J.*, **246**, 20.
- Fabian, A.C., Zarnecki, J.C., Culhane, J.L., Hawkins, F.J., Peacock, A., Pounds, K.A. & Parkinson, J.H. 1974. *Astrophys. J. (Letters)*, **189**, L59.
- Fabian, A.C. & Nulsen, P.E.J. 1977. *Mon. Not. R. astr. Soc.*, **180**, 479.
- Fabian, A.C., Schwartz, J. & Forman, W. 1980. *Mon. Not. R. astr. Soc.*, **192**, 135.
- Fabian, A.C., Hu, E.M., Cowie, L.L. & Grindlay, J. 1981. *Astrophys. J.*, **248**, 47.
- Fabian, A.C., Nulsen, P.E.J. & Canizaries, C.R. 1982. *Mon. Not. R. astr. Soc.*, **201**, 933.
- Faber, S.M. & Gallagher, J.S. 1979. *Ann. Rev. Astron. Astrophys.*, **59**, L5.
- Fabricant, D. & Gorenstein, P. 1983. *Astrophys. J.*, **267**, 535.
- Fanti, C., Fanti, R., Feretti, L., Ficara, A., Gioia, I.M., Giovanni, G., Gregorini, L., Mantovani, F., Marano, B., Padrielle, Parma, P., Tomasi, P. & Vettolani, G. 1982. *Astr. & Astrophys.*, **105**, 200.
- Fernley, J.A. & Bhavsar, S.P. 1984. *Mon. Not. R. astr. Soc.*, **210**, 883.
- Fitchett, M. & Webster, R. 1987. *Astrophys. J.*, **317**, 653.
- Fitchett, M. & Merritt, D. 1988. *Astrophys. J.*, **335**, 18.
- Fitchett, M. 1988. preprint.
- Forman, W., Schwartz, J., Jones, C., Liller, W. & Fabian, A.C. 1979. *Astrophys. J. (Letters)*, **234**, L27.
- Forman, W., Bechtold, J., Blair, W., Giacconi, R., Van Speybroeck, L. & Jones, C. 1981. *Astrophys. J.*, **243**, L133.
- Fraser, G.W., Pearson, J.F. & Lees, J.E. 1987. *Nucl. Instr. Meth.*, **A254**, 447.
- Frenk, C. 1988. preprint.
- Giacconi, R., Murray, S., Gursky, H., Kellogg, E.M., Schreier, E. & Tananbaum, H. 1972. *Astrophys. J.*, **178**, 281.
- Giacconi, R. *et al.* 1979. *Astrophys. J.*, **230**, 540.
- Gioia, I.M., Maccacaro, T., Schild, R.E., Stocke, J.T., Liebert, J.W., Danziger, I.J., Kunth, D. & Lub, J. 1984. *Astrophys. J.*, **283**, 495.
- Giovanelli, R. & Haynes, M.P. 1985. *Astrophys. J.*, **292**, 404.
- Gorenstein, P., Fabricant, D., Topka, K., Hardern, F.R., Jr. & Tucker, W.H. 1978. *Astrophys. J.*, **224**, 718.

- Green, M.R., Godwin, J.G. & Peach, J.V. 1988. *Mon. Not. R. astr. Soc.*, **234**, 1051.
- Gregory, S.A. & Thompson, L.A. 1984. *Astrophys. J.*, **286**, 422.
- Gunn, J.E. & Gott, J.R. 1972. *Astrophys. J.*, **176**, 1.
- Gursky, H., Kellogg, E., Leong, C., Tananbaum, H. & Giacconi, R. 1971a  
*Astrophys. J. (Letters)*, **165**, L43.
- Gursky, H., Kellogg, E., Murray, S., Leong, C., Tananbaum, H. & Giacconi, R. 1971b  
*Astrophys. J. (Letters)*, **167**, L81.
- Hanisch, R.J. & Ulmer, M.P. 1985. *Astr. J.*, **90**, 1407.
- Hanisch, R.J. 1986. in *NRAO Greenbank Workshop No.16, Radio Continuum Processes in Clusters of Galaxies*, ed. C.P. O'Dea and J.M. Uson, p. 191.
- Harris, D.E., Costain, C.H. & Dewdney, P.E. 1984. *Astrophys. J.*, **280**, 532.
- Heiles, C. 1975. *Astr. & Astrophys. Suppl.*, **20**, 37.
- Henriksen, M.J. & Mushotzky, R.F. 1985. *Astrophys. J.*, **292**, 441.
- Henriksen, M.J. & Mushotzky, R.F. 1986. *Astrophys. J.*, **302**, 287.
- Henry, J.P., Henriksen, M.J., Charles, P.A. & Thorstensen, J.R. 1981. *Astrophys. J.*, **243**, L137.
- Henry, J.P., Soltan, A., Briel, U. & Gunn, J.E. 1982. *Astrophys. J.*, **262**, 1.
- Hill, J.M., Hintzen, P., Oegerle, W.R., Romanishin, W., Lesser, M.P., Eisenhamer, J.D. & Batuski, D.J. 1988. *Astrophys. J.*, **332**, L23.
- Hintzen, P. & Scott, J.S. 1979. *Astrophys. J. (Letters)*, **232**, L145.
- Hintzen, P., Hill, J.M., Lindley, D., Scott, J.S. & Angel, J.R.P. 1982. *Astr. J.*, **87**, 1656.
- Hoessel, J.G., Gunn, J.E. & Thuan, T.X. 1980. *Astrophys. J.*, **241**, 486.
- Hu, E.M., Cowie, L.L. & Wang, Z. 1985. *Astrophys. J. Suppl.*, **59**, 447.
- Hughes, J.P., Yamashita, K., Okumura, Y., Tsumemi, H. & Matsuoka, M. 1988.  
*Astrophys. J.*, **327**, 615.
- Hughes, J.P., Gorenstein, P. & Fabricant, D. 1988. *Astrophys. J.*, **329**, 82.
- Hughes, J.P. 1989. *Astrophys. J.*, in press.
- Johnstone, R.M., Fabian, A.C. & Nulsen, P.E.J. 1987. *Mon. Not. R. astr. Soc.*, **224**, 75.
- Jones, C. & Forman, W. 1984. *Astrophys. J.*, **276**, 38.
- Kaastra, J.S. & de Korte, P.A.J. 1988. *Astr. & Astrophys.*, **192**, 77.
- Kaiser, N. 1986. *Mon. Not. R. astr. Soc.*, **222**, 323.
- Kellogg, E.M., Gursky, H., Tananbaum, H., Giacconi, R. & Pounds, K.A. 1972.  
*Astrophys. J. (Letters)*, **174**, L65.
- Kellogg, E.M., Baldwin, J. R. & Koch, D. 1975. *Astrophys. J.*, **191**, 299.
- Kent, S.M. & Sargent, W.L.W. 1979. *Astrophys. J.*, **230**, 667.

- Kent, S.M. 1981. *Astrophys. J.*, **245**, 805.
- Kent, S.M. & Gunn, J.E. 1982. *Astr. J.*, **87**, 945.
- Kent, S.M. & Sargent, W.L.W. 1983. *Astr. J.*, **88**, 697.
- King, I.R. 1966. *Astr. J.*, **71**, 64.
- Laing, R.A. & Bridle, A.H. 1987. *Mon. Not. R. astr. Soc.*, **228**, 557.
- Lahav, O., Rowan-Robinson, M. & Lynden-Bell, D. 1988. *Mon. Not. R. astr. Soc.*, **234**, 677.
- Lahav, O., Edge, A.C., Fabian, A.C. & Putney, A. 1989. *Mon. Not. R. astr. Soc.*, **238**, 881.
- Lawrence, A. 1978. *Mon. Not. R. astr. Soc.*, **185**, 423.
- Lea, S.M. & de Young, D.S. 1976. *Astrophys. J.*, **210**, 647.
- Lea, S.M., Reichart, G., Mushotzky, R.F., Baity, W.A., Gruber, D.A., Rothschild, R.E. & Primini, F.A. 1981. *Astrophys. J.*, **246**, 369.
- Lea, S.M., Mushotzky, R.F. & Holt, S.S. 1982. *Astrophys. J.*, **262**, 24.
- Loewenstein, M. & Fabian, A.C. 1989. *Mon. Not. R. astr. Soc.*, submitted.
- Lucey, J.R., Currie, M.J. & Dickens, R.J. 1986a *Mon. Not. R. astr. Soc.*, **221**, 453.
- Lucey, J.R., Currie, M.J. & Dickens, R.J. 1986b *Mon. Not. R. astr. Soc.*, **222**, 427.
- Lynden-Bell, D. 1967. *Mon. Not. R. astr. Soc.*, **136**, 101.
- Matilsky, T., Jones, C. & Forman, W. 1985. *Astrophys. J.*, **291**, 621.
- Magri, C., Haynes, M.P., Forman, W., Jones, C. & Giovanelli, R. 1988. *Astrophys. J.*, **333**, 136.
- Markert, T., Winkler, P., Laird, F., Clark, G., Hearn, D., Sprott, G., Li, F., Bradt, V., Lewin, W. & Schnopper, H. 1979. *Astrophys. J. Suppl.*, **39**, 573.
- Materne, J. & Hopp, U. 1983. *Astr. & Astrophys.*, **124**, L13.
- M<sup>c</sup>Glynn, T.A. & Fabian, A.C. 1984. *Mon. Not. R. astr. Soc.*, **208**, 709.
- M<sup>c</sup>Hardy, I.M. 1978. *Mon. Not. R. astr. Soc.*, **184**, 783.
- M<sup>c</sup>Hardy, I.M. 1979. *Mon. Not. R. astr. Soc.*, **188**, 495.
- M<sup>c</sup>Hardy, I.M., Stewart, G.C., Edge, A.C., Cooke, B., Yamashita, K. & Hatsukade, I. 1989. *Mon. Not. R. astr. Soc.*, in press.
- M<sup>c</sup>Kee, J.D., Mushotzky, R.F., Boldt, E.A., Holt, S.S., Marshall, F.E., Pravdo, S.H. & Serlemitsos, P.J. 1980. *Astrophys. J.*, **242**, 843.
- Mellier, Y., Mathez, G., Mazure, A., Chauvineau, B. & Proust, D. 1988. *Astr. & Astrophys.*, **199**, 67.
- Melnick, J. & Sargent, W.L.W. 1977. *Astrophys. J.*, **215**, 401.
- Milgrom, M. 1983a *Astrophys. J.*, **270**, 365.
- Milgrom, M. 1983b *Astrophys. J.*, **270**, 371.
- Milgrom, M. 1983c *Astrophys. J.*, **270**, 384.

- Miller, L. 1986. *Mon. Not. R. astr. Soc.*, **220**, 713.
- Miller, R.H. 1988. *Comments on Astrophysics.*, Vol. **13**, 1.
- Mitchell, R.J., Culhane, J.L., Davison, P.J. & Ives, J.C. 1976. *Mon. Not. R. astr. Soc.*, **176**, 29p.
- Mitchell, R.J., Dickens, R.J., Bell Burnell, S.J. & Culhane, J.L. 1979.  
*Mon. Not. R. astr. Soc.*, **189**, 329.
- Mitchell, R.J. & Mushotzky, R.F. 1980. *Astrophys. J.*, **236**, 730.
- Morrison, R. & McCammon, D. 1983. *Astrophys. J.*, **270**, 119.
- Moss, C. & Dickens, R.J. 1977. *Mon. Not. R. astr. Soc.*, **178**, 701.
- Mould, J.R., Aaronson, M. & Huchra, J. 1980. *Astrophys. J.*, **238**, 458.
- Mould, J.R., Oke, J.B. & Nemec, J.M. 1987. *Astr. J.*, **92**, 53.
- Mushotzky, R.F., Serlemitsos, P.J., Smith, B.W., Boldt, E.A. & Holt, S.S. 1978. *Astrophys. J.*, **225**, 21.
- Mushotzky, R.F., Holt, S.S., Smith, B.W., Boldt, E.A. & Serlemitsos, P.J. 1981.  
*Astrophys. J. (Letters)*, **244**, L47.
- Mushotzky, R.F. 1984. *Physica Scripta*. Vol.T7, 157.
- Mushotzky, R.F. & Szymkowiak, A.E. 1988. In *Cooling Flows in Galaxies and Clusters*, ed. A.C. Fabian Dordrecht: Reidel.
- Mushotzky, R.F. 1988. in proceedings of NATO ASI "Hot Thin Plasmas in Astrophysics" ed Pallavacini, Reidel, p.273.
- O'Dea, C.P. & Owen, F.N. 1985a *Astr. J.*, **90**, 927.
- O'Dea, C.P. & Owen, F.N. 1985b *Astr. J.*, **90**, 954.
- Okumura, Y., Tsunemi, H., Yamashita, K., Matsuoka, M., Koyama, K., Hayakawa, S., Masai, K. & Hughes, J.P. 1988. *Publ. astr. Soc. Japan*, **40**, 639.
- Owen, F.N., White, R.A., Hilldrup, K.C. & Hanisch, R.J. 1982. *Astr. J.*, **87**, 1083.
- Pallister, I.C. 1985. *Mon. Not. R. astr. Soc.*, **215**, 335.
- Parker, Q.A., MacGillivray, H.T., Hill, P.W. & Dodd, R.J. 1986. *Mon. Not. R. astr. Soc.*, **220**, 901.
- Parmar, A.N. & Izzo, C. 1986. *EXOSAT Express No.16*, 21.
- Perrenod, S.C. 1980. *Astrophys. J.*, **236**, 373.
- Piccinotti, G., Mushotzky, R.F., Boldt, E.A., Holt, S.S., Marshall, F.E., Serlemitsos, P.J. & Shafer, R.A. 1982. *Astrophys. J.*, **253**, 485.
- Piro, L. & Fusco-Femiano, R. 1988. *Astr. & Astrophys.*, **205**, 26.
- Phillips, M.M. & Malin, D.F. 1982. *Mon. Not. R. astr. Soc.*, **199**, 905.
- Postman, M., Huchra, J.P., Geller, M.J. & Henry, J.P. 1985. *Astr. J.*, **90**, 1400.
- Primini, F.A., Basinska, E., Howe, S.K., Lang, F., Levine, A.M., Lewin, W.H.G., Rothschild, R., Baity, W.A., Gruber, D.E., Knight, F.K. & Matteson, J.L. 1981. *Astrophys. J. (Letters)*, **243**, L13.
- Pryor, C. & Geller, M.J. 1984. *Astrophys. J.*, **278**, 457.

- Quintana, H. & Melnick, J. 1982. *Astr. J.*, **87**, 972.
- Quintana, H., Melnick, J., Infante, L. & Thomas, B. 1985. *Astr. J.*, **90**, 410.
- Raphaelli, Y. 1987. *Mon. Not. R. astr. Soc.*, **225**, 851.
- Raymond, J.C., Cox, D.P. & Smith, B.W. 1976. *Astrophys. J.*, **204**, 290.
- Raymond, J.C. & Smith, B.W. 1977. *Astrophys. J. Suppl.*, **35**, 419.
- Richter, O.-G., Materne, J. & Huchtmeier, W.K. 1982. *Astr. & Astrophys.*, **111**, 193.
- Rosner, R. & Tucker, W.H. 1989. *Astrophys. J.*, in press.
- Rothenflug, R. & Arnaud, M. 1985. *Astr. & Astrophys.*, **144**, 431.
- Rothschild, R., Baity, W.A., Marscher, A.P. & Wheaton, W.A. 1981. *Astrophys. J. (Letters)*, **243**, L9.
- Rudnick, L. & Birkinshaw, M. 1986. in *NRAO Greenbank Workshop No.16, Radio Continuum Processes in Clusters of Galaxies*, ed. C.P. O'Dea and J.M. Uson, p. 339.
- Salpeter, E.E. 1988. in proceedings of NATO ASI "Hot Thin Plasmas in Astrophysics" ed Pallavicini, Reidel, p.261.
- Sarazin, C.L. 1988. "X-ray Emissions from Clusters of Galaxies", Cambridge University Press.
- Sargent, W.L.W., Young, P.J., Boksenberg, A., Shortridge, K., Lynds, C.R. & Hardwick, F.D.A. 1978. *Astrophys. J.*, **211**, 731.
- Scalo, J.M. & Struck-Marcell, C. 1986. *Astrophys. J.*, **301**, 77.
- Schnopper, H.W., Devaille, J.P., Epstein, A., Helmken, H., Harris, D.E., Strom, R.G., Clark, G.W. & Jernigan, J.G. 1977. *Astrophys. J. (Letters)*, **217**, L15.
- Schombert, J.M. 1986. *Astrophys. J. Suppl.*, **60**, 603.
- Schombert, J.M. 1987. *Astrophys. J. Suppl.*, **64**, 643.
- Schombert, J.M. 1988. *Astrophys. J.*, **328**, 475.
- Schreier, E.J., Gorenstein, P. & Feigelson, E.D. 1982. *Astrophys. J.*, **261**, 42.
- Semeniuk, I. 1982. *Acta Astronomica.*, **30**, 337
- Serlemitsos, P.J., Smith, B.W., Boldt, E.A., Holt, S.S. & Swank, J.H. 1977. *Astrophys. J. (Letters)*, **211**, L63.
- Sharples, R.M., Ellis, R.S & Gray, P.M. 1988. *Mon. Not. R. astr. Soc.*, **231**, 479.
- Silk, J., Djorgovski, G., Wyse, R.F.G. & Bruzal, G.A. 1986. *Astrophys. J.*, **307**, 415.
- Singh, K.P., Westergaard, N.J. & Schnopper, H.W. 1986. *Astrophys. J.*, **308**, L51.
- Singh, K.P., Westergaard, N.J. & Schnopper, H.W. 1988a *Astrophys. J.*, **330**, 620.
- Singh, K.P., Westergaard, N.J. & Schnopper, H.W. 1988b *Astrophys. J.*, **331**, 672.
- Skillman, E.D., Bothun, G.D., Murray, M.A. & Warmels, R.H. 1987. *Astr. & Astrophys.*, **185**, 61.
- Smith, B., Mushotzky, R.F. & Serlemitsos, P. 1979. *Astrophys. J.*, **227**, 37.
- Stark, A.A, Bally, J. Heiles, C. & Linke, R.A. 1988. Private communication.

- Stewart, G.C., Canizares, C.R., Fabian, A.C. & Nulsen, P.E.J. 1984a *Astrophys. J.*, 278, 536.
- Stewart, G.C., Fabian, A.C., Jones, C. & Forman, W. 1984b *Astrophys. J.*, 285, 1.
- Struble, M.F. & Rood, H.J. 1987. *Astrophys. J. Suppl.*, 63, 543.
- Sunyaev, R.A. & Zel'dovich, Ya.B. 1972. *Comm. Astrophys. Sp. Sci.* 4, 173.
- Tadeka, H., Nulsen, P.E.J. & Fabian, A.C. 1984. *Mon. Not. R. astr. Soc.*, 208, 261.
- Tarengi, M., Chincarini, G., Rood, H.J. & Thompson, L.A. 1980 *Astrophys. J.*, 235, 724.
- The, L.S. & White, S.D.M. 1986. *Astr. J.*, 92, 1248.
- The, L.S. & White, S.D.M. 1988a *Astr. J.*, 95, 15.
- The, L.S. & White, S.D.M. 1988b *Astr. J.*, 95, 1642.
- Tucker, W.H. & Rosner, R. 1982. *Astrophys. J.*, 267, 547.
- Tully, R.B. 1988. *Nature*, 334, 209.
- Turner, M.J.L., Smith, A. & Zimmerman, H.U. 1981. *Sp. Sci. Rev.*, 30, 479.
- Turner, T.J. 1988. *Ph. D. Thesis*, University of Leicester.
- Ulmer, M.P., Cruddace, R.G., Fenimore, E.E, Fritz, G.G. & Snyder, W.A. 1987. *Astrophys. J.*, 319, 118.
- Uson, J.M. 1986. in *NRAO Greenbank Workshop No.16, Radio Continuum Processes in Clusters of Galaxies*, ed. C.P. O'Dea and J.M. Uson, p. 225.
- Valentijn, E.A. & Bijleveld, W. 1983. *Astr. & Astrophys.*, 125, 223.
- van de Laan, H. & Perola, G.C. 1969. *Astr. & Astrophys.*, 3, 468.
- West, M.J., Oemler, A. & Dekel A. 1988. *Astrophys. J.*, 327, 1.
- White, N.E. & Peacock, A. 1988. preprint.
- White, R.A., Sarazin, C.L., Quintana, H. & Jaffe, W.J. 1981. *Astrophys. J. (Letters)*, 245, L1.
- White, S.D.M. 1976. *Mon. Not. R. astr. Soc.*, 177, 717.
- Wolf, M. 1906. *Astron. Nachr.* 170, 211.

## Acknowledgements

I acknowledge financial support from the SERC.

None of the work done for this thesis would have been possible without the software system built up through the combined effort of many people but most notably Dick Willingale, Mike Watson, Clive Page and Gordon Stewart. I may have sworn long and loud at the computer but never at the software! Nor would it have been possible without the efficiency and skill of the *EXOSAT* observatory team.

I must congratulate Gordon Stewart for putting up with me for 3 (and a bit) years and providing me with advice when all my wild ideas died. There are many people within the group who have helped make this sojourn bearable; Ian George, for following me to Cambridge (before I left!); Jane (né Tracey) Turner, for showing me how to finish a thesis; Alan Fitzsimmons, for being “wackier” than me; Loz Breedon, for her “no nonsense” attitude to life; Paul Nandra, for showing me how to play ‘golf’; Hongchao Pan, for excellent Chinese food; Jane Page, for talks between the boredom; John Lees, for finishing at the same time as me; Rees Williams, for the ‘free’ beers; but most of all my office-mates Andy Norton, Jackie Butcher and Mark H. Jones with whom I have shared many a problem and a laugh. I would also like to thank Andy Fabian for believing in me and providing the carrot at the end of the tunnel!

Surviving a PhD. is not just a matter of work, but also all those people who will listen to your problems whether they understand them or not! To friends across the country, Peter Luty, Jenny Pope, Keith Shipman, Anne Lane, all the residents of 4 Batten St. (past and present) and the 52 Knighton Drive Crew I salute your patience. I must thank my parents for going well beyond the bounds of parental duty keeping me over the final months and the rest of my family across the world (Grandmother(s), Gordon, Aran and Mark) for their love and support. Last, but most important, the person I owe the most to over the last 3 years is Irena Lentowicz who made so much possible and to whom I dedicate this thesis.

# X-RAY EMISSION FROM CLUSTERS OF GALAXIES

Alastair C. Edge

## Abstract

Clusters of galaxies are the largest gravitationally bound systems known. The study of clusters can therefore provide information on the distribution of matter in the Universe on the largest scales. The X-ray emission from clusters is of particular interest, as the gas held within the gravitational potential well of a cluster responds to the total mass ('Dark' and 'Visible') of that cluster.

This thesis is based upon a sample of 44 observations of clusters made by *EXOSAT* which provided both imaging and spectral data. The data give well determined luminosities, temperatures, iron abundances and mass flow rates for these clusters. The results provide constraints on models for cluster dynamics and formation.

The theoretical models and previous observations of clusters are reviewed in Chapter 1, concentrating on the X-ray domain. The results from the imaging telescopes and proportional counters are given in Chapters 2 and 3. Detailed observations of Virgo, Coma and Perseus are described in Chapter 4. A correlation analysis of the X-ray, optical and radio results is presented in Chapter 5. The implications of these correlations are discussed in Chapter 6. The thesis concludes with a brief look forward to future missions.